Università degli Studi di Napoli Federico II

Scuola Politecnica e delle Scienze di Base

Dipartimento di Ingegneria Industriale

PhD Thesis

INNOVATIVE APPROACHES FOR TYRE CHARACTERIZATION AIMED AT ROAD CONTACT MODELLING FOR AUTOMOTIVE APPLICATIONS

SUPERVISORS
Prof. Eng. Riccardo Russo
Prof. Eng. Flavio Farroni

PhD CANDIDATE
Eng. Antonio Maiorano

PhD COORDINATOR
Prof. Eng. Michele Grassi

XXXIII CICLO

Non si scoprirebbe mai niente se ci si considerasse soddisfatti di quello che si è scoperto.

Lucio Anneo Seneca

Aknowledgments

The following PhD can be considered as the synthesis of three wonderful years of research lived with passion at the Industrial Engineering Department of the University of Naples Federico II. The results described would never have been achieved if I had not received the invaluable support of my tutors, Prof. Eng. Riccardo Russo and Prof. Eng. Flavio Farroni, who inspired and led me throughout the entire course. I would also thank the Prof. Eng. Francesco Timpone, who has always been a figure you can always count on not only for professional and academic issues, but also for what concerns extra-academic life. I also extend a warm thanks to Prof. Eng. Aleksandr Sakhnevych, Prof. Eng. Andrea Genovese and Eng. Francesco Carputo, who have always been central figures to deal with in the elaboration of this thesis, as well as the other members of the Applied Mechanics research group of the Industrial Engineering Department. Finally, I will forever thank my loved ones, because they have always believed in me and have given me support to move forward in the darkest moments of these three years.

Naples, July 12, 2021

Antonio Maiorano

Table of contents

List of Figures

List of Tables

Nomenclature

Chapter 1

Symbol	Description	Units
γ	Camber Angle	rad
α	Side slip angle	rad
F_x	Global longitudinal interaction force	N
F_y	Global lateral interaction force	N
F_z	Global vertical interaction force	N
M_x	Global roll moment	Nm
M_y	Global pitch moment	Nm
M_z	Global yaw moment	Nm
V_x	Longitudinal velocity of the tyre	m/s
V_y	Lateral velocity of the tyre	m/s
Ω	Wheel angular velocity	rad/s
R	Rolling radius	m
s_x	Longitudinal slip ratio	(-)
s_y	lateral slip ratio	(-)
$s_{x,BT}$	Longitudinal slip ratio, braking conditions	(-)
$s_{x,DT}$	Longitudinal slip ratio, driving conditions	(-)
C_x	Tyre braking/driving stiffness	N/m
$C_{y,\alpha}$	Tyre cornering stiffness	N/rad
$C_{y,\gamma}$	Tyre stiffness with respect the camber thrust	N/rad

Chapter 2

σ	Applied stress	Pa
η	Dynamic viscosity coefficient	Pa/s
ε	Material strain	(-)
J	Creep compliance modulus	Pa^{-1}
E	Stress relaxation modulus	Pa
ω	Solicitation frequency	rad/s
δ	Stress-strain phase angle	rad
E^*	Dynamic complex modulus	Pa
$E'(E_1)$	Viscoelastic storage modulus	Pa
$E''(E_2)$	Viscoelastic loss modulus	Pa
$\tan(\delta)$	Viscoelastic loss factor	(-)

T_g	Glass transition temperature	K
T_0	Reference temperature	K
a_T	Frequency shift factor	(-)
C_1	William-Landel-Ferry equation coefficient	(-)
C_2	William-Landel-Ferry equation coefficient	K
E_a	Activation energy	J
R	Gas universal constant	$JK^{-1}mol^{-1}$
a_i, b_i	Viscoelastic model parameters	(-)
M_0, M_i	Spring stiffness constant	N/m
μ, μ_i	Dashpot viscosity constant	Nsm^{-1}
$\overline{\sigma}, \overline{\varepsilon}$	Fourier Transform of stress/strain	(-)
α_i, β_i	Orders of fractal derivatives	(-)
E_0	Viscoelastic storage modulus at low frequency	Pa
E_∞	Viscoelastic storage modulus at high frequency	Pa
τ_r	Relaxation time	s
ω_p, ω_z	Pole and zero coefficients	(rad/s)

Chapter 3

S	Quasi-static stiffness	N/m
f	Indentation force	N
h	Indentation depth	m
S_h	Quasi-static stiffness depending on indentation depth	N/m
$\tan(\delta)$	Viscoelastic loss factor	(-)
Δt	Time displacement between applied force and corresponding strain	s
ω	Pulsating frequency	rad/s
Z^*	Complex impedance of the dynamic contact model	(-)
R_M	Mechanical resistance of the dynamic contact model	(-)
X_M	Mechanical reactance of the dynamic contact model	(-)
M	Moving mass	kg
S_M^0	Elastance of the instrument spring	(-)
S_M	Elastance of the compound	(-)
P_0	Magnitude of the force oscillation	N
h_0	Magnitude of the displacement oscillation	m
m	System mass	kg
K_s	System spring stiffness	N/m
C_s	System damping coefficient	Ns/m

$\boldsymbol{\delta}$	Phase angle	rad
$\boldsymbol{C_s}$	System damping coefficient	Ns/m
$\boldsymbol{E_r}$	Sample reduced modulus	N/m^2
$\boldsymbol{r}$	Contact radius	m
$\boldsymbol{A_c}$	Tip-sample contact area	m^2
$\boldsymbol{E_s}$	Elastic modulus of the sample	N/m^2
$\boldsymbol{\nu_s}$	Poisson’s coefficient of the sample	(-)
$\boldsymbol{E_i}$	Elastic modulus of the indenter	N/m^2
$\boldsymbol{\nu_i}$	Poisson’s coefficient of the indenter	(-)
$\boldsymbol{E_r'}$	Reduced storage modulus	N/m2
$\boldsymbol{E_r''}$	Reduced loss modulus	N/m2
$\boldsymbol{F}$	Indentation force of Shore A durometer	N
$\boldsymbol{B_1, B_2, B_3}$	Fitting coefficient of Shore A durometer	(-)
$\boldsymbol{H_{S_A}}$	Hardness value measured through Shore A durometer	(-)
$\boldsymbol{E'}$	Viscoelastic storage modulus	N/m^2
$\boldsymbol{E''}$	Viscoelastic loss modulus	N/m^2
$\boldsymbol{\alpha}$	Damping coefficient for a propagating wave in a medium	dB/mm
$\boldsymbol{c}$	Measured sound velocity in a medium	m/s
$\boldsymbol{A_0}$	Amplitude of the transmitted ultrasonic wave	dB
$\boldsymbol{A_1}$	Amplitude of the front echo	dB
$\boldsymbol{A_2}$	Amplitude of the back echo	dB
$\boldsymbol{A_1'}$	Amplitude of the secondary front echo	dB
$\boldsymbol{\varepsilon}$	Cost function to optimize	dB
$\boldsymbol{A_{1_{EVAL}}, A'_{1_{EVAL}}}$	Estimated amplitudes of the echoes of interest	dB
$\boldsymbol{D_w}$	Attenuation coefficient for a wave propagating in the water delay line	(-)
$\boldsymbol{R_{wc}^*}$	Complex reflection coefficient at water-compound interface	(-)
$\boldsymbol{T_{wp}}$	Transmission coefficient at water-probe interface	(-)
$\boldsymbol{R_{wp}}$	Reflection coefficient at water-probe interface	(-)
$\boldsymbol{Z_c^*}$	Complex acoustic impedance of viscoelastic compound	kgs^2/m
$\boldsymbol{Z_w}$	Water acoustic impedance	kgs^2/m
$\boldsymbol{\rho}$	Compound density	kg/m^3
$\boldsymbol{V_0}$	Applied voltage amplitude	V
$\boldsymbol{I_0}$	Measured current amplitude	A
$\boldsymbol{R}$	Resistance of the equivalent electrical circuit	Ω
$\boldsymbol{C}$	Capacitance of the equivalent electrical circuit	F
$\boldsymbol{Z', Z''}$	Real and imaginary part of the impedance of the equivalent circuit	Ω
$\boldsymbol{\epsilon_r}$	Relative permittivity	J^{-1} C^2 m^{-1}

ϵ_0	Vacuum permittivity	$\mathrm{J^{-1}\ C^{2}\ m^{-1}}$
ϵ^*	Complex permittivity of the compound	$\mathrm{J^{-1}\ C^{2}\ m^{-1}}$
ϵ', ϵ''	Real and imaginary part of the complex permittivity	$\mathrm{J^{-1}\ C^{2}\ m^{-1}}$
M^*	Dielectric modulus of the compound	$\mathrm{J\ C^{-2}\ m}$
d	Distance between electrodes	m
A	Area of the smallest electrode	$\mathrm{m^2}$
a, b	Radius of the inner and outer electrodes	m
l	Length of the electrode	m
$y(t)$	VESevo rod position	m
y_0	VESevo indenter start contact position	mm
ω_S	VESevo damped frequency	Rad/s
ϕ	Phase angle	rad
α_s	Extinction coefficient	$\mathrm{s^{-1}}$
ε_s	Cost function	m
ω_N	VESevo natural frequency	rad/s
K_c	VESevo indenter-compound contact stiffness	N/m
σ_c	VESevo indenter-compound contact damping coefficient	Ns/m
m_{rod}	VESevo indenter mass	kg
ζ_c	VESevo characteristic damping ratio	(-)
A_c	Contact area of the VESevo rod with the compound	$\mathrm{m^2}$
s_{Min}	Maximum indentation depth of the VESevo indenter	m
r_c	Contact radius of VESevo indenter	m
r_{rod}	VESevo indenter radius	m

Chapter 4

z	Roughness profile	m
σ	Roughness profile standard deviation	m
m	Roughness profile mean value	m
$\phi(z)$	Probability density function	1/m
z^*	Standard normalized roughness profile	(-)
$\phi(z^*)$	Probability density function of the standard normalized roughness profile	(-)
R_a	Roughness profile mean line	m
σ^2	Roughness profile variance	$\mathrm{m^2}$
R_q	Roughness profile root means square	m
S_k	Roughness profile skewness	(-)
K	Roughness profile kurtosis	(-)

N_p	Number of peaks per unit length	1/m
N_0	Number of times the profile crosses the mean line per unit length	1/m
λ_a	Average wavelength number of the profile	m
Δ_a	Mean slope of the roughness profile	(-)
D	Fractal dimension of self-affine profile	(-)
δ	Dimension of the Euclidean space	(-)
H	Hurst exponent	(-)
$\xi_{\parallel}$	Parallel correlation length of the profile	m
$\xi_{\perp}$	Perpendicular correlation length of the profile	m
C_z	Height difference correlation function	m^2
λ	Horizontal wavelength	m
Γ_z	Auto-correlation function of the profile	m^2
λ_x	Horizontal wavelength between macro and micro roughness scale	m
H_M	Hurst exponent of macro roughness scale	(-)
H_m	Hurst exponent of micro roughness scale	(-)
ω	Frequency associated with the horizontal wavelength	rad/s
$S(\omega)$	Power spectrum density of the self-affine profile	m^3
$S_M(\omega)$	Power spectrum density of the self-affine profile in the macro scale	m^3
$S_m(\omega)$	Power spectrum density of the self-affine profile in the micro scale	m^3
ω_{min}	Frequency associated with the maximum horizontal wavelength	rad/s
ω_x	Frequency associated with the switching horizontal wavelength	rad/s
β_M	Power spectrum slope in the macro roughness scale	(-)
β_m	Power spectrum slope in the micro roughness scale	(-)
v	Rubber sliding velocity on the substrate	m/s
q	Space wavenumber vector of the PSD	rad/m
C_{1D}	Power spectrum density for 1D profile data (Persson's nomenclature)	m^3
C_{2D}	Power spectrum density for 2D surface data (Persson's nomenclature)	m^4
$\overline{C}_{2D}$	Angular average of the PSD of 2D data	m^4
λ_{min}	Minimum contact length of micro scale roughness profile	m
d	Distance between the rubber and concrete substrate reference line	m
P	Contact pressure between the rubber and concrete substrate reference line	Pa
n_s	Macroscopic summit density distribution	m^{-2}
R	Radius of the spherical indenter associated to the macro asperity	m
m_2	Second spectral moment of the roughness profile	m^{-2}
m_4	Fourth spectral moment of the roughness profile	m^{-4}
F_0	Greenwood-Williamson for exponent equal to zero	m^2
$F_{\frac{3}{2}}$	Greenwood-Williamson for exponent equal to 3/2	m^2

z_s	Summit heights profile	m
s	Affine transformation parameter	(-)
ϕ_s	Summit height normal distribution	(-)
$\tilde{n}_s$	Microscopic summit density distribution	(-)
σ_s	Standard deviation of the summit height profile	m
t	Normalised gap between the rubber and the substrate reference line	(-)
t_s	Normalised gap between the rubber and the substrate reference line	(-)
h'_{rms}	Root mean square slope of the profile	m
q_{min}	Minimum space wavenumber vector of the PSD	rad/m
q_{max}	Maximum space wavenumber vector of the PSD	rad/m
${\mu'}_{hys}$	Simplified viscoelastic friction coefficient	(-)

Chapter 5

F_T	Total frictional resistance	N
F_A	Adhesive frictional contribution	N
F_H	Hysteretic frictional contribution	N
F_C	Cohesion loss contribution	N
u_z	Displacement along z direction during indentation	m
R	Rigid sphere radius	m
r	Radial direction	m
d	Indentation depth	m
p	Contact pressure at distance r from the centre	Pa
p_0	Maximum contact pressure at $r = 0$	Pa
a	Effective contact radius (Hertz theory)	m
E^*	Dynamic modulus	Pa
E_I	Dynamic modulus of the indented substrate	Pa
E_{II}	Dynamic modulus of the rigid indenter	Pa
ν_I	Poisson’s coefficient of the indented substrate	(-)
ν_{II}	Poisson’s coefficient of the rigid indenter	(-)
F	Normal force during the contact	N
U	Hertzian elastic deformation	(-)
F_T	Hertzian frictional force	N
A_c	Contact area	m^2
χ	Shear strength	N $m\text{-}^2$
μ_H	Hertzian friction coefficient	(-)
σ_{xx}^N	Sackfield-Hills stress along x direction due to normal force	Pa
σ_{yy}^N	Sackfield-Hills stress along y direction due to normal force	Pa

$\boldsymbol{\sigma_{zz}^{N}}$	Sackfield-Hills stress along z direction due to normal force	Pa
$\boldsymbol{\tau_{xy}^{N}}$	Sackfield-Hills shear stress in x y plane due to normal force	Pa
$\boldsymbol{\tau_{xz}^{N}}$	Sackfield-Hills shear stress in x z plane due to normal force	Pa
$\boldsymbol{\tau_{yz}^{N}}$	Sackfield-Hills shear stress in y z plane due to normal force	Pa
$\boldsymbol{\sigma_{xx}^{T}}$	Sackfield-Hills stress along x direction due to tangential force	Pa
$\boldsymbol{\sigma_{yy}^{T}}$	Sackfield-Hills stress along y direction due to tangential force	Pa
$\boldsymbol{\sigma_{zz}^{T}}$	Sackfield-Hills stress along z direction due to tangential force	Pa
$\boldsymbol{\tau_{xy}^{T}}$	Sackfield-Hills shear stress in x y plane due to tangential force	Pa
$\boldsymbol{\tau_{xz}^{T}}$	Sackfield-Hills shear stress in x z plane due to tangential force	Pa
$\boldsymbol{\tau_{yz}^{T}}$	Sackfield-Hills shear stress in y z plane due to tangential force	Pa
$\boldsymbol{J, u, F_0, H_0}$	Sackfield-Hills equations parameters	(-)
$\boldsymbol{\mu_{hys}}$	Hysteretic contribution of friction	(-)
$\boldsymbol{\langle \delta \rangle}$	Mean layer thickness of excited compound volume	m
$\boldsymbol{\sigma_0}$	Nominal contact pressure	Pa
$\boldsymbol{v_s}$	Sliding velocity	m/s
$\boldsymbol{\omega}$	Contact solicitation frequency	rad/s
$\boldsymbol{S(\omega)}$	Profile power spectrum density	m^4
$\boldsymbol{\langle z_p \rangle}$	Mean indentation depth	m
$\boldsymbol{b}$	Indentation parameter linked to strain percentage	(-)
$\boldsymbol{\mu_{adh}}$	Adhesive contribution of friction	(-)
$\boldsymbol{\tau_s}$	Local shear stress	Pa
$\boldsymbol{A_c}$	Effective contact area	m^2
$\boldsymbol{A_0}$	Nominal contact area	m^2
$\boldsymbol{\tau_{s_0}}$	Quasi-static local shear stress	Pa
$\boldsymbol{E_\infty}$	Dynamic modulus at glassy plateau	Pa
$\boldsymbol{E_0}$	Dynamic modulus at rubbery plateau	Pa
$\boldsymbol{v_c}$	Critical sliding velocity	m/s
$\boldsymbol{H(\tau)}$	Relaxation time spectra of compound	(-)
$\boldsymbol{n, m}$	Parameters of the relaxation time spectra of compound	(-)
$\boldsymbol{\tau}$	Compound relaxation time	s
$\boldsymbol{a_0}$	Atomic cut-off length	m
$\boldsymbol{p}$	Local slope of the gamma function for $\tau = 1/\omega$	(-)
$\boldsymbol{\Gamma}$	Gamma function	(-)
$\boldsymbol{P(q)}$	Effective contact area (Persson's notation)	(-)
$\boldsymbol{\phi}$	Angle between sliding direction and rough profile orientation	rad
$\boldsymbol{\tau_f}$	Local shear stress (Persson's notation)	Pa

$\boldsymbol{\tau_{f_0}}$	Local shear stress (Persson’s notation) in quasi-static conditions	Pa
$\boldsymbol{c, \epsilon, k_B}$	Compound parameters of Persson’s theory of adhesion	(-)
$\boldsymbol{w}$	Local dissipated energy during sliding due to hysteresis in control volume	Watt/m^3
$\boldsymbol{m_2}$	Mean quadratic slope of the rough profile	(-)
$\boldsymbol{V}$	Compound control volume in GrETA model	m^3
$\boldsymbol{R_i}$	Indenter radius linked to i-th spatial frequency λ_i	m
$\boldsymbol{F_i}$	Applied normal load	N
$\boldsymbol{N_C}$	Number of contacts between indenter and compound control Volume	(-)
$\boldsymbol{a_i}$	Contact radius linked to indenter radius R_i	m
$\boldsymbol{T}$	Period linked to spatial frequency and sliding velocity	s
$\boldsymbol{\Sigma_0}$	Amplitude value of period stress field	Pa
$\mathbf{E_0}$	Amplitude value of period strain field	(-)
$\boldsymbol{w_{p,i}}$	Power weight linked to i-th spatial wavelength	(-)
$\boldsymbol{W_{tot}}$	Total dissipated energy due to hysteresis in control volume	Watt
$\boldsymbol{\xi_{max}}$	Maximum magnification level in GrETA model	(-)
$\boldsymbol{\mu}$	Total friction value predicted by GrETA model	(-)

Chapter 6

$\boldsymbol{L_{cont}}$	Contact length of pendulum arm	m

Introduction

In Automotive the role of the tyre mechanics and physics is crucial for the optimization of vehicle stability, performance and safety. Most engineers usually face with the analysis of tyres' mechanical and viscoelastic properties with the aim to comprehend the interaction phenomena between the tread and the road.

In the last decades, compound-substrate modelling has been discussed a lot in the scientific literature. Many theories have been developed to determine the frictional behaviour of rubber sliding on a texture in a wide working range in terms of temperature, contact pressure, profile roughness, etc. The most common and recent theories, such as Klüppel's and Persson's [1, 2], are widely employed because they try to explain the contact modelling problem following different approaches and hypothesis.

However, the analysis of the contact problem requires full knowledge of the roughness profile and the rubber viscoelastic properties. The identification of the macro-roughness scales and especially of the micro-scales is an enigma yet to be unequivocally solved for the optimization of the multiscale theories [3]. On the other side, the properties of the rubber compound are complex to determine, unless the tyre tread can be destroyed to obtain a specimen and then perform the Dynamic Mechanical Analysis (DMA), which usually requires expensive machines and a long time for a full time-temperature characterization of the material according to William-Landel-Ferry theory [4, 5]. Nonetheless, in most applications, as well as Motorsport ones, the tyres are linked to restrictions and they cannot be analysed by the standard and laboratory procedures.

In this scenario, the main activities described in the present PhD thesis deal with the tyre tread compound characterization through innovative methodologies and devices in order to overcome the limits that Motorsport racing teams or tyre manufacturers are used to face with. The non-destructive viscoelastic analysis through the device developed thanks to the precious support of the skilled and motivating research team of the Industrial Engineering Department of the University of Naples Federico II, which is called VESevo (Viscoelasticity Evaluation System evolved), is an advantageous testing procedure proving indication of the tyre viscoelastic properties variations with respect to the temperature, wear phenomena, ageing, etc. Ergonomics, portability and smart analysis are key features of this device, allowing it to be widely used by engineers of racing teams on tracks during Motorsport race and events and further by operators in tyre manufacturers facilities, that also need a fast and reliable analysis of the trustworthiness of their final product series.

Once introduced the innovative approaches for tyres characterization, the contact mechanics models have been analysed in-depth highlighting their features and limits for automotive applications. Particularly, the GrETA (Grip Estimation for Tyre Analyses) tool, developed by the Applied Mechanics group of the Industrial Engineering Department of the University of Naples Federico II and improved during the PhD research period, is proposed as a multi-contact simplified physical model for the analysis of adhesive and hysteretic contributions to the overall friction between the rubber and the substrate macro and micro asperities. The main parameters of the GrETA have been identified thanks to specific experimental friction benches, which have involved the last part of the PhD program.

The results achieved can be considered as a baseline for innovative approaches in terms of tyre characterization and contact modelling for friction prediction. Actually, some limits concerning the experimental friction analysis have been faced during the research program, which will be overcome thanks to the realization of the new proposed friction test bench allowing to strengthen the identification of the contact mechanics models and focus on new research scenarios, as well as the analysis of rubber wear phenomena.

Chapter 1

The mechanics of tyre

1.1 Introduction to the tyre

The wheel is considered one of the most important inventions because it found use in a wide range of applications, as well as transportation vehicles, construction equipment and internal parts of machineries. Particularly, the wheel was a development of earlier devices such as rollers used to move heavy objects [6].

The most important step referring to the wheels and tyres development was probably in 1849, when Thompson was granted a patent for an elastomeric air tube fixed on to a wheel to reduce the power necessary to carry on a baggage, make the motion easier and reduce the noise. This concept was much refined in the 1880s, when the first pneumatic tyre was developed for the use on tricycles. The credit of the polymer vulcanization discovery, instead, belongs to Charles Goodyear (1839), when the industrialization of Europe and North America enabled the tyre to evolve from rubberized canvas covering a rubber tube into a complex fabric, steel and elastomeric composite [6].

Nowadays, there are tyres for several categories based on vehicle's applications: tyres for racing vehicles, passenger vehicles and tyres for light trucks. In such tyres, significant quantities of canvas are used as reinforcement. Larger tyres, such as those for heavy trucks, farm and agricultural vehicles tend to contain both steel wire and fabric reinforcements [7].

Regardless of the design or application of the tyre, all pneumatic tyres must fulfil some fundamental tasks, such as providing load - carrying capacity, providing dampening, transmitting driving and braking torque, providing cornering force, generating minimum noise and minimum vibrations, etc. The dampening characteristics, elastic properties of rubber and unique deformability and recovery properties make the tyre the only product that satisfies all of the above-mentioned tasks [8, 9].

1.2 Tyre structure and manufacturing

The tyre is an under pressure, inextensible and deformable body build – up with polymeric material together with some fillers, such as carbon black and silica, and reinforcing steel canvases. It has the shape of a revolution solid similar to a toroidal ring and it is able to bear static and dynamic loads, transfer all the transversal and longitudinal forces to the contact patch and ensure the vehicle directionality and stability [6, 7].

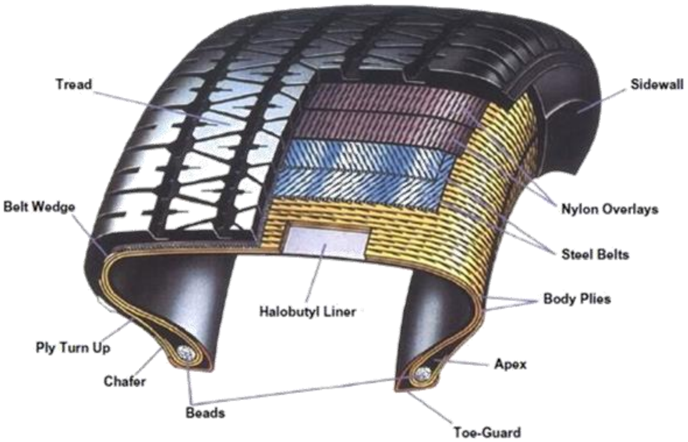

Fig. 1.1 High performance tyre structure

A pneumatic tyre is an assembly of a series of parts (Fig. 1.1), each of which performs a specific task in the service and performance of the product. Nowadays, the *tubeless tyre* is the most adopted in the passenger or high - performance vehicles and its key components are below described [6, 7]:

- *Tread* is the part of the tyre in contact with the road, which have a suitable wear resistance. It must also provide traction and good cornering characteristic with minimum noise generation and low heat build – up. The tread components usually consist of blends of natural rubber, the commonest used are polybutadiene (BR) and styrene butadiene rubber (SBR), compounded with carbon black, silica and vulcanizing chemicals in order to improve its fatigue resistance.
- *Tread Shoulder* is the upper portion of the sidewall that affects tread heat dissipation and tyre cornering properties.
- *Sidewall* is the part protecting the casing from side abrasion. It controls vehicle – tyre ride characteristics and assists in tread support. It further improves the ride quality by allowing the tyre to expand and compress with the road. The sidewall compounds consist of natural rubber (SBR and BR) along with carbon black and other fillers.

- *Beads* are inextensible steel wire loops, which anchor the plies and lock the tyre on the wheel so that it will not slip on the rim. The bead area components include the bead filler; the chafer, which protects the wire bead components; the chipper, which protects the lower sidewall and the flipper, which helps hold the bead in place.
- *Plies* are textile or steel cords extending from bead to bead and working as primary reinforcing material in the tyre casing.
- *Belts* are layers of textile or steel wire lying under the tread so that they can stiffen the casing, allowing tyres to improve their wear performance and handling response, in addition to giving protection to the ply cords against hits with road barriers.
- *Inner Liner* is made of rubber or halogenated derivatives of polymers, which is designed so that it will preserve the compressed air inside the tyre at typical pressure values.

All the numerous components are usually built up on a drum and then cured in a press under heat and pressure. Heat facilitates a polymerization reaction that cross-links rubber monomers to create long elastic molecules. These polymers create the elastic quality permitting the tyre to be compressed in the area where the contact with the road surface occurs. An example of the tyre manufacturing process is shown in Fig. 1.2 [7].

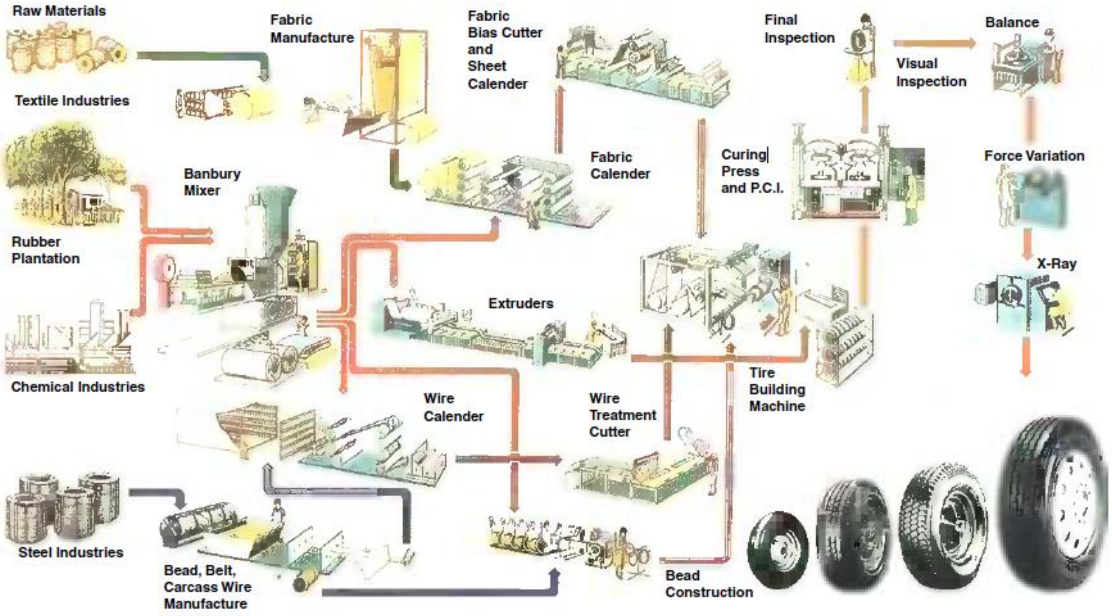

Fig. 1.2 Tyre manufacturing process

1.3 Tyre mechanics

The tyre plays a fundamental role in vehicle dynamics field and many automotive companies spend a lot of time and resources on the development of tyre structure in order to improve its behaviour within the contact are with the road. Therefore, the tyres must fulfil several functions [6, 9], such as the providing sufficient traction for driving and braking manoeuvres or adequate steering control and direction stability. For these purposes, the analysis of the tyre mechanics is essential for comprehending the vehicle performances.

1.3.1 Tyre reference system

To describe the phenomena involved in tyre-road interaction and its forces and moments systems arising during the vehicle motion, an axis reference system need to be defined. One of the commonest used axis systems is recommended by ISO855 standard and it is shown in Fig. 1.3 [10].

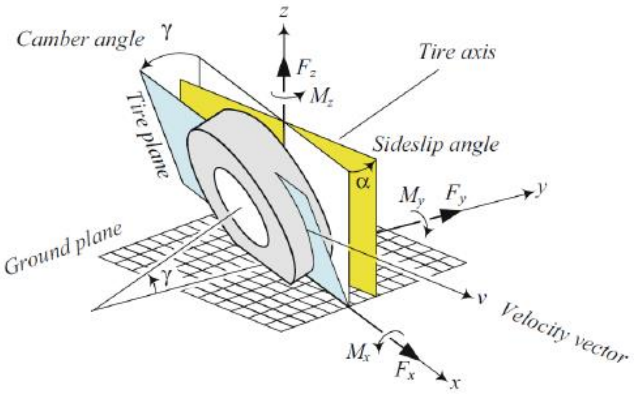

Fig. 1.3 Tyre ISO reference system

In this reference system, the road is considered as flat and nondeformable. The x-axis is along the intersection line of the tyre-plane and the ground. The tyre plane is defined as the plane made by narrowing the tyre to a flat disk. The z-axis is perpendicular to the ground and upward, and the y-axis direction is chosen so that the axis system satisfies the right-hand rule.

The tyre orientation is defined by two angles. The camber angle γ is the angle between the tyre-plane and the equatorial plane passing through the x-axis; the sideslip angle α is the angle between the x-axis and the forward velocity vector **v** as shown in Fig. 1.3.

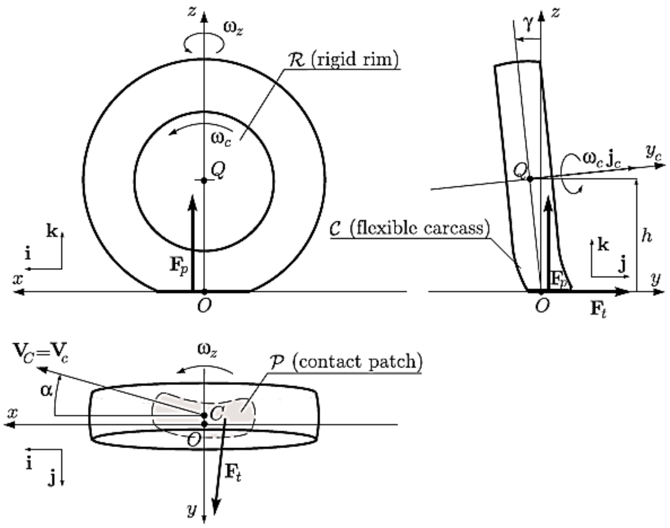

Fig. 1.4 Reference system planes

The resultant force system occurring during the tyre-road interaction is assumed to be located at the centre of the tyre footprint and it can be decomposed along x, y and z axes. Therefore, the interaction of the tyre with the road generates a three-dimensional force system including three forces and moments shown in Fig. 1.3:

- *Longitudinal force* F_x is the tangential force acting along the x-axis and it is also called forward force. This force is positive during accelerations manoeuvres; otherwise is negative.
- *Normal force* F_z is the vertical force normal to the ground plane. It is also defined as wheel load. If the resultant force is upward, this magnitude is positive.
- *Lateral force* F_y is the force tangent to the ground and orthogonal to both F_x and F_z. This force is positive if its application direction matches with y-axis.
- *Roll moment* M_x is the longitudinal moment about the x-axis. It is also called overturning moment.
- *Pitch moment* M_y is the lateral moment about the y-axis and it is known as rolling resistance torque. This magnitude is positive if tends to turn the tyre about the y-axis and moves it forward.
- *Yaw moment* M_z is the upward moment about the z-axis and it is defined as aligning moment or self-aligning moment.

1.3.2 Tyre kinematic

Let Q be a point on the rim axis y_c as shown in Fig. 1.4. The position of the rim with respect to the flat road depends only on the height h of the point Q and on the camber angle γ. The latter is the angle between the rim axis and the road plane. The rim, being a rigid body, has a defined angular velocity $\boldsymbol{\Omega}$. Therefore, the velocity of any point P of the space moving together with the rim is given by the well – known equation:

$$\boldsymbol{V}_P = \boldsymbol{V}_Q + \boldsymbol{\Omega} \times \overline{QP} \tag{1.1}$$

Where $\boldsymbol{V}_Q$ is the velocity of the point Q and $\overline{QP}$ is the vector connecting Q to P. The three components of $\boldsymbol{V}_Q$ together with the $\boldsymbol{\Omega}$ ones are the six parameters that completely determine the rim velocity field. The angle between the velocity $\boldsymbol{V}_c$ corresponding to the centre of contact patch, which is parallel to the flat road, and the x axis of the reference system is called slip angle α. The latter is fundamental in the lateral interaction between the tyre and road. In order to describe the wheel motion, it is used to evaluate the following vectorial magnitude, also called *slip*:

$$\boldsymbol{s} = \frac{(\boldsymbol{V} - \boldsymbol{\Omega} \times R)}{V_x} \tag{1.2}$$

Where $\boldsymbol{V}$ is the wheel centre velocity, which is parallel to the flat road, $\boldsymbol{\Omega}$ is the angular velocity of the wheel, R is the pure rolling radius and V_x is the x axis component of the wheel centre velocity. The quantity $\boldsymbol{\Omega} \times R$ is defined pure rolling velocity and matches with the wheel centre velocity as soon as the tyre works in pure rolling conditions. Distinguishing the slip components along x and y axis, we can define the following magnitudes:

$$\begin{gathered} s_x = \frac{(V_x - \Omega R)}{V_x} \\ s_y = \frac{V_y}{V_x} = tg(\alpha) \approx \alpha \end{gathered} \tag{1.3}$$

The first quantity is called longitudinal slip, whereas lateral slip is the second one. About the longitudinal slip, it is possible to differentiate the following cases:

- Wheel working in pure rolling condition: there are any differences between the wheel centre and each rim point velocity;
- wheel working in global slip condition (traction phase): the tyre rotates among the wheel axis, but the vehicle does not move forward;

- wheel working in global locking condition (braking phase): the tyre behaves as a rigid body during the vehicle-braking phase.

However, taking into account what happens in the contact patch (Fig. 1.1), the tyre tread usually works in pseudo – slippage condition. Actually, the tread of a tyre is deformable, whereas its belt is not stretchable. Consequently, for example, when a vehicle brakes, the road surface pulls the contact patch backwards, but only the tread is distorted. The tread blocks recline, and this outcomes in a relative movement between the bottom of the rubber block, in contact with the road surface, and the belt. This is the shear phase (or pseudo – slippage), which occurs at the leading edge of the contact patch [11, 12].

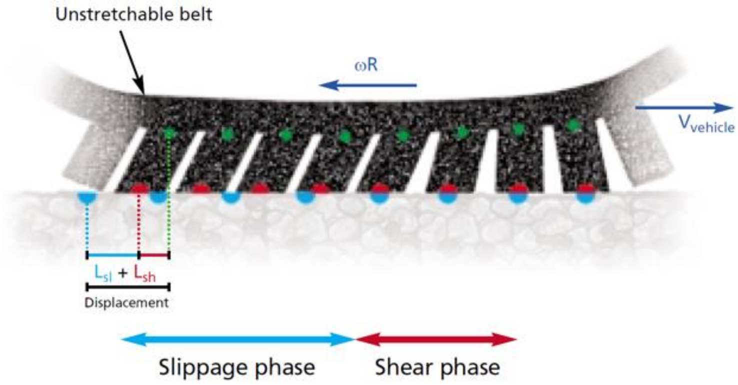

Fig. 1.5 Pseudo-slippage condition

As the rubber tread block gets closer to the trailing edge of the contact patch, the stress increases and the rubber block, whilst remaining sheared, goes into effective slippage condition with the road surface. This means that a mismatch in the velocity value occurs between the points of the tread in contact with the road (red points, Fig. 1.5) and the road surface ones (blue point).

1.3.3 Mechanism involved in tyre-road interaction

As previously described, the tread is made of rubber, which is an elastomeric material to which they owe a large part of their grip capacity. Grip implies contact between two surfaces: one is the tyre surface and the other is the road surface. The contact patch is the region where the tyre is in contact with the road. The patch shape and the position with respect to the reference system depend on the tyre operating conditions: forward speed, load condition, wheel alignment, internal pressure, road roughness and tyre temperature [9, 12, 13].

Road roughness

The grip depends on the type of road surface, the road roughness and wet or dry conditions. More precisely, grip comes from road roughness effects and molecular adhesion [14, 15]. These are mechanisms involved in the relative slippage between the elastomer ad the road surface. The first mechanism is about the frequency excitation of the material by the road texture. Indeed, the rubber is distorted when it slips over the rough acnes, whose size varies form 1 centimetre to 1 micron. This mechanism is also known as indentation phenomenon, which emphasises the penetration of the road asperities into tyre tread rubber. The second mechanism takes place in a microscale and is amplified by slippage. Therefore, in both tyre-road phenomena, the viscoelastic properties of the tread rubber and its hysteresis, which are characterized by destructive and non-destructive techniques, as well as ultrasound method, play an important role.

In the road roughness effects analysis, two main features of the road geometry must be examined considering the tyre grip: the macro and micro roughness. The macroroughness is the name given to the road surface texture when the distance between two adjacent acnes is between 100 microns and 10 millimetres. This roughness level contributes to indentation: the tread block strikes against the rough spot and deforms, but, by a hysteresis effect, it does not immediately revert to its initial shape on the other side of the rough spot. This asymmetrical deformation generates a force field that counteract the slippage [9, 12, 16].

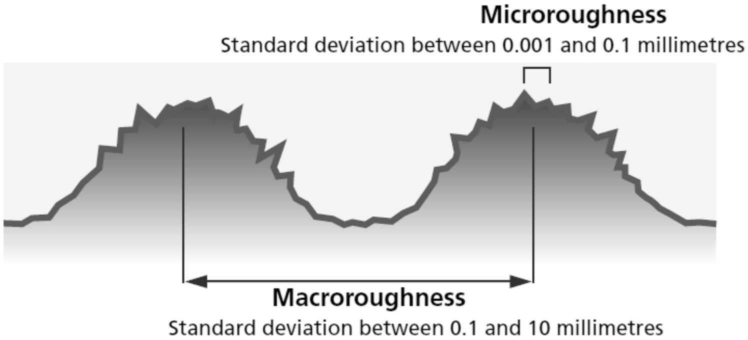

Fig. 1.6 Road macro and micro roughness scales

The microroughness, instead of macro one, refers to the road surface texture, when the distance between two consecutive rough spots is less than 100 microns. This is related to the surface roughness of the aggregates and sands within the road composition. Since the road roughness effects on the tyre tread arise from small bumps on road spots, the corresponding phenomena occur within a range of stress frequencies between 100 Hz and 1 MHz. The molecular adhesion, instead of roughness effects, outcomes from molecular interactions occurring at the tyre tread-road interface and involves the Van der Waals bonding. Indeed, the rubber molecular chains follow a cycle of stretching and braking, which generates friction phenomena between internal particles in a specific material volume (viscoelastic behaviour). The stress cycle provides three phases: the first phase consists in creating bonds between the tread and the road; in the second one, the molecular chains are stretched and a friction force is generated due to viscoelastic behaviour that opposes the skidding phenomenon; in the last phase, the bond breaks and forms again farther on. It is clear that the essential condition for adhesion to be operative is a direct contact between the tread rubber and the road surface (i.e. when the road is clean and dry). Molecular adhesion phenomenon usually occurs in a frequency range between 1 MHz and 1 GHz.

Tyre Compound

The viscoelastic behaviour of the tyre tread rubber leads some phenomena involved in the interaction with the road. The consideration of viscoelasticity is important for an accurate stress-strain analysis of the tyre structure, as well as the computation of energy loss for tyre rolling resistance, which is principally the total effect of the hysteretic losses that occurs as a tyre rolls on the road. For this reason, a part of the mechanical energy is converted to heat as a result of the rolling resistance phenomenon: effectively, the tyre consumes a portion of the power transmitted to the wheels, thus leaving less energy available for moving the vehicle forward. Therefore, the rolling resistance plays an important part in increasing the vehicle fuel consumption [6].

The rolling resistance could be also identified as the effort required tyre to keep rolling. It depends on the tyre employed, the nature of the surface on which it rolls and the operating conditions, such as inflation pressure, load and speed. As already mentioned, rolling resistance is largely a result of energy dissipation within the volume of the tyre. Indeed, hysteretic losses amount for about 80 ÷ 95% of the total rolling resistance and most research efforts, which are related to reducing rolling resistance, always focus on this aspect. This dissipation occurs as consequence of the tyre materials, as soon as they are cyclically deformed during rolling.

As schematically represented in Fig. 1.7a, the rolling resistance arises because the normal pressure p(x) in the leading half of the contact patch is higher than that in the trailing half. This pressure field asymmetry is clearly due to the hysteresis in the tyre, as said before. Therefore, the vertical resultant F_Z of the pressure distribution is offset towards the front of the contact patch [9].

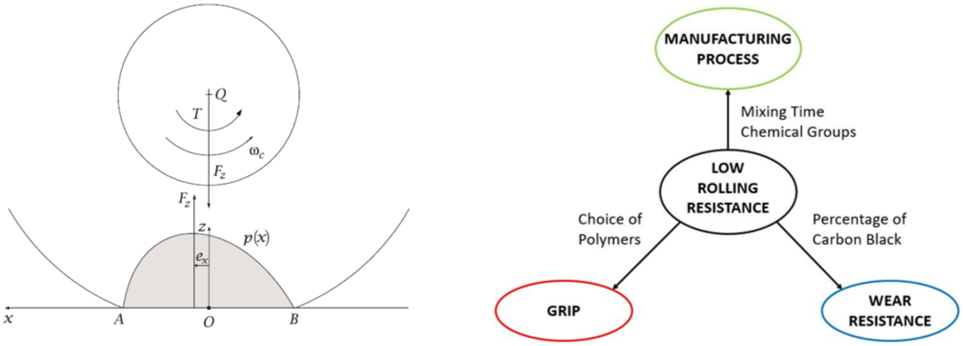

a) b)

Fig. 1.7 a) Rolling resistance; b) grip-wear phenomena dependence

However, the tread rubber exhibits a viscoelastic behaviour together with suitable flexibility and the tyre is designed so that it safeguards these properties when is in service. In this way, both flexibility and hysteresis are helpful to friction, which produces grip thanks to the road roughness effects and the molecular adhesion. Unfortunately, at the same time the viscoelastic behaviour of tyre tread is responsible of the rolling resistance generated in a frequency range of 10 ÷ 150 Hz. For these reasons, the tyre design is constantly developing in order to find a compromise between the viscoelastic behaviour effects.

The viscoelastic behaviour is an advantage in terms of tyre grip with the road, but it generates the rolling resistance phenomenon due to the hysteresis and energy loss. As a loaded tyre completes a revolution, it deforms within the contact patch area and dissipates a part of the energy stored. To reduce the rolling resistance, it is necessary to minimize the energy loss due to the cycle deformation of the tread rubber. This means selecting less hysteretic polymers in the tyre composition or increasing the distances between reinforcing fillers and other raw materials, such as sulphurs and oils. However, the implementation of both solutions it is quite difficult because minimizing tyre energy loss means compromise the tread grip and resistance to wear. The main effort is to find the best trade-off solution for the overall tyre performance in order to achieve a good grip, high wear resistance and low rolling resistance in any tyre working conditions [6, 7], as shown in Fig. 1.7b.

1.3.4 Tyre dynamics

The tyre plays a fundamental role in the vehicle dynamics; the latter is usually subjected to three different types of force fields: the gravitational forces field, the aerodynamic forces and the tyre-road interaction forces one.

The interaction forces field refers to the phenomena occurring in the contact patch between the tyre and the road. This field is due to the application of a torque-driving or braking-round the wheel axis and a force applied on the centre of each tyre. These magnitudes are transmitted to the road thanks to the tyre contact patch. This force-torque system at a given point of the contact patch is statically equivalent to any set of forces or distributed load. Therefore, regardless of the degree of roughness of the road, the distributed normal and tangential loads in the contact patch yield a resultant force **F** and a resultant torque vector **M**:

$$\begin{aligned} \boldsymbol{F} &= F_x\boldsymbol{i} + F_y\boldsymbol{j} + F_z\boldsymbol{k} \\ \boldsymbol{M} &= M_x\boldsymbol{i} + M_y\boldsymbol{j} + M_Z\boldsymbol{k} \end{aligned} \qquad (1.4)$$

The resultant couple **M** is simply the moment about the point O, but any other point could be selected (Fig. 1.3). The traditionally components of the magnitudes in equations (1.4) are the following: F_x is the longitudinal force, F_y is the lateral force; F_z is the vertical load (or normal force); M_x is the over - tuning moment, M_y is the rolling resistance moment and M_z is the self-aligning torque [6, 9, 12].

Thanks to the experimental tests carried out on tyres and the physical – analytic models, it is possible to determine the tyre – road interaction forces law, nowadays. These expressions state that the vertical load depends on tyre crushing, whereas the longitudinal and lateral forces on the corresponding slip factor, longitudinal and lateral slips, respectively. In the following paragraphs, the longitudinal and lateral load will be briefly described.

Pure longitudinal interaction

The tyre testing aims at the full identification of the functions that are the relationships between the motion and the position of the rim and the force and moment exchanged with the road in the contact patch. It is meaningful to perform experimental tests for the so-called pure slip conditions. It means setting that the longitudinal and lateral forces depend only on the corresponding slip factors and on the vertical load, whereas the self – aligning moment on the vertical load and lateral slip factor [6, 9, 12].

To comprehend the phenomena involved in the contact patch during the longitudinal interaction, a vehicle next to braking conditions should be taken into account. As soon as the driver presses on the brake pedal, a braking torque is applied to the four wheels through the brake circuit. At this point, the angular speed of the wheels decreases, and the rolling speed of the tyre drops below the vehicle one. To compensate this difference, the tyres begin to slip on the road in agreement with a longitudinal slippage rate in braking conditions:

$$s_{x,BT} = \frac{(V_x - \Omega R)}{V_x} \cdot 100\% \tag{1.5}$$

The magnitude in eq. (1.5) is a measurement of the difference between vehicle velocity and the rolling velocity of the tyre at its point of contact with the road; V_x is the longitudinal vehicle speed, R is the rolling radius and Ω is the angular velocity of the tyre. As soon as the driver brakes too sharply on a low grip road, the four wheels may lock, whereas the vehicle still slides forward. In this case, the wheel rolling speed is equal to zero, but the vehicle continues to move (100% slippage condition in contact patch).

Since the driver try to accelerate severally the vehicle on a hill or on a low grip road, the wheels go around, but the vehicle does not move forward. In this case, the wheel rolling speed is very high, but the vehicle speed remains nil. The longitudinal slip ratio in driving conditions is infinite: (1.1)

$$s_{x,DT} = \frac{(\Omega R - V_x)}{V_x} \cdot 100\% \tag{1.6}$$

Therefore, when a driving or a braking torque is applied on the vehicle, the contact patch can be split in two different areas. The first one, considered in adherence, in which the local forces are proportional to the tyre blocks strains along x direction. The second one, where the sliding phenomena occur between tyre blocks and the point of the road surface, which are linked to the contact pressure distribution and the dynamic friction coefficient. If no sliding takes place on the contact patch, the relationship between the longitudinal force F_x and the longitudinal slip s_x can be considered as linear:

$$F_x = C_x s_x \tag{1.7}$$

where s_x can be $s_{x,BT}$ in traction phase or $s_{x,DT}$ in braking phase. C_x is the tyre longitudinal stiffness, also called braking stiffness:

$$C_x = \left.\frac{dF_x}{ds_x}\right|_{s_x=0} \tag{1.8}$$

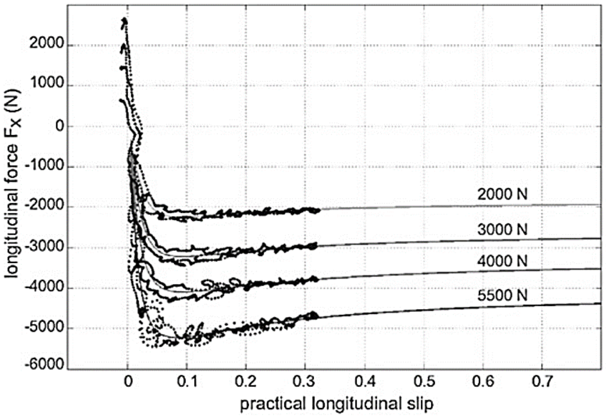

Fig. 1.8 Longitudinal interaction

In Fig. 1.8, the typical behaviour of the longitudinal Force F_x as a function of the practical longitudinal slip under braking conditions, for several values of the vertical load F_z, is shown. It is important to point out that the longitudinal forces decrease as a linear function of the slippage ratio in a small range of longitudinal slip ratio s_x. In this case, the longitudinal tyre stiffness definition is correct and the tyre blocks work in adherence. Moreover, the vertical load influence on the longitudinal force F_x: the latter grows less than proportionally with respect to the vertical one. Hence, the global longitudinal friction coefficient μ_x can be defined as the ratio between the peak value of the longitudinal force and the corresponding vertical load.

Pure lateral interaction

When a tyre is not subjected to any force perpendicular to the wheel plane, it will move along this last; if a side force F_s is applied to a wheel, a lateral force will be developed at the contact patch, and the tyre will move along a path at an angle equal to the side slip angle α with the wheel plane, mainly due to the lateral elasticity of the tyre, as shown in Fig. 1.9.

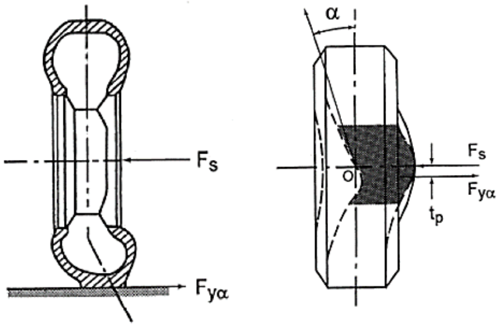

Fig. 1.9 Lateral interaction physics

The lateral force developed at the tyre-ground contact patch is usually called cornering force $F_{y\alpha}$ when the camber angle of the wheel is zero; the relationship between the cornering force and the slip angle plays a fundamental role into the directional control and stability of road vehicle. When the tyre is moving at a uniform speed, the side force F_s applied at the wheel centre and the cornering force $F_{y\alpha}$ developed in the ground plane are usually not collinear: at small slip angles, the cornering force in the ground plane is normally behind the applied side force, giving rise to a torque which tends to align the wheel plane with the direction of motion. This torque is called the “aligning torque” or “self-aligning torque”, and it is one of the restoring moments which help the steered tyre return to the original position after performing a curve manoeuvre. The distance t_p between the side force and the cornering force is called the “pneumatic trail”, and the product of the cornering force and the pneumatic trail determines the self-aligning torque.

To properly approach a vehicle within a turn, the driver has to act on the steering wheel. Every vehicle taking a bend is subjected to a side force, F_c, which tends to force it out of its curve. To keep vehicle on the path, in each tyre-road contact area must arise a centripetal force, F_y, which globally stabilize the side force [6, 9, 12]. The relationship between the cornering force and the slip angle is of fundamental importance to the vehicle handling and stability of road. Typical plots of the cornering force as function of the slip angle show that for angles below a certain range, the lateral force is approximately proportional to the slip values. Beyond them, the cornering force increases at a lower rate with an increment of the slip angle and reaches its maximum value as soon as the tyre begins sliding laterally.

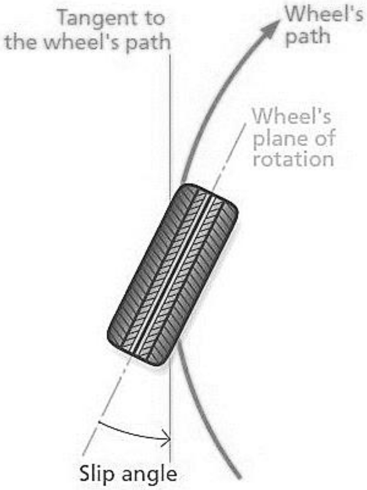

Fig. 1.10 Lateral interaction slip angle

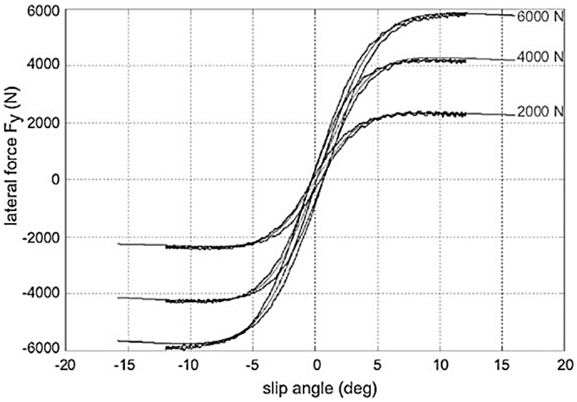

Fig. 1.11 Lateral interaction

It is noticeable from Fig. 1.11 that for low slip angle values the lateral force increases linearly. Therefore, the relationship between the friction force and the corresponding kinematic parameter can be expressed as follows:

$$C_{y,\alpha} = \frac{dF_{y\alpha}}{d\alpha}\bigg|_{\alpha=0} \tag{1.9}$$

Where C_{α} is known as cornering stiffness. This magnitude indicates the slope of the curve at the origin of the coordinate axis system. The cornering stiffness generally increases with the load, but the rate of increase declines as load increases (see Fig. 1.12). High performance vehicles on a dry road will exhibit their maximum cornering ability using large tyres operating at relatively high loads. Inflation pressure usually has a moderate effect on the cornering properties of a tyre, but in general, cornering stiffness increases with an increase of inflation pressure [6, 12, 17].

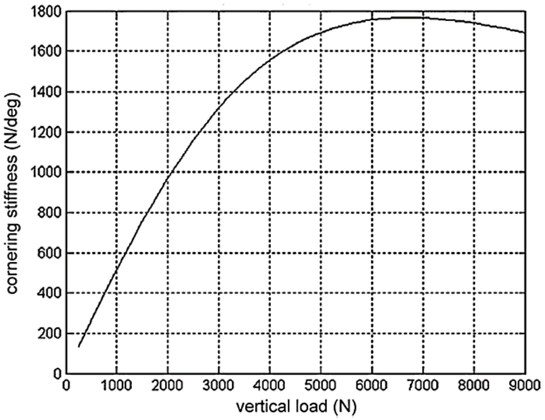

Fig. 1.12 Tyre cornering stiffness

However, the relationship between the lateral force and the normal load is non – linear. This means that the transfer load from the inside to the outside tyre during a bend will reduce the total cornering force that a pair of tyres, the front or rear one, can perform, making so possible o act on the under/over steering behaviour of the whole vehicle modifying the value of the roll stiffness, able to manage the load transfers [18, 19].

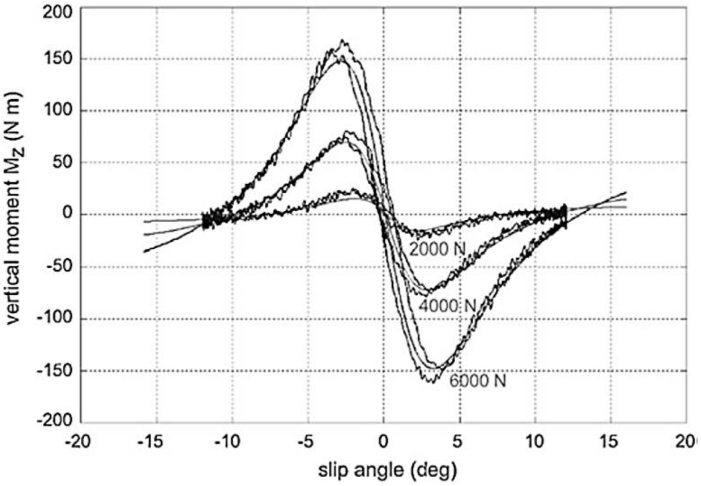

Fig. 1.13 Self-aligning torque Mz

It is further necessary to point out that the centrifugal force F_s applied at the wheel centre and the cornering force $F_{y\alpha}$ developed in the ground are usually not collinear, when a vehicle takes a bend path. At small slip angles, the cornering force is usually behind the applied centrifugal force, giving rise to a torque, which tends to align the wheel plane with the direction of motion. This torque is called self – aligning torque and depends on the slip angles values and vertical load ones.

Camber thrust

Camber causes a lateral force usually denoted as “camber thrust” $F_{y\gamma}$, and the development of this thrust may be explained in the following way: a free-rolling tyre with a camber angle would revolve about point O, as shown in Fig. 1.14; however, the cambered tyre in a vehicle is constrained to move in a straight line, developing a lateral force in the direction of the camber in the ground plane. It has been shown that the camber thrust is approximately one fifth the value of the cornering force obtained from an equivalent slip angle for a bias-ply tyre and somewhat less for a radial-ply tyre.

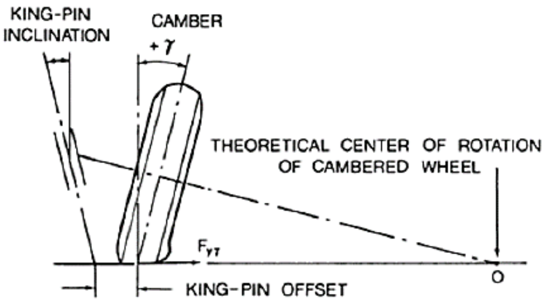

Fig. 1.14 Cambered tyre behaviour

To provide a measure for comparing the camber characteristics of different tyres, a parameter caller "camber stiffness" is often used; it is defined as the derivative of the camber thrust with the respect to the camber angle evaluated at zero camber angle:

$$C_{y,\gamma} = \left.\frac{dF_{y\gamma}}{d\gamma}\right|_{\gamma=0} \tag{1.10}$$

As well as the cornering stiffness, normal load and inflation pressure have an influence on the camber stiffness. It has been calculated that for truck tyres, the value of the camber stiffness is approximately one tenth to one fifth of the cornering stiffness under similar operating conditions [6]. The total lateral force of a cambered tyre operating at a certain slip angle is the sum of the cornering force and the camber thrust:

$$F_y = F_{y\alpha} \pm F_{y\gamma} \tag{1.11}$$

If the cornering force and the camber thrust are in the same direction, the positive sign should be used in eq. (1.11(1.11). For small slip and camber angles, the relationship between the cornering force and the slip angle and the one between the camber thrust and the camber angle are essentially linear; the total lateral force of a cambered tyre at a slip angle can be determined as follows:

$$F_y = C_{y,\alpha}\alpha \pm C_{y,\gamma}\gamma \tag{1.12}$$

Combined interaction

In the discussion about the cornering behaviour of tyres, the effect of the longitudinal force has not been considered. However, quite often both the side force and the longitudinal force are present, such as braking in a turn. In general, tractive (or braking) effort will reduce the cornering force that can be generated for a given slip angle; the cornering force decreases gradually with an increase of the tractive or braking effort. At low values of tractive (or braking) effort, the decrease in the cornering force is mainly caused by the reduction of the cornering stiffness of the tyre. A further increase of the tractive (or braking) force results in a pronounced decrease of the cornering force for a given slip angle.

This is due to the mobilization of the available local adhesion by the tractive (or braking) effort, which reduces the amount of adhesion available in the lateral direction. It is interesting to point out that if an envelope around each family of curves is drawn, a curve approximately semi-elliptical in shape may be obtained. This enveloping curve is often referred to as the friction ellipse.

The friction ellipse concept is based on the assumption that the tyre may slide on the ground in any direction if the resultant of the longitudinal force (either tractive or braking)and lateral (cornering) force reaches the maximum value defined by the coefficient of friction and by the normal load on the tyre. However, the longitudinal and lateral force components may not exceed their respective maximum values $F_{x,max}$ and $F_{y,max}$ as shown in Fig. 1.15. $F_{x,max}$ and $F_{y,max}$ can be identified from measured tyre data and constitute respectively the major and minor axis of the friction ellipse.

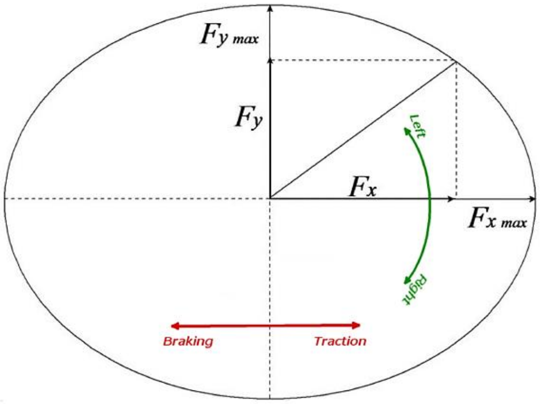

Fig. 1.15 Friction ellipse

1.4 Tyre working conditions effect

The vehicle usually operates under a range of different external conditions, so the passenger or race tyres are subjected to varying load, pressure, speed and temperature. All these conditions influence not only the rolling resistance, but also the tyre tread response in transient phenomena during the interaction of the road [6, 12, 20].

1.4.1 Temperature effect on rubber behaviour

The working temperature of a tyre usually depends on several aspects, as well as the type of the tyre itself, the way the vehicle is driven and the environmental temperature. Typically, the internal temperature of a standard passenger tyre lies between 20 and 60°C. Clearly, the tyre temperature increases as soon as the external one is higher. In the usual working temperature conditions, the amount of energy dissipated by the tyre tread compound, which exhibits a viscoelastic behaviour, when subjected to a cyclic load, decreases as the temperature increases, as shown in Fig. 1.16.

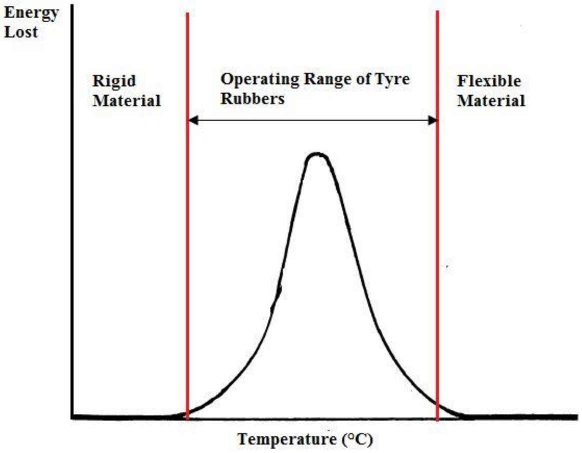

Fig. 1.16 Temperature effect on energy dissipation

The suitable temperature working range matches with the maximum energy lost area due to viscoelastic behaviour so that friction coefficients are high. Very low temperatures turn the tyre tread behaviour into rigid one. This means that in braking transient conditions, the tyre is not able to compensate the difference between the wheel centre and the rolling speed (see eq. (1.5)) and the speed of the vehicle, because the tread compound is less deformable, and the vehicle's wheels may be locked. Contrariwise, in driving conditions, the wheels go round and the vehicle does not move forward at the same time (the longitudinal slip ratio is infinite). In cornering conditions, instead, the vehicle goes straight rather than taking the bend, if the tyre rubber behaves as a rigid material. Actually, the slip angle (see the previous paragraph) indicates how the tyre is deformed in order to let the vehicle rightly corner. This means that the velocity vector changes its direction slower than tyre one due to viscoelastic behaviour of the tread rubber.

1.4.1 Pressure effects on tyre rolling resistance

Each vehicle tyre is subjected to an applied vertical load F_z, which influences the longitudinal and lateral loads in the tyre-road contact patch. Particularly, the relationship between the longitudinal/lateral and vertical load is non-linear due to contact patch saturation phenomenon along the x and y axis according to the reference system adopted (see Fig. 1.3). Further, it is found that the rolling resistance increases nearly proportionally to the applied load due to the increased levels of bending and shearing that take place.

Although the rolling resistance is nearly a linear function of the normal load, the energy lost increment due to higher loads generates a tyre temperature rising. The latter outcomes in a lower hysteretic loss coefficient for tyre tread elastomer material. Therefore, the rolling resistance coefficient often decreases with an increasing load [6].

The inner pressure variations usually affect the global deformation of the tyre, as well as the vertical load. Particularly, a decreasing of the pressure produces a rapidly increasing of the rolling resistance, because it reduces the compression of tyre blocks in the contact patch. This also generates an increment of bending and shear stresses of tyre tread. For passenger car tyres, the inflation pressure is not usually higher enough for compression to be a meaningful source of the total energy loss.

Because of these phenomena occurring at different temperatures, the variation of the rolling resistance as function of the temperature, and thus of the heat radial generative term within the tyre structure, is not linear; clearly, it is lower when the external temperature is higher: between 10 and 40°C, an increase of 1°C corresponds to a reduction in rolling resistance of about the 0.6% under normal load conditions.

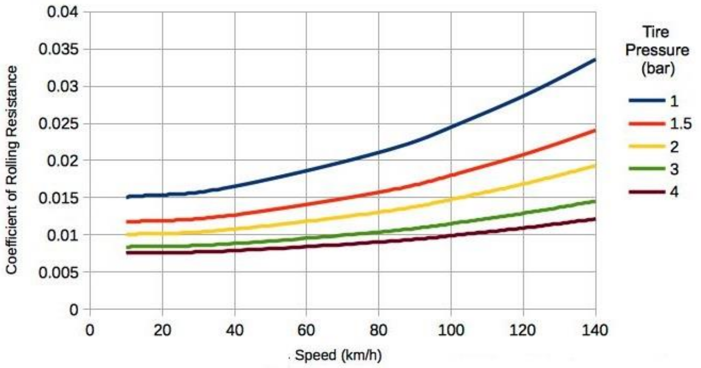

Fig. 1.17 Pressure effects on rolling resistance

As we can see in the above diagrams, in addition to the pressure, the rolling resistance also depends on vehicle speed. Principally, as soon as the centre wheel velocity rises, the frequency of deformation of tyres increases, causing an increment of the tyre tread rubber loss factor. At the same time, a higher heat generation occurs: so, the tyre temperature rises, whereas the tyre loss factor decreases. The combined influence of the above effects give rise to a typical increment of the rolling resistance with vehicle speed, but in some cases, it may decrease due to temperature effects on the tyre tread behaviour and the loss factor. Anyway, the variation of rolling resistance as function of the speed are generally much smaller than the pressure and temperature ones, as clearly reported in Fig. 1.17.

Chapter 2

Tyre Compound Viscoelastic Behaviour

2.1 Viscoelastic materials

The viscoelastic material is a deformable material with a behaviour which lays between that of viscous liquid and an elastic solid. This kind of solid does not show a linear relationship between stress and applied strain. Indeed, their behaviour deviates from Hooke's law and exhibits elastic and viscous characteristics at the same time. The most generic equation that describes this feature is the Newton's Law [7, 21]:

$$\sigma(t) = \eta \frac{d\varepsilon(t)}{dt} \tag{2.1}$$

This relation defines the connection between the stress and the strain- rate through the viscosity coefficient η. All materials, which satisfied the eq. (2.1), are called viscoelastic materials and the stress-strain relationship depends on the time. Indeed, in a viscoelastic material, the most important characteristic is the time-dependent behaviour and the load application speed at an established temperature value.

It is necessary to point out that viscoelasticity is not plasticity [22]. A viscoelastic material will return to its original shape after any deforming force has been removed, even though it will take time to do so. The reason of this phenomenon is that the deformation energy is not totally stored, but partially dissipated (hysteretic behaviour). Contrariwise, when a perfectly elastic solid, like a spring, is subjected to a force, it distorts instantaneously in proportion to the applied load. Then, as soon as the force is no longer applied, the body returns to its initial shape.

Further, it is important to notice that the viscoelasticity of tyre rubber depends on the molecular structure of the material. Actually, the constituent rubber of the tyre are vulcanised elastomers. These elastomeric materials are made up of one or more polymers, long molecular chains, which spontaneously take on the shape of a wool ball and became entangled with each other. During the tyre manufacturing, these materials are vulcanised, which means they are treated with an incorporation of sulphur. This causes the creation of sulphur bridges between the polymer chains, as shown in Fig. 2.1.

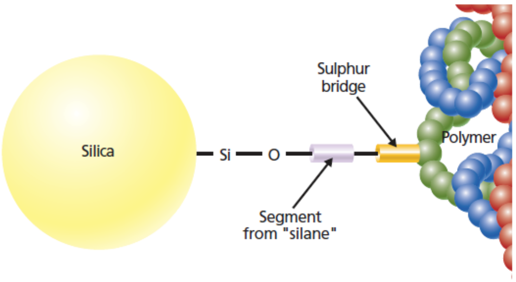

Fig. 2.1 Polymer chains and sulphur bridges

To better understand the mechanical behaviour in viscoelastic materials, two major types of experiment are usually carried out: transient and dynamic. While static characterization regards the quasi-static application of load or deformation, transient and dynamic testing procedures concern the analysis of material response to a time applied deformation or load function (elongation or shear). Two important categories, regarding the transient material testing, are commonly performed: creep experiment and stress relaxation experiment.

2.1.1 Creep experiment

In the creep experiment, the material is subjected to uniform load in order to analyse the strain time changes, as shown in Fig. 2.2. Creep phenomenon is one of the most important features, which points out the viscoelastic behaviour of materials. Creep consists in progressive increasing of deformation under uniform load applied on the specimen.

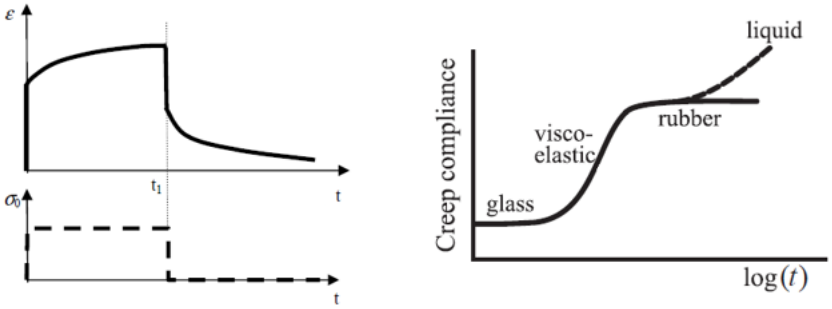

Fig. 2.2 Creep experiment and creep compound compliance

Creep phenomenon is one of the most important phenomena to characterize the viscoelastic behaviour of materials. Creep consists in progressive increasing of deformation under uniform load applied on the specimen. As described in Fig. 2.2 (on left), the strain quickly with time as the stress step function is applied, reaching the steady-state conditions at time t_1. Furthermore, if the load applied is instantly removed, the strain shows a transitional period to reach the unload initial conditions. The creep compliance module J (Fig. 2.2, on right) is defined as the ratio between the strain, obtained at define instant of time, and the load step applied:

$$J(t) = \frac{\varepsilon\ (t)}{\sigma_0} \tag{2.2}$$

From eq. (2.2), it is clear that creep compliance is time dependent. Particularly, the material behaves as a glassy solid if the load is applied with higher frequency values and it is similar to rubbery solid if the load is applied quasi statically. In the middle time range, the compliance shows a linear slope where the solid behaves as a viscoelastic material. In particular, in the middle time range which characterizes the linear viscoelastic slope trend, the creep compliance proportionally increases with time [4, 7].

2.1.2 Stress relaxation experiments

During the stress-relaxation experiment, material is subjected to a fixed deformation and the load required to maintain the deformation at a constant value is measured with time, as represented in Fig. 2.3.

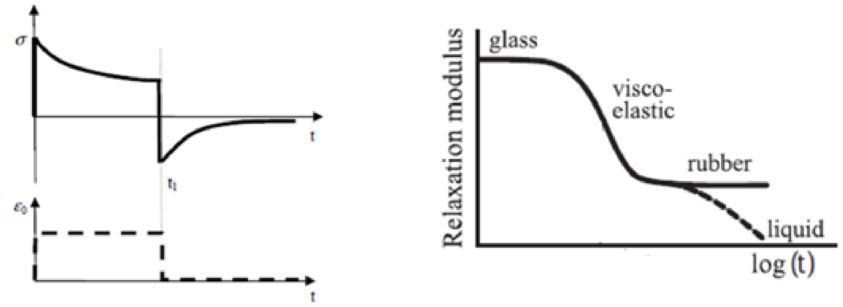

Fig. 2.3 Stress relaxation test and relaxation modulus

Once the strain is applied to the specimen, the stress trend initially shows an instantaneous reaction, then it gradually decreases with time. As soon as the material comes back to undeformed shape, it tends to react with a stress opposite to the initially applied strain; then this stress tends to zero value. As well as for the Creep Compliance, we can define the Relaxation Modulus E is expressed as:

$$E(t) = \frac{\sigma\ (t)}{\varepsilon_0} \tag{2.3}$$

In Fig. 2.3 (on right), the relaxation modulus $E(t)$ variation with time is shown. Moreover, it is also possible to distinguish the rubbery and glassy plateaus, in which the material exhibits quite opposite behaviours [23].

These transient tests allow us to characterize the viscoelastic material reaction to a stress/strain load step. Another phenomena class, which describes the viscoelastic behaviour, is the dynamic experiments. These tests usually involve analysing the material reaction to a cyclic stress or strain applied:

$$\sigma(t) = \sigma_0 * \sin(\omega t) \tag{2.4}$$

where ω the angular frequency of is sinusoidal stress and depends on the time. In elastic materials, the strain generated by the stress also exhibits a sinusoidal trend with the same phase of the applied load. Contrarily, in viscoelastic materials the strain reaction shows a delay compared to stress, which is characterized by a phase angle δ. Therefore, the strain is given by [4, 21]:

$$\sigma(t) = \varepsilon_0 * \sin(\omega t - \delta) \tag{2.5}$$

The phase angle δ identifies the time displacement between applied stress and strain, as shown in Fig. 2.4:

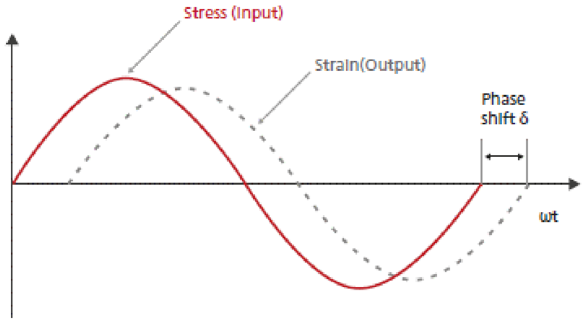

Fig. 2.4 Stress-strain time displacement

Because of the phase displacement, the material dynamic stiffness can be considered as a complex variable E^*, according to Euler's formulation [4, 7]:

$$\frac{\sigma(\omega)}{\varepsilon(\omega)} = E^* = E' + iE'' \tag{2.6}$$

Where E' is called Storage Modulus and E'' is called Loss Modulus. These quantities are deeply linked to the way the material dissipates a part of energy provided by means of a load/stress time function. Therefore, the both moduli are related to the phase angle δ, according to the vector diagram in Fig. 2.5.

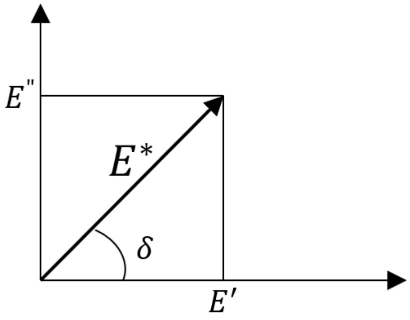

Fig. 2.5 E* vector diagram

Therefore, the phase angle value can be easily obtained by means of the ratio between imaginary and real part of the complex modulus E^*:

$$\tan(\delta) = \frac{E''}{E'} \tag{2.7}$$

The phase angle tangent is called *Loss Tangent* and it denotes the entity of damping phenomenon in viscoelastic materials. It is important to see that all these quantities, which characterized the viscoelastic behaviour, are function of the frequency at which the sinusoidal load is applied.

To easily comprehend in which way these magnitudes are interconnected, a simple time load function can be applied to a polymer specimen. Analysing the material response, a part of the applied load is stored in the polymer to be release once the applied load is removed, meanwhile another part of the applied load is lost due to the internal mechanism of energy dissipation. On one hand, an increase of loss tangent indicates that the tested material dissipates a great amount of stored energy; on the other hand, a decrease of the loss tangent means that the polymer has more potential to store the elastic energy rather than to dissipate it.

2.2 Influence of frequency and temperature on the viscoelastic materials

The modulus, the energy loss and hysteresis of a viscoelastic material change in relation to two parameters: the frequency with which the force is applied and the material temperature the phenomena are evaluated on. It is important to point out that load frequency and material temperature produce opposite effects on the rubber behaviour, as represented in Fig. 2.6.

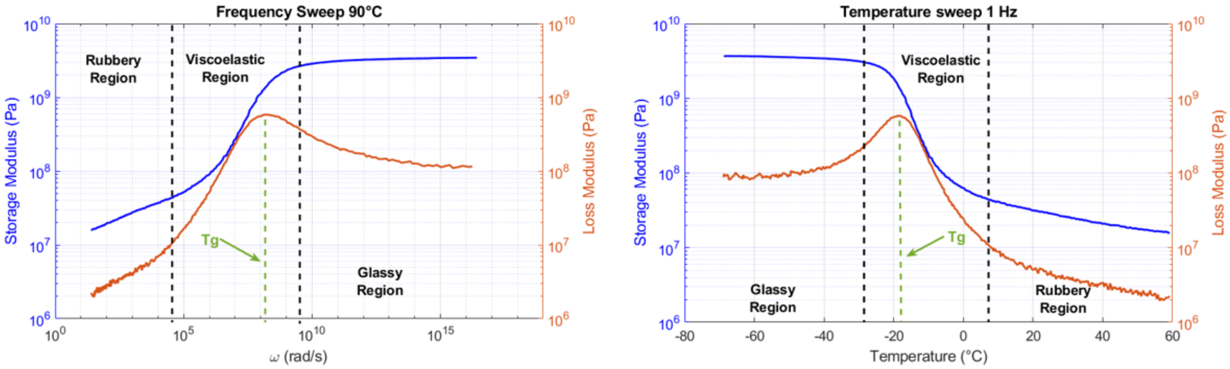

Fig. 2.6 Frequency and temperature sweep curves

2.2.1 Frequency influence

Once the temperature was fixed, the Storage and Loss Modulus tendencies in frequency domain can be analysed.

From a physical point of view, at low frequency the deformation occurs slowly. Keeping in mind the Voigt model, this means that the force required to move the dashpots is slight [24], offering a small resistance. In this case, the spring side is dominant, and the material appears to be fairly elastic (rubbery region). When this happens, the material is in a rubbery state and its hysteresis is low.

Once the frequency increases, the force required to move the dashpot also increases due to its higher resistance. Hence, the material shows a viscoelastic behaviour (viscoelastic region). This is the most suitable behaviour range for tyre grip, because the hysteresis term is maximum in this frequency range. Indeed, the Loss Modulus E'' reaches its highest value in this frequency-range. Clearly, if the frequency increases still further, the viscoelastic features fall again, and the material behaviour turns into glassy (glassy region).

At this point, it is interesting to understand what happens inside the material. When the polymer molecular chains are subjected to stress, they start moving and being stretched in some directions and compressed in others. Each time the force is released, the chains relaxation occurs. The speed with which the chains return to undeformed shape depends on molecular mobility. So, there are three possible cases [25, 26]:

1. At low stress frequency, the polymer chains are relatively mobile and appear to be flexible and elastic;
2. if the frequency increases, the return to undeformed shape is delayed and the energy dissipation is marked (hysteresis phenomenon);

3. if the stress frequency still increases, the chains do not have the time to move and regress to initial conditions. Hence, the material becomes glassy and stops being viscoelastic.

All the above information linked to hysteretic behaviour are also valid, if we analyse the relationship between the Loss Factor (also called Loss Tangent) and the stress frequency. As soon as the Loss Tangent reaches its maximum, the material exhibits a hysteretic behaviour with energy loss. The presence of one loss peak is characteristic of most materials. Their loss factor peak is, in general, in the order of 0.6 or 0.8, such as for rubbers or rubber – like materials). Low loss peak $(10^{-1}\ 10^{-3})$ is distinctive of hard plastic and other structural materials (steel, wood, etc.) [27].

2.2.2 Temperature influence

It has already been affirmed the frequency, with which the force is applied to polymer, and the temperature of the material affect the rubber in opposite ways. As shown in the temperature sweep diagram in Fig. 2.6, at very low temperatures, the storage modulus of the rubber is high. In this condition, at given frequency, the material is rigid and shows a glassy behaviour. At high temperature, the storage modulus is decreased, and the material more flexibly and elastically behaves.

In the intermediate temperature range, situated around the glass transition temperature, denoted as T_G, the material exhibits a viscoelastic behaviour. The T_G is known as the temperature below which the rubber tends closer to the glassy plateau and above which the polymer shows an increasingly rubbery state. At higher temperature, the polymer is sufficiently deformable in such a way that the chain segments between the sulphur bridges are able to move. During this motion, they scrub against adjacent chains, slowing down their movement and producing the energy dissipation (hysteresis) [28, 29].

The Glass Transition Temperature, as illustrated in Fig. 2.6, occurs near to the loss modulus maximum and is close to the middle point of the storage modulus into transition area. This feature usually takes place in rubbers with a very low fillers percentage. Anyway, if the examined rubber is a compound, just how usually happens in tyre structure, the maxima of loss factor and loss modulus do not match (see Fig. 2.7). This is due to the complexity of dynamic mechanical behaviour of these composites, which arises from the restricted movement of rubber molecules in presences of fillers [21, 23, 29].

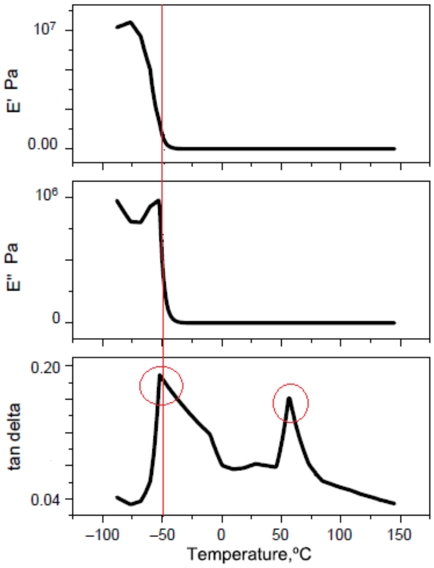

Fig. 2.7 Filler effects on compound

Moreover, the Loss Tangent diagram sometimes shows two peaks. Each peak is characteristic of the transition temperature for each filler in the rubber compound. The first peak usually occurs at low temperature, because it relates to the dynamic-mechanical behaviour of the rubber matrix, which exhibits the greatest damping (or hysteretic) effect. The second peak takes place at higher temperature and it arises from the mechanical behaviour of the additive fillers.

2.2.3 Time-temperature superposition principle

As already mentioned, the viscoelastic properties are related to the stress frequency and the material temperature. Actually, the frequency and temperature dependences are two phenomena closely interlinked to each other: there is an inversely proportional relation between an increase in the temperature and a reduction in the stress frequency. Whenever the stress frequency is increased at a given temperature, the polymer turns into glassy state; conversely, if the material heats up at a given stress frequency, it becomes softer [5, 7, 30].

These features arise from the balance between molecular velocity and the strain – rate. On one hand, if the strain-rate is greater than the speed at which the molecular chains can move in the polymer’s structure, the material appears glassy; on the other, if the strain rate is lower than the molecular speed, the compound exhibits rubbery behaviour. Besides, the motion speed of chains inside the molecular structure is strictly dependent on the temperature at which the material is.

This polymers’ behaviour can be mathematically and physically explained introducing the Time-temperature superposition principle (or T.T.S.). The T.T.S. states that, considering for example the Storage Modulus E', at two different temperature T_1 and T_0 such that $T_1 > T_0$, the value assumed by the modulus at the frequency ω_1 and the temperature T_1 will be the same at the frequency ω_0 and temperature T_0, which is also called reference temperature. Therefore, if T_1 is higher than T_0, the molecular processes are faster, and it is verified that $\omega_0 < \omega_1$. This phenomenon can be mathematically expressed as follows:

$$E'\left(\omega_{T_1}, T_1\right) = E'\left(\omega_{T_0}, T_0\right) \tag{2.8}$$

All the materials satisfying the equation (2.8) are called simple thermo-rheologic materials and their behaviour agrees with the time-temperature superposition theory. In this way, as the temperature changes, for example, (see Fig. 2.8, on left), the curve corresponding to $E' = f(\omega)$ relationship exhibits a horizontal *shift* according to the non-linear dependence on the temperature between the frequencies ω_1 and ω_0:

$$\omega_0 = \frac{\omega_1}{a_T(T_1)} \tag{2.9}$$

where the magnitude $a_T(T)$ is called shift factor and is defined by the following properties:

$$\begin{aligned} T_1 < T_0 &\rightarrow a_T(T_1) < 1 \\ T_1 = T_0 &\rightarrow a_T(T_1) = 1 \\ T_1 > T_0 &\rightarrow a_T(T_1) > 1 \end{aligned} \tag{2.10}$$

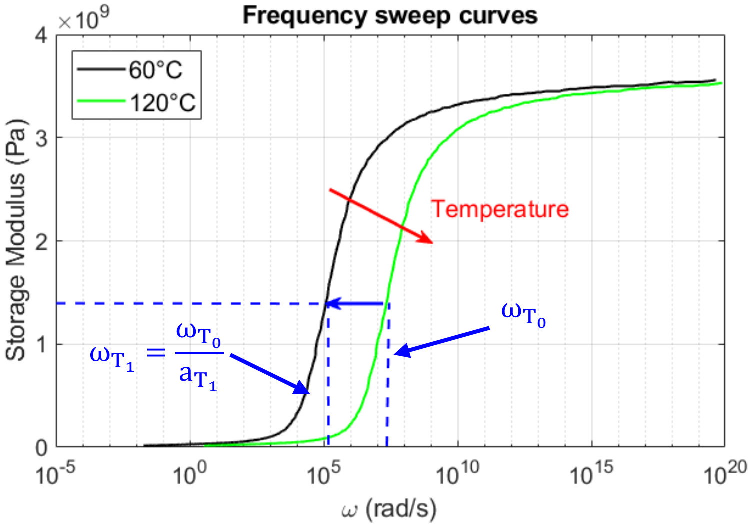

Fig. 2.8 Temperature shift in frequency domain

Therefore, the superposition principle is used to determine the temperature dependency for mechanical properties of linear viscoelastic material from known properties at a reference temperature T_0. Moreover, the time – temperature superposition avoids the inefficiency of measuring a polymer's behaviour over long periods of time at a specified temperature by assuming that at higher temperatures and longer time the material will behave the same [4, 5, 30, 31].

In order to represent the E' curves at higher or lower temperatures, which superpose with the master curve at the reference temperature T_0, the shift factor has to be determined. This magnitude a_T is generally computed by means of an empirical relation first established by Malcolm L. Williams, Robert F. Landel and John D. Ferry. This relationship is known as W.L.F. equation and is expressed as:

$$\log(a_T) = \frac{-C_1 * (T - T_0)}{C_2 + (T - T_0)} \tag{2.11}$$

where T is the temperature, T_0 is the reference temperature chosen to construct the generic master curve, C_1 and C_2 are empirical constants adjusted to fit the values of the superposition parameter a_T. The equation (2.11) can be used to fit discrete values of the shift factor a_T towards the temperature, as shown in Fig. 2.9.

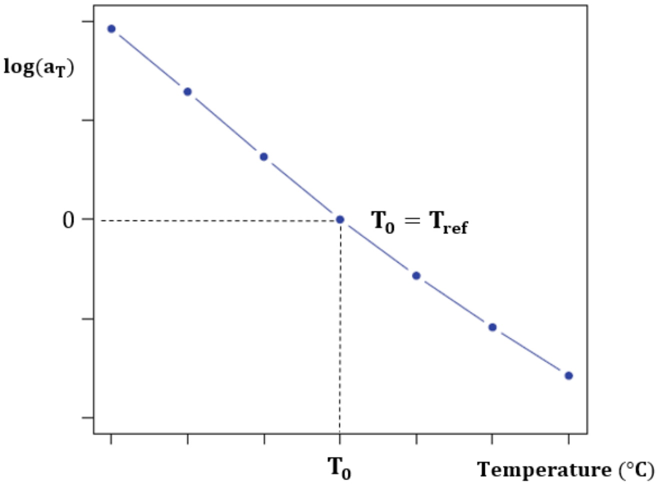

Fig. 2.9 Shift factor dependence on temperature

The discrete values of the shift factor in Fig. 2.9 are determined thanks to experimental viscoelastic curves obtained at a series of temperatures over a specific time period. The values of the storage modulus frequency sweep tests estimated by means of a rheometer are shown in the left diagram in Fig. 2.10. After choosing a specific reference temperature, 120 degrees for example, the curves are then shifted one by one along the times scale until they superimpose and the master curve is identified, as shown in the right diagram in Fig. 2.10. Curves above the reference temperature are shifted to the right, and those below are shifted to the left. [4, 5].

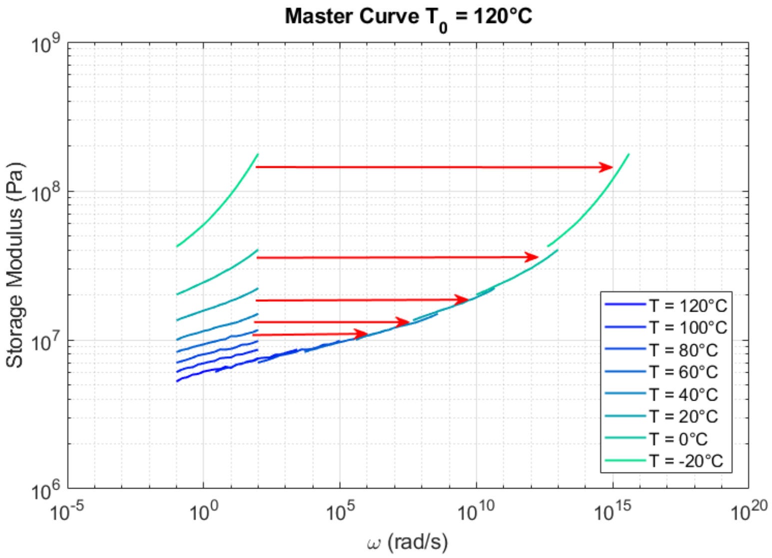

Fig. 2.10 Frequency shift and identified master curve

Hence, the WLF equation allows to estimate the shift factors for different temperatures at which the material has been tested. However, when the WLF constants are found with data at temperatures above the glass transition temperature, the WLF can be used to temperatures at or above the glass transition ones.

Another common way to estimated shift factor at temperature below the glass transition ones is the method based on Arrhenius Law [7, 22]:

$$log(a_T) = \frac{E_a}{2.303 * R}\left(\frac{1}{T} - \frac{1}{T_0}\right) \tag{2.12}$$

where E_a is the activation energy, R is the universal gas constant and T_0 is the reference temperature expressed in Kelvin. The activation energy in (2.12) can be evaluated through the modified Arrhenius equation:

$$\omega = \omega_0 * e^{E_a/(R*T)} \tag{2.13}$$

where ω is the measuring frequency and ω_0 is the frequency when the temperature approaches to infinity. The shift factor a_T, which is obtained thanks to equation (2.13), has the same value for all viscoelastic functions and it depends on the temperature chosen.

2.3 Linear viscoelasticity models

To define a constitutive law for linear viscoelasticity, at least three different common approaches can be adopted: integral model, linear differential models and fractional derivative models.

2.3.1 Boltzmann superposition theory and integral model

The definition of a constitutive law for linear viscoelasticity, the Boltzmann superposition theory could be taken into account, according to which the creep in a specimen is a function of the entire loading history and each increment of load makes an independent and additive contribution to the total deformation [32–34].

The first condition above refers to material *memory function*: the response of the material is influenced by what has happened to it so far, so that it is remembering deformations long past and allowing them to influence the current behaviour.

The second condition states that if a specimen is loaded and is creeping under load, then the addition of an extra load will produce exactly the same additional creep as if that total load had been applied to the unloaded material and it allowed to creep for the same amount of time. In such a way to find a mathematical formulation of this theory, we need to consider a generic transient deformation imposed to the specimen, which can be broken down in two or more step function with a duration time equal to $\Delta\tau$, as reported in Fig. 2.11.

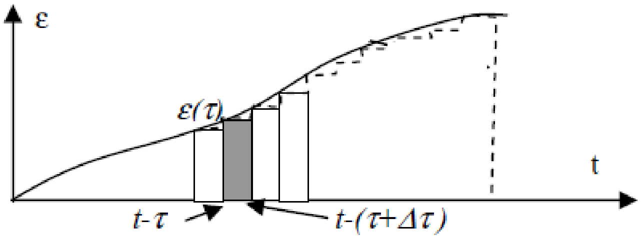

Fig. 2.11 Transient strain

Each strain step function can be expressed as follows:

$$\varepsilon(t) = \varepsilon(\tau)[H(t-\tau) - H\big(t-(\tau+\Delta\tau)\big) \tag{2.14}$$

Moreover, since the modulus $E(t)$ is known through stress-relaxation test, the response to the step function in (2.14) returns an infinitesimal increase of load, which is evaluated as:

$$d\sigma(t) = \varepsilon(\tau)[E(t-\tau) - E\big(t-(\tau+\Delta\tau)\big) \tag{2.15}$$

Calculating the limit for $\Delta\tau \to 0$, we get the following relation:

$$d\sigma(t) = -\varepsilon(\tau)\frac{dE(t-\tau)}{d\tau}d\tau \tag{2.16}$$

At this point, the response to the generic transient strain can be evaluated through the finite integral. We note that the final strain at time t is not equal to zero. Therefore, we need to add the instantaneous response at the step function of amplitude $\varepsilon(t)$ taking into account the starting value of relaxation modulus $E(t=0)$:

$$\sigma(t) = -\int_0^t \varepsilon(\tau)\frac{dE(t-\tau)}{d\tau}d\tau + E_{t=0}\,\varepsilon(t) \tag{2.17}$$

In order to obtain the viscoelastic constitutive law in the final form, also called Integral Model, per parts integral of the function in (2.16) must be computed:

$$\sigma(t) = \int_0^t E(t-\tau)\frac{d\varepsilon(\tau)}{d\tau}d\tau \tag{2.18}$$

which allows to calculate the material response to a generic strain transient load, if creep test has been carried out in order to know the relaxation modulus $E(t)$.

In a similar way, the strain for a generic stress transient load can be evaluated:

$$\varepsilon(t) = \int_0^t J(t-\tau)\frac{d\sigma(\tau)}{d\tau}d\tau \tag{2.19}$$

The constitutive laws expressed in equations (2.18) and (2.19) show how the viscoelastic behaviour depends on the entire loading history (stress or strain load).

2.3.2 Linear differential models

The Boltzmann Superposition Theory is a starting point for the Linear Viscoelasticity, but there is one more convenient way to describe the behaviour of polymers [32, 35, 36]. This method involves correlating stress and strain through linear differential equation in its general form:

$$\sigma(t) + \sum_{i=1}^{n} b_i * \frac{d^i\sigma(t)}{dt^i} = a_0 * \varepsilon(t) + \sum_{i=1}^{m} a_i * \frac{d^i\varepsilon(t)}{dt^i} \tag{2.20}$$

The equation (2.20) is called rheological constitutive equation, in which t is the time and a_0 , a_i , b_i are parameters dependent on the material. This equation is based on thermodynamics, and there is a strict relation between the orders of the derivatives: i.e. $m = n$ or $m = n + 1$.

The specific forms of (2.14) are mathematical basis of widely used mechanical-viscoelastic models, which involve combinations of ideally elastic springs and dashpots. On one hand, spring is a perfect elastic element, following Hooke's law and behaving like an elastic solid; on the other hand, dashpot is a perfect viscous element, following Newton's Law (2.1). The simplest mechanical systems, which model the linear viscoelastic behaviour, are the Kelvin-Voigt model and the Zener model [37, 38].

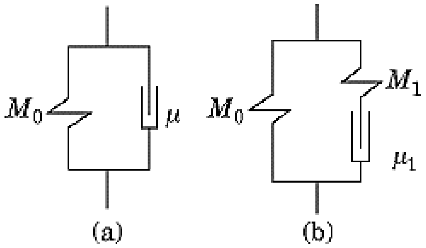

Fig. 2.12 a) Kelvin-Voigt model; b) Zener model

For the Kelvin- Voigt model and Zener model the equation (2.20) turns into:

$$\sigma(t) = a_0\varepsilon(t) + a_1\frac{d\varepsilon(t)}{dt}$$

$$\sigma(t) + b_1 * \frac{d\sigma(t)}{dt} = a_0 * \varepsilon(t) + a_1 * \frac{d\varepsilon(t)}{dt} \tag{2.21}$$

The relations of the spring constants (M_0, M_1) and the dashpot viscosities $(\mu,\ \mu_1)$ with the coefficients of the differential equation are the following:

$$M_0 = a_0 \quad \mu = a_1 \quad M_1 = \frac{a_1}{b_1} - a_0 \quad \mu_1 = M_1 b_1 \tag{2.22}$$

The complex moduli for these models can easily be derived by taking the Fourier transform F of both sides of the $\sigma - \varepsilon$ differential equation, bearing in mind that:

$$F\left(\frac{d\varepsilon(t)}{dt}\right) = (i\omega)F\varepsilon(t) = i\omega\bar{\varepsilon}(i\omega) \tag{2.23}$$

Assumed that $F\varepsilon(t)$ or $F\sigma(t)$ exists. Hence, the complex modulus can generally be defined as follows:

$$E^* = \frac{\bar{\sigma}(i\omega)}{\bar{\varepsilon}(i\omega)} = E'(\omega) + iE''(\omega) = E'(\omega) * [1 + i * tan(\delta)] \tag{2.24}$$

where $\overline{\sigma}(i\omega)$ and $\overline{\varepsilon}(i\omega)$ are the Fourier transforms of the stress and strain-time functions, $\omega = 2\pi f$ is the angular frequency and i the imaginary unit. Indeed, the complex modulus of elasticity describes the dynamic behaviour of viscoelastic materials in the frequency (or time) domain. Because E^* is a complex function, both the Storage Modulus and Loss Modulus, and the Loss Tangent, are dependent on frequency.

2.3.3 Fractional derivative models

The linear differential models, through which the dynamic elastic and damping properties of viscoelastic materials can be analysed considering their dependency on the frequency, as the Kelvin-Voigt and the Zener models have been introduced, as the simplest viscoelastic systems involving ideally elastic springs and viscous dashpots.

Anyway, they cannot accurately reproduce the dynamic behaviour of real materials, for example, the slope of the experimental curves is always smaller than that of the ones predicted by the models. The reason for the inaccuracy of the simple spring- dashpot models can be found in the stress-strain relationship, which is defined in time- domain by a linear differential equation of integer (2.20) . However, this differential equation can be generalized by replacing the integer order of derivatives with fractional order ones. So developed models are called Fractional Derivative Models [38–40].

Four-parameters fractional derivative model

When the Voigt and Zener models were introduced, we have considered springs and dashpots in their structure. The main reason to their inaccuracy takes place in the adoption of basic elements. Indeed, using dashpots we have assumed that the internal friction of the solid exhibits a viscous nature, like a fluid, and the Newton's Law (2.1) is satisfied. It is evident that pure viscous friction could not be characteristic of a viscoelastic solid and it is more realistic to assume that the stress due to internal friction depends on the strain time variation in a lesser extent than in the case of fluid. In order to mathematically express this physical feature, a time derivative of order smaller than unity is introduced in the stress-strain relationship [21, 41]:

$$\sigma(t) \sim \frac{d^{\alpha}\varepsilon(t)}{dt^{\alpha}} \tag{2.25}$$

where $0 < \alpha < 1$. The α-th order fractional derivative of a generic function, for example $\varepsilon(t)$, is easily expressed in frequency domain through the Fourier Transform as follows:

$$F\left(\frac{d^{\alpha}\varepsilon(t)}{dt^{\alpha}}\right) = (i\omega)^{\alpha}F\varepsilon(t) = (i\omega)^{\alpha}\overline{\varepsilon}(i\omega) \tag{2.26}$$

In this manner, the differential equation of Kelvin-Voigt and Zener model (2.21) can be generalized in these new expressions respectively:

$$\begin{gathered} \sigma(t) = a_0\varepsilon(t) + a_1\frac{d^{\alpha 1}\varepsilon(t)}{dt^{\alpha 1}} \\ \sigma(t) + b_1\frac{d^{\beta 1}\sigma(t)}{dt^{\beta 1}} = a_0\varepsilon(t) + a_1\frac{d^{\alpha 1}\varepsilon(t)}{dt^{\alpha 1}} \end{gathered} \tag{2.27}$$

The first equation is the generalized form of the fractional Kelvin-Voigt model consisting of three parameters $a_0,\ a_1$ and α_1. The second relation corresponds to the fractional Zener model with five parameters $a_0,\ a_1,\ \alpha_1,\ b_1$ and β_1. Anyway, the generalized Zener model can be simplified shifting from five to four parameters, since the modelling of most material has shown that $\alpha_1 \approx \beta_1$. Consequently, the four-parameter fractional model is enough to study the dynamic behaviour of real viscoelastic materials in a wide frequency range. So, the differential equation for the four-parameter fractional model can be written as follows:

$$\sigma(t) + \tau_r^{\alpha}\frac{d^{\alpha}\sigma(t)}{dt^{\alpha}} = E_0\varepsilon(t) + E_{\infty}\tau_r^{\alpha}\frac{d^{\alpha}\varepsilon(t)}{dt^{\alpha}} \tag{2.28}$$

In the equation (2.28) we can distinguish:

- $E_0 = a_0$ is the Storage Modulus at zero frequency;
- $\tau_r = {}^{\eta}/_{E_0} = b_1^{\frac{1}{\alpha}}$ is the material relaxation time and it can be also evaluated as the time corresponding to Loss Modulus maximum peak;
- $E_{\infty} = {}^{a_1}/_{\tau_r^{\alpha}}$ is the high frequency limit value of the Storage Modulus.

Turning the quantity ${}^{d^{\alpha}}/_{dt^{\alpha}}$ in $(i\omega)^{\alpha}$ in the equation (2.28) and shifting into Frequency Domain through the Fourier Transform, the complex modulus can be expressed (if the fractional derivative order is equal to unity, the modulus should be the same of the original Zener model):

$$E^{*}(i\omega) = \frac{E_0 + E_{\infty}(i\omega\tau_r)^{\alpha}}{(1 + (i\omega\tau_r)^{\alpha})} \tag{2.29}$$

The Storage Modulus, the Loss Modulus and Loss Tangent can be obtained from the above equation, splitting the real part from the imaginary part. Once defined these magnitudes:

- $c = \frac{E_0}{E_\infty}$;
- $\omega_n = \omega \tau_r$;

The viscoelastic properties can be written as follows:

$$
\begin{gathered}
\frac{E'(\omega)}{E_0} = \frac{1 + (c+1)\cos(\alpha\pi/2)\,\omega_n^{\alpha} + c\omega_n^{2\alpha}}{1 + 2\cos(\alpha\pi/2)\omega_n^{\alpha} + \omega_n^{2\alpha}} \\
\frac{E''(\omega)}{E_0} = \frac{(c-1)\sin(\alpha\pi/2)\,\omega_n^{\alpha}}{1 + 2\cos(\alpha\pi/2)\,\omega_n^{\alpha} + \omega_n^{2\alpha}} \\
\tan(\delta) = \frac{(c-1)\sin(\alpha\pi/2)\,\omega_n^{\alpha}}{1 + (c+1)\cos(\alpha\pi/2)\,\omega_n^{\alpha} + c * \omega_n^{2\alpha}}
\end{gathered}
\tag{2.30}
$$

In Fig. 2.13 the diagram of the Storage Modulus vs Frequency is reported [38], assuming that the value of the ratio c is fixed ($E_0/E_\infty = 100$). As expected, the Storage Modulus increases as the frequency growths, if instead the αth fractional derivatives order decreases (dashed lines), the curve slope in the linear viscoelastic range becomes slighter than the slope in the case of original Zener model (solid line in the plot). Analysing the diagrams, it is noticeable how the slope of the Loss Modulus and Loss tangent are influenced by the order of the fractional derivatives, as well as their maxima values. The result is again a decreasing of the curve slope as soon as $\alpha < 1$.

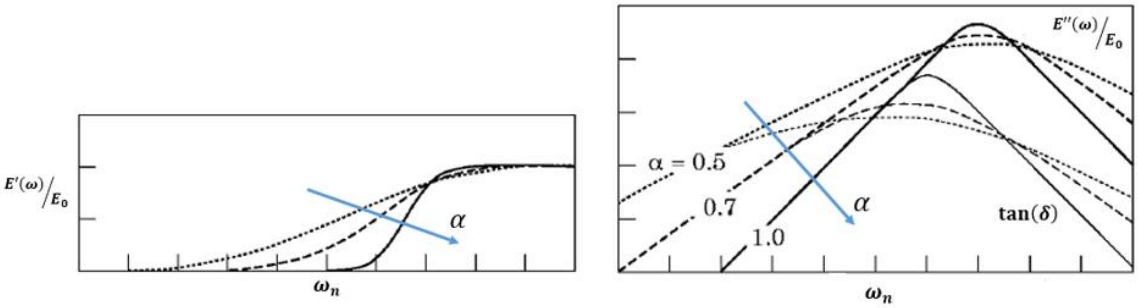

Fig. 2.13 Four-parameter fractional model sensitivity

It is necessary to point out that the order of the fractional derivatives influences the extension of the loss factor peak: if the fractional order is lesser than the unitary, the peak can extend for a wider frequency range. So, the smaller value for the derivative order effects on the slope of the Storage Modulus in frequency domain; in the same way, the increase or decrease of Loss Tangent and Loss Modulus slopes are determined by α below and above their maxima.

Furthermore, it is possible to calculate the frequency at which the Loss Tangent maximum occurs in the frequency domain through the following expression [38]:

$$\omega_{\tan(\delta)} = \frac{1}{\tau_r}\left(\frac{E_0}{E_\infty}\right)^{\frac{1}{2\alpha}} = \frac{1}{\tau_r} c^{\frac{1}{2\alpha}} \tag{2.31}$$

According to the figures above, the value of the fractional derivatives order has effects on the position of the loss factor peak in the frequency domain: if smaller values of the fractional order are adopted, the loss tangent maximum occurs at lower normalized frequency.

It is important to emphasize that the development of the four-parameter fractional derivative model has been made without restrictions on the material types. Besides, the model can be adopted for different kinds of materials, provided that their dynamic properties are frequency dependent. This model is used successfully for loss materials and high loss vibration damping polymers.

Five-parameters fractional derivative model

The four – parameter derivative model is well used when the material exhibits a quite symmetric loss tangent peak in the investigated frequency range. Indeed, the typical behaviour is that the loss factor maximum is asymmetrical in the frequency domain, especially if a wide range is considered. In addition to this, the experimental data on some polymeric damping materials at very high frequency, far from the peak centre, show that the loss factor-frequency curve flattens and seems to approach an asymptotic value, while the Storage modulus exhibits a weak monotonic increase at these frequencies, as shown in Fig. 2.14. Although the Zener four-parameter model is robust and has solid theoretical basis, it is not able to describe the asymmetry of the loss peak and the high-frequency behaviour of the dynamic properties.

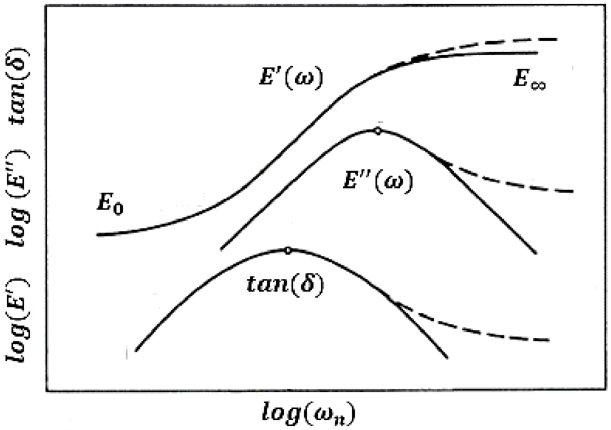

Fig. 2.14 Dynamic properties flattering

For these reasons, there is the need of introducing a better version of the fractional derivative Zener Model, which is characterized by five parameters, referred to as five-parameter fractional derivative Zener Model [39]. This model is able to describe not only the asymmetrical broadening of the loss factor peak, but also the peculiar high-frequency behaviour of the dynamic properties of some polymeric damping materials. In order to describe the five-parameter model, a new constitutive law with different number of stress and strain time derivatives has to be considered. In particular, the number of time derivatives of stress must not be larger than that of strain in order to satisfy the thermodynamic constraints. The new equation is the following:

$$\sigma(t) + b_1 \frac{d^{\beta 1}\sigma(t)}{dt^{\beta 1}} = a_0\varepsilon(t) + a_1 \frac{d^{\alpha 1}\varepsilon(t)}{dt^{\alpha 1}} + a_2 \frac{d^{\alpha 2}\varepsilon(t)}{dt^{\alpha 2}} \tag{2.32}$$

where $\alpha_2 > \alpha_1$ .This equation holds seven parameters, but two of them are unnecessary at this moment. In order to reduce the number of parameters, it is assumed by the analogy of the four – parameter model that $\alpha_1 = \beta_1 = \beta$. The parameters can be written as:

$$\begin{array}{lll} E_1 = E_0 & E_2 = E_\infty & b_1 = \tau_r^\beta \\ a_0 = E_0 & a_1 = E_1\tau_r^\beta & a_2 = E_2\tau_r^\alpha \end{array} \tag{2.33}$$

Therefore, the five parameters will be $E_0, E_\infty, \alpha, \beta,$ and τ_r. The form of the (2.32) turns into the following expression:

$$\sigma(t) + \tau_r^\beta \frac{d^\beta\sigma(t)}{dt^\beta} = E_0\varepsilon(t) + \left(E_1\tau_r^\beta\right)\frac{d^{\alpha 1}\varepsilon(t)}{dt^{\alpha 1}} + (E_2\tau_r^\alpha)\frac{d^{\alpha 2}\varepsilon(t)}{dt^{\alpha 2}} \tag{2.34}$$

The above equation implies a restriction on the relation between α and β. Particularly, α must be major than β value. This restriction is necessary to ensure that the five-parameter model is physically meaningful. The complex modulus for the five-parameter model is easy to derive as follows:

$$E^*(\omega) = E_0 + (E_\infty - E_0) * \left(\frac{(i\omega\tau_r)^\alpha}{1 + (i\omega\tau_r)^\beta}\right) \tag{2.35}$$

Through some mathematical manipulation on the real and imaginary part of the (2.35) conduct to the following equation, which are used to evaluate the dynamic properties in the frequency domain:

$$E'(\omega) = E_0 + E_0(c-1)\left(\frac{\cos\,(\alpha\pi/2)\omega_n^{\alpha} + \cos\,[(\alpha-\beta)\,\pi/2]\omega_n^{\alpha+\beta}}{\left(1+2\cos(\beta\pi/2)\,\omega_n^{\beta} + \omega_n^{2\beta}\right)}\right)$$

$$E''(\omega) = E_0(c-1)\left(\frac{\sin\,(\alpha\pi/2)\omega_n^{\alpha} + \sin\,[(\alpha-\beta)\,\pi/2]\omega_n^{\alpha+\beta}}{\left(1+2\cos(\beta\pi/2)\,\omega_n^{\beta} + \omega_n^{2\beta}\right)}\right) \tag{2.36}$$

$$\tan(\delta) = \frac{(c-1)\{\sin\,(\alpha\pi/2)\omega_n^{\alpha} + \sin\left[(\alpha-\beta)\,\pi/2]\omega_n^{\alpha+\beta}\right\}\}}{\left(1+2\cos(\beta\pi/2)\,\omega_n^{\beta} + \omega_n^{2\beta}\right) + (c-1)\cos\,(\alpha\pi/2)\omega_n^{\alpha} + \cos\,[(\alpha-\beta)\,\pi/2]\omega_n^{\alpha+\beta}}$$

The frequency variations of the Storage Modulus, Loss Modulus and Loss Tangent were studied numerically in respect to the role of the difference between α and β, bearing in mind that $\alpha > \beta$. For example, in Fig. 2.15 the results with parameters of $\alpha = 0.7$ $c = 10^3$ and different values of β are shown [39, 40].

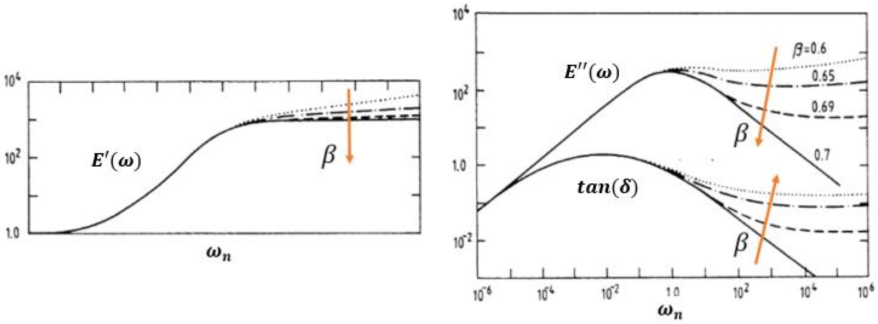

Fig. 2.15 Fractional order sensitivity on model response

The figure above demonstrates that there is a striking difference between the behaviours of the five-parameter and four-parameter models at high frequencies, as said before. Particularly, the physical meaning of the five model parameters can be further explained:

- α leads the low frequency increase of the loss modulus and loss factor;
- β, or more precisely the difference between α and β, leads the asymmetry of the loss tangent peak and the high frequency behaviour of the viscoelastic dynamic properties;
- E_∞ is related to the high frequency value of the Storage Modulus, but, in contrast to the four – parameter Zener model, it is not the asymptotic value.

2.3.4 Generalized Maxwell models

Since the experimental characterization of the viscoelasticity of the compounds is particularly important to properly feed the procedures of so many different application areas, the question arises about which could be the analytical model that is able to reproduce the viscoelastic behaviour in an optimal and robust way employing the minimum number of parameters. In other words, the aim is to investigate the simplest constitutive model able to reproduce the experimental viscoelastic behaviour in the widest range of operating frequencies.

The simple Maxwell or Kelvin models fail in representing the actual response of viscoelastic materials at low and high frequencies, respectively, while the generalized models are able to provide more reliable results. As this paper is focused on viscoelastic solids, the GM model and FDGM model are considered and refer to a spring in parallel with (respectively) Maxwell cells and fractional Maxwell cells [42, 43]. These cells are composed of a spring and a dashpot arranged in series, while the fractional Maxwell element is obtained by replacing the dashpot elements with the so-called spring-pot elements. Fig. 2.16 depicts the rheological model considered [44].

In this paragraph, the Generalized Maxwell (GM) and the Fractal Derivative Generalized Maxwell (FDGM) models are mathematically described. Starting from the models' definition in the time domain, the frequency domain expressions are derived by means of the Fourier transform to obtain the pole-zero formulation of both the models under analysis.

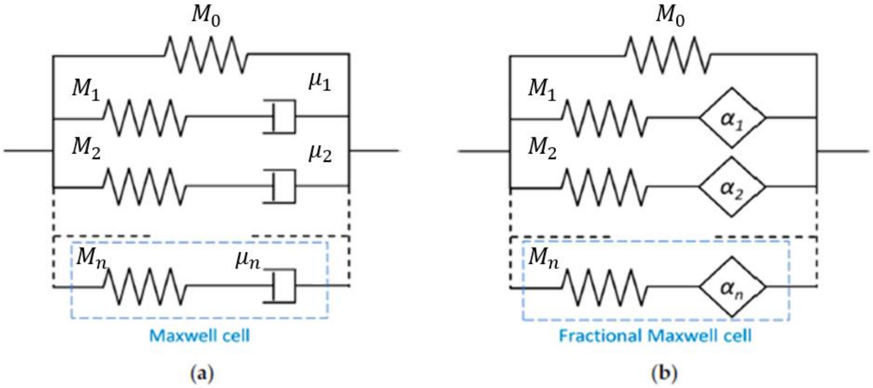

Fig. 2.16 a) Generalized Maxwell; b) Fractal derivative

Generalized Maxwell model

Considering the (2.20), the differential equation of the GM model formulation can be expressed in general form as:

$$\sum_{i=0}^{N} b_i \frac{d^i \sigma(t)}{dt^i} = \sum_{i=1}^{M} a_i \frac{d^i \varepsilon(t)}{dt^i} \tag{2.37}$$

where the parameters $a_0 = 0$ and $M = N$ are assumed for the considered case of Maxwell model. The complex modulus can be derived transforming equation (2.37) into the frequency domain. Calculating the Fourier transform, the following expression for the complex moduli is derived:

$$E^*(i\omega) = M_0 + \sum_{k=1}^{N} \frac{i\omega M_k \mu_k}{M_k + i\omega\mu_k} \tag{2.38}$$

where the parameters M_k and η_k represent the springs stiffness and dashpots viscosity, respectively, as represented in Fig. 2.16 (on left side), and ω is the angular frequency.

Renaud et al. [26] have demonstrated that the GM model, mathematically described in (2.38) in a frequency domain, can be equivalently expressed in the pole-zero formulations:

$$E^*(i\omega) = M_0 \prod_{k=1}^{N} \frac{1 + \frac{i\omega}{\omega_{z,k}}}{1 + \frac{i\omega}{\omega_{p,k}}} \tag{2.39}$$

where ω_z and ω_p are the zero and pole, respectively.

Fractal derivative generalized Maxwell model

In case of Fractal model, the generic constitutive equation (2.32) can be also expressed as:

$$\sum_{n=0}^{N} b_n \frac{d^{\beta_n}\sigma(t)}{dt^{\beta_n}} = \sum_{m=0}^{M} a_m \frac{d^{\alpha_m}\varepsilon(t)}{dt^{\alpha_m}} \tag{2.40}$$

assuming $M = N$ and $b_0 = 0$ for the considered case of Maxwell model. Turning to frequency domain, and taking into account that $\alpha = \beta$, the equation (2.40) becomes [45, 46]:

$$E^*(i\omega) = M_0 + \sum_{k=1}^{N} \frac{(i\omega)^{\alpha_k} M_k \mu_k}{M_k + (i\omega)^{\alpha_k}\mu_k} \tag{2.41}$$

In analogy with the GM model (2.39), the equation (2.41) can be equivalently expressed in the pole-zero formulations [47]:

$$E^*(i\omega) = M_0 \prod_{k=1}^{N} \frac{1 + \left(\frac{i\omega}{\omega_{z,k}}\right)^{\alpha_k}}{1 + \left(\frac{i\omega}{\omega_{p,k}}\right)^{\alpha_k}} \tag{2.42}$$

Generalized Maxwell models comparison

As described in [44], an identification procedure for cost function optimization has to be carried out in order to determine the poles and zeros of equations (2.39) and (2.42) taking into account the experimental data of the viscoelastic compound properties at different frequency ranges matching with a reference temperature [26, 48].

In the application of the GM and FDGM, the first analysis requires the comprehension of the minimum number of parameters that can describe the dynamic characteristics of the considered viscoelastic material. As shown in Fig. 2.17, the GM model composed of 15 elements appears totally insufficient to describe the compounds' frequency response because it shows unphysical oscillations although it seems to follow the global trend. Increasing the number of Maxwell elements, the fitting of experimental data of storage modulus and loss factor is improved as well. However, it should be noted that to have significant improvements in GM model results, several elements must be added with a consequent increase in the parameter to be identified.

In Fig. 2.18, the FDGM model results are shown. For each compound, the experimental data are compared with model composed by a spring in parallel with 3, 4 and 5 spring-pot elements (see Fig. 2.16). It should be noted that this model is able to give an acceptable representation of the curves' shapes with a three-element model. In this case, increasing the number of Maxwell elements, the fitting of experimental data improves. It is noteworthy that the number of parameters to be identified highly affects the computational load in terms of efficiency and effectiveness. Thus, the comparison between the FDGM models with the GM models points out that the FDGM is preferable because of the limited number of parameters to be determined, which means a significant reduction in frequent mathematical difficulties encountered in the ill-posed problem of identification procedures from experimental data.

Once analysed the efficiency of the Maxwell models in terms of number of elements, the comprehension of the minimum amount of experimental data in terms of viscoelastic properties, which feed up the cost function in the identification algorithms, is fundamental for the real applications [44]. Adopting all the five zones to identify the parameters of the three-element FDGN model, it is possible to obtain an equally good fitting of the case in which all experimental data are take into account. This condition points out that the chosen five zones represent remarkable points of the curves that unequivocally determine the characteristics of a compound (see Fig. 2.19, a). On the other hand, the experimental data in two frequency ranges are totally insufficient to describe the compound dynamic behaviour (see Fig. 2.19, b). These results were predictable considering that the information of the loss facto peak has not been taken into account. The last data combination (see Fig. 2.19, c) gives good results being able to fit the global compound behaviour taking into account only the information of the upper and low frequency plateaus plus the loss tangent peak area.

Therefore, the analysis proposed [44] has returned that both GM an FDGM models are able to fit the viscoelastic behaviour of the compounds in the entire frequency range in which they are experimentally characterized, but the GM model needs a number of elements that are higher than the FDGM one. This means that FDGM can provide good matching with the simple configuration with only ten variables (three elements), while comparable results can be obtained with the GM model identifying more than 51 parameters (25 elements).

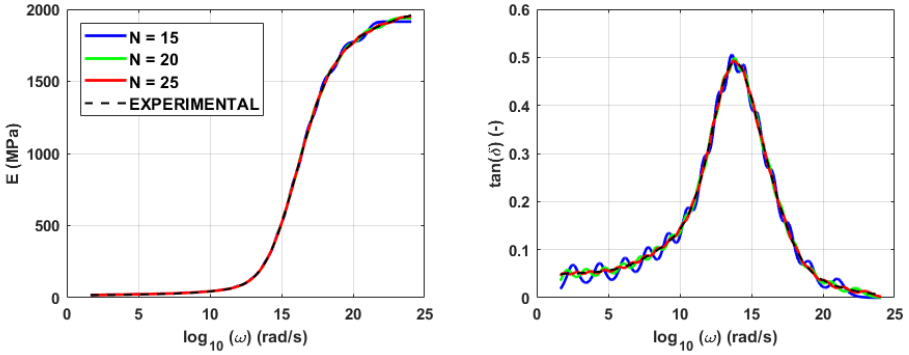

Fig. 2.17 Storage modulus and loss tangent for a generic SBR compound: experimental data(dashed line) vs. GM model with 15 (blue line), 20 (green line) and 25 (red line) elements

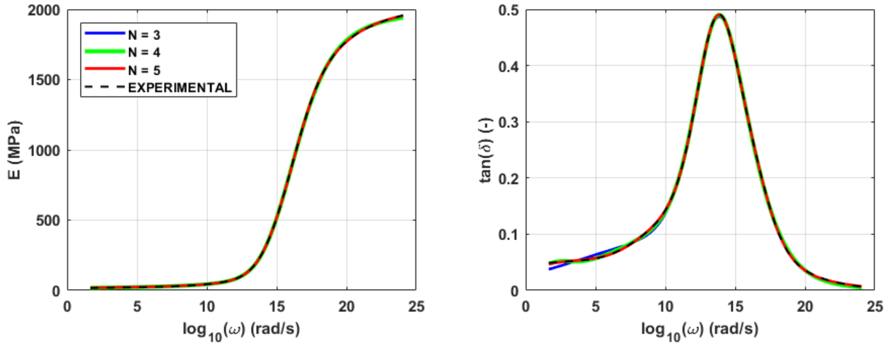

Fig. 2.18 Storage modulus and loss tangent for a generic SBR compound: experimental data (dashed line) vs. FDGM model with three (blue line), four (green line) and five (red line) elements.

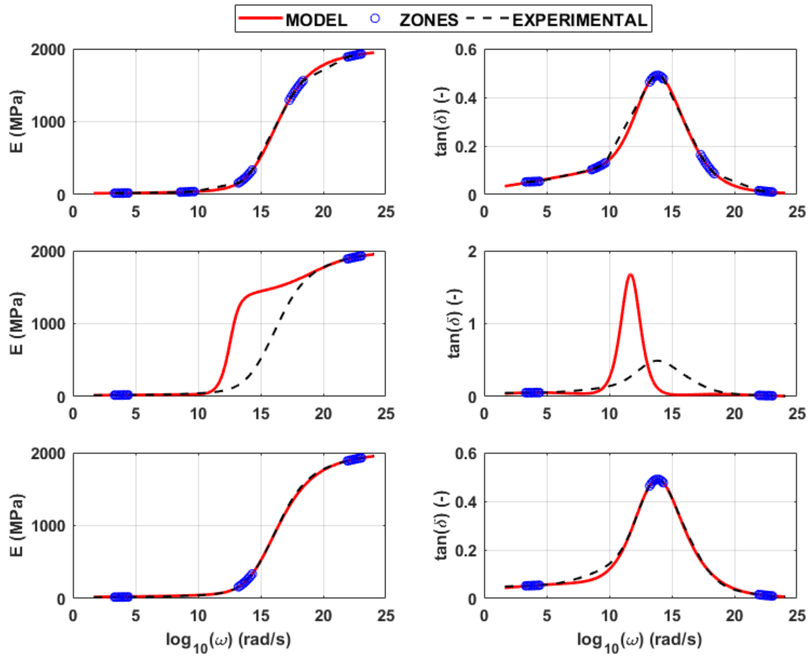

Fig. 2.19 FDGM estimation of storage modulus and loss tangent for a generic SBR compound adopting limited zones of experimental data

Chapter 3

Viscoelasticity Characterization Methodologies

Tyres are made of different elastomeric materials with peculiar viscoelastic properties to which tyres owe a large part of their grip capacity. In the following chapter, the special properties of these materials, linked to the phenomena involved in friction and tyre-road contact, are deeply examined.

The evaluation and analysis of tyre tread viscoelasticity is a fundamental topic in a wide range of activities concerning the development of polymers for innovative compounds, the parametrization of physical contact models and the optimization of vehicle performance and safety. In these applications, the viscoelastic properties determination of a tyre block, which depends on rubber temperature and frequency solicitation of bitumen asperities, is essential for contact mechanics modelling and the prediction of the limit value of the local friction coefficient [2, 49]. The Dynamic Mechanical Analysis (DMA) is widely employed into the characterization of viscoelasticity in order define the hysteretic behaviour of the compound following the Time-Temperature Superposition principle [50, 51]. This testing approach perfectly fits with polymer specimens manufactured with specific dimension for the DMA and, unfortunately, it cannot be always applied for the viscoelasticity characterization of components constituting the mechanical system of interest. For example, Motorsport racing teams use to face with the restrictions linked to the employment of confidential tyres, provided by tyre makers and not available to invasive testing. Further, these DMA procedures involve complex and very expensive machines for the analysis of a generic compound sample.

Regarding the evaluation of the parameters of contact and friction models, the availability of thermal and structural properties of the effective tread compound provides an increase in reliability of the prediction of magnitudes of interest by means of the proposed model [52–54] and available ones in scientific literature [13–15, 55].

For these reasons, the development of innovative methodologies, as well as the non-destructive, are an attractive solution replacing the standard test methods involving complex and expensive benches for the investigation of a compound specimen manufactured in different conditions respect to the final product provided by tyre makers.

Hence, during his research period, the author, supported by the Vehicle Dynamics research group of the Department of Industrial Engineering of the University of Naples Federico II, has designed and developed innovative and non-invasive characterization procedures for tyre compounds that will be discussed, once focused on the available dynamic mechanical analysis methodologies. These techniques are outlined in Fig. 3.1 and they will be analysed and compared in this chapter.

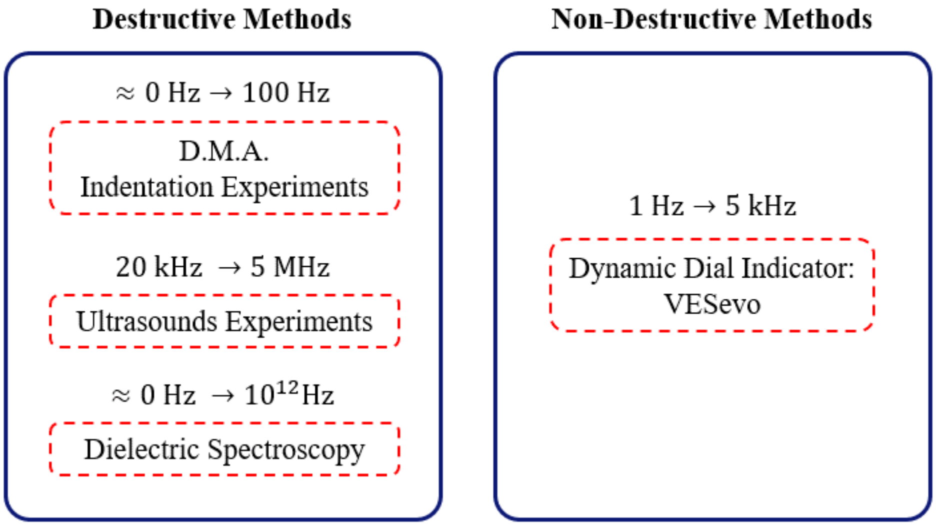

Fig. 3.1 Viscoelasticity characterization methods

3.1 Dynamic Mechanical Analysis (DMA)

Dynamic Mechanical Analysis, otherwise known as DMA, is a technique where a small deformation is applied to a sample in a cyclic manner. This allows the materials response to stress, temperature, frequency and other values to be studied. General types of DMA tests include temperature sweeps, frequency sweeps, studies of curing behaviour or vitrification, stress–relaxation and creep–recovery, among others [30, 50]. DMA is also called DMTA for Dynamic Mechanical Thermal Analysis.

The DMA are usually carried out by means of applying a dynamic load with a certain frequency to a viscoelastic specimen at different temperatures. The applied mechanical load causes a corresponding strain, whose amplitude and phase shift can be determined (see Fig. 2.4).

In DMA measurements, because of the design apparatus [30, 50], the applied load is small. Consequently, the material exhibits an almost purely elastic or, at least, a linear-viscoelastic response. Since the main difference between the complex modulus and the storage modulus is the non-elastic part, it follows that E^* becomes equal to E'. Only in the glass transition, where the non-elastic strain per oscillations shows its maximum (see Fig. 2.6), the difference between the two magnitudes is higher and the storage modulus declines many degrees earlier than the complex modulus.

There are two different types of DMA measurements: strain-controlled and force-controlled. The first one is carried out applying a sinusoidal deformation to the specimen and measuring the stress achieved; the second one applying a dynamic load and measuring the corresponding strain. The dynamic load can be applied in free vibration or in forced vibration [50].

The material is subjected to forced vibrations at a frequency far from the resonance and involve a dynamic mechanical analyser and a thermal analysis tool. During this experiment, a suitable shaped rod is necessary, which works in contact with the specimen and on LVDT (Linear Voltage Differential Transformer), that accurately checks the rod displacements.

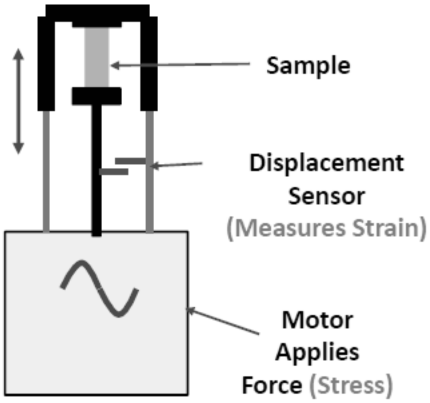

Fig. 3.2 Rheometer scheme for DMA

The DMA can be carried out in two ways: the viscoelastic properties are determined in relation with the temperature, since the stress and the frequency are fixed (temperature sweep mode); otherwise, the temperature is fixed and the test is performed changing the frequency (frequency sweep mode). Both methodologies can measure the phase angle δ as the lag between stress and strain sinusoids on a chart or a digital recorder. Anyway, another better method for the phase determination is the evaluation of the elliptic $\sigma - \varepsilon$ curve. In case of lag sufficiently large, the phase angle can be easily determined by the width of the elliptic curve. In materials with low loss, instead, the ellipse is very thin and close to a straight line, as shows in Fig. 3.3.

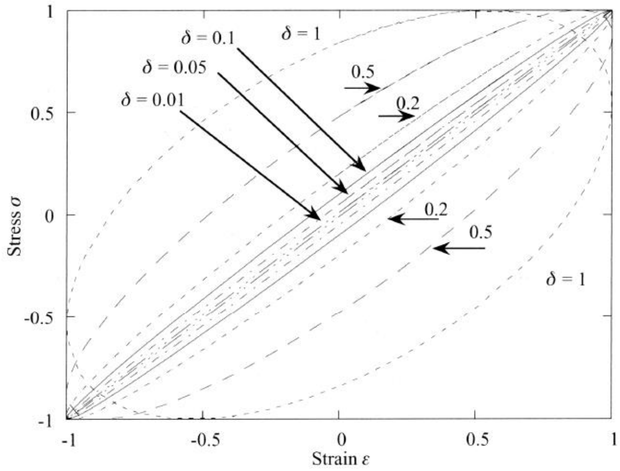

Fig. 3.3 Hysteretic loop

Since the standards do not favour specific geometries for specific tasks, there is no consensus on which geometry is required for polymers. The DMA instrument manufacturers do suggest sample dimension ranges for given geometries [56, 57] but do not discuss how a three order of magnitude modulus change through the glass transition can affect DMA measurements. Numerous researchers favour the 3-point bending geometry [58], other favour the dual cantilever geometry [59], and others prefer the scanning calorimetry one [60]. However, in [56] and others is claimed that the 3-point bending geometry is best suited for high modulus materials, such as metals, ceramics, and high filled thermosetting polymers showing a little change in modulus throughout the test. Duncan [56] also suggests that the SC and DC clamps are better suited for characterizing material through the glass transition, although SC is preferred, especially for materials with high thermal expansion.

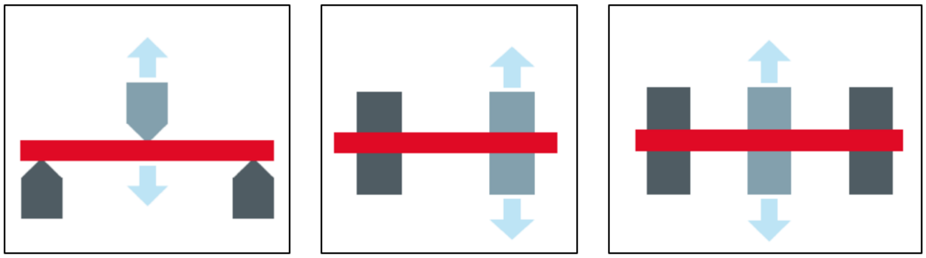

a) b) c)

Fig. 3.4 Axial fixture for DMA: a) 3-point bending; b) single cantilever; c) dual cantilever

3.1.1 *Axial and torsional deformation*

DMA analysers are normally built to apply the stress or strain in two ways. The first can apply the force in a bending motion, the second requires testing the sample in torsion. Torsional analysers normally permit continuous shear and normal force measurements. Axial analysers are generally designed for solid and semisolid materials and apply a linear force to the sample. Despite the traditional selection of torsional instruments for melts and liquids and axial instruments for solids, there is considerable overlap between the types of instruments. With a proper choice of sample geometry and good fixtures, both types can handle similar samples.

Axial deformation

Axial analysers allow a great deal of flexibility in the choice of fixtures in order to test a wide range of materials. A bending or flexure fixtures commonly used is the 3-point bending (Fig. 3.4, a). This procedure depends on the specimen being a freely moving beam, and about 10% longer on each end than the span. The four sides of the span should be true, i.e., parallel to the opposite side and perpendicular to the neighbouring sides. There should be no nicks or narrow parts because they could affect the result of the test. The sample is loaded so the three edges of the bending fixture are perpendicular to the long axis of the sample.

Cantilever fixtures clamp the ends of the specimen in place, introducing a shearing component to the distortion and increasing the stress required for a set displacement. Two types of cantilever fixtures are used: dual cantilever, in Fig. 3.4 c, and single cantilever, in Fig. 3.4 b. Both cantilever geometries require the specimen to be true as described above and to be loaded with the clamps perpendicular to the long axis of the sample. In addition, care must be taken to clamp the specimen evenly, with similar forces, and not to introduce a twisting or distortion in clamping. Particularly, dual cantilever geometry is slightly different from 3-point bending: in this case the sample is clamped at the extremity and in the middle.

Torsional deformation

Dynamic measurements in torsion have been performed extensively on rotational rheometers and are often considered as an industrial standard [61]. They provide characterization of the dynamic mechanical response of a wide variety of materials including glasses [62], filled and vulcanized systems, as well as soft gels. In the past, oscillatory torsional tests were performed by applying relatively large deformations on cylindrical specimens and recording both torque and normal force response as a function of time. Different types of specimen geometries can be used in torsional tests. In the rheological literature, the most commonly used has been a cylindrical rod with different aspect ratios. For cylindrical specimens undergoing torsional deformation, the geometry and clamping barely affect the shear moduli and the measurements essentially coincide with those using parallel plates. In contrast, a clear dependence of the storage modulus on the aspect ratio is detected for specimens having rectangular cross section [37, 63].

On the torsional measurements, Szabo [64] speculated the occurrence of extensional and compressional stresses in torsion with rectangular specimens, and in particular, in the region in contact with the clamps. The above literature review points to the need for a general protocol for assessing torsional measurements based on appropriate choices of experimental and material geometries. The simplest geometry in torsional shear consists of a pair of parallel plates, as shown in Fig. 3.5 a. The height or gap here is determined by the viscosity of the sample. Enough space is required between the plates to obtain a decent flow behaviour, but not so much that the material flies out of the instrument.

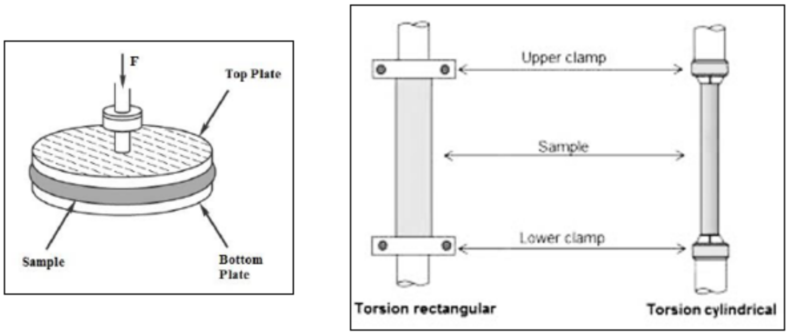

a) b)

Fig. 3.5 Torsional deformation: a) parallel plates; b) rectangular and cylindrical torsions

The edge of the sample should be spherical without fraying or rippling. These plates have an uneven strain field across them: the material at the centre of the plate is strained very little, as it barely moves. At the edge, the same degree of turning corresponds to a much larger movement. So, the measured strain is an average value and the real strain is inhomogeneous. The thrust against the plates can be used to calculate the normal stress difference in steady shear runs.

Stiff and solid samples in a torsional analyser are usually tested as bars or rods and twisted about their long axis (see Fig. 3.5 b). The sample is first clamped and after suitably positioned in the rheometer. The right choice of the sample geometry is not easy and depends on the application.

3.2 Micro-indentation experiments

Indentation methods are suitable for the determination of local mechanical properties of polymers, particularly elastomer systems [65]. This approach requires a probe penetrating into the surface of a viscoelastic material in which the mechanical magnitudes like hardness or the stiffness of the material can be determined through the measurement of the force-indentation curves [66, 67]. The measurement of these quantities in different regions of a viscoelastic sample allows the mechanical inhomogeneity of the material to be determined.

The indentation experiment can be quasi-static or dynamic [65, 68]. The first class requires a probe penetrating into the surface of the viscoelastic specimen very slowly inducing a solicitation frequency almost equal to zero. In the case of a linear force-indentation curve the measurement of the force during the penetration allows the quasi-static stiffness to be determined as follows:

$$S = \frac{f}{h} \tag{3.1}$$

where f is the indentation force and h the indentation depth. If a non-linear force-indentation curve is measured, the contact stiffness can be defined as:

$$S_h = \frac{\partial f}{\partial h} \tag{3.2}$$

so that the stiffness S_h can depend on the level of indentation depth. On the other hand, the dynamic indentation tests firstly require the application of a static pre-indentation matching with a fixed depth value h_0, then a sinusoidal indentation with the amplitude Δh and the frequency ω is carried out, as shown in Fig. 3.6. According to the measurement of viscoelastic properties, the corresponding force signal Δf is detected. The viscoelastic stiffness is then given as:

$$S^* = \frac{\Delta f}{\Delta h} \tag{3.3}$$

The determination of the phase angle δ between depth and force signals, which depends on their time delay and the applied frequency, lead to the viscoelastic loss factor evaluation:

$$\tan(\delta) = \tan\left(\Delta t \frac{\omega}{2\pi}\right) \tag{3.4}$$

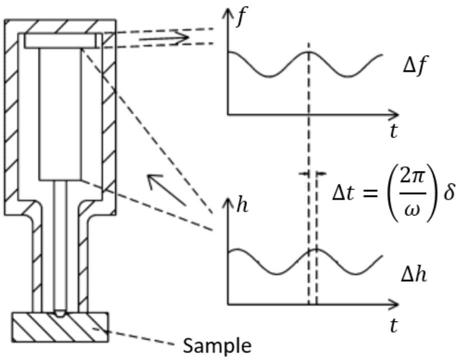

Fig. 3.6 Dynamic indentation test

In Fig. 3.7, the typical trends of S^* and $\tan(\delta)$ towards the indentation depth for an inhomogeneous sample (SBR/NR-composite) of 8 mm thickness cured at 130° are shown [65]. This diagram demonstrates that the average stiffness of the specimen in the SBR-phase is higher than NR-phase at this cure temperature. This means that in the NR-phase the sample is characterized by a softer behaviour and less damping effect due to hysteresis.

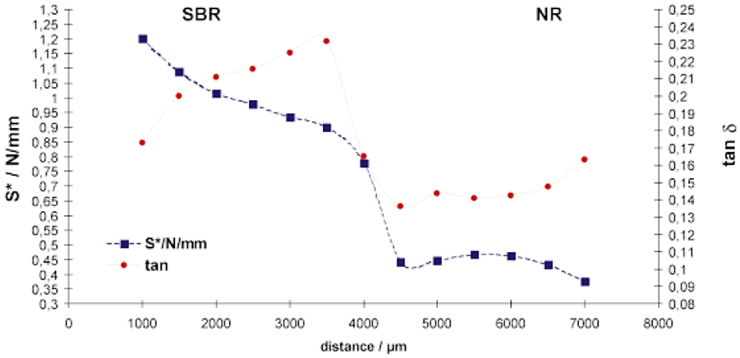

Fig. 3.7 Contact stiffness and loss factor trends for an inhomogeneous sample

3.2.1 Viscoelastic properties evaluation through micro-indentation

For the viscoelasticity evaluation, a model of a damped harmonic oscillator, which includes a collection of spring and dashpots, such as that shown in Fig. 3.8, is typically used, and Z^* is modelled by a parallel arrangement of a spring, S_M, accounting for the sample *elastance* and a dashpot, R_M, accounting for the sample *frictance*, with the terminology of Ferry [4, 69]. This parallel arrangement does not correspond to a Voigt/Kelvin constitutive element, as S_M and R_M do not represent the sample modulus and viscosity [69].

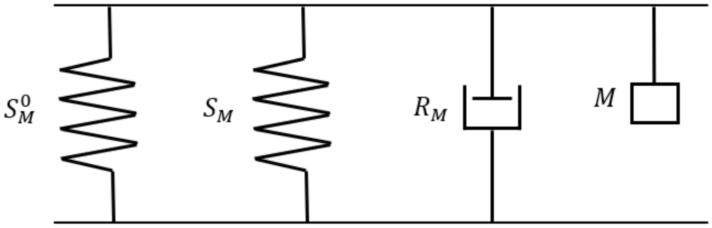

Fig. 3.8 Schematic illustration of the dynamic model of the apparatus according to Ferry

Rather, in the case of driving the model in Fig. 3.8 by a sinusoidal force, they are related the real and imaginary components of Z^* as follows:

$$Z^* = R_M + iX_M = R_M + i\left(\omega M - \frac{S_M}{\omega} - \frac{S_M^0}{\omega}\right) \tag{3.5}$$

where ω is the pulsating frequency, M is the mass of the moving element, S_M^0 is the elastance of the instrument springs, and R_M and X_M are the mechanical resistance and reactance.

Like the rheological instrumentation (Fig. 3.2), the dynamic instrument-sample interaction for the instrumented indentation of viscoelastic materials is based on a damped harmonic oscillator model in which the mechanical impedance of the instrument-specimen contact phenomenon modelled by a parallel arrangement of springs and dashpots, as previously described. However, unlike DMA machines, the relationships between the viscoelastic properties $(E', E")$ and the elastance S_M and frictance R_M has to be assumed with a basis in the elastic solution to the indenter-sample contact problem [66, 70]. According to the notation in Fig. 3.9, which is common in instrumented indentation literature, the sample impedance is made up of the tip-sample contact stiffness, S, and the tip-sample damping factor, C_s.

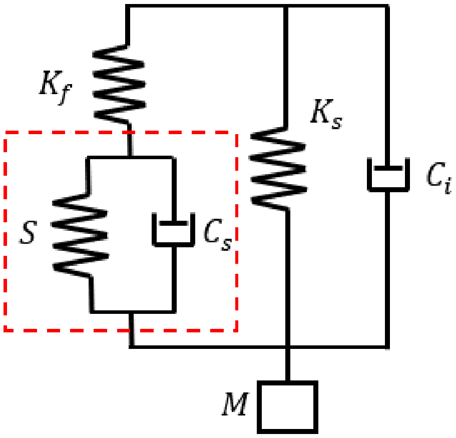

Fig. 3.9 Dynamic model of the depth-sensing indentation system with sample

Solving for the real and imaginary part of the impedance results in expressions for S and C_s:

$$\begin{gathered} S = \frac{P_0}{h_0}\cos(\delta) + \omega^2 m - K_s \\ C_s = \frac{P_0}{h_0}\sin(\delta) - C_i \end{gathered} \tag{3.6}$$

thus S is a function of calibrated instrument and measured test parameters, including the system spring stiffness K_s, system damping coefficient C_i, system mass m, frequency ω, phase angle δ, magnitude of the force oscillation P_0 and magnitude of the displacement oscillation h_0.

Considering the magnitudes determined by means of equations (3.6), the sample reduced modulus E_r can be continuously measured with the following equation [71–74]:

$$E_r = \frac{S}{2r} = \frac{S\sqrt{\pi}}{2\sqrt{A_c}} \tag{3.7}$$

where the cross section of the indenter is assumed to be circular with respect to the contact radius, r, to the projected area of the tip-sample contact, A_c. A small correction is sometimes applied for non-circular cross sections [75], and an additional minor corrections have also been suggested [76]. The reduced modulus accounts for deformation of both the indenter (elastic modulus E_i and Poisson's ratio ν_i) and the sample (elastic modulus E_s and Poisson's ratio ν_s) and is given by:

$$E_r = \frac{E_s}{(1-\nu_s^2)} + \frac{E_i}{(1-\nu_i^2)} \tag{3.8}$$

The equation (3.7) is based on the elastic solution for quasi-static indentation [67, 70, 77]. In case of a viscoelastic specimen, the calculations of the reduced storage modulus E_r' and the reduced loss modulus E_r'' depending on the contact stiffness and damping coefficients can be expressed as:

$$\begin{gathered} E_r' = \frac{S\sqrt{\pi}}{2\sqrt{A_c}} \\ E_r'' = \frac{\omega C_s\sqrt{\pi}}{2\sqrt{A_c}} \end{gathered} \tag{3.9}$$

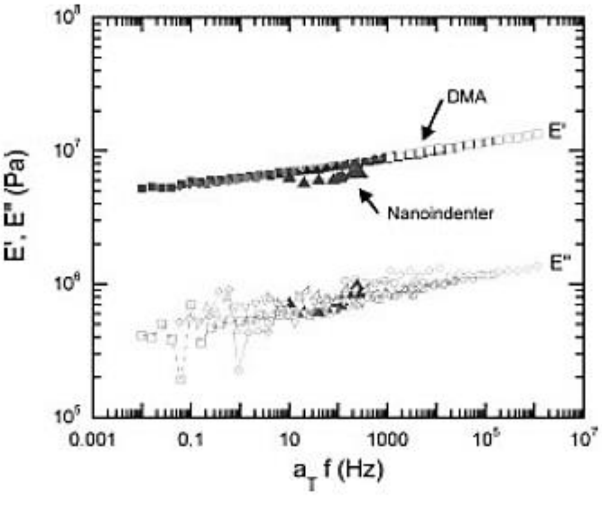

Fig. 3.10 Indentation results compared to DMA curves

In Fig. 3.10, the comparison between the viscoelastic properties of the analysed specimen [78] and the DMA master curves of storage and loss modulus is shown. Each marker represents the average value of 10 measurements for the indentation data and a single measurement for the dynamic mechanical data. These values have been time-temperature shifted [4, 5] to a reference temperature of 20°C. Considering the frequency range of the indentation test, a good agreement between the bulk and the indentation data is observed. The scatter in the loss modulus is believed to be attributable to the baseline stability in the calibration of the instrument employed.

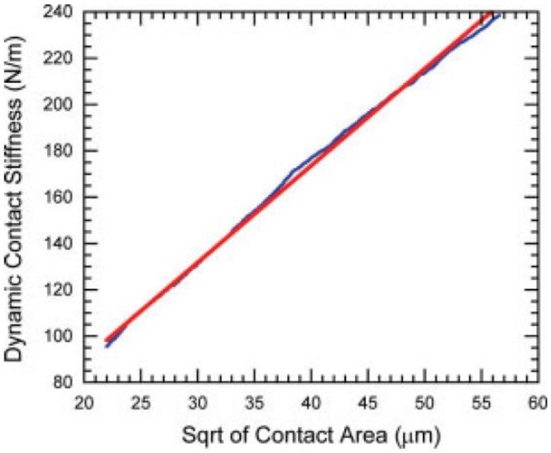

Fig. 3.11 Dynamic contact stiffness variation

The dynamic contact stiffness arising from a single indentation test exhibits a linear trend over the square root of the contact area. The linear dependence and fit curve in Fig. 3.11 suggest a homogeneous material response over these depths and that inaccuracies in the contact area appear not to play a significant role in properties evaluation [68, 78].

3.3 Durometer experiments at the UniNa Tyre Lab

The durometer experiments still belong to the micro-indentation class. This technique is suitable for the characterization of both tyre surface and tread compound thanks to its transportability and easy way to use. This kind of experiments has been applied during the research activity at the *Tyre Lab* of the Department of Industrial Engineering of the University of Naples Federico II.

Despite the micro-indentation procedures described in section 3.2 Micro-indentation experiments, the characterization through the durometer only provides the storage modulus E' of the viscoelastic specimen at different temperatures taking into account the measurement of the material hardness [79].

In the experimental sessions, the Shore A hardness has been measured for different SBR compound samples employing a specific durometer according to the DIN 53505 and DIN EN ISO 868 standards [80].

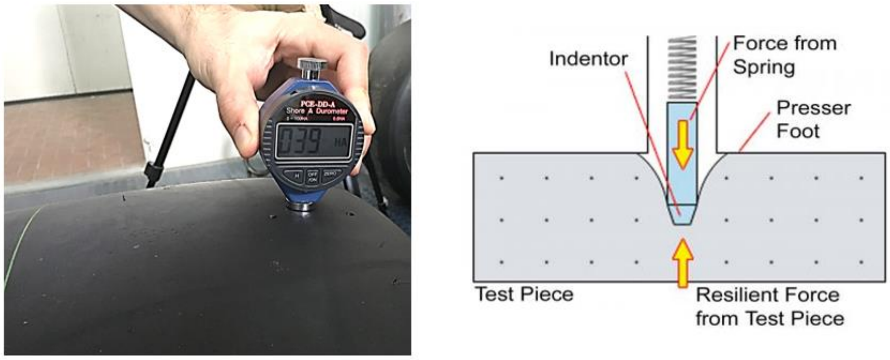

a) b)

Fig. 3.12 a) Durometer experiments on tyre tread; b) Durometer working principle

The durometer consists of an indenter in the shape of a truncated cone, which is pressed on the specimen under the force of spring with a suitable stiffness, as shown in Fig. 3.12 (b). The elastic penetration depth is a magnitude measured between 0 and 100, which refers to the Shore A material hardness. During the experiments, an air flux, generated by a heating gun, gives the tyre compound specimen heat in order to measure the hardness at different temperatures. The temperature of the specimen in the indentation area is measured by a thermal camera (see Fig. 3.13). In the case of testing at low temperatures, the specimen is positioned in a suitable climatic cell.

Fig. 3.13 Heating gun (on the left); thermal camera (on the right)

A linear relationship exists between the depth of the penetration and the Shore A hardness as well as between the depth of the penetration and the spring force as follows:

$$\begin{gathered} F = B_1 + B_2 H_{S_A} \\ h = B_3\left(109 - H_{S_A}\right) \end{gathered} \tag{3.10}$$

where F is the spring force, h the penetration depth, H_{S_A} is the measured Shore A hardness and B_1, B_2 and B_3 depends on the employed instrument. Their values and dimensions for a Shore A durometer are respectively: 0.549 N, 0.07516 N and 0.025 mm [79, 80].

The fact that, when measuring the hardness, an indenter with high stiffness is pressed into a test specimen with low stiffness, thereby deforming it elastically, suggests using the theory of Boussinesq [81] for the theoretical description of the relationships between the load and the deformation. This starts with the action of a single force on the linearly elastic half-space and ultimately leads via an analytical path to the associated stress and displacement functions for the rotationally symmetrical case. Applying these laws to loading of the half-space by a rigid indenter with a finite diameter yields for the relationship between the loading force and the depth of the penetration by the indenter equation below [82]:

$$h = \frac{F(1-\nu_s^2)}{2\,E_s\,r} \tag{3.11}$$

where E_s is the elasticity modulus of the sample (or the storage modulus of a viscoelastic one), ν_s is the Poisson's ratio and r is the contact radius of the indenter. Upon inserting the equations (3.10) into (3.11), one obtains a direct relationship between the modulus of elasticity and the Shore hardness in the form:

$$E_s = \frac{1-\nu_s^2}{2\,r\,C_3}\frac{C_1 + C_2 H_{S_A}}{100 - H_{S_A}} \tag{3.12}$$

In this model, the rigid indenter represents the Shore A indenter quite well, even though the latter has the shape of a truncated cone. The elastic half-space, however, represents a very significant idealisation of the test specimen that not only ignores the effects of its finite dimensions but also the possible deviations from linear deformation behaviour as well as the friction between the indenter and the test specimen. Nevertheless, the equation (3.12) can serve quite well as the basis for describing the actual situation during a Shore hardness test.

3.3.1 Experimental sessions and modulus evaluation

After studying the relationship between the specimen dynamic properties and the hardness, the experiments have been carried out on different tyres compounds in order to get the dynamic properties values in the temperature range of interest.

The experimental procedure is established by ISO standards. They involve placing the specimen on a hard and horizontal plane surface, holding the durometer in a vertical position with the point of the indenter and applying the force necessary to keep the presser foot in contact with the material. The hardness value shall be read on the device scale within 3 seconds.

To comprehend the reliability of the elasticity modulus E_s determined by means of this experimental procedure, a meaningful test session has been carried out on passenger tyre slabs, of which the viscoelastic master curves in terms of temperature sweep at 1 Hz at different strain percentage were obtained through DMA. The dimensions of the tested samples are reported in Table 3-1.

Table 3-1 Slabs dimensions

Sample	Dimensions (mm)
Slab A	50x50x5.30
Slab B	50x50x5.00
Slab C	50x50x5.20
Slab D	50x50x5.35

The tested compounds are shown in Fig. 3.14 together with the measured Shore A hardness. Analysing the data reported in the diagram, the dependence of the compound behaviour on the temperature is clear: at low-temperature values, the stiffness is higher and close to the maximum measurable by the instrument; on the other side, the temperature increment leads to a softening phenomenon of the tested materials and a significant reduction of the hardness.

Furthermore, a different behaviour among the tested slabs can be detected, especially at high temperatures: the specimen D, for examples, seems to be the softest, whereas the A the hardest. These differences can be only verified and confirmed by means of an accurate analysis of DMA temperature sweep curves.

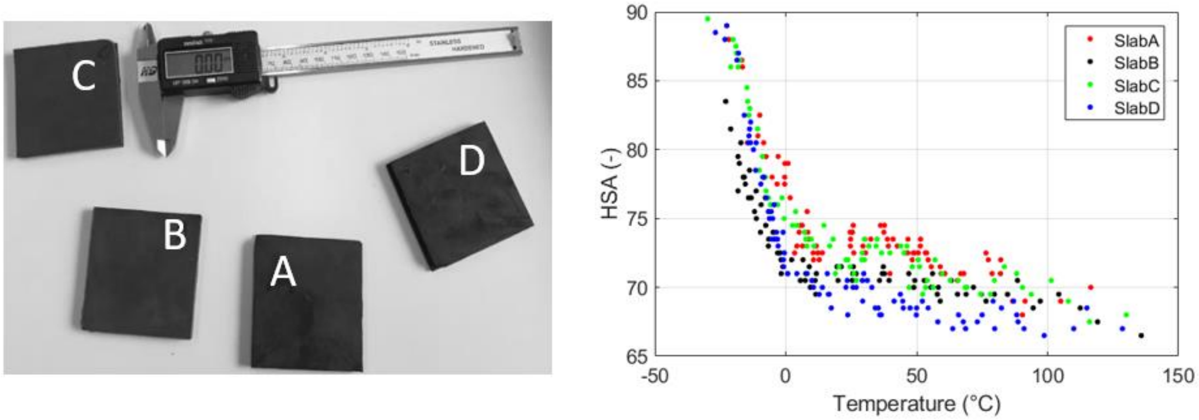

Fig. 3.14 Tested compounds (on the left); measured hardness (on the right)

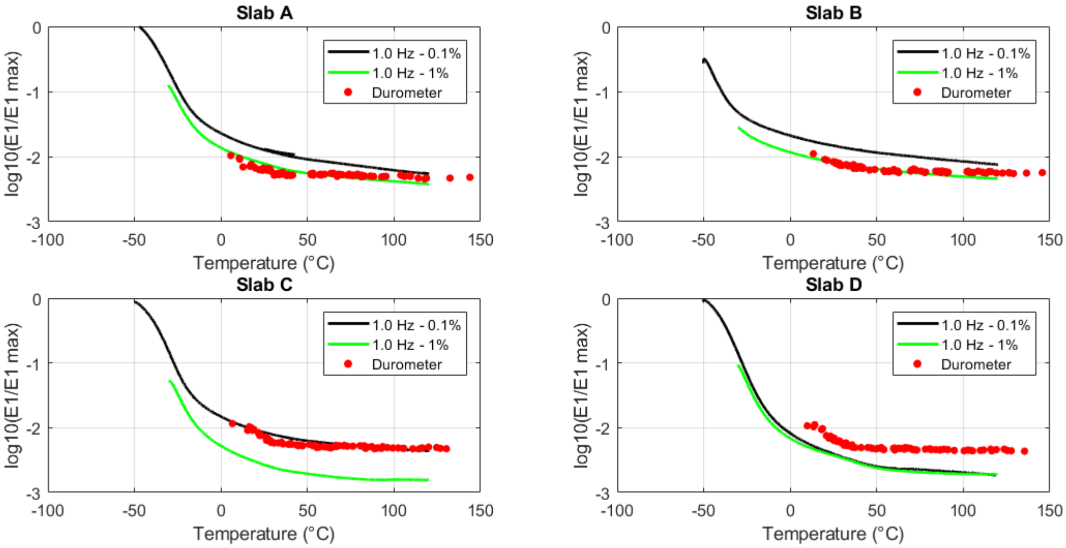

Fig. 3.15 Durometer experiment results compared with DMA curves

The storage modulus of the tested compounds has been determined by means of equation (3.12) taking into account the measured hardness values in Fig. 3.14. The results are reported in Fig. 3.15 together with the temperature sweep curves at 1 Hz and 0.1% and 1.0% strain percentage. Analysing these data, a good agreement with the master curves is observed: in case of slab A and B, the durometer experiments lead to storage modulus values close to 1% strain DMA curves; whereas close to 0.1% strain curve for slab C. The durometer results of the slab D only exhibit a significant mismatch with the dynamic properties. This may be due to imprecision during the usage of the instrument, which does not guarantee a high repeatability and accuracy during the test sessions. Moreover, a flatter trend of the red markers is generally noticeable rather than the master curves. This feature may be a consequence of a characterization procedure based on compression solicitation and depending on the tip shape and geometry [30, 83].

A similar experimental session has been also carried out on different truck tyres employing the durometer for Shore A measurements. In Fig. 3.16, different storage modulus values are shown together the linear fit curves: the blue markers correspond to a new reference truck tyre, the black ones to the same truck tyre 3-year aged and never used, the green markers to a compound similar to the blue and the last cluster to a thermal treated truck specimen (90 days at 60°C in a climatic cell).

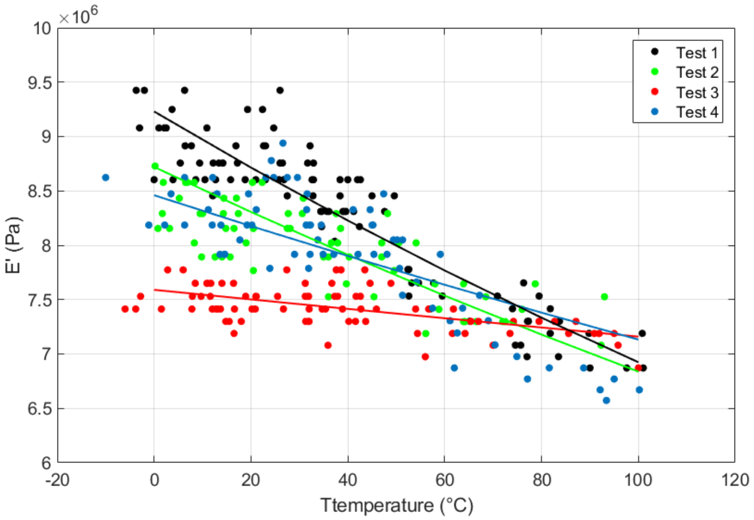

Fig. 3.16 Durometer results on different truck tyres

The curves exhibit a clear variation of the storage modulus depending on the working life of the specimen. Particularly, the ageing effect generates an increase of the compound stiffness and the storage modulus, consequently; otherwise a further thermal treatment gives rise to a decrease of the softness of the compound [4, 21].

Hence, the results shown in this section state that the durometer experiment is a valid technique for fast analysis of the viscoelastic behaviour of the tyre compound in terms of dynamic modulus over the temperature. The main issues of this procedure are related to the low repeatability of the measures and the lack of analysis of the pure hysteretic behaviour, which will be overcome by means of the non-destructive device developed during the research activity period by the author.

3.4 Ultrasounds experiments at the UniNa Tyre Lab

As discussed in the previous paragraph, for small deformable polymers, the properties are determined by means of Dynamic Mechanical Analysis. This method requires testing a specimen of suitable dimensions within a frequency range from 0.1 Hz to 100 Hz [50] by means of a rheometer distinguished in three point bending or dual cantilever for dynamic modulus E^* evaluation or a torsional plate [84] for shear modulus G^*. This methodology is the most widespread and reliable technique for viscoelastic properties evaluation.

However, one of the most efficient and simplest techniques for the viscoelastic characterization in a wide frequency domain requires the analysis of the ultrasonic waves propagation and attenuation in the medium [30, 85]. The ultrasound transmission is very suitable for viscoelasticity inspection and it is also widespread in Mechanics and Biomedical fields [85–87], detecting internal defects in machine or thickness measurement, monitoring the severity of corrosion or diagnostic and biomedical imaging processing. The ultrasonic waves can be further employed for the evaluation of the viscoelastic properties of the specimen of interest. In both Lionetto's [88, 89] and Mc Hugh's [90] research, the transmitter mode outlined in Fig. 3.17, which involves a transmitter probe and a receiver one, was adopted in order to evaluate directly the viscoelastic properties analysing the transmitted and received signals through the Fourier's transform [86, 91]. This methodology is the simplest for dynamic behaviour analysis thanks to the direct measurement of the transmitted wave travelling through the compound specimen. This mode is not suitable in many mechanical systems, in which a mixing of the polymer with other types of materials occurs or in the cases where one side of the component under investigation in not accessible, such in case of tyre testing.

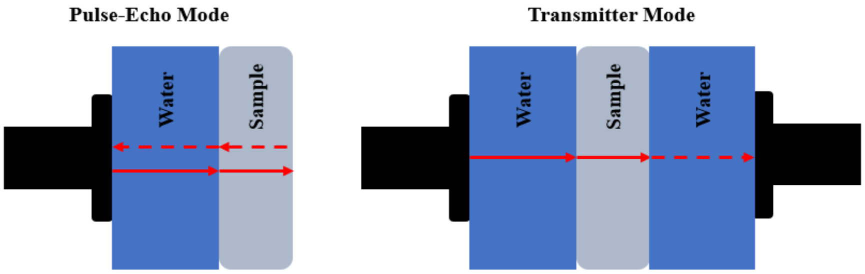

Fig. 3.17 Pulse-echo and transmitter mode inspections

In opposition to the transmitter technique, the pulse-echo mode requires the usage of a single probe working simultaneously as transmitter and receiver, as shown in Fig. 3.17. In this case, only the reflected waves at each interface can be acquired. In the work by Carlson at al. [92], the equations of continuous-wave propagation in a medium were considered in order to evaluate the density, the sound velocity and the attenuation coefficient of polymers as a function of temperature and frequency. However, the acoustic properties of the specimens were not considered as complex magnitudes, as previously known [25, 93], in the processing of the data, leading to possible inaccuracies in the measurement of the attenuation coefficient and loss factor.

For the reasons stated above, a novel methodology for the evaluation of viscoelastic properties through ultrasound as a function of temperature and frequency has been proposed in this research thesis [94, 95]. This approach consists of the optimization of a cost function by means of the identification of the attenuation coefficient taking into account the equations set of the first echo and its multiple reflections. For this purpose, an experimental bench has been set up at the Tyre Lab of the Department of Industrial Engineering of the University of Naples, Federico II in order to acquire the data and process them for viscoelasticity analysis. The results and methodologies outlined in the following paragraphs will refer to a preliminary study and application of ultrasonic waves for tyre viscoelasticity characterization.

3.4.1 Theory of ultrasounds propagating in a dissipative material

As described in paragraph 2.1 Viscoelastic materials, viscoelastic material hallway behaves as between a purely elastic material and a purely viscous one [21, 41]. This means that the stress-strain relationship is defined by a complex dynamic modulus as the amount of the overall resistance to deformation of the compound, where the real part is known as storage modulus and the imaginary one as loss modulus. These magnitudes are deeply associated with the material dissipation of a part of the energy provided by means of a load/stress time function by the definition of the loss factor through eq. (2.7).

The propagation of a pressure wave in a dissipative material, such as a viscoelastic, is associated with an amplitude damping phenomenon described by the attenuation coefficient α expressed in dB/mm, as highlighted in Fig. 3.18. This magnitude measures the amplitude attenuation per unit length and is directly associated with the loss factor through [88, 89]:

$$\tan(\delta) = \frac{E''}{E'} = \frac{2(\alpha \cdot c/\omega)}{1 - \left(\alpha \cdot \frac{c}{\omega}\right)^2} \tag{3.13}$$

To determine properly the attenuation coefficient α during the experiments, the viscoelastic specimen must satisfy requirements on regularity and flatness of the surface on which the ultrasonic waves will be reflected.

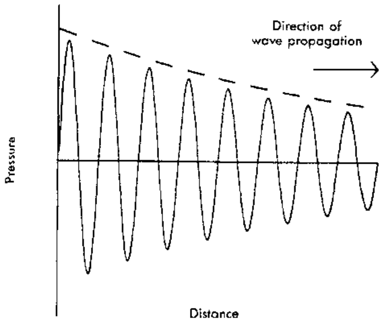

Fig. 3.18 Attenuation phenomenon of a pressure wave propagating in a medium

As shown in Fig. 3.19, an irregular interface gives rise to a wave scattering at the boundary and high inaccuracy in data acquisition. For this reason, an innovative procedure useful to evaluate the viscoelastic properties of flat slabs of vulcanized compound employing the pulse-echo method has been developed [92].

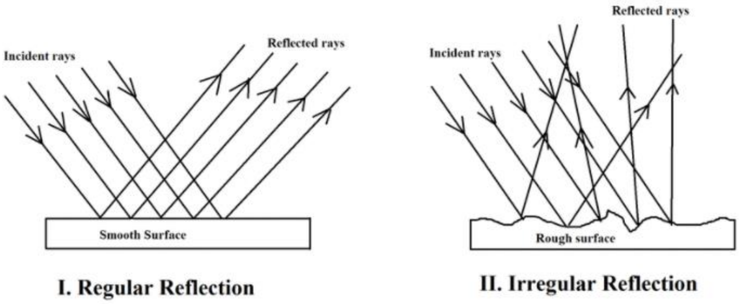

Fig. 3.19 Regular reflections compared to irregulars

3.4.2 UniNa ultrasound bench description

To perform the underwater ultrasonic tests, the bench in Fig. 3.20a has been set up in the Tyre Lab of Department of Industrial Engineering at the University of Naples Federico II [94]. This bench involves a water tank, in which the vulcanized compound sample (Fig. 3.20b (3)) is immersed. The water has been chosen as coupling fluid due to its suitable acoustic impedance and sound attenuation coefficient at different temperatures [89, 90]. Three electrical heating resistors (Fig. 3.20b (4)) have been used to heat up the water and the compounds. In addition, a pump (Fig. 3.20 b (5)) is used for water circulation so that the temperature is homogeneous at each point of the tank.

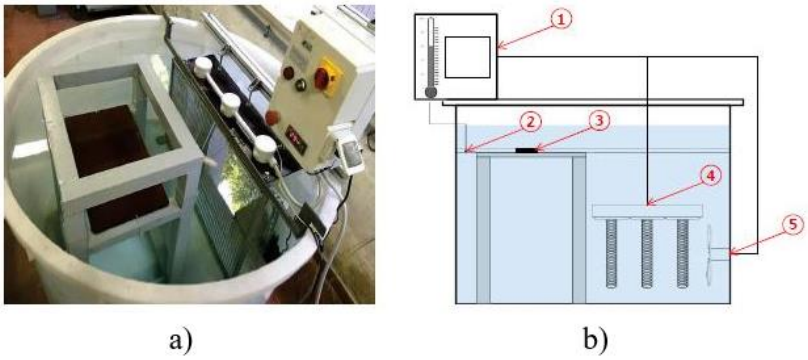

Fig. 3.20 a) Ultrasound bench; b) conceptual rig scheme;

A thermostat (Fig. 3.20b (1)) checks the temperature by means of a thermocouple (Fig. 3.20b (2)), setting the water and thus the compound temperature in the tank.

To generate ultrasonic waves the echograph and a pair of immersion probe, showed in Fig. 3.21, have been employed. The first instrument is used to produce electrical signal in the range of 60–320 V, which is converted into pressure wave by piezoelectricity phenomenon [96]. Each probe generates longitudinal ultrasounds at a specific frequency, 0.4 MHz and 1.2 MHz, respectively. The pulse-echo measurement method has been performed. On the echograph display, the user can analyse the amplitude values of the backward reflected waves in a decibel scale according to the A-Scan representation in Fig. 3.22. In particular, for the experimental test sessions carried out during the research activities, the maximum amplitude of the front echo A_1 and its multiple reflection A_1' have been measured for the viscoelasticity analysis. The back echo maximum amplitude A_2 could be also considered. However, this measurement can be affected by the acoustic impedance of the material below the compound sample, such as the belt plies of tyre.

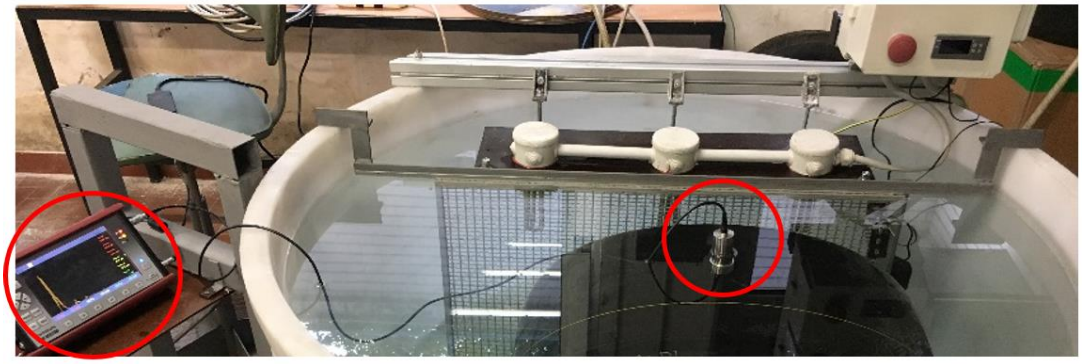

Fig. 3.21 Echograph and immersion probe used for the ultrasound analysis

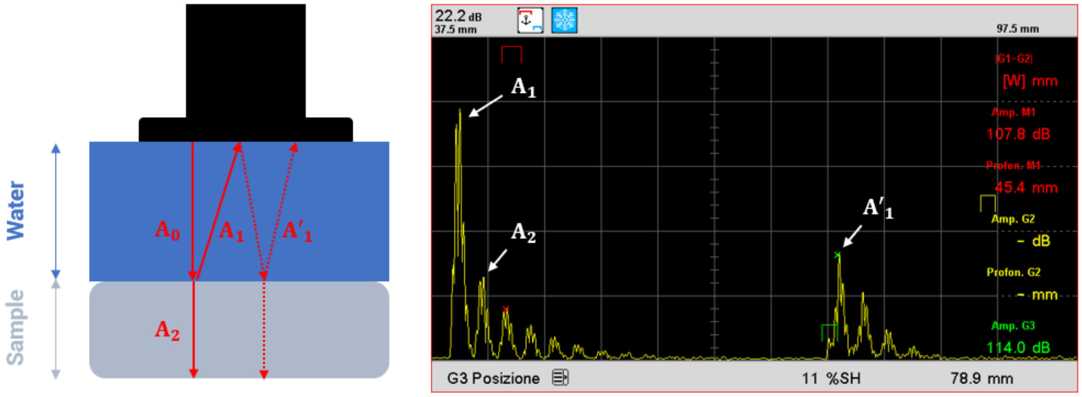

Fig. 3.22 Reflected wave acquired through pulse-echo and the corresponding A-Scan

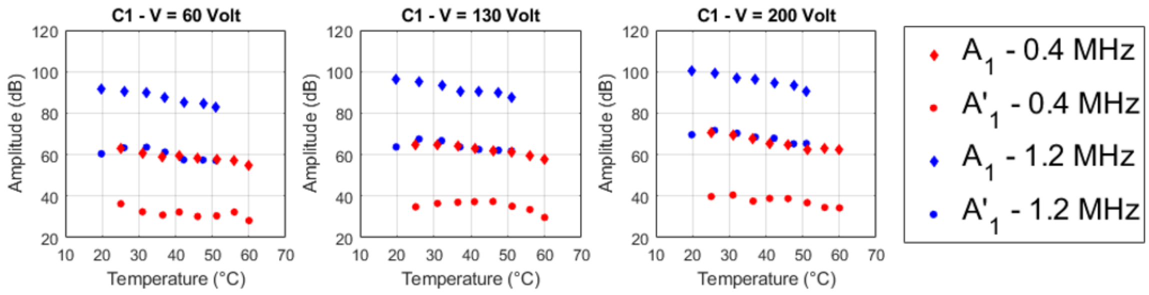

Fig. 3.23 Measured amplitudes as function of temperature and frequency for compound C1

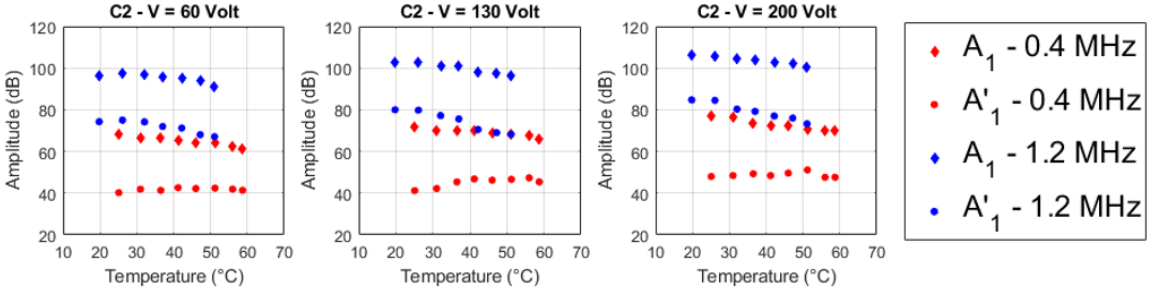

Fig. 3.24 Measured amplitude as function of temperature and frequency for compound C2

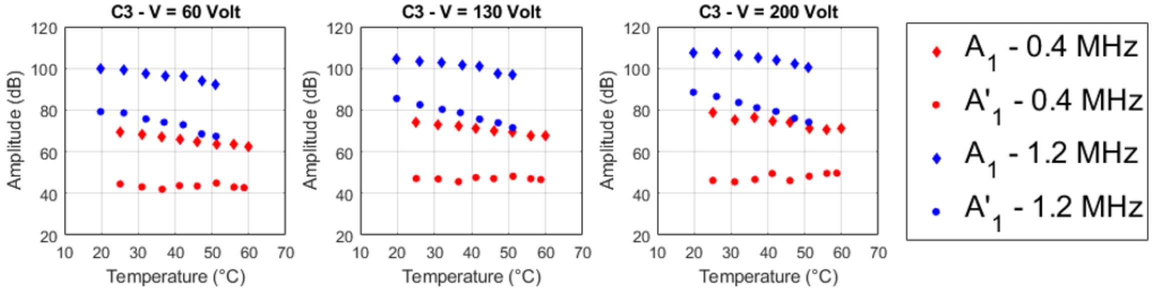

Fig. 3.25 Measured amplitude as function of temperature and frequency for compound C3

3.4.3 Data acquisition and processing

In the experimental session, three specimens of vulcanized polymers, denoted as compound C1, C2 and C3, whose dimension are almost the same of the Table 3-1 ones, have been tested. The employment of slabs is advantageous for their flat surface. For each specimen, the test temperature range is approximately 15-60 degrees due to immersive probe working limit conditions. As mentioned before, the pulse-echo measurement method has been performed and a 20 mm water delay line has been settled, as shown in Fig. 3.22, in order to acquire properly the amplitude values associated with the reflected waves at the interfaces.

The acquired values for each tested compound are diagrammed in Fig. 3.23, Fig. 3.24 and Fig. 3.25. As noticeable, the measures have been carried out taking into account three transmitter voltages for each specimen in order to store a proper amount of data for the viscoelasticity analysis in every condition. The sound velocity towards the temperature have been measured for each specimen employing both probes by means of the Time of Flight theory [91]: the front echo amplitudes and the sound velocity values exhibit a downward trend as the temperature increases, as shown in Fig. 3.26. This means that the material properties, as well as the acoustic ones, change over the temperature due to the weakening of the polymer chains.

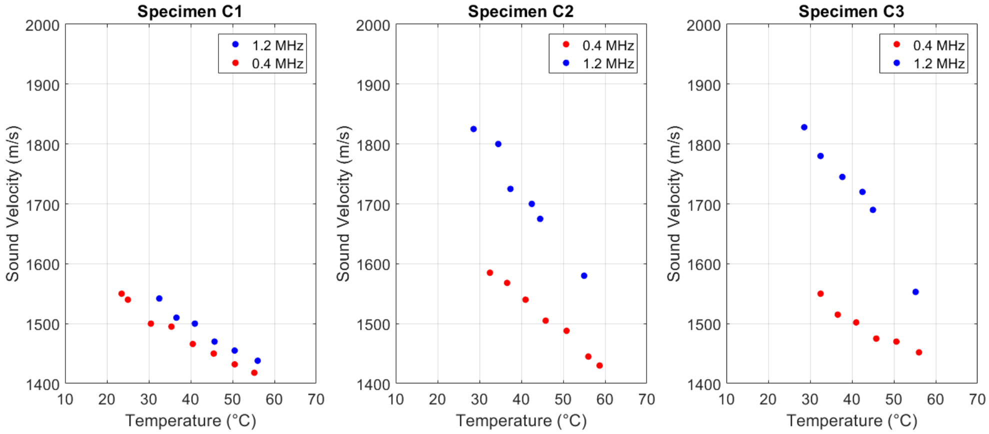

Fig. 3.26 Measured sound velocity values for each specimen

The experimental data acquired on the tyre tread specimens have been used to firstly characterize the compound acoustic properties and then, the viscoelastic loss factor. Particularly, taking into account the measured amplitudes (Fig. 3.23, Fig. 3.24 and Fig. 3.25) and sound velocity (Fig. 3.26) values, the wave damping coefficient within the medium has been determined as the unknown parameter to be identified for optimizing the following cost function in each test conditions in terms of frequency and temperature through a routine developed in Matlab environment and based on nonlinear least-square solver [97–99]:

$$\varepsilon = \left[\left(A_1 - A_{1_{EVAL}}\right) ; \left(A_1' - A'_{1_{EVAL}}\right)\right] \tag{3.14}$$

where A_1 and A_1' are the data acquired during the experimental test session; $A_{1_{Eval}}$ and $A'_{1_{EVAL}}$ are evaluated in the proposed algorithm as follows:

$$\begin{aligned} A_{1_{Eval}} &= A_0 \cdot D_w \cdot |R_{wc}^*| \cdot |T_{wp}| \\ A'_{1_{EVAL}} &= A_0 \cdot D_w^2 \cdot |R_{wc}^*|^2 \cdot \left|T_{wp}\right| \cdot \left|R_{wp}\right| \end{aligned} \tag{3.15}$$

where A_0 is the transmitted pulse, T_{wp} is the transmission coefficient at the water-probe interface, and R_{wp} is the reflection coefficient at the water-probe interface. These magnitudes depend on the transmitter voltage and temperature and they are provided by the probe manufacturer. $|R_{wc}^*|$ is the modulus of the complex reflection coefficient at water-compound interface:

$$R_{wc}^* = \frac{Z_c^* - Z_w}{Z_c^* + Z_w} \tag{3.16}$$

where Z_w is the water acoustic impedance and Z_c^* is the complex acoustic impedance of the viscoelastic specimen, which depends on the unknown attenuation coefficient, compound density, sound velocity and frequency [88, 90]. This can be expressed as follows:

$$Z_C^* = \frac{\rho c}{1 + (\alpha \cdot c/\omega)^2} + i\frac{(\alpha \cdot c/\omega)\rho c}{1 + (\alpha \cdot c/\omega)^2} \tag{3.17}$$

Replacing the equation (3.17) in equations (3.15), the wave attenuation coefficient is only the unknown parameter to identify in order to optimize the cost function in equation (3.14). The relationships from (3.15) to (3.17) are also employable in case of testing an elastic material sample: neglecting the attenuation coefficient α, the acoustic impedance Z_c^* the reflection and transmission coefficients will be equal to the real magnitudes.

The results of the identified attenuation coefficient values in terms of dB/mm for each compound as function of the wave frequency and compound temperature are shown in Fig. 3.27.

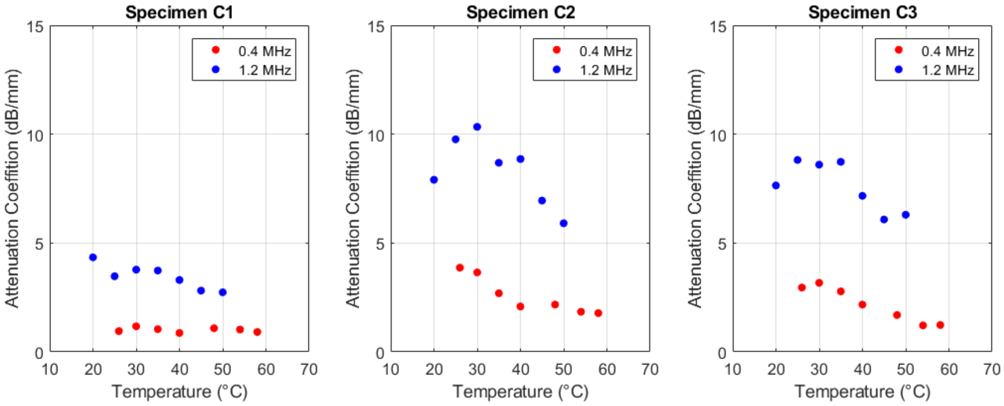

Fig. 3.27 Identified attenuation coefficient for each compound

As noticeable, the curves exhibit a decreasing trend towards the temperature according to what is expected: the higher the temperature, the lower the acoustic impedance of the material due to the weakening of polymer chains is [50, 51].

3.4.4 Achieved results

To evaluate the loss factor values at 0.4 and 1.2 MHz as function of temperature, as shown in eq. (3.13), for each different compound specimen it is necessary to consider the density values, the sound velocity and the estimated attenuation coefficient. The viscoelastic index values thus obtained refer to the temperature corresponding to the test experimental sessions and are in agreement with the working limit conditions of the specific immersive probe used.

Table 3-2 Viscoelastic properties of the compounds

Compound	Density (kg/m^3)	T_0 (K)	C1 (-)	C2 (K)
Compound C1	1190	393.15	32.35	473
Compound C2	1245	393.15	18.20	330
Compound C3	1292	393.15	30.8	399.5

To verify the trustworthiness of the identified viscoelastic loss factor, the comparison of these values with the master curve performed in temperature sweep at 1 Hz in a cantilever clamp is necessary. Particularly, the William-Landel-Ferry relationship is applied in order to evaluate the temperature shifting in according to the following formula [5, 31].

The temperature shifting from the starting value corresponding to 0.4 MHz and 1.2 MHz to the equivalent ones at the frequency of interest (1 Hz) has led to the comparison of the ultrasound tests acquired data with the DMA master curve, as shown in Fig. 3.28.

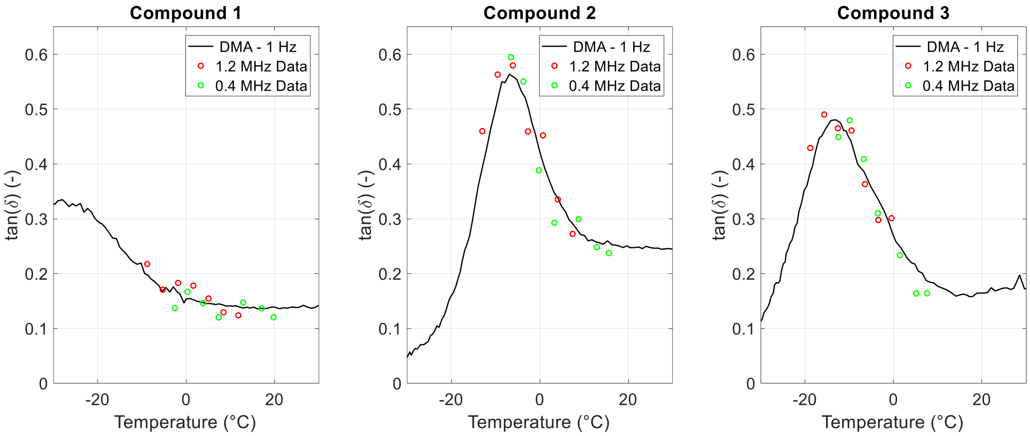

Fig. 3.28 Ultrasound characterization results compared to 1 Hz DMA

As noticeable, how the acquired data with the innovative ultrasound methodology are in good agreement with the DMA temperature sweep master curves in the shifted temperature range. Particularly, the higher the frequency of the ultrasounds, the lower the minimum shifted temperature: thus, the analysis can provide an indication of the glass transition temperature of the compound, especially for compound 2 and compound 3.

The trustworthiness of the achieved results should be considered as a baseline for the viscoelastic materials properties evaluation through non-destructive technique. Further analysis will be focused on testing employing ultrasonic waves in a wide frequency spectrum in order to characterize the compounds viscoelastic behaviour within the entire temperature range of interest.

3.5 Dielectric spectroscopy of tyre tread compounds specimen

Dielectric spectroscopy is the measurement of complex permittivity (or dielectric constant) as a function of frequency. This quantity is measured by placing a sample in contact with electrodes and applying a sinusoidal voltage. Dielectric spectroscopy is analogous to dynamic mechanical analysis (DMA). However, instead of the mechanical oscillation employed by DMA, an electrical oscillation is applied to the sample. One of the primary advantages of dielectric spectroscopy over DMA and other techniques is the extreme breadth of the frequency range (from 10^{-6} to 10^{12} Hz). Besides, is one of the few techniques that can follow transformation from low-viscosity liquids to rubbery solids to hard glassy solids [100–102].

When a voltage is applied across the electrodes, an electric field exists within the viscoelastic sample, which becomes polarized, and the current generated is measured. Obviously, if the voltage is sinusoidal the response current is also sinusoidal, as shown in Fig. 3.29, where the current is shifted along the time axis. The quantities that relate the current response to dielectric material quantities are the phase shift, δ, and the relative change in amplitude.

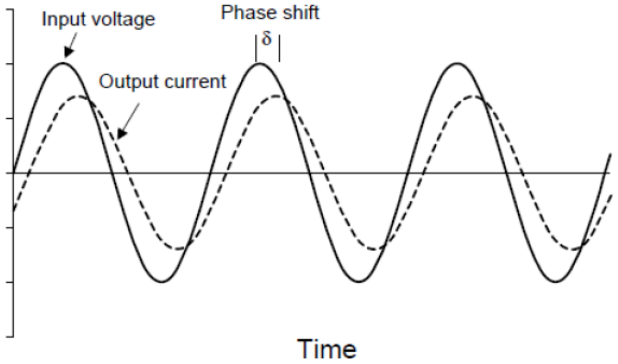

Fig. 3.29 Voltage and current response in dielectric spectroscopy

The real part of the waveforms for the voltage and current can be expressed by the following equations:

$$\begin{aligned} Re|V(t)| &= V_0 \cos(\omega t) \\ Re|I(t)| &= I_0 \cos(\omega t + \delta) \end{aligned} \tag{3.18}$$

where V_0 and I_0 are the voltage and the current amplitudes and ω is the angular frequency. The sample within the electrodes can be presented as a simple circuit element with a characteristic impedance [100]:

$$Z^* = \frac{V}{I} = Z' + iZ" \tag{3.19}$$

The polymers are modelled as a resistor and a capacitor connected in parallel each other, as shown in Fig. 3.30. Thus, the impedance is related to the capacitance, C, and the resistor, R, by the following:

$$Z^{*-1} = R^{-1} - i\omega C \tag{3.20}$$

Referring to the circuit in Fig. 3.30, the real and the imaginary part of the impedance are:

$$\begin{gathered} Z' = \frac{R}{1 + \omega^2 R^2 C^2} \\ Z" = \frac{\omega R^2 C}{1 + \omega^2 R^2 C^2} \end{gathered} \tag{3.21}$$

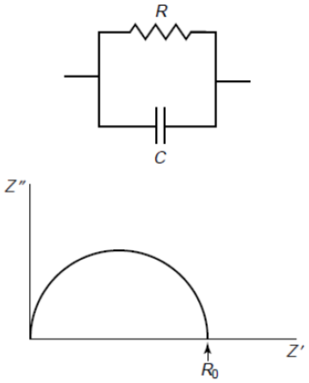

Fig. 3.30 Polymer’s impedance and complex impedance diagram

Combining these equations:

$$\left(Z' - \frac{R}{2}\right)^2 + (Z'')^2 = \frac{R^2}{4} \tag{3.22}$$

which is the equation of the circle in Fig. 3.30. The complex impedance plots are useful for providing insight into the processes that contribute to a particular sample dielectric behaviour. They are also useful for situations where complicated electrode geometries must be used so that quantitative calculations of permittivity are not practical.

By far the most used electrode geometry is the parallel-plate arrangement but there are also other electrodes like the concentric cylinder configuration and the interdigitated comb electrode, as shown in Fig. 3.31. It is important to point out the different configurations because the permittivity calculation depends on the different electrodes geometry [103].

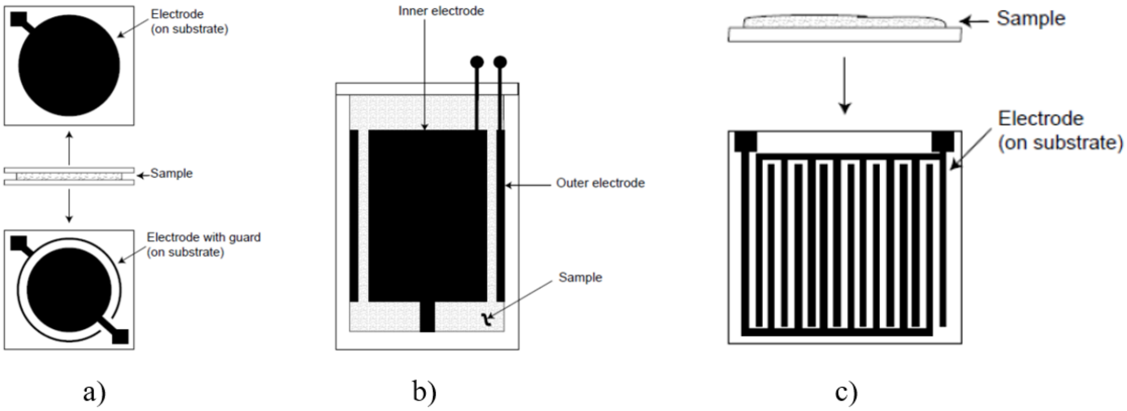

Fig. 3.31 a) Parallel-plate; b) Concentric cylinder; c) Interdigitated comb electrodes configurations

To determine the permittivity, two important assumptions must be taken into account. The first is that the measurement is linear. In other words, the measured impedance is independent of applied voltage. The second assumption made when interpreting dielectric data is that the measured property is time invariant. Another important effect can occur in ionically conductive polymers is the blocking of ions by the electrodes. Blocking electrode effects can obscure the bulk properties of the sample. This blocking effect is caused by the pile-up of the sample's mobile ions at the electrode/sample interfaces and is especially prevalent in samples where ion mobility is high. In order to account for the pile-up of ions at the electrodes, the parallel resistor and capacitor model must be modified by adding a second capacitance in series with the original circuit [103]. In this way, the impedance changes as follows:

$$Z' = \frac{R}{1 + \omega^2 R_{bulk}^2 C_{bulk}^2}$$

$$Z" = \frac{\omega R_{buk}^2 C_{bulk}}{1 + \omega^2 {R_{bulk}}^2 C_{bulk}^2} + \frac{1}{\omega C_{blocking}} \tag{3.23}$$

3.5.1 Calculated parameters

For a material such as a polymer, an applied electric field induces an electric polarization of the sample. Usually, the magnitude of this polarization is linearly proportional to the applied field. The proportionally constant in this case is called permittivity and is denoted by the symbol ϵ. The permittivity is usually expressed as the relativity permittivity, the ratio between the material permittivity and the permittivity of a vacuum [100, 102], $\epsilon_0 = 8.854 * 10^{-12}$ J^{-1} C^{2} m^{-1}:

$$\epsilon_r = \frac{\epsilon}{\epsilon_0} \tag{3.24}$$

In oscillating field, the permittivity is represented by a complex number:

$$\epsilon^* = \epsilon' - i\epsilon" \tag{3.25}$$

where ϵ' is the real part while ϵ” is the imaginary one. Therefore, the dielectric loss factor can be defined in the same way of the mechanical one:

$$\tan(\delta) = \frac{\epsilon"}{\epsilon'} \tag{3.26}$$

It is often desirable to compare the permittivity to dynamic mechanical modulus data. However, since it is not directly analogous, a dielectric modulus, M, is usually defined:

$$M^* = \frac{1}{\epsilon^*} \tag{3.27}$$

In Table 3-3 the calculation of the permittivity for different electrodes configurations is shown [101, 103]. In this table, the following parameters must be explained. A is the area of the smallest electrode, d is the distance between electrodes, l is the length, a is the inner electrode radius, b the outer electrode radius.

Table 3-3 Calculation of permittivity and loss factor from measured impedance data

Sample	Parameter	Formulation
Parallel plate electrode	Dielectric Permittivity	$\epsilon_r' = \frac{d}{\omega\epsilon_0\|Z\|^2 A} Z"$
	Dielectric Loss Factor	$\epsilon_r'' = \frac{d}{\omega\epsilon_0\|Z\|^2 A} Z'$
	Loss Tangent	$tan(\delta) = \frac{\epsilon"}{\epsilon'} = \frac{Z'}{Z''}$
Concentric cylinder electrode	Dielectric Permittivity	$\epsilon_r' = \frac{\ln(b/a)}{\omega\epsilon_0\|Z\|^2 l} Z"$
	Dielectric Loss Factor	$\epsilon_r'' = \frac{\ln(b/a)}{\omega\epsilon_0\|Z\|^2 l} Z'$
	Loss Tangent	$tan(\delta) = \frac{\epsilon"}{\epsilon'} = \frac{Z'}{Z''}$

Dielectric spectroscopy allows to evaluate the mechanical properties of a polymer, such as its relaxation behaviour; it can be further used to follows chemical changes such as polymer cure or aging [103]. Another important are of synthetic polymers where dielectric spectroscopy is useful is in the characterization of polymer latex emulsions or to monitor chemical and physical changes because of their environment (radiation or humidity, for example). A final application of dielectric spectroscopy is the evaluation of composites.

After this brief examination of the various uses of dielectric spectroscopy, attention is now focused on the viscoelastic characterization of interest. By way of example in some polymer properties are shown in Fig. 3.32, like the permittivity, the dielectric modulus and loss factor [103].

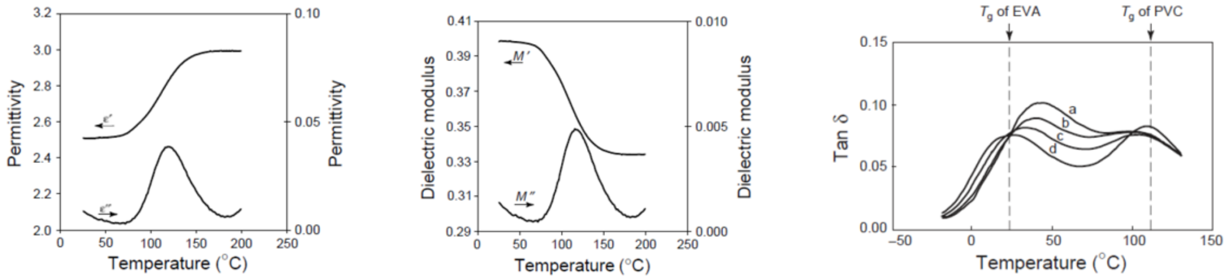

a) b) c)

Fig. 3.32 a) Permittivity of amorphous PET; b) Dielectric modulus of amorphous PET; c) Loss factor for different thermal histories

3.6 VESevo: innovative device for non-destructive viscoelasticity analysis

3.6.1 Description of the innovative device and its main purpose

The evaluation of tyre tread viscoelasticity is a fundamental topic in a wide range of activities concerning the development of polymers for innovative compounds, the parametrization of physical contact models and the optimization of vehicle performance and road safety.

In these applications, the viscoelastic properties determination of tyre block, which depends on rubber temperature and frequency solicitation of bitumen asperities, is essential for contact mechanics modelling and the prediction of the limit value of the local friction coefficient [2, 16, 49]. The Dynamic Mechanical Analysis (DMA) is widely employed into the characterization of viscoelasticity in order define the hysteretic behaviour of the compound following the Time-Temperature Superposition principle [50]. On one hand, this testing approach perfectly fits with polymer specimens manufactured with specific dimension and it cannot be always applied for tread characterization because of the need to destroy the tyre; on the other hand, these common testing procedures involve complex and very expensive machines for the analysis of a generic compound sample.

For these reasons, the development of innovative methodologies, as well as the non-destructive ones, are an attractive solution replacing the standard test methods involving complex and expensive benches for the investigation of a compound specimen manufactured in different conditions respect to the final product provided by tyre makers. Further, Motorsport racing teams use to face with the restrictions due to the employment of confidential tyres and not available to invasive testing. Therefore, a non-destructive procedure for the acquisition of the data for tyre viscoelasticity characterization within the working thermal range could be very useful for vehicle setup optimization and definition of vehicle simulation tools.

Hence, an innovative and portable device, defined VESevo, which is the acronym of Viscoelasticity Evaluation System evolved and the ancient name of the volcano Vesuvius, has been developed during the research period at the Department of Industrial Engineering at the University of Naples Federico II. The main purpose of this device is to allow the users, especially racing teams, to characterize the tyre tread viscoelastic properties and its variations due to cooling or heating and monitor the performances with the progressive mileage or aging depending on vehicle applications [104]. Thus, engineers, especially in Motorsports, can analyse useful information concerning confidential tyres by means of this portable device. The VESevo can be also very advantageous for tyre manufactures because it could be employed into the monitoring the goodness of a huge number of final products in a very short time by the operators compared to the standardized procedures requiring specific and expensive test benches, as well as rolling machines or MTS flat tracs.

The idea of the development of a non-destructive testing methodology for tyres starts from preliminary analyses carried out by means of a dynamic dial indicator [105] build-up according to the scheme layout in Fig. 3.33.

a) b) c)

Fig. 3.33 a) Experimental dynamic dial indicator bench; b) rod-spring mechanism; c) Functional scheme

The dynamic dial indicator consists of a rod-spring mechanics: a 4 mm – diameter steel rod with a semi-spherical indenter, which slides into a low-friction guide, is adopted and a basement on which the viscoelastic specimen is usually placed on. The spring guarantees the necessary minimum preload. The motion of the indenter is measured by an optical laser sensor with a very high frequency response. As depicted in Fig. 3.33, the focus of the optical laser is pointed on the rod head, which is manually lifted until a specific position and then released being free to bounce on the sample surface at a specific temperature. This information is acquired by an infrared pyrometer close to the indentation area.

However, the bench above described cannot be employed into the characterization of final viscoelastic products, as well as tyres, because it is only suitable for the analysis of very compact specimens, as DMA requires. Therefore, this bench has been redesigned with the aim to develop the compact and ergonomic device, called VESevo.

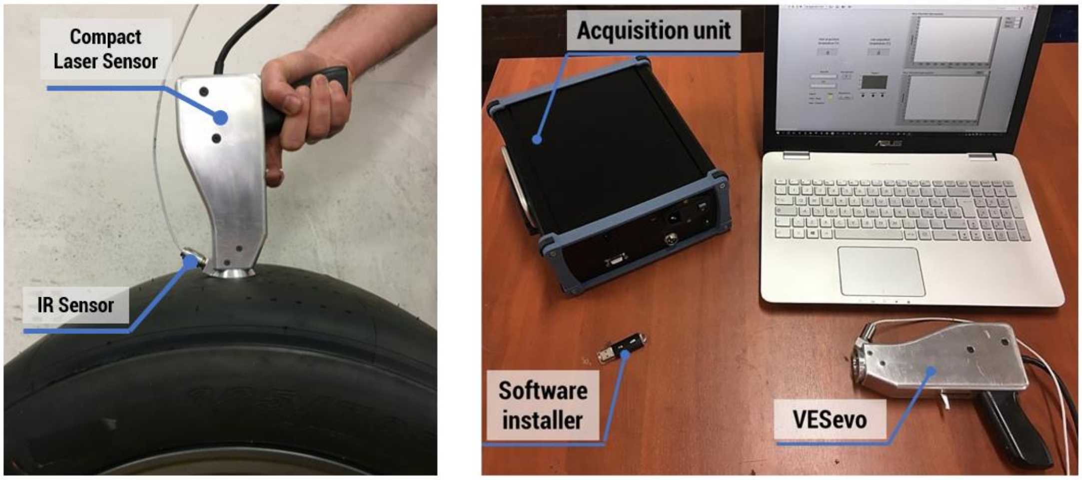

a) b)

Fig. 3.34 a) VESevo prototype; b) Device and Acquisition unit

As shown in Fig. 3.34 a), the ergonomics of the innovative device enables the testing of manufactured tyres of any category (passenger, motorsport and even truck ones) thanks to the employment of a very compact laser sensor, which measures the motion of the semi-spherical indenter with a high accuracy and frequency response close to 100 kHz. An infrared sensor monitors the tread surface temperature close to the indentation area. Furthermore, the inner hardware developed according to a patented technology guarantees the release of the rod with a very high repeatability in order to reduce the inaccuracies due to the operator’s hand. The displacement and temperature raw signals are acquired by means of a user-friendly LabVIEW GUI on the personal laptop through a data acquisition unit, as shown in Fig. 3.34 b). The latter consists of a data logger for the buffering and resampling of raw data and the conditioning electronic logics for the employed sensors. All the specifications above described make the VESevo a very advantageous device for its portability and non-destructive characterization in-situ.

3.6.2 Raw Signal Description and Testing procedure

To perform a single acquisition by means of the VESevo, this test procedure must be followed:

- position of the tyre or tread compound slab in correspondence of the semi-spherical indenter;
- the indenter is manually raised until the mechanic lock in order to obtain each acquisition with the same starting position and velocity;
- once reached the maximum point, the rod is totally released thanks to the patented technology, and the rod displacement curve is shown on the acquisition software.

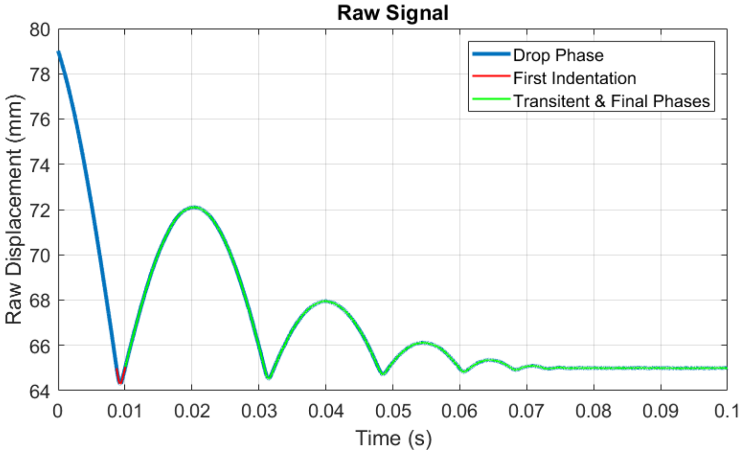

Fig. 3.35 Acquired raw signal

In Fig. 3.35, the typical raw signal of the indenter displacement towards the time is shown. As highlighted using the colours, different phases can be identified: in blue is indicated the drop of the rod until the first contact with the material; the red part of the signal represents the phase of the first indentation; finally, the green line represents the transient phase, which consists in the bouncing of the rod on the material, plus the final phase of until the end of the motion that establishes the full contact condition between the rod and the compound surface (final phase). It should be noted that the indentation phase is shorter than the other phases.

To explore the polymers behaviour, the rod displacement curves are acquired varying the specimen temperature. The compounds of interest have been heated or cooled by means of a climatic cell and the measurements have been carried out during the corresponding natural cooling or heating phase until the ambient temperature. In case of testing a full tyre, a heating gun is used for warming up to the temperature of interest and the freezing butane air spray for cooling the surface down the 0 degrees.

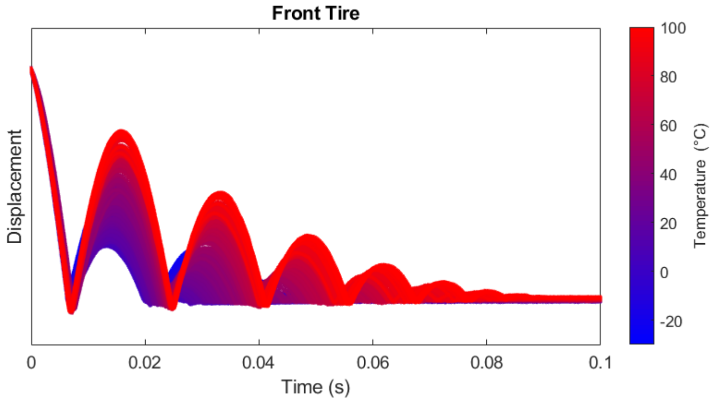

Fig. 3.36 Acquired raw signal at different temperatures

Fig. 3.36 shows the motion of the rod in the temperature range [-30, 100°C] for a generic compound sample. Observing the shape of the acquired displacement curves of the indenter towards the temperature is clear that the response of the material is largely depending on its temperature and the proposed methodology is able to highlight this phenomenon. Focusing on the transient phase it is possible to observe that, starting form 40°C until 100°C, this part of the displacement is longer, and more bounces occur in 0.1 seconds. This means that the compound behaves as pure rubber and a low dissipation of the potential energy of the rod is observed. On the other hand, reducing the temperature from 40 °C to -20 °C, the transient phase is shorter and low bounces occur: the compound returns the highest energy dissipation measured in terms of rod displacement and this means that the material moves to the glassy behaviour. From a qualitative point of view, here is inserting to point out that the duration of the indentation phase increases with the temperature in accordance with the observation that at low temperature range, the behaviour of the compound is similar to glassy one; whereas, at high range, it is analogous to rubbery. The quantitative study of the indentation phase is detailed in the next paragraphs. Finally, it worth noting that as concerns the drop phase, it is independent form the temperature as this phase does not involve the material under investigation but is only characterized by the rod-spring mechanism.

3.6.3 Data Acquisition GUI Description

The data are acquired by means of a self-made acquisition GUI developed in LabVIEW environment. The user interface is shown in Fig. 3.37:

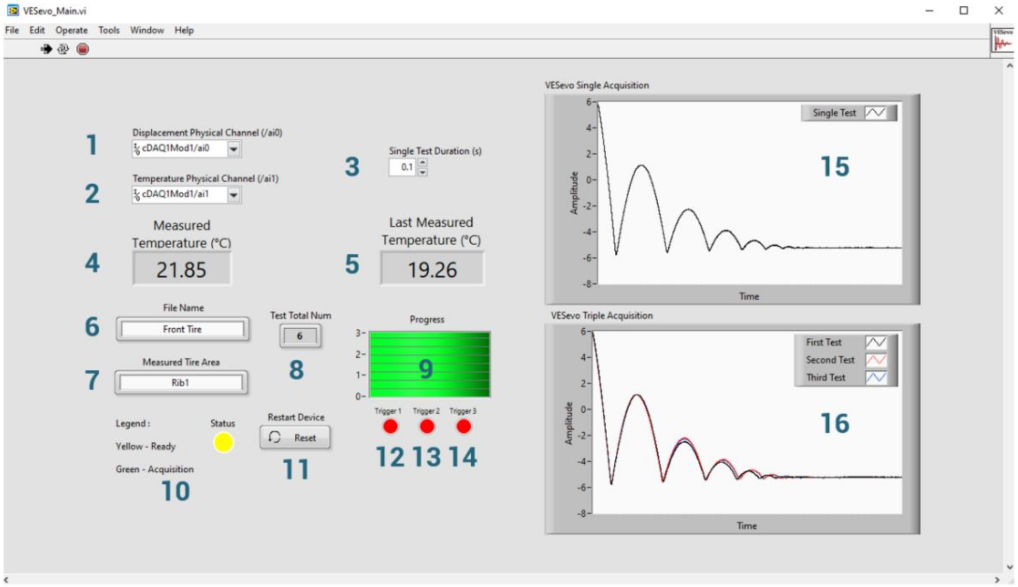

Displacement Physical Channel (/ai0): cDAQ1Mod1/ai0
Temperature Physical Channel (/ai1): cDAQ1Mod1/ai1
Single Test Duration (s): 0.1
Measured Temperature (°C): 21.85
Last Measured Temperature (°C): 19.26
File Name: Front Tire
Measured Tire Area: Rib1
Test Total Num: 6
Legend : Yellow - Ready Green - Acquisition

Fig. 3.37 GUI developed in LabVIEW environment

The acquisition software is developed in order to acquire three consecutive displacement signals over the time in the same area. Actually, a progress bar (Fig. 3.37 (9)) helps the user to check the progress of the triplet. The GUI also displays the measured temperature of the last single acquisition (Fig. 3.37 (5)) and the real-time temperature of the target surface (Fig. 3.37 (4)). This feature is very useful if the data acquisition is carried out changing the position of the device on the tyre tread. Moreover, the user can analyse the single motion of the road associated with the last measurement (Fig. 3.37 (15)) and the last triple acquisition for a repeatability check of the data (Fig. 3.37 (16)). A reset button is implemented (Fig. 3.37 (11)) in order to remove the wrong triple acquisition and then, update the test total number (Fig. 3.37 (8)). The trigger 1 (Fig. 3.37 (12)) indicates that the displacement signal is ready to be acquired, the trigger 2 (Fig. 3.37 (13)) turns green as the rod is lifted until its maximum height through the slider and the trigger 3 (Fig. 3.37 (14)) activates after 1.5s the trigger 2 indicating the start of the acquisition.

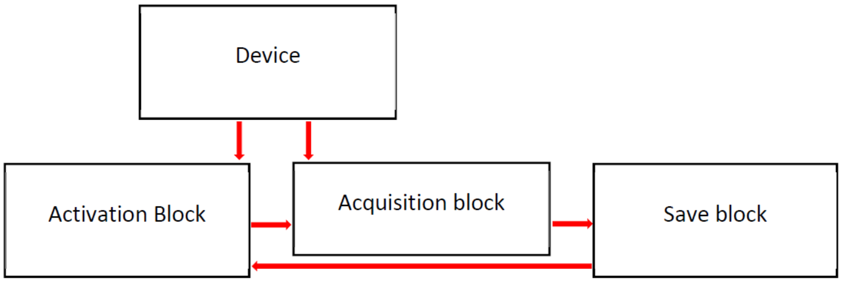

Fig. 3.38 Data Flow

The main flow behind the LabVIEW GUI is described in the block diagram in Fig. 3.38. the activation block has the task of starting the acquisition phase, which is contained in the next block, only lifting the device trigger without interacting with the graphic window. In this phase the device is in continuous communication with the software displaying the real-time temperature of the sample. The acquisition block has the task of allowing the acquisition of data from every single measurement. Even this block, like the previous one, is in continuous communication with the device that sends data relating to the position of the rod and the temperature. These data will not be stored but used to start the acquisition. The save block has only the task of saving the acquired data at the end of each triplet. When this block ends its task, the program will automatically return to the activation block to start a new acquisition.

3.6.4 Raw Data Processing

A fundamental and preliminary operation before the data processing for the viscoelasticity analysis is the identification of the first contact phase between the indenter and the specimen surface after the rod drop. Referring to the generic displacement signal (Fig 3.35), is fundamental to identify when the rod drop phase finishes and, consequently, the indentation phase starts in order to define the zero value of displacement curve. Moreover, it is important to understand how long the indentation phase is. For this purpose, a generic velocity signal can be considered and compared to the corresponding displacement. The rod velocity is evaluated by means of the derivative of the displacement, once filtered through a low-pass filter with 8kHz as cut-off frequency. This value has been chosen as the lowest through which the filtering procedure does not modify the acquired signal.

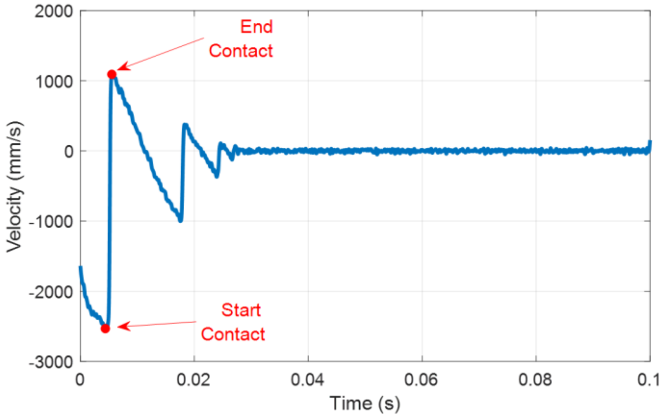

Fig. 3.39 Velocity Signal of the rod at ambient temperature

A typical velocity signal is shown in Fig 3.39. Comparing this diagram to the displacement one, plotted in Fig. 3.35, the duration of the first contact can be identified as follows. In correspondence with the absolute minimum value of the displacement, the velocity is equal to zero, the maximum deceleration is reached, and the maximum indentation depth can be measured. Before this moment, the rod is free to fall from its release point and reaches the maximum speed when the contact with the compound begins. Therefore, the instant of time, at which the lowest value of the velocity is observed, matches with the beginning of the contact between the rod and the specimen. On the contrast, after the maximum indentation, the rod is subjected to the reaction of the material due to the substrate deformation and, consequently, it will be accelerated as long as there is contact between the bodies. The moment associated with the highest velocity value defines the end of the contact after the first indentation. The duration of this phase depends on the temperature of the specimen in a single acquisition. The lower the temperature, the shorter the contact duration; in opposition, increasing the temperature, the compound behaves as a pure viscous solid and the indentation phase will be longer, as shown in Fig. 3.40.

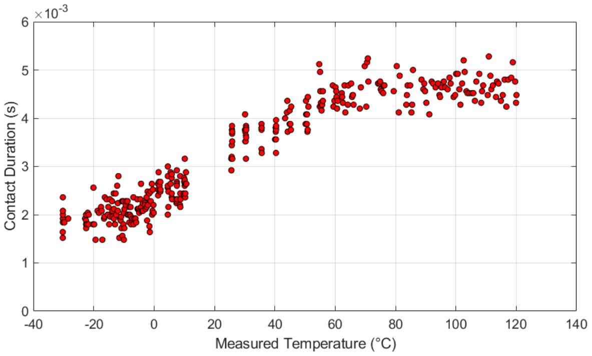

Fig. 3.40 Duration of the first indentation towards the temperature

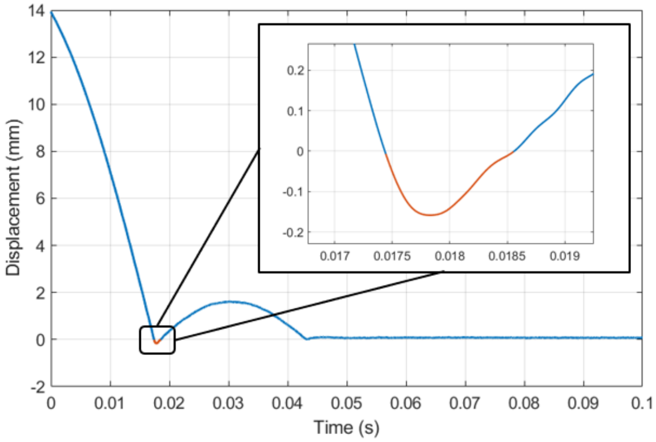

Fig. 3.41 Zoom plot on the identified first indentation area

Once identified the contact duration, the shape of the displacement curve in this range can be analysed as shown in Fig. 3.41. As expected from the velocity signal, the slope before the maximum indentation is different from the second phase one and it could be related to the same shape of a second order non-conservative mass-spring system. Actually, the motion of the rod is damped due to the bounce on a viscoelastic material being the internal passive resistance of the mechanical system neglectable (the rod slides through a guide designed with a low-friction material). Taking into account this hypothesis, the motion during the first contact can be described by means of the following relationship:

$$y(t) = y_0 + \frac{\dot{y}_0}{\omega_s} e^{-\alpha_s t} \sin(\omega_s t + \phi) \qquad (3.28)$$

where y_0 and $\dot{y}_0$ are the displacement and velocity values corresponding to the start of the contact, known from the experimental measurements, ω_s is the frequency of the damped motion of the rod on the viscoelastic surface, α_s is the extinction curve exponent and ϕ is the phase. The parameters ω_s, α_s and ϕ can be estimated by means of an identification algorithm with the aim to minimize the following cost function:

$$\varepsilon_s = |\bar{y}(t) - y(t)| \qquad (3.29)$$

where $\bar{y}(t)$ is the experimental displacement curve corresponding to the first contact area. This cost function is optimized by means of a non-linear least-squares solver implemented in Matlab environment for each single test acquired at a certain temperature. The values identified towards the temperature are shown in Fig. 3.42.

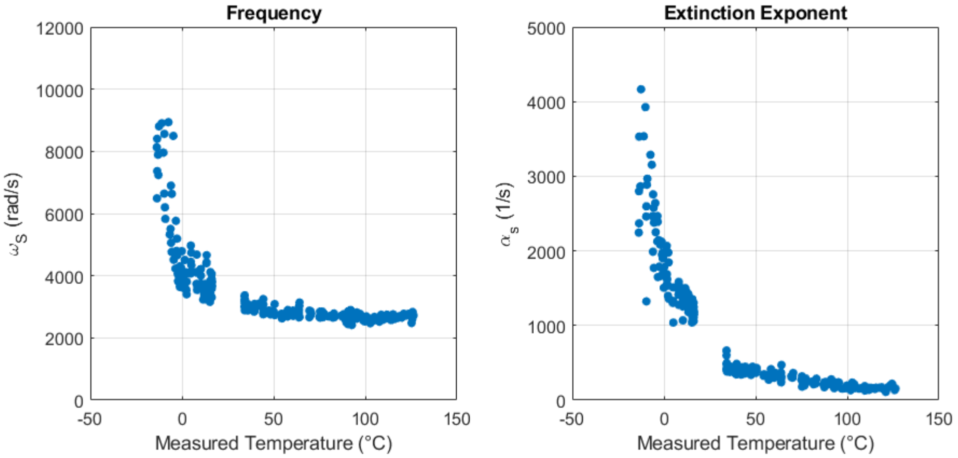

Fig. 3.42 Identified damped frequency and extinction exponent towards the temperature

As shown in Fig. 3.42, the damped frequency values depend on the temperature at which the compound surface is during each single test. This variation is associated with the different contact duration of the indenter with the specimen, whose viscoelastic properties are different from low and high temperatures. Particularly, increasing the temperature, the compound behaves as rubbery and then, the contact duration is higher; on the other hand, decreasing the temperature, the material is closer to pure glassy conditions and a shorter indentation is noticeable. The extinction coefficient exhibit almost the same trend of the damped frequency.

Once identified these magnitudes, the stiffness and the damping coefficients during the contact can be estimated through the following relationships:

$$K_c = \omega_N^2 \cdot m_{rod} \tag{3.30}$$

$$\sigma_c = \alpha_s \cdot 2\, m_{rod} \tag{3.31}$$

where m_{rod} is the mass of the indenter and is equal to 2.5g and ω_N is the natural frequency of the motion during the contact phase. The latter can be determined as follows:

$$\omega_N = \frac{\omega_S}{\sqrt{1-\zeta_c^2}} \tag{3.32}$$

where ζ_c is the characteristic damping ratio determined according to the following:

$$\zeta_c = \sqrt{\frac{\sigma_c^2}{\alpha_s^2 + \omega_S^2}} \tag{3.33}$$

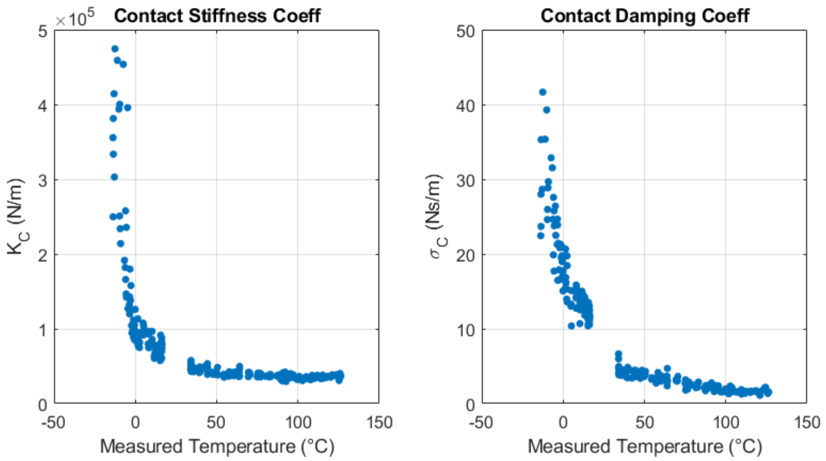

Fig. 3.43 Estimated contact stiffness and damping coefficients from identified variables

The values of the contact stiffness and damping coefficient are shown in Fig. 3.43. As displayed in these diagrams, these properties are function of the measured temperature because the viscoelasticity of the specimen surface on which the rod bounces. It is fundamental to highlight that these parameters belong to tested compound being the internal spring stiffness coefficient of the rod very low (almost 60 N/m) and the internal passive resistance of the rod sliding system neglectable.

Once analysed these magnitudes, the viscoelastic Storage Modulus E' and Loss Modulus E'' are estimated according to the Sneddon's theory of indentation relationships [67, 69]:

$$E' = \sqrt{\frac{\pi}{A_c}} \frac{K_c}{2} \tag{3.34}$$

$$E'' = \sqrt{\frac{\pi}{A_c}} \frac{\sigma_c \omega_S}{2} \tag{3.35}$$

$$\tan(\delta) = \frac{\omega_S \sigma_c}{K_c} \tag{3.36}$$

where A_c is the contact area between the semi-spherical indenter and the compound. This magnitude is determined by means of the Hertz's theory from the measurement of the depth at each temperature as follows:

$$A_c = \pi \cdot r_c^2 = \pi \cdot (s_{Min} \cdot r_{rod}) \tag{3.37}$$

In equation (3.37), r_c is the contact radius and s_{Min} is the maximum depth reached during the first indentation, as shown in Fig. 3.41. The typical values of these magnitudes towards the temperature are displayed in Fig. 3.44.

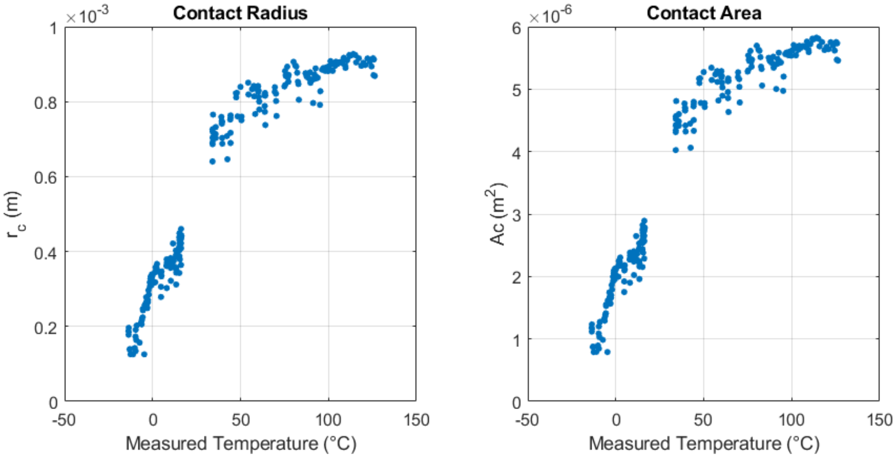

Fig. 3.44 Estimated contact radius and contact area during first indentation

The values of Storage Modulus and Loss Factor according to equations (3.34) and (3.36) are shown in Fig. 3.45 towards the measured temperature. Each marker of this diagram matches with a specific value of the frequency ω_S according to the Time – Temperature superposition concept. Therefore, the Sneddon's relationships do not provide a master curve as temperature sweep for a reference and constant frequency, as well as DMA. This is due to the VESevo testing methodology, which does not allow to keep the temperature or the solicitation frequency constant during each test because of the procedure is based on the free release and motion of the rod on the specimen surface.

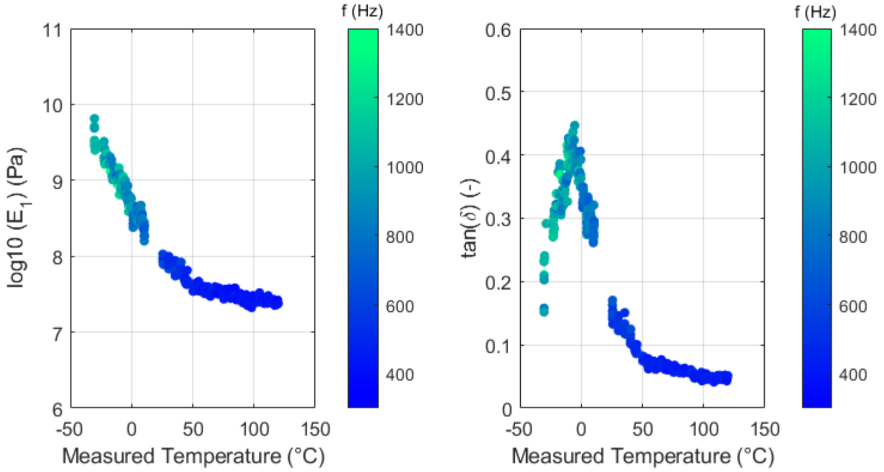

Fig. 3.45 Estimated contact radius and contact area during the first indentation

To determine the viscoelastic master curves from VESevo data processing, it is necessary to shift each marker according to a specific ΔT estimated by means of the William-Landel-Ferry relationship introduced in equation (2.11). The comparison of the viscoelastic curves with the shifted ones is shown in Fig. 3.46. In the description and analysis of the following results achieved by means of the VESevo experiments, the compound properties will be always described in terms of shifted temperatures. As possible, the amount of the temperature shift is determined taking into account the WLF relationship coefficient specific of the tested compound; in the other cases, the universal constants are used with the aim to focus on the relative differences among the compounds at different conditions for Motorsport/Automotive applications.

3.6.5 Comparison of VESevo results to DMA reference curves

To check the goodness of the viscoelastic results obtained by means of the processing of the VESevo experimental data, the final viscoelastic master curves have been compared to the DMA temperatures sweep 1 Hz performed in dual cantilever configuration. For this purpose, four different SBR compounds have been tested through the VESevo in a very wide temperature range [-30°C, 120°C] and the acquired data have been processed according to the procedure described in section 3.6.4 Raw Data Processing. During the tests, the specimens have been positioned in a suitable sample-holder in order to improve the acquisition at each temperature, as shown in Fig. 3.46. The compounds nomenclature and William-Landel-Ferry coefficients determined by DMA are shown in Table 3-4.

Table 3-4 WLF coefficients of the reference specimens

Compound	Density (kg/m^3)	T_0 (K)	C1 (-)	C2 (K)
Slab A	1190	393.15	32.35	473
Slab B	1245	393.15	18.20	330
Slab C	1292	393.15	30.8	399.5
Slab D	1145	393.15	33.5	470.5


a) b)

Fig. 3.46 a) 40 mm diameter compound specimen; b) Specimen in the suitable holder for testing

The comparison between the VESevo master curves at 1 Hz and the DMA temperature sweep data of the above-mentioned compounds are shown from Fig. 3.47 to Fig. 3.50. The values on the plot axes are not indicated because of the industrial confidentiality agreement with the compound manufacturer. Therefore, qualitative analysis can be outlined in this paragraph. As highlighted in the following diagrams, the red markers corresponding to VESevo 1Hz viscoelastic properties values are quite in agreement with the DMA master curves carried out through dual cantilever clamp. Particularly, the processing algorithm has been capable of identifying from the VESevo data the glass transition temperatures T_g for the Slab A, C and D, which are almost similar to the DMA ones analysing the loss factor curves, except for the Slab B. In this case, the testing procedure and data processing has returned values that do not totally follow the slope of DMA curves in the shifted temperature range [-50°C, 0°C]. Hence, thanks to this analysis with the DMA curves, the results of the viscoelastic characterization through the VESevo non-destructive measurements can be considered consistent and reliable for Automotive and Motorsport applications. Particularly, some of the main applications in these fields achieved during the research period are shown to point out the advantages of using this innovative device.

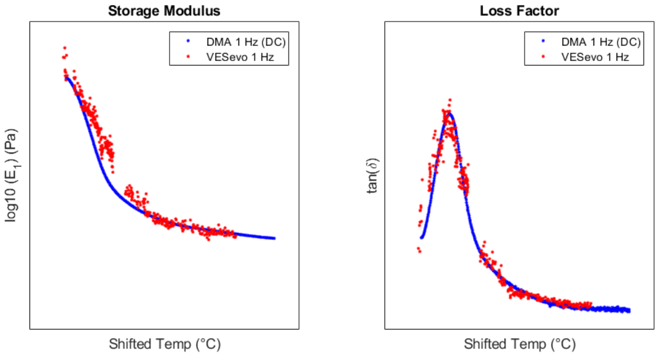

Fig. 3.47 Slab A: VESevo results compared to DMA 1Hz

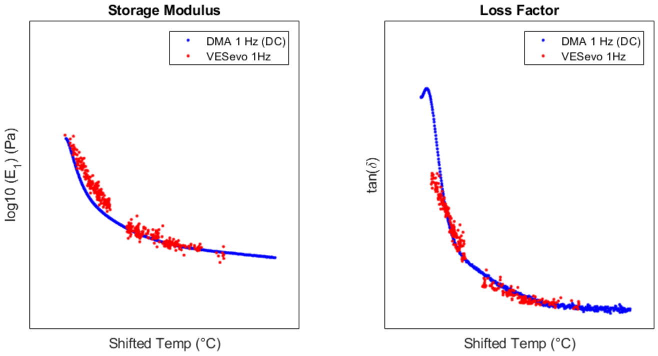

Fig. 3.48 Slab B: VESevo results compared to DMA 1Hz

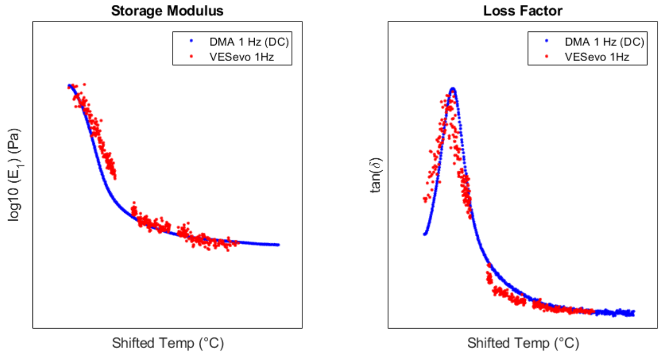

Fig. 3.49 Slab C: VESevo results compared to DMA 1Hz

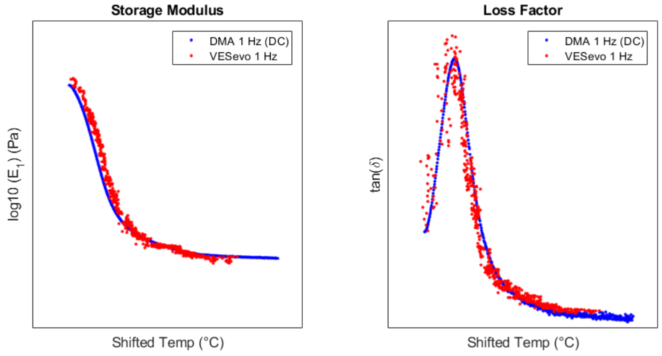

Fig. 3.50 Slab D: VESevo results compared to DMA 1Hz

3.6.6 VESevo characterization: Motorsport application

The main applications of the VESevo deal with the Motorsport field. Actually, one of the reasons why this innovative device was developed is to overcome the restrictions attached to the characterization of racing tyres by motorsport teams, who cannot destroy them and then perform standard DMA. Therefore, in this scenario, the VESevo could be a powerful instrument for "confidential" tyres characterization during the typical track routines of engineers.

A typical VESevo testing program involves the viscoelastic characterization of the front and rear tyres in order to check the homogeneity of the properties and then optimize the vehicle set-up and balance according to possible differences. For each tyre, the testing procedure should be the following:

1. Ambient temperature measurements through the VESevo on the tread surface;
2. Low-temperature measurements on the tread surface. In this case, a freezing air spray is commonly used on track because the climatic cell for tyres is not always available: the data are acquired from the lowest temperature until the ambient one during the natural heating-up phase of the tread;

3. High-temperature measurements on the tread surfaces. For this testing, thermal blankets are widely used by engineers in order to heat the tyre until the performance temperature of interest. The VESevo data are acquired during the natural cooling down of the tyre once removed the thermal blanket.

In this paragraph, the author highlights that the full images of the tested tyres must not be inserted and the values on axes are normalized to the maximum due to industrial confidentiality agreement with the racing teams involved in the research project. In Fig. 3.51, the results of the VESevo characterization carried out on the new front left (FL) and rear right (RR) tyres are shown as different tinted markers. Analysing these data, it is noticeable how the viscoelastic properties of the tyre of each axle are very similar and the same loss factor peak values and glass transition temperatures have been identified.

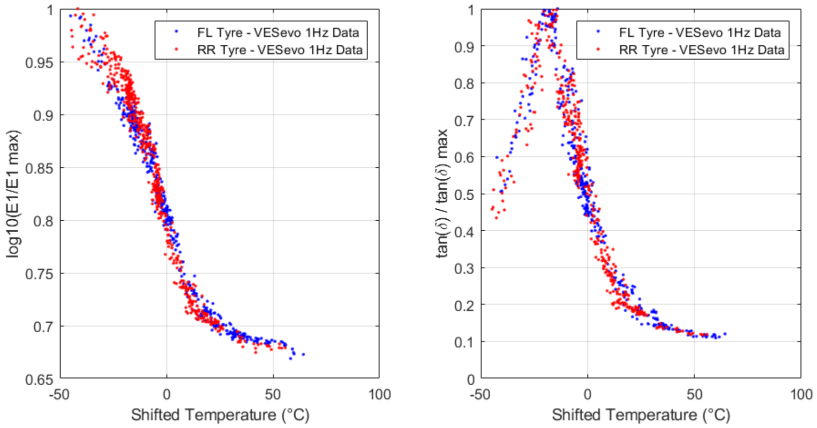

Fig. 3.51 VESevo characterization results on Motorsport new tyres

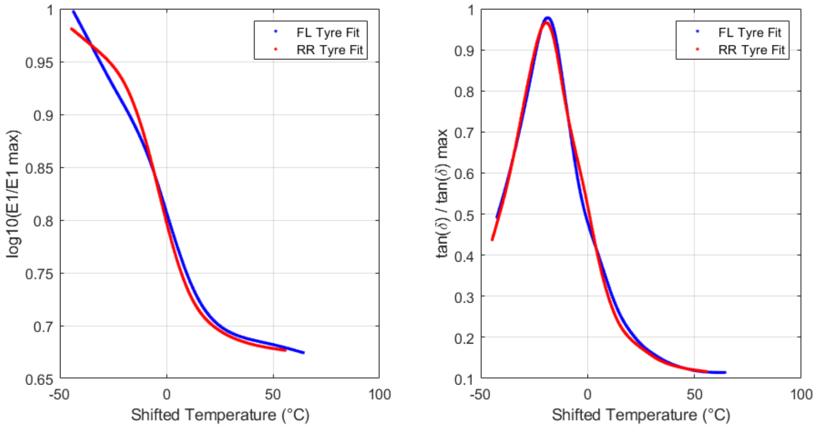

Fig. 3.52 Smoothing spline fit curves of VESevo data

To improve the visualization of the VESevo results in the next figures, the smoothing spline fit curves are determined for each tyre data, as plotted in Fig. 3.52. The trustworthiness of the fittings is checked by taking into account an adjusted R^2 value higher than 0.95. The slight differences occurring at very low temperatures in the Storage Modulus diagram could be affected by the cooling procedure with the freezing air spray, which is not a testing procedure as much robust as the climatic cell one.

For racing teams, it is also advantageous to analyse how the viscoelastic properties can change due to the wear phenomena on track and how the results of the VESevo experiment correlates with the telemetry data or driver feedbacks with the aim to improve the vehicle set-up strategy. In Fig. 3.53 and 3.54, the variations of the viscoelastic properties due to the progressive mileage on track are shown.

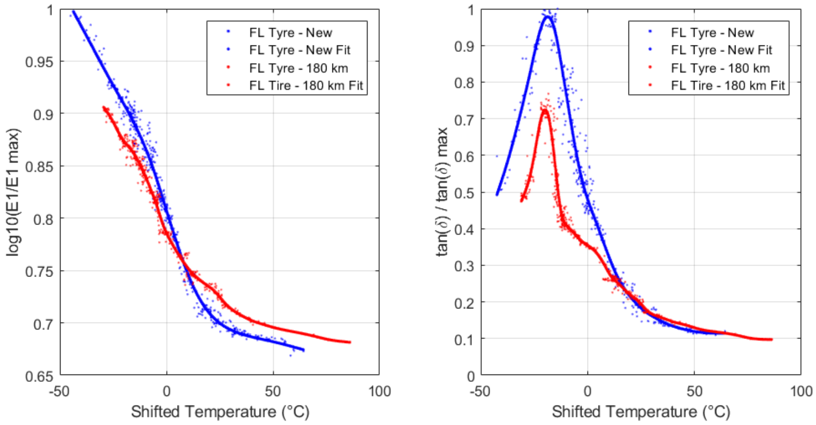

Fig. 3.53 Covered mileage effects on the FL tyre properties (normalized to FL maxima)

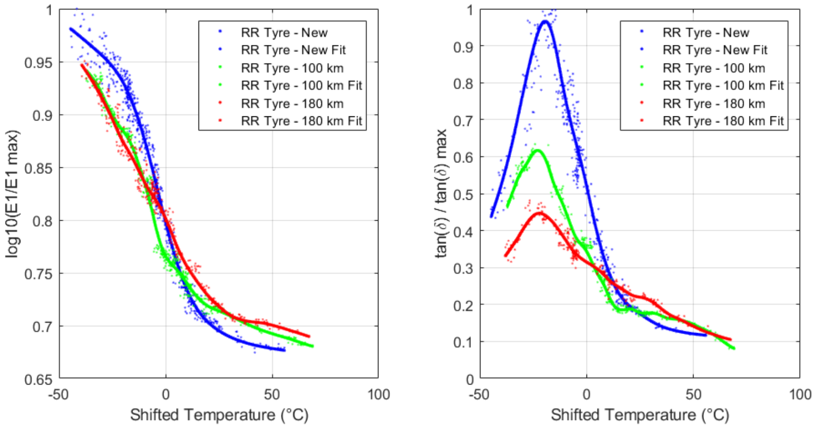

Fig. 3.54 Covered mileage effects on the RR tyre properties (normalized to FL maxima)

Analysing the results in the above diagrams, a relevant reduction of the loss factor peak value has been identified for both FL and RL tyres together with a slight decrease of the glass transition temperatures. This means that the overall trend of the tan(δ) curve is affected by the high mileage covered. On the other hand, the storage modulus slope changes exhibiting values greater than the new condition at high temperatures. Therefore, both properties variations negatively affect the vehicle performance and tyre-road grip coefficient in terms of adhesive and hysteretic rates, as described in paragraphs 5.4 Klüppel’s multiscale contact model and 5.5 Persson’s multiscale contact model Furthermore, comparing the front and rear axles results after 180 km covered, a different performance variation between FL and RR tyres is highlighted: this phenomenon maybe since the rear tyres are subjected to more aggressive wear due to higher slip ratios being the tractive wheels of the vehicle.

The different wear effects on viscoelastic properties due to vehicle set up (inclination angle of tyre or toe) can be also detected through VESevo testing, as shown in Fig. 3.55: external area of the RR tread exhibits properties values almost close to the new conditions with a sort of “activation effect” due to scrubbing at the high temperatures, where a higher loss factor and storage modulus trends are noticeable. The inner tread zone (full red line) is subjected to more significant degradation and abrasion with respect to the centre and outer ones.

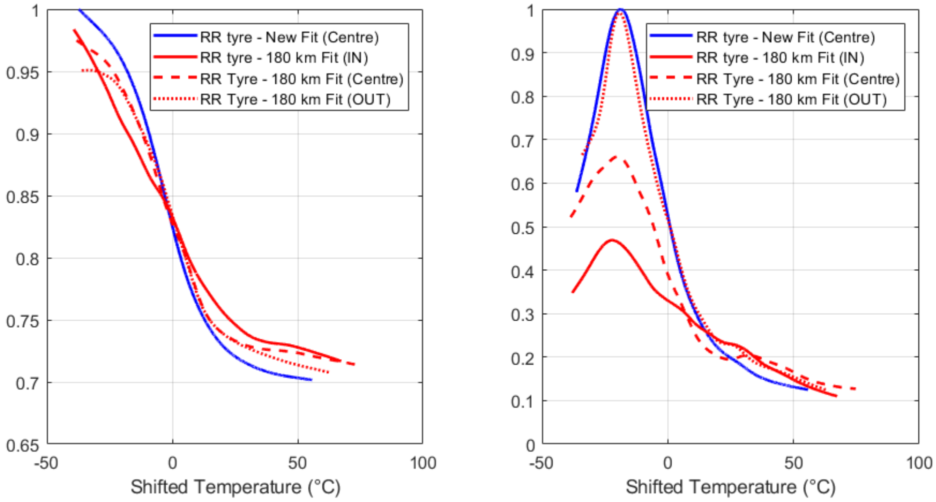

Fig. 3.55 Different wear effects due to vehicle set up on RR tyre properties

The overall results described in this paragraph are an example of the physical considerations advantaging for racing teams because the VESevo provides the variations of tyre properties and performance over the different conditions and the time, which cannot be usually measured but only deducted and comprehended from the vehicle data and driver feedback. Hence, this innovative device for non-destructive testing is a powerful and smart instrument in this scenario.

3.6.7 VESevo characterization: Uniformity analysis of tyre series

The VESevo has been also employed in the analysis of viscoelastic properties uniformity among different tyres of the same production series thanks to its smart characterization of the compound.

The inspection of the mechanical behaviour of the manufactured tyres is a fundamental topic for tyre makers because it can be considered as the final validation of the product before its sale and use by the customer. One of the marker tests commonly adopted is the rolling resistance on specific benches, such as the flat track or the drum according to ISO 28580 [6, 106, 107]: the tyre is mounted on a free-rolling spindle with no camber or slip angle, loaded against a large-diameter powered test drum, turned by the drum to simulate on-road rolling operation, and a measure of the rolling resistance is determined as the effort required to keep a given tyre rolling. This magnitude depends on the tyre compound used, the nature of the surface on which it rolls and the operating conditions, such as angular speed, pressure, and normal load. The Force Method is usually employed as a procedure to estimate the rolling resistance and rank the reliability of the compound.

As can be guessed, the procedure described above requires a lot of time for testing a considerable number of tyres, as well as resources in terms of operators and maintenance of the benches. In this scenario, the VESevo can be an innovative instrument to be employed into the final validation of the mechanical compound behaviour thanks to its smart and non-destructive characterization. Being a very ergonomic device, the VESevo could be also used by a single operator to test many tyres in a short time.

Fig. 3.56 Tread area of truck tyres tested by means of VESevo

In the analysis described in this paragraph, which was carried out in collaboration with a truck tyres manufacturer, three series of product have been considered. Each tyre of the set has been tested at ambient temperature (~15°C) in the tread areas outlined in Fig. 3.56. The results shown in the next bar plot diagrams correspond to the average value over 30 measurements on these tyre areas and they have been normalized respect to the maximum value of storage modulus and loss factor due to industrial confidentiality agreement with the tyre manufacturer.

Analysing the reported bar plot diagrams, ten products have been tested for the first series, six tyres for the second and five tyres for the last one. In the first set, the tyre 3 exhibits a storage and loss factor, which are lower than the average values estimated over the full series. In the second cluster, all the tyres are characterized by a lower storage modulus in the centre rib compared to the inner and outer ones. In the last group, all the products analysed exhibit almost the values of loss factor and slight differences between external ribs and centre ribs in terms of E_1.

The main differences among tyres of each production set identified by means of VESevo measurements are very useful and detailed for the tyre manufacturer because the classic rolling resistance test returns a coefficient that could not justify in depth possible differences among many specifications.

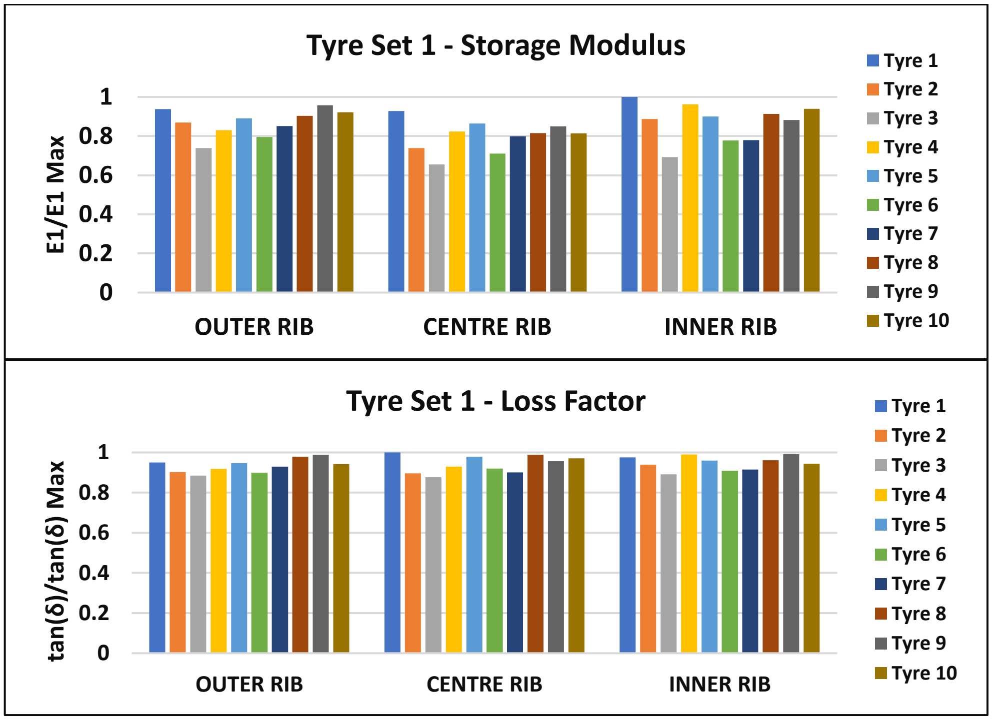

Fig. 3.57 Tyre series 1 results: Storage modulus and loss factor normalized values

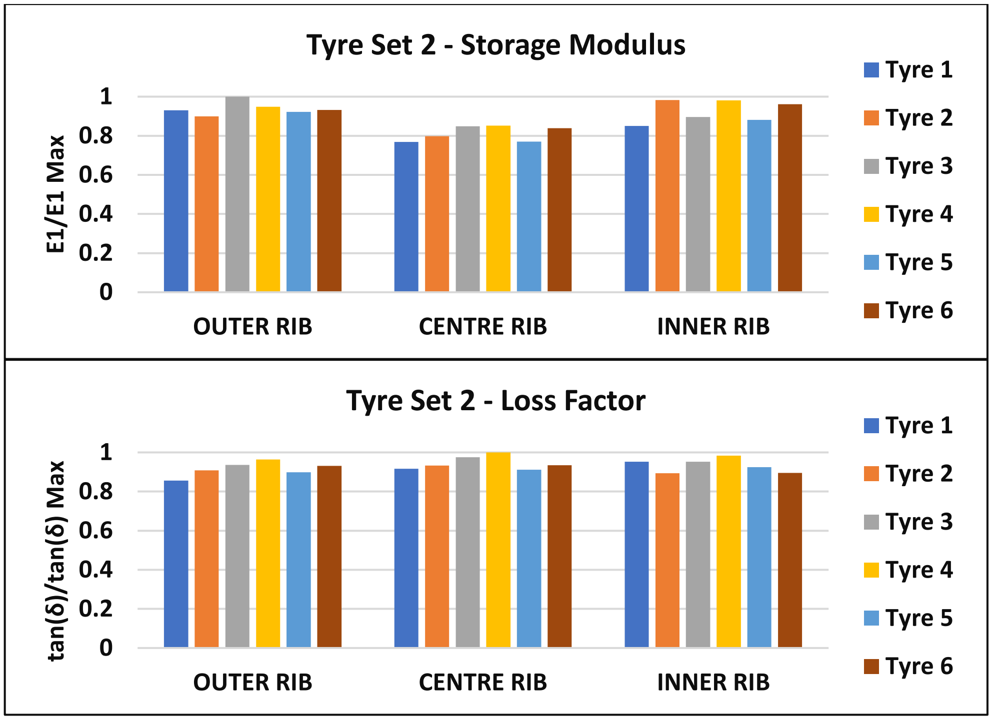
Tyre Set 2 - Storage Modulus

Tyre Set 2 - Loss Factor

Fig. 3.58 Tyre series 2 results: Storage modulus and loss factor normalized values

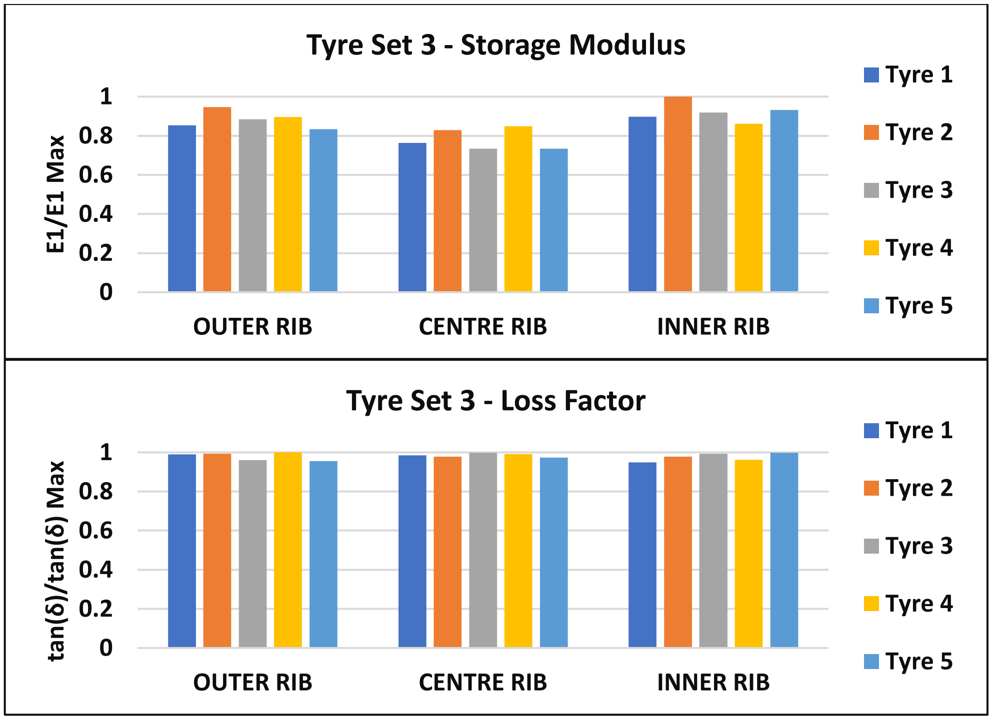
Tyre Set 3 - Storage Modulus

Tyre Set 3 - Loss Factor

Fig. 3.59 Tyre series 3 results: Storage modulus and loss factor normalized values

What is evidenced in the bar plots is usually a consequence of a non-optimal manufacturing process of tyres in the corresponding mould, during which the polymer vulcanization and temperature are not totally homogeneous at each point of the tread surface. For this reason, the manufacturers focus their main efforts on the optimization of the tyre series production to avoid undesired phenomena, such as irregular wear on the tread or sudden cracks in the inner layers of tyres during the usual working cycle of these products, which affect the safety and performance of the products or, further, give rise to economic losses, especially in case of final costumers, as truck fleets companies, who could face with unexpected vehicle stops during the transport of necessities.

A further analysis that could be carried out for final product validation is the viscoelastic characterization of truck tyres at each sector of the tread circumference, as shown in Fig. 3.60 a). The normalized loss factor values with respect to the maximum corresponding to VESevo measurements on 5 tread ribs over 28 sectors are displayed in Fig. 3.61 b). As noticeable, each rib is characterized by a different mean value of the loss factor estimated over the defined sectors. Each marker matches with the average value over 15 tests on the central tread block of the N-sector. This kind of analysis has again highlighted the possible differences of the mechanical properties in different tread areas due to the manufacturing process and the needing to develop a new device based on the concept of a “multi-VESevo” in collaboration with the tyre maker, which could be capable of testing the tread circumference simultaneously and autonomously in different points and providing smart and fast feedback on the whole final product homogeneity.

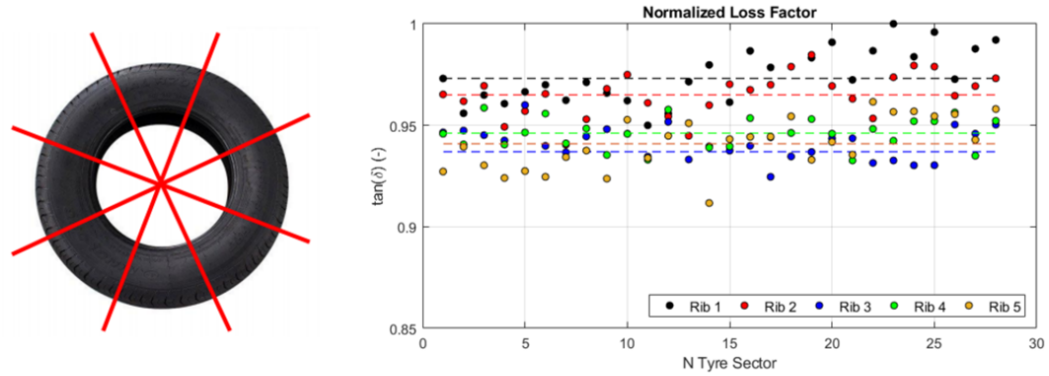

a) b)

Fig. 3.60 a) Truck tyre sectors; b) VESevo characterization results over 28 area

Chapter 4

Road Roughness Analysis

The quantitative evaluation of surface roughness is of a major interest in many industrial applications. The analysis of road surface texture is a fundamental in pavement engineering as it determines among other factors the noise emission from the tyre-road interface, the frictional forces that can be transmitted between tyre and pavement and the water drainage capacity [108].

A surface, by definition, is an interface, a marked discontinuity form one material to another. Any real surface has a finite depth, and in a characterizing surface one must consider just what this depth is at some point. All surface prepared by mechanical techniques contain defects resulting from plastic deformation, fracture, heating and contamination, nature of material, the method of surface preparation, which causes a complex structure and complex properties. Therefore, properties of solid surfaces are critical to the pavement interaction since surface properties affect the real area of contact between the solids, friction, wear and lubrication [109]. For this reason, the main road roughness characterization methods, which have been applied during the research period, are discussed in this chapter analysing the advantages and disadvantages of each technique.

4.1 Introduction to road roughness properties

The first step in the mechanical contact analysis is the surface characterization. To analyse the surface texture starting from the three-dimensional topography (as shown in Fig. 4.1) many methods could be adopted for each surface topology, as outlined in Fig. 4.2.

Surface roughness most commonly refers to the variations in height of the surface relative to a reference plane. It is measured either along a single lone profile or along a set of parallel line profiles (surface maps).

Statistical parameters are used to characterize the road roughness, but it is usual to prefer a spectral analysis that allows to obtain better results.

The different statistical parameters useful for characterizing the road surface together with the typical tools of spectral analysis will be analysed in the following, highlighting the magnitudes which are commonly used as input into the well-known tyre-road contact models available in literature and the friction model, denoted as GrETA, developed during the research period at the Department of Industrial Engineering of the University of Naples Federico II.

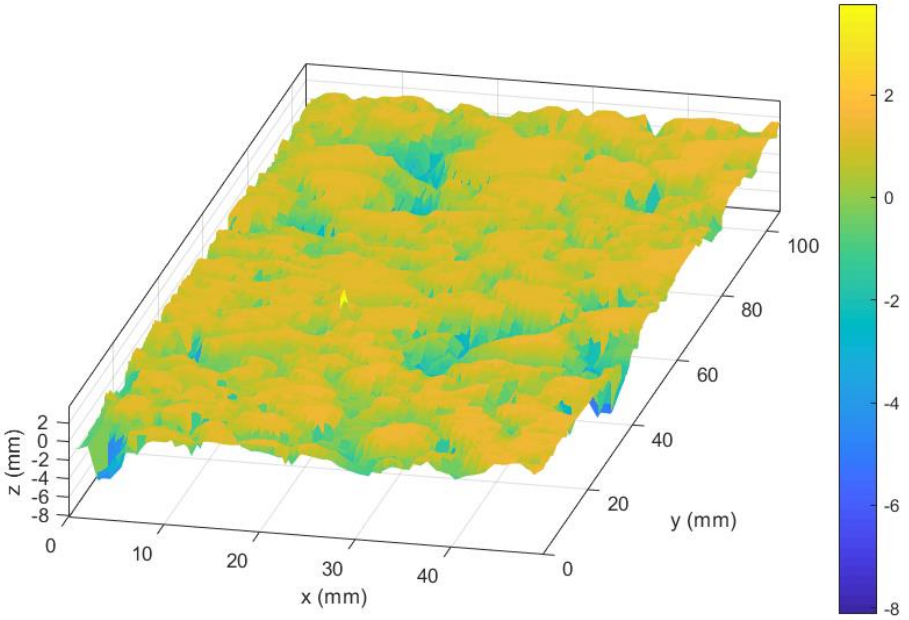

Fig. 4.1 3D road texture

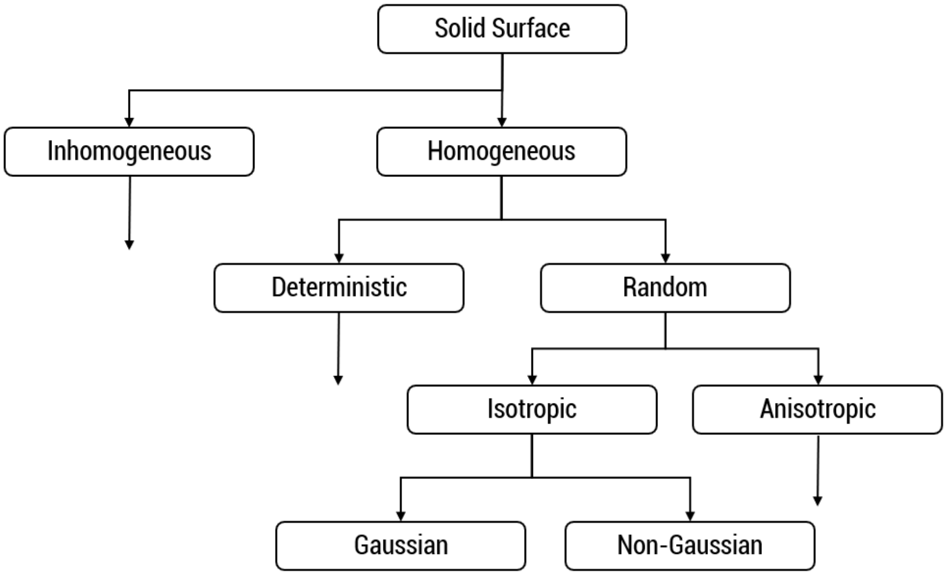

Fig. 4.2 General topology of surfaces

4.2 Statistical analysis of the road texture

4.2.1 Amplitude probability distribution and density functions

The cumulative probability distribution function, or simply cumulative distribution function (CDF), $P(h)$ associated with the random variable $z(x)$, which can take any value between $-\infty$ and $+\infty$ or $z_{\min}$ and z_{max}, is defined as the probability of the event $z(x) \leq h$, and is denoted as:

$$P(h) = prob(z \leq h) \tag{4.1}$$

where $P(-\infty) = 0$ and $P(+\infty) = 1$.

The probability structure is commonly described by means of the density function (PDF), indicated with $p(z)$, which is defined as:

$$p(z) = \frac{dP(z)}{dz} \tag{4.2}$$

The cumulative distribution function is the integral of the probability density function:

$$\begin{gathered} P(z \leq h) = \int_{-\infty}^{h} \phi(z) dz = P(h) \\ P(h_1 \leq \ z \leq h_2) = \int_{h_1}^{h_2} \phi(z) dz = P(h_2) - P(h_1) \end{gathered} \tag{4.3}$$

The data usually tend to exhibit a Gaussian or normal probability density function:

$$\phi(z) = \frac{1}{\sigma\sqrt{2\pi}} \exp\left(-\frac{(z-m)^2}{2\sigma^2}\right) \tag{4.4}$$

where σ is the standard deviation and m is the mean value.

For convenience, the Gaussian function is plotted in terms of a normalized variable, which has zero mean and unity standard deviation. Therefore, the normal probability function is defined as follows:

$$\phi(z^*) = \frac{1}{\sqrt{2\pi}} \exp\left(-\frac{z^{*2}}{2}\right) \tag{4.5}$$

where $z^* = \frac{z-m}{\sigma}$.

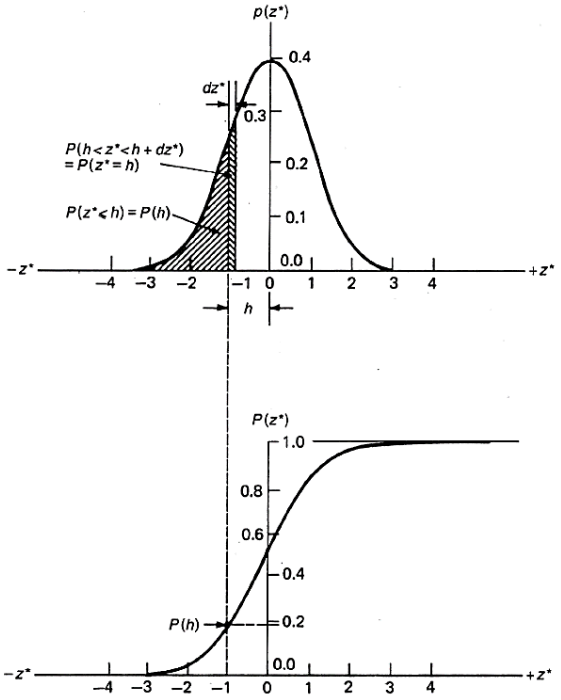

Fig. 4.3 Gaussian probability density and Gaussian probability distribution functions

4.2.2 Road roughness amplitude parameters

The surface is usually characterized by one of the two statistical height descriptors advocated by the American National Standards Institute (ANSI) and the International Standardization Organization (ISO) [110]: the R_a, mean line, and the standard deviation or variance, σ, or root mean square, R_q.

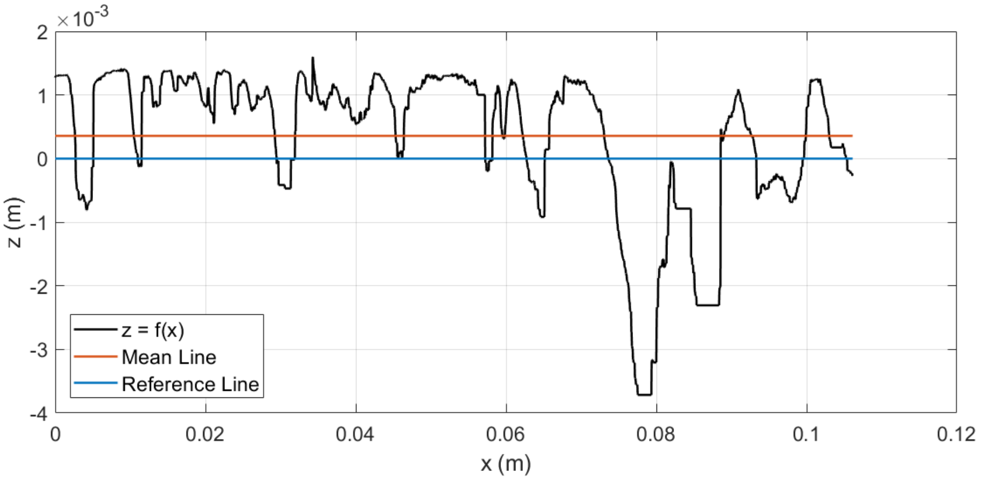

Fig. 4.4 Surface profile z(x)

As shown in Fig. 4.4, a generic profile $z(x)$ is assigned. In mathematical form, the statistical height descriptors are defined in this way:

- Mean line R_a

$$R_a = \frac{1}{L}\int_0^L |z - m|dx \tag{4.6}$$

where L is the sampling length of the profile and m is the mean, defined as:

$$m = \frac{1}{L}\int_0^L zdx \tag{4.7}$$

- The variance σ^2

$$\sigma^2 = \frac{1}{L}\int_0^L (z - m)^2 dx = R_q^2 - m^2 \tag{4.8}$$

where σ is the standard deviation and R_q the root mean square, expressed as:

$$R_q^2 = RMS^2 = \frac{1}{L}\int_0^L z^2 dx \tag{4.9}$$

There are further height descriptors that can be used for the road roughness analysis [111]. The skewness of a profile is defined as the third central moment of profile amplitude probability density function, measured over the assessment length. It is used to measure the symmetry of the profile about the mean line. This parameter is sensitive to occasional deep valleys or high peaks and is expressed as follows:

$$S_k = \frac{1}{\sigma^3 L}\int_0^L (z - m)^3 dx \tag{4.10}$$

A symmetrical height distribution, i.e., with as many peaks as valleys, has zero skewness. Profiles with peaks removed or deep scratches have negative skewness, as shown in Fig. 4.5. The skewness can be also used to distinguish between two profiles having the same R_a or R_q values but different shapes.

On the other hand, the Kurtosis coefficient is the fourth central moment of profile amplitude probability density function, measured over the assessment length. It describes the sharpness of the probability density of the profile and it is calculated as:

$$K = \frac{1}{\sigma^4 L}\int_0^L (z - m)^4 dx \tag{4.11}$$

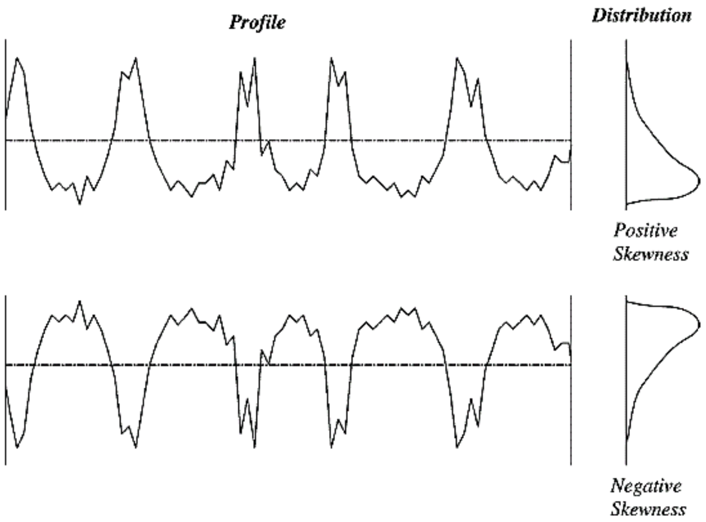

Fig. 4.5 Definition of skewness and amplitude distribution curves

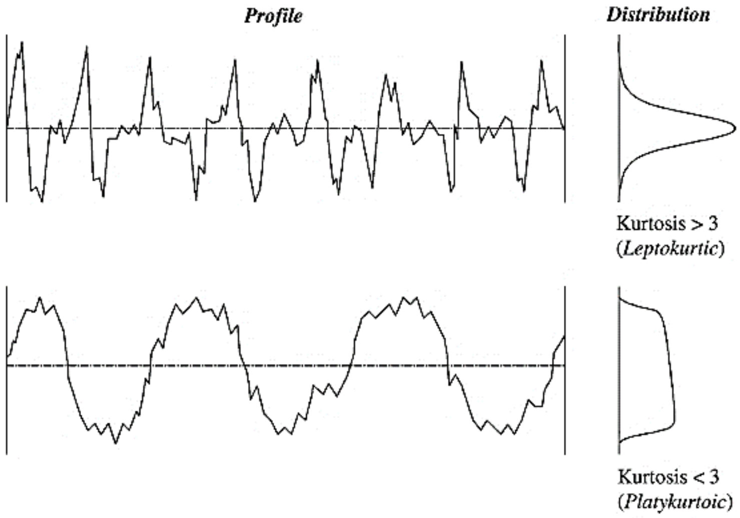

Fig. 4.6 Definition of kurtosis parameter

If $K < 3$ the distribution curve is said to be platykurtic and has relatively few high peaks and low valleys. On contrast, the distribution curve is said to be leptokurtic and has relatively many high peaks and low valleys, as shown in Fig. 4.6.

4.2.3 Road roughness spacing parameters

The spacing parameters are those which measure the horizontal characteristics of the surface deviations. The spacing parameters are very important, and their evaluation is useful for obtaining the necessary amount of information for the tyre-road contact modelling. Some parameters used are the number of peaks of the profile per unit length, N_p, and the number of times the profile crosses the mean line per unit length, N_0.

Although the profile contains a wide and continuous range of wavelengths, the average wavelength parameter can be considered as a measured of the spacing between local peaks and valleys, taking into account their relative amplitudes and individual spacing frequencies [111]. This parameter can be calculated from the following equation:

$$\lambda_a = \frac{2\pi R_a}{\Delta_a} \tag{4.12}$$

where Δ_a is the means slope of the mean slope of the profile, defined as:

$$\Delta_a = \frac{1}{L}\int_0^L \left|\frac{dz}{dx}\right| dx \tag{4.13}$$

4.3 Self-affine surfaces characterization

The road surface is commonly considered as a self-affine surface in many friction models [112]. In this regard, the properties of this type of surface and the various methods used to identify the peculiar features that represent input for the rubber-substrate contact model will be described and analysed.

In recent years, many studies on self-affine surfaces appear in literature [1, 14, 15]. The term “self-affine” was introduced by Mandelbrot [113] when he studied geometrical objects that are statistically invariant under anisotropic dilatations. It represents a generalization of the term “self-similarity” that denotes invariance under isotropic dilatation [14].

If the profile $z(x)$ of a rough surface without overhangs, i.e., of a vertical cross-section of the surface, is considered, then the surface is self-affine if the transformation $x \rightarrow \lambda x, z \rightarrow \lambda^H x$ leaves the surface statistically invariant [14], as shown in Fig. 4.7. The exponent H is the Hurst coefficient $(0 \leq H \leq 1)$ and it is related to the fractal dimension D according to the following expression:

$$D = \delta - H \tag{4.14}$$

where δ is the dimension of the Euclidean space ($\delta = 2$ for 2D surface and $\delta = 3$ for 3D surface).

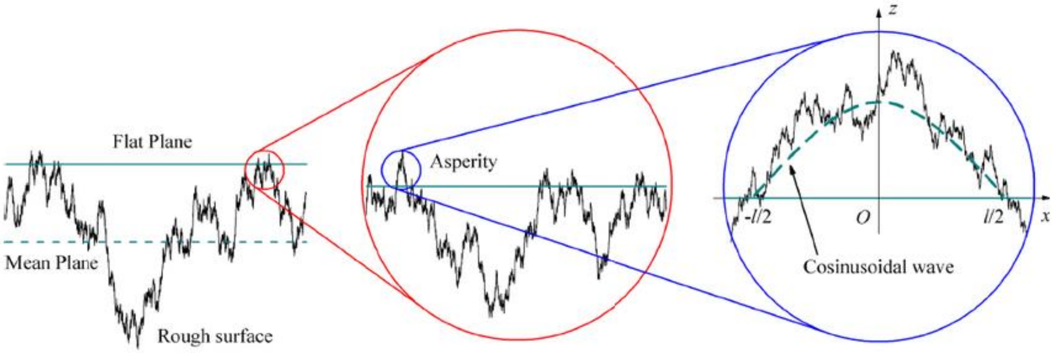

Fig. 4.7 Self-affine fractal surface

4.3.1 Height correlation functions for self-affine surfaces

In addition to the surface fractal dimension, two further length scales are necessary to characterize a self-affine surface:

- $\xi_{||}$, the correlation length parallel to the surface, corresponding to the average wavelength of the macroroughness scale;
- the variance, i.e., the root mean square fluctuations around the mean height:

$$\sigma^2 = \langle (z(x) - \langle z \rangle)^2 \rangle \tag{4.15}$$

where $\langle z \rangle$ is the mean height of the surface, while $\langle - \rangle$ is the average of the set of observations of surface topography. The variance, usually, is expressed as:

$$\sigma^2 = 2\xi_{\perp}^2 \tag{4.16}$$

where $\xi_{\perp}$ is the correlation length normal to the surface, corresponding to the roughness R_a as shown in Fig. 4.8.

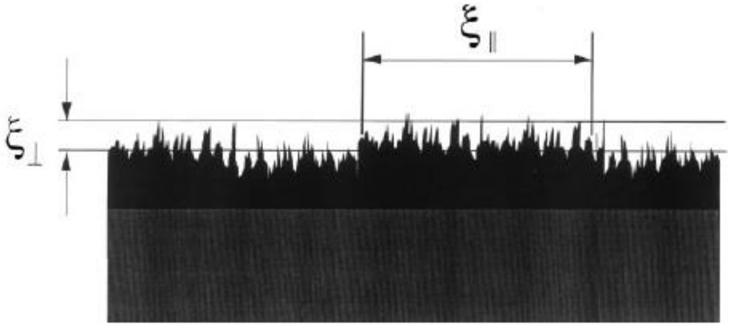

Fig. 4.8 Profile correlation lengths

These correlation lengths can be evaluated through the correlation functions of the surfaces. The height difference correlation function (HDC function) is commonly adopted for this purpose. According to this function, the mean square height-fluctuations of the surface, $C_z(\lambda)$, with respect to the horizontal length scale λ is determined as follows [14, 114]:

$$C_z(\lambda) = \left\langle \big(z(x+\lambda) - z(x)\big)^2 \right\rangle \tag{4.17}$$

For self-affine surfaces, $C_z(\lambda)$ follows a power a law with exponent $2H$ on small length scales for $\lambda < \xi_{\parallel}$ and approaches the constant value $\xi_{\perp}$ for $\lambda > \xi_{\parallel}$ [1, 14, 114, 115]:

$$C_z(\lambda) = \left(\frac{\lambda}{\xi_{\parallel}}\right)^{2H} \tag{4.18}$$

Another approach is the evaluation of the height correlation function, $\Gamma_z(\lambda)$, also named auto-correlation function [14, 115]:

$$\Gamma_z(\lambda) = \langle z(x+\lambda)z(x)\rangle - \langle z(x)\rangle^2 \tag{4.19}$$

The function $\Gamma_z(\lambda)$ characterizes the correlations of heights at two different positions and is related to $C_z(\lambda)$ by the following expression:

$$C_z(\lambda) = 2\big(\sigma^2 - \Gamma_z(\lambda)\big) \tag{4.20}$$

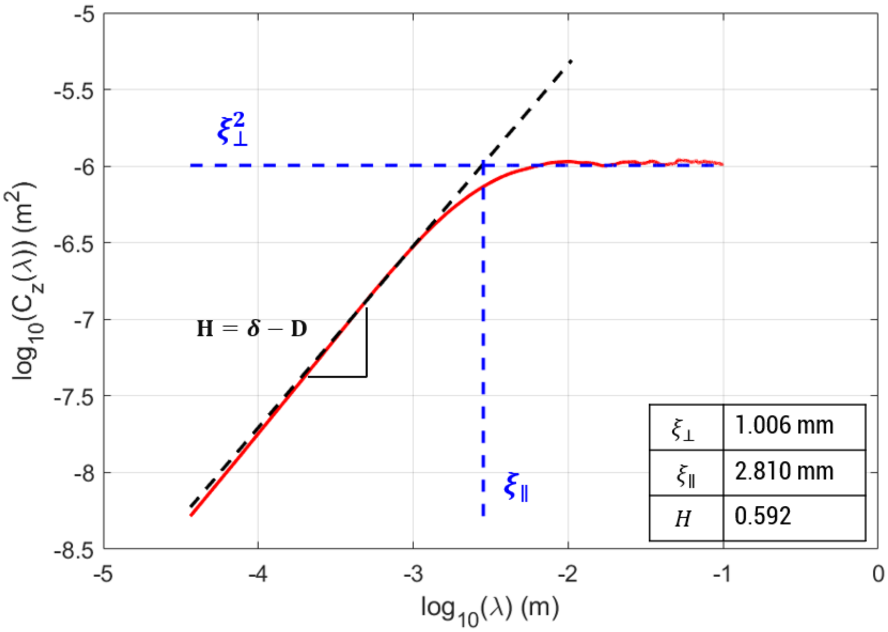

Fig. 4.9 HDC function for a self-affine 2D profile

In Fig. 4.9, the HDC function for a self-affine 2D profile is shown. In this diagram, it is noticeable how the parameters describing the surface can be determined: the correlation length parallel to the profile, the variance and the Hurst coefficient by considering the slope of the linear shape of $C_z(\lambda)$ function. Particularly, $\xi_{\parallel}$ is determined as the x-value at which the linear function with slope H is equal to the square of the variance.

However, the equation (4.18) allows describing the spectrum of self-affine surfaces by only these parameters. If more scaling ranges should be necessary for a reasonable description of surface roughness, this formula can be expanded to any number of scaling ranges with different Hurst exponents [1, 55]. In this case, the function $C_z(\lambda)$ is defined as:

$$C_z(\lambda) = \xi_{\perp}^2 \left(\frac{\lambda}{\xi_{\parallel}}\right)^{2H_M} \tag{4.21}$$

$$C_z(\lambda) = \xi_{\perp}^2 \left(\frac{\lambda_x}{\xi_{\parallel}}\right)^{2H_M} \left(\frac{\lambda}{\lambda_x}\right)^{2H_m} \tag{4.22}$$

The equation (4.21) is valid for $\lambda_x \leq \lambda \leq \xi_{\parallel}$, whereas the equation (4.22) for $\lambda < \lambda_x$. The magnitude λ_x is defined as the intersection point of the two scaling ranges identified in the $C_z(\lambda)$ function, as shown in Fig. 4.10 [1]. H_m and H_M give information about the fractal scaling of the identified scale ranges, micro and macro scale, respectively.

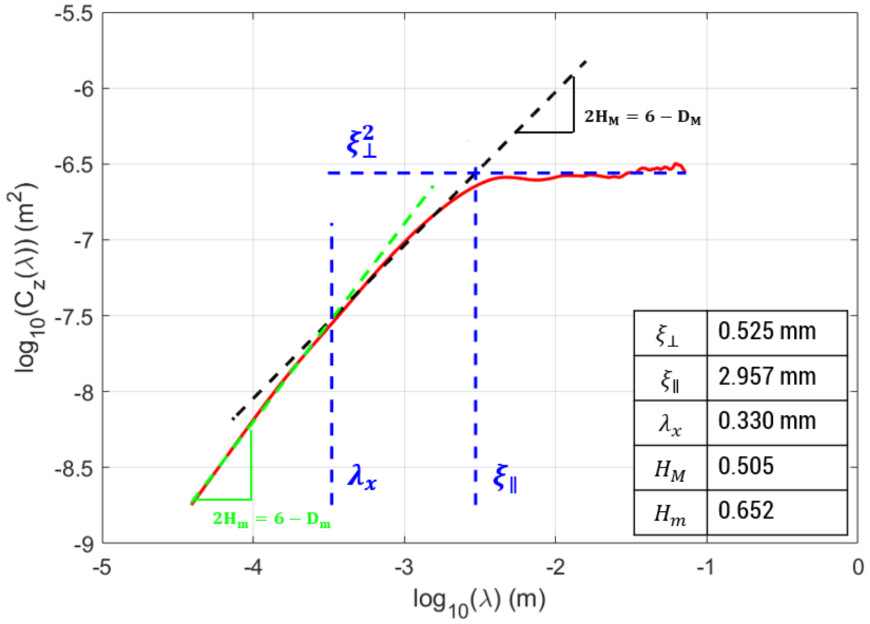

Fig. 4.10 HDC function for a two-scale roughness ranges profile

4.3.2 Power spectral density analysis for self-affine surfaces

The power spectral density (PSD) represents an alternative correlation function for describing self-affine rough surfaces [1, 14, 15, 55, 114]. For stationary surfaces, the Fourier-transform of $\Gamma_z(\lambda)$ equals the power spectral density $S(f)$, where f is the spatial frequency according to the Wiener-Khinchin Theorem [55]:

$$\Gamma_z(f) = \int_{f_{min}}^{\infty} S(f) e^{-2\pi i f \lambda} df \tag{4.23}$$

where the minimum frequency f_{min} is the inverse parallel correlation length, $\xi_{\parallel}$, and represents the maximum wavelength of the modulation surface ($f_{min} = \xi_{parallel}^{-1}$) [55].

For one scaling regime, the PSD is identified by three parameters: $\xi_{\perp}$, $\xi_{\parallel}$, and H. For a two-scale roughness ranges, the PSD is described by the following relationships [1, 116]:

$$S_M(\omega) = S_{M,0}\left(\frac{\omega}{\omega_{min}}\right)^{-\beta_M} \tag{4.24}$$

$$S_m(\omega) = S_{m,0}\left(\frac{\omega}{\omega_x}\right)^{-\beta_m} \tag{4.25}$$

The equation (4.24) is valid for $\omega_{min} \le \omega \le \omega_x$, whereas the equation (4.25) for $\omega_x < \omega$. For both equations, ω is defined as the frequency related to the wavenumber $\frac{1}{\lambda}$. The other magnitudes occurring in equations (4.24) and (4.25) are defined as follows:

$$S_{M,0} = \frac{(3 - D_M)\xi_{\perp}^2}{2\pi v \xi_{\parallel}} \tag{4.26}$$

$$S_{m,0} = \frac{(3 - D_M)\xi_{\perp}^2}{2\pi v \xi_{\parallel}}\left(\frac{\omega_x}{\omega_{min}}\right)^{-\beta_M} \tag{4.27}$$

In the equations defined above the following parameters appear:

- v, the sliding velocity of the rubber solid on the analysed substrate;
- $\beta_M = 2H_M + 1 = 7 - 2D_M$, the slope of the PSD for lower spatial frequency associated with the macro asperities;
- $\beta_m = 2H_m + 1 = 7 - 2D_m$, the slope of the PSD for higher spatial frequency associated with the micro asperities;
- $\omega_{min} = \frac{2\pi v}{\xi_{\parallel}}$, the smallest frequency related to the largest length scale $\xi_{\parallel}$;
- $\omega_x = \frac{2\pi v}{\lambda_x}$, the crossing frequency between macro and micro length scale.

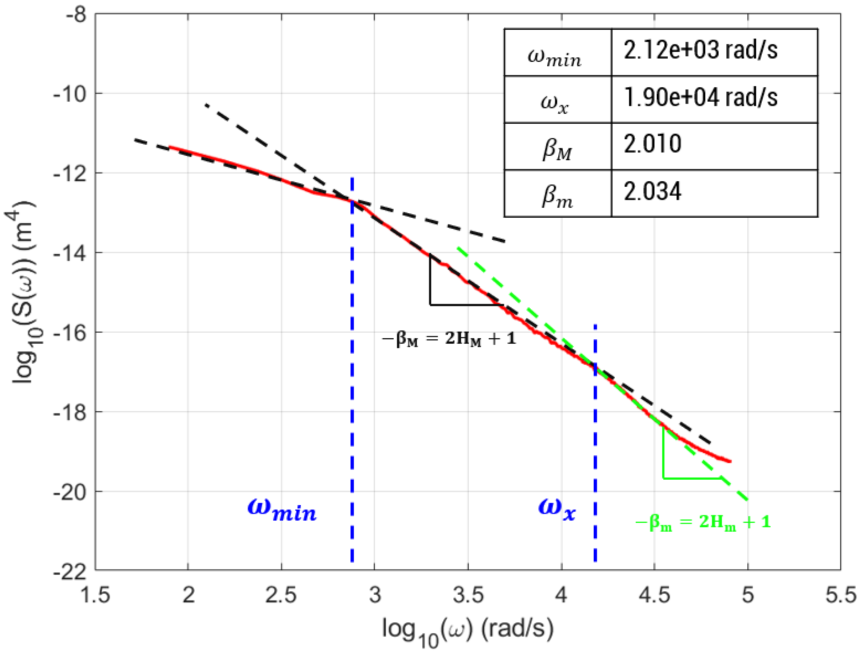

Fig. 4.11 PSD for a two-scale roughness ranges profile

Randomly rough surfaces, where the statistical properties are transitionally invariant, but not necessarily isotropic, are considered until this part of the analysis. In this case, complete information about the statistical properties of the surface is generally obtained by measuring the height profile over a square (or rectangular) surface area, i.e., a single line scan does not contain the full information about the statistical properties of the surface [2, 112].

Generally, the 2D power spectral density, C_{2D}, cannot be evaluated from 1D power spectral density (C_{1D}), unless in two cases:

- Isotropic surface roughness;
- 1D surface roughness;

In particular, in the case of a 2D isotropic surface roughness, the power spectral density is evaluated in this way [2, 117]:

$$C_{2D}(q) = \frac{1}{\pi}\int_q^\infty dq' \, \frac{[-C'_{1D}(q')]}{\sqrt{q'^2 - q^2}} \tag{4.28}$$

where q is the wavenumbers vector, determined as the inverse of the wavelengths vector according to the Persson’s nomenclature [2, 15, 112]. In Fig. 4.12, typical PSD curves are shown. The red curve is obtained by means of the application of the equation (4.28) on a full 2D self-affine surface; the green on is the result of the equation (4.28) on 1D self-affine data, determined as the averaged value over 850-line scans of the same 2D data.

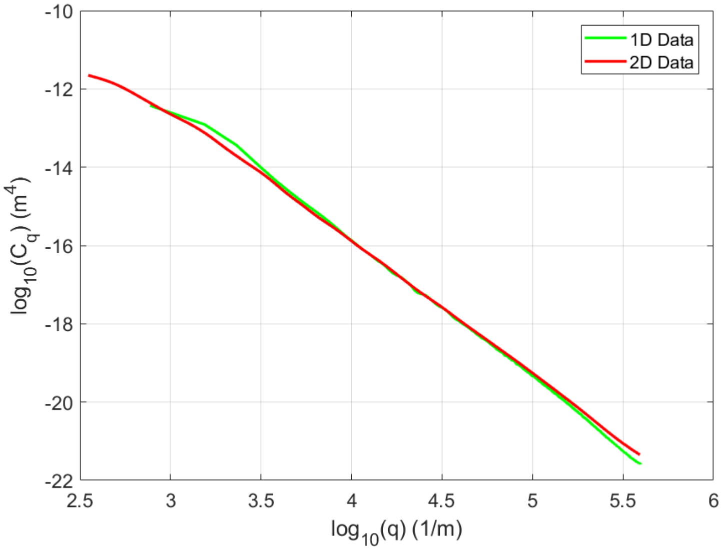

Fig. 4.12 PSD for a 2D surface data (red curve); PSD for a 1D surface data (green curve)

As noticeable, both procedures applied have returned the same results in terms of PSD for 1D and 2D self-affine data. Furthermore, the power spectral density is also evaluated by the following relationship, once chosen a specific direction [2] and it refers to the case where the surface is perfectly anisotropic:

$$C_{2D}(q) = C_{1D}(q_x)\delta(q_y) \tag{4.29}$$

In many applications the angular average of $C_{2D}(q)$ enters, which only depends on the magnitude q of the wave vector; in this case:

$$\bar{C}_{2D}(q) = \frac{C_{1D}(q)}{\pi q} \tag{4.30}$$

4.4 Minimum contact length identification for self-affine surfaces

In the rubber-substrate multiscale contact modelling for friction coefficient prediction, the knowledge of the minimum contact length λ_{min} plays a fundamental role, because this value identifies the cut-off wavelength of the micro-roughness scale until which the roughness spectrum must be taken into account [1, 13, 112]. If the evaluation of the macro wavelength can be easily entrusted to the analysis of the HDC or the PSD, as shown in Fig. 4.10 and Fig. 4.11, the same cannot be said for the minimum contact length.

4.4.1 Klüppel and Le-Gal theory for minimum contact length identification

In the literature, the Klüppel and Le-Gal theory for the identification of the minimum contact length between the rubber sample and substrate is one of the most known [1, 55, 115]. Their study is an extension of the Greenwood-Williamson theory [55, 118] to self-affine rough surfaces and, specifically, it assumes that a profile impacts with a rubber substrate and indents at a certain height d, as shown in Fig. 4.13.

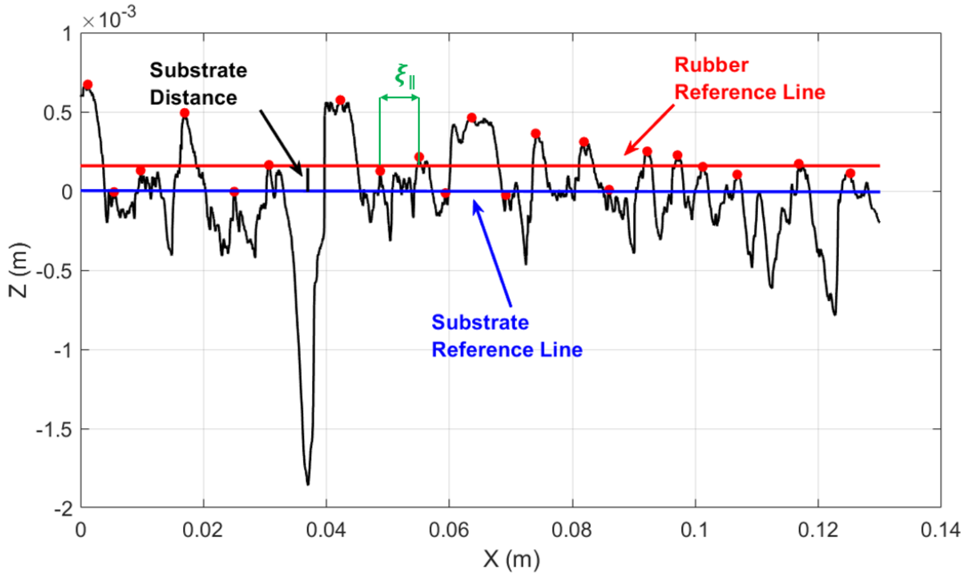

Fig. 4.13 Distance between the rubber and substrate reference lines

The magnitude d depends on the rubber properties and contact pressure according to the Greenwood-Williamson theory. Particularly, during the interaction between the two bodies, the roughness asperities will start to interact and a defined pressure will arise [119]:

$$P = \frac{4}{3} n_s \sqrt{R} |E^*(\omega_{min})| * F_{\frac{3}{2}}(d) \tag{4.31}$$

The equation (4.31) is based on the Hertzian contact between the rubber and the macro-asperities distanced according to the parallel correlation length, $\xi_{\parallel}$. Each contact asperity is assumed to be a spherical indenter of radius[120]:

$$R = \frac{3\sqrt{\pi}}{8\sqrt{m_4}} \tag{4.32}$$

In equation (4.31), the other magnitudes are defined as follows:

- $n_s = \frac{m_4}{6\pi\sqrt{3}m_2}$ is the summit density distribution, which depends on the second and fourth momenta of the roughness spectrum [1, 14, 120];

- $E^*(\omega_{min})$ is the complex dynamic modulus of the rubber determined at the simulation temperature and minimum solicitation frequency, defined as the ratio of the sliding velocity to the parallel correlation length, $\xi_{\parallel}$, obtained by means of the application of the HDC function. This viscoelastic property value can be estimated through the knowledge of the master-curve and the fitting coefficients of the William-Landel-Ferry relationship, as described in eq. (2.11);
- $F_{\frac{3}{2}}(d)$ is the Greenwood-Williams function $F_n(d)$ particularised into the form with the exponent $\frac{3}{2}$ [1]:

$$F_{3/2}(d) = \int_d^{\infty} (z-d)^{\frac{3}{2}} \phi(z) dx \tag{4.33}$$

where, the quantity $\phi(z)$is defined as the height distribution of the profile z.

For the identification of the minimum contact length, Klüppel and Le-Gal have introduced the summit heights distribution of a new profile, denoted as z_s [1]. As shown in Fig. 4.13, different asperities, considered as spherical indenters, are recognizable in the roughness profile z with a spacing frequency equal to $\xi_{\parallel}$. These asperities are characterised by a summit heights distribution, $\phi_s(z)$, with a non-null average value, contrary to $\phi(z)$, as shown in Fig. 4.14.

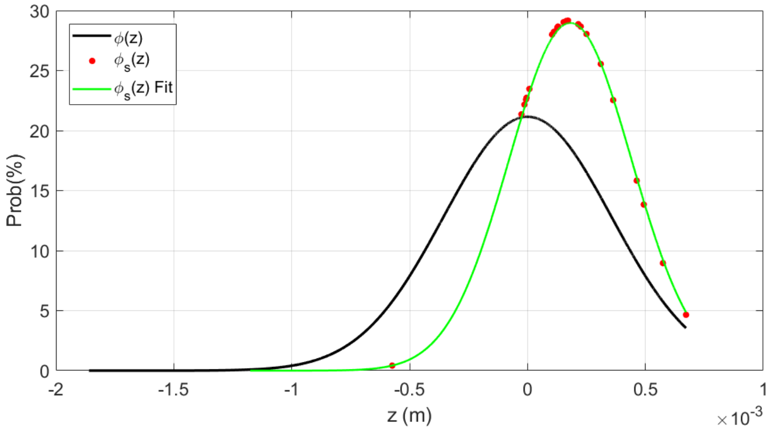

Fig. 4.14 Height density function and summit height density function

To define the new profile, z_s, an affine transformation of the original profile, z, can be applied by involving the affine parameter, s, which is characteristic for each rough profile [1, 55]. The affine transformation delivers for each height z of the substrate profile with height distribution $\phi(z)$ a corresponding height z_s for the summit height distribution $\phi_s(z)$ of macroscopic asperities as follows:

$$z_s = z_{max} + \frac{z - z_{max}}{s} \tag{4.34}$$

with z_{max} being the maximum height of the substrate. Considering that the mean value of the substrate height distribution $\phi(z)$ is zero, the average of the summit height distribution $\phi_s(z)$ is then given by:

$$\langle z_s \rangle = z_{max}\left(1 - \frac{1}{s}\right) \tag{4.35}$$

In addition, the standard deviation of the summit height distribution is linked with the origin standard deviation by the affine transformation parameter:

$$\sigma_s = \frac{\sigma}{s} \tag{4.36}$$

In praxis, to determine the affine parameter s, an algorithm has been developed which follows these steps:

1. a numerical procedure identifies the local maxima along the measured profiles which are equidistantly distributed within a distance $\xi_{\parallel}$. This length corresponds to the largest asperities, where the approach of Greenwood-Williamson is assumed to be valid;
2. the height distribution $\phi_s(z)$ of the macro asperities, which are assumed to be spherical indenter of radius R, is determined and is shifted compared to $\phi(z)$ distribution;
3. an iterative identification algorithm identifies the optimal value of the affine parameter s until the new distribution $\phi_s(z)$ of the new profile z_s is almost equal to the summit height distribution of the macro asperities. For asphalts, the affine parameter is usually equal to 1.4 [1].

According to this implemented algorithm, the green gaussian curve shown in Fig. 4.14 defines the height distribution of the new profile z_s obtained with an affine parameter $s = 1.36$. As noticeable the z_s distribution is almost equal to the summit heights one.

Once determined the affine transformation parameter of the profile, the minimum contact length can be determined as follows [1, 55]:

$$\frac{\lambda_{min}}{\xi_{\parallel}} \approx \left(\left(\frac{\lambda_x}{\xi_{\parallel}}\right)^{3(D_m - D_M)} \frac{0.09\pi s^{1.5}\xi_{\perp}F_0(t)|E^*(\omega_{max})|\tilde{n}_s}{\xi_{\parallel}|E^*(\omega_{min})|F_{3/2}(t_s)}\right)^{\frac{1}{3D_m-6}} \tag{4.37}$$

In the above equation, the only unknown parameter is λ_{min}, which occurs in both members of the relationship. Actually, ω_{max} is defined as the ratio of the sliding velocity of the rubber block to the minimum contact length. Therefore, the equation (4.37) can be solved as a problem specified in the form $F(\lambda_{min}) = 0$ at each simulation condition referring to the contact pressure, compound pressure and velocity of sliding. Further magnitudes must be explained for the resolution:

- $\tilde{n}_s = 6\pi\sqrt{3}\lambda_c^2 n_s$ where $\lambda_c = 10^{-10}$m is the lowest possible contact length, as given by the crossover from disordered fractal to ordered atomic length scale [1, 14, 120];
- $t = \frac{d}{\sigma}$ is the normalized gap distance d between rubber and substrate, referring to the standard deviation σ of the height distribution $\phi(z)$;
- $t_s = \frac{d_s}{\sigma_s}$, where d_s and σ_s are corresponding parameters of the summit height distribution $\phi_s(z)$ of macro asperities;
- $F_0(t)$ is the Greenwood-Williams function $F_n(t)$ particularised into the form with the exponent 0 [1], which displays the probability that the contact occurs above t:

$$F_0(t) = \int_t^{\infty} \phi(z)dx \qquad (4.38)$$

4.4.2 Application of the Klüppel and Le-Gal theory

Once analysed in-depth the Klüppel and Le-Gal theory, this procedure has been used for the identification of the micro contact length, which is useful for the rubber-substrate contact modelling for friction coefficient prediction as described in the next chapter.

To determine the goodness of the Klüppel and Le-Gal theory, two different SBR compounds have been chosen; particularly, sample 1 and sample 3 defined in Table 3-2. For each compound the viscoelastic properties are known in terms of 1 Hz master curves obtained by means of dual cantilever DMA, as shown in Fig. 4.15.

The time-temperature superposition principle is valid for these compounds taking into account the William-Landel-Ferry relationship coefficients provided in Table 3-2. The roughness profile chosen for the analysis is the same represented in Fig. 4.13. The corresponding height and summit height distributions determined with the affine parameter equal to 1.36 are shown in Fig. 4.14. Applying the equation (3.17) to the chosen profile, the function $C_{z(\lambda)}$ can be estimated, as shown in Fig. 4.16.

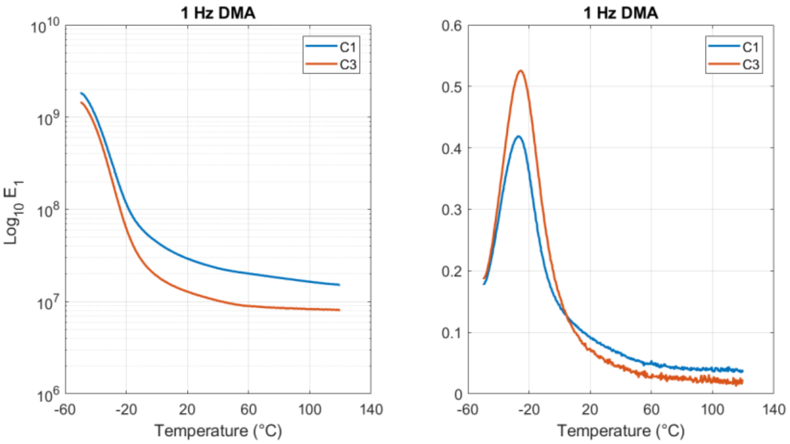

Fig. 4.15 Viscoelastic master curves for minimum contact length analysis

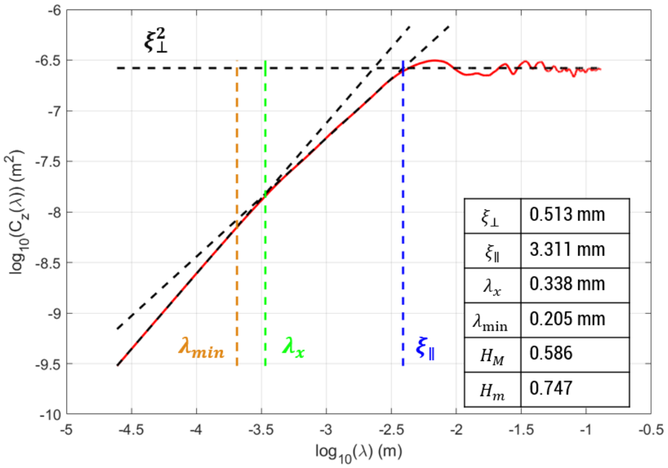

Fig. 4.16 HDC function for asphalt self-affine profile and roughness parameters

In the diagram shown in Fig. 4.16, the minimum contact length, λ_{min}, is also represented. This magnitude is determined by means of the equation (4.37) taking into account the HDC function output parameters, the values of the Greenwood-Williamson functions and the viscoelastic properties of the compound C3, choosing 0.01 m/s as sliding velocity, 100 kPa as contact pressure ad 25°C as compound temperature. These quantities are outlined in Table 4-1:

Table 4-1 Parameters for minimum contact length evaluation

Parameter	s	t	t_s	$F_0(t)$	$F_{3/2}(t_s)$	$\tilde{n}_s$	$E^*(\omega_{max})$	$E^*(\omega_{min})$
Value	1.36	0.954	0.811	0.169	0.114	0.234	4.45e7 (Pa)	2.53e7 (Pa)

Hence, applying the Klüppel and Le-Gal procedure, the minimum contact length for each compound can be determined at different contact pressure, compound temperature and sliding velocity values taking into account the same roughness profile. Thus, 3D surfaces can be generated for the ratio $\xi = \xi_{\parallel} \backslash \lambda_{min}$, denoted as magnification level, at different contact conditions.

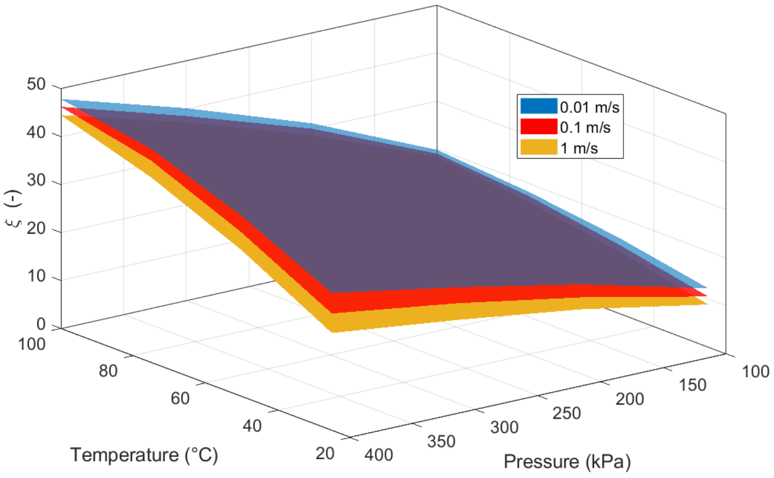

Fig. 4.17 Magnification values for compound C1

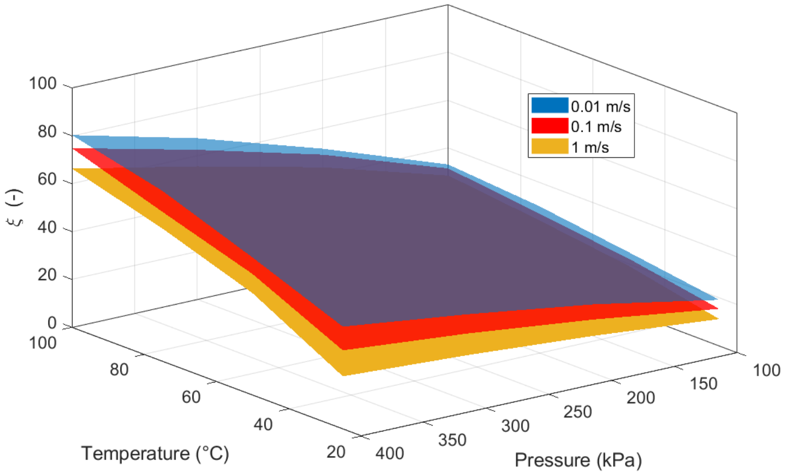

Fig. 4.18 Magnification values for compound C3

As globally shown in Fig. 4.17 and Fig. 4.18, the magnification depends on the specific working condition for the rubber on the substrate. Particularly, increasing the sliding velocity, the solicitation frequency for the compound is higher. This means the material will be glassier and the material deforms less encountering a lower number of micro asperities. The same phenomenon occurs decreasing the temperature, according to the time-temperature superposition, or decreasing the contact pressure.

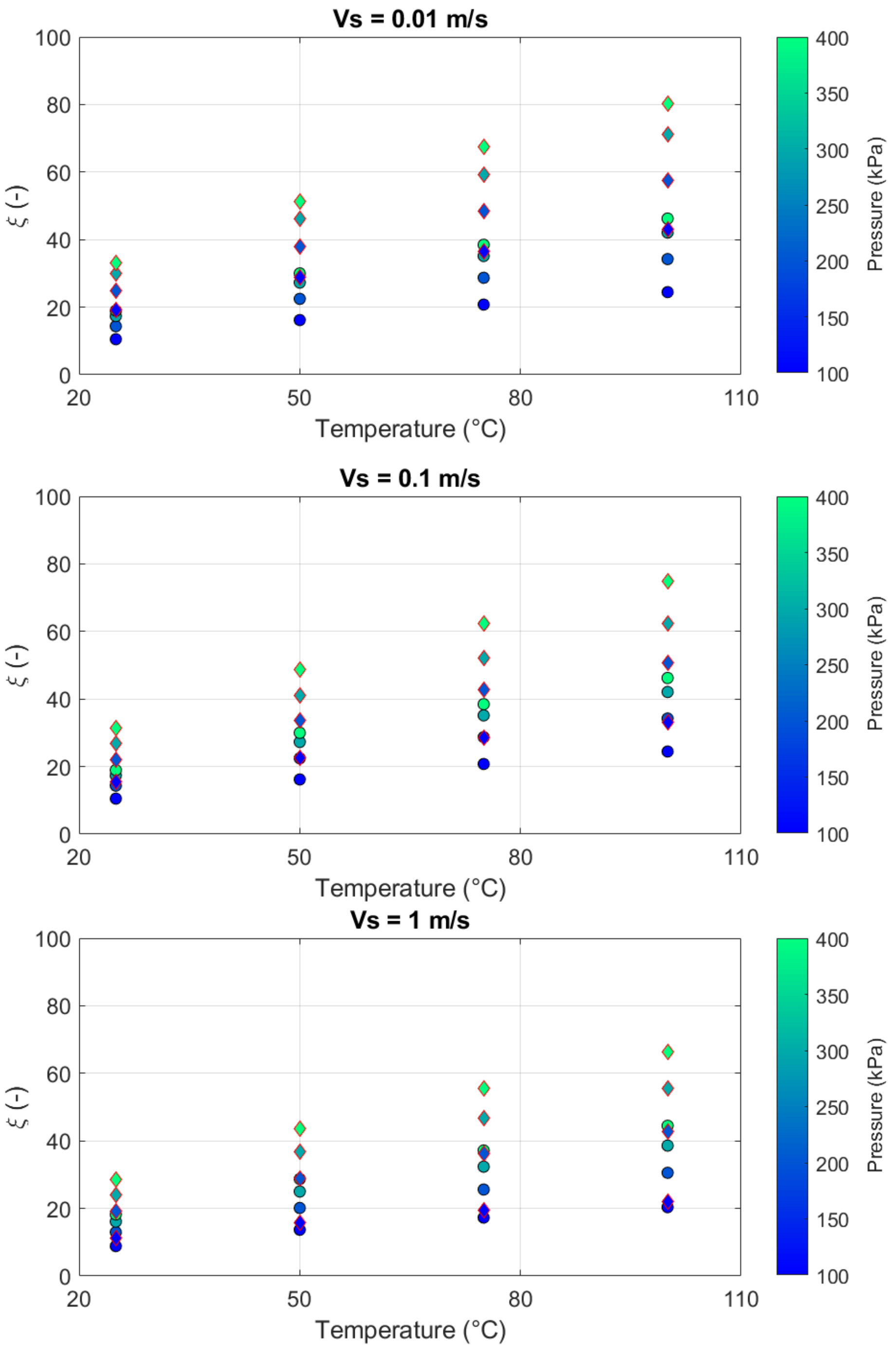

Fig. 4.19 Minimum contact length as function of pressure and temperature: compound C1 (circular markers) ; compound C3 (diamond markers)

Furthermore, it is noticeable how the minimum contact length depends on the viscoelastic properties: in the case of compound C3, which exhibits lower storage modulus in the simulation working range rather than compound C1, higher values of the magnification level have been identified. In addition, the iso-pressure magnification values towards the temperature shown in Fig. 4.19 highlight in-depth the minimum contact length differences between the two compounds.

4.4.3 Persson's approach for the minimum contact length identification

The Persson's theory [2, 13, 16], as described in-depth in the next chapter, seems to have evolved more rigorously in the contact mechanics treatment (they are approximate, but these approximations have been corrected over the years). Contrariwise the Klüppel's, which seem to remain attached to the Greenwood-Williamson asperities description of roughness, Persson has proposed a new empirical solution for the problem of the truncation of roughness at microscales. Particularly, for a self-affine roughness profile, the following magnitude is introduced:

$$h_{rms}^2 = \frac{1}{2\pi}\int_{q_{min}}^{\infty} C_{2D}(q)q\,dq \tag{4.39}$$

where $C_{2D}(q)$ is the power spectrum density of the self-affine profile, q is the space wavenumber vector and q_{min} is the smallest feasible space wave number associated to the macro asperities wavelength. The equation (4.39) determines the root mean square slope of the profile. Taking into account this relationship, Persson defines q_{max} as the highest space wavenumber of the power spectrum density of the self-affine profile at which corresponds the rms slope value of 1.3:

$$h_{rms}^2 = 1.3 = \frac{1}{2\pi}\int_{q_{min}}^{q_{max}} C_{2D}(q)q\,dq \tag{4.40}$$

However, as pointed out in [13], fundamental questions on the physical meaning of this quantity and on the role that it plays in modern theories of viscoelastic friction have been posed.

To demonstrate the limited goodness of this method of truncation of roughness scale, different parameters set, shown in Table 4-2, have been chosen in order to feed up the equation for the evaluation of hysteretic contribution to friction coefficient [13] taking into account the same power spectrum density of the roughness surface and viscoelastic properties of the sliding compound used by Persson [121].

Table 4-2 Summary of parameters set for friction calculation

SET	**A**	**B**	**C**	**D**	**E**
q_{max}	2e9	2e6	2e7	2e5	3e4
h'_{rms}	3.6	1.3	1.85	0.9	0.63

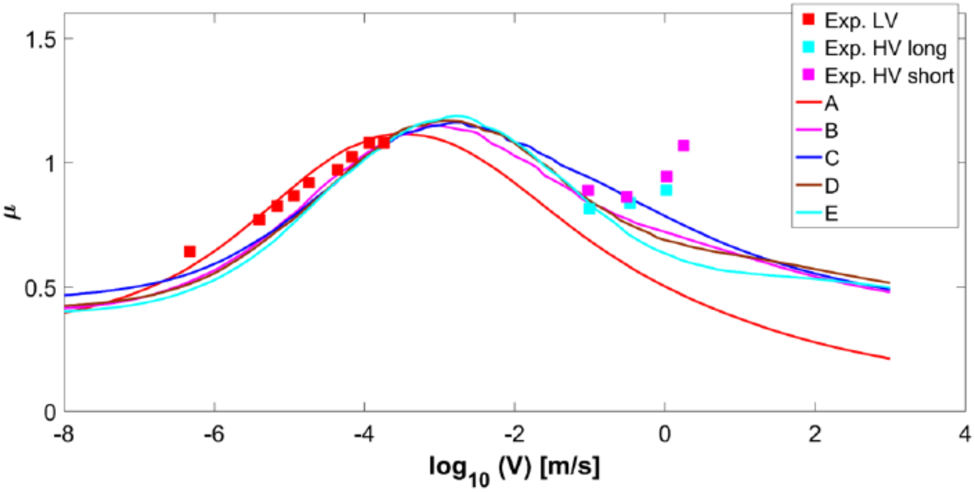

Fig. 4.20 Measured grip values [121] and calculated friction coefficient with different parameters sets

In Fig. 4.20, the friction coefficient curves together with the experimental grip values are shown. The grip data are presented as square markers and they were acquired at different velocity ranges according to the experimental bench described in [121]. All the proposed fit corresponding at each parameter set predict quite accurately the low-velocity experimental data, while at high velocities the goodness is generally poor. Furthermore, it is noticeable that almost equally good friction curves are estimated by varying the high-wavenumber cut-off q_{max} of several orders of magnitude. Particularly, the parameters set A, characterized by the highest wavenumber chosen form PSD, has returned a better fitting of the grip experimental data compared to the set B, where the Persson's approach for the cut-off q_{max} estimation has been applied. For these reasons, it seems unclear how to rigorously truncate the $C_{2D}(q)$ curve for friction coefficient prediction in the proposed theory.

To sum up, the approaches outlined in this paragraph pointed out how the identification of the minimum contact length is still an unsolved problem in terms of friction coefficient prediction. The Persson's theory, as previously discussed, proposes a purely empirical result based on the acquired experimental grip data without taking into account the rubber behaviour changes while reducing the roughness asperities scale. On the other hand, the Klüppel and Le-Gal approach is based on modified version of the Greenwood-Williams asperity description of roughness, considering the evaluation of the minimum contact length through the HDC function. The analysis proposed in this paragraph has actually highlighted that the choice of the cut-off length is an opened and very debated question: this magnitude is strongly related to the chemical changes occurring on the very superficial rubber layer, which in turn depend on the stress-temperature acting on this zone. On the other side, there are no mechano-chemical respected descriptions and models of the rubber structural and chemical surface evolution and thus, scientists have been proposing different approaches in the corresponding literature.

In this scenario, being still struggling the microscale roughness truncation procedure, the author has proposed a new empirical magnification level for the truncation of the HDC or PSD curves for the friction coefficient prediction by means of the tyre block-track contact model proposed in the next chapter, which has led to interesting grip results in comparison to the acquired experimental data.

Chapter 5

Tyre-road contact modelling approaches: multiscale theories for friction prediction

5.1 Introduction to the Contact Mechanics problem

The Contact Mechanics and the physics of friction are fundamental disciplines of the engineering sciences [109], i.e., Vehicle Dynamics, where the knowledge of the friction coefficient plays a key role in the improvement of driving safety and performance at each driving condition (dry, wet, ice or worn tyres, etc…) [54, 112].

Friction leads to energy dissipation and in micro-contacts, where extreme stress occurs, to micro-fractures and surface wear. Friction is usually minimized during the design to save energy, but it is necessary in different applications: without friction, it is impossible to walk or to drive, for example. However, in many situations, it is necessary to maximize friction like between tyres and road during braking or cornering manoeuvres [19, 52].

Friction and wear are very closely connected with the phenomenon of adhesion. While adhesion does not play a considerable role on a large scale in the contact between two bodies, such as metal or wood, in instances in which one of the bodies in contact is soft, the role of adhesion becomes very noticeable and can be taken advantage of in many applications [109].

In the scientific literature, many theories of contact mechanics and friction modelling have been proposed [13]. After the fundamental study by Grosch [122, 123], who took advantage of the other essential analysis of William, Landel and Ferry [4], which relates temperature and rate dependence of viscoelastic properties, two main theories appeared: the Klüppel-Heinrich & Le-Gal [1, 114] and the Persson [15, 16] theories, both concentrating heavily on the multiscale nature of surfaces and their fractal roughness, which introduced more than one complication.

In this chapter, the scenario of these most recent known theories describing the contact between two bodies will be analysed and compared to the friction model results, called GrETA [52, 54], developed during the research activities at the Department of Industrial Engineering at the University of Naples Federico II.

5.2 Rubber friction

By the 1960s, it had been widely accepted that two distinguishable friction mechanisms develop in rubber: (1) adhesion F_A and (2) bulk deformation hysteresis F_H [124]. Rubber friction is not associated with abrasion.

Particularly, Kummer [125] proposed a model for tyres that takes the following form:

$$F_T = F_A + F_H + F_C \tag{5.1}$$

where:

- F_T is total frictional resistance developed between a sliding tyre and pavement;
- F_A is the frictional contribution from combined van der Waals' adhesion of the two surfaces;
- F_H is the frictional contribution from bulk deformation due to hysteresis in the rubber block;
- F_C is the cohesion loss contribution from rubber wear, which is almost irrelevant.

Kummer postulated that F_A and F_H are not entirely independent of each other because adhesion can increase the extent of rubber draping over a chip beyond what F_H would produce.

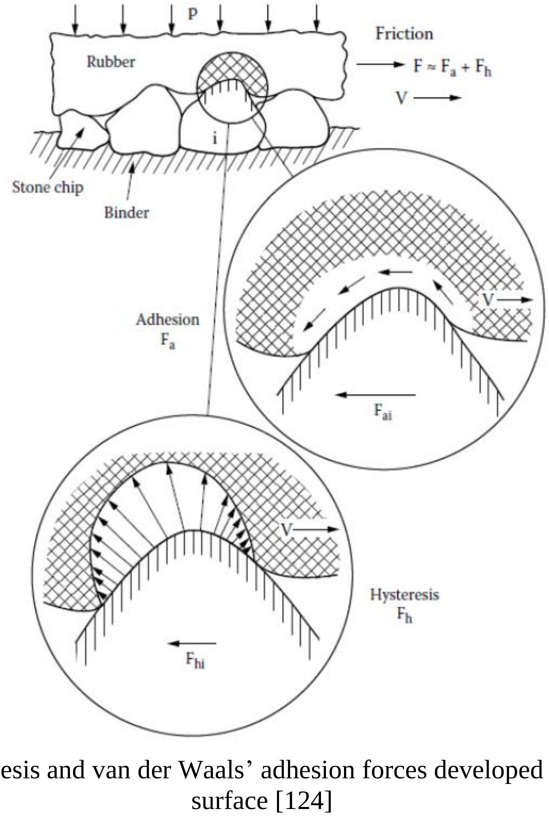

Fig. 5.1 Bulk deformation hysteresis and van der Waals' adhesion forces developed between rubber tyres and road surface [124]

Savkoor [126] agreed with Bartenev and Lavrentjev that adhesion in rubber arises almost totally from van der Waals' forces. These forces are weaker than the atom-to-atom adhesion found in metals. Savkoor formulated equations expressing the adhesive force component of rubber friction based on the energy required to break the van der Waals' bonds.

Besides, Tabor [127] made different studies on the rubber rolling resistance and stated that this mechanism was linked to the hysteresis in the rubber, the "bulk deformation hysteresis" arose when the rolling cylinders or spheres, used in his experiments, compressed or stretched the rubber elastically. The rubber then experienced elastic release as the rolling objects moved out of contact. Such compression or extension resulted in energy losses, constituting a hysteretic deformational friction component. Because a portion of the bulk of the rubber was involved, bulk deformation hysteresis was the operative mechanism [124].

The bulk hysteretic losses elucidated by Tabor constitute a basic friction force developed in rubber. When this rolling or sliding mechanism is experienced by rubber in contact with smooth surfaces, it is often seen that negligible permanent deformation occurs. Consequently, such deformation can take place without significant wear. When wear in a rubber material does occur, the friction associated ascribed to another mechanism: cohesion losses.

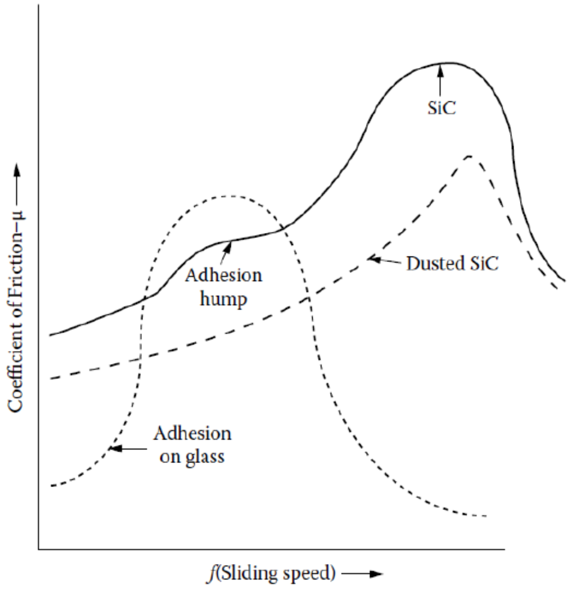

SiC = Silicon carbide

Fig. 5.2 Generalized master curves showing concurrent development of adhesion bulk deformation hysteresis in rubber samples [124]

5.3 Hertzian contact theory

The most simple case that can be analysed is the contact between two spheres [128, 129]. Starting from this problem the contact sphere-plane can be deduced by imposing an infinite radius of curvature to one of the two spheres.

The displacement of the points on the surface in the contact area between an originally even surface and a rigid sphere of radius R is equal to:

$$u_z = d - \frac{r^2}{2R} \tag{5.2}$$

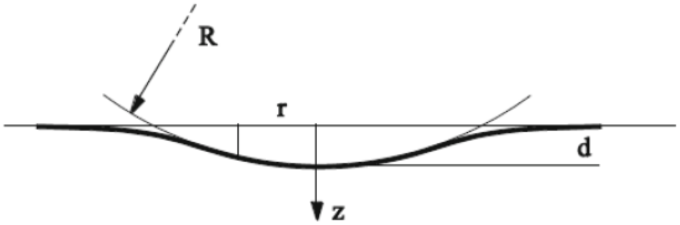

Fig. 5.3 A rigid sphere in contact with an elastic half-space [128]

For a quadratic pressure distribution (see Fig. 5.4) such as:

$$p = p_0 \sqrt{1 - \frac{r^2}{a^2}} \tag{5.3}$$

The vertical displacement is equal to:

$$u_z = \frac{\pi p_0}{4E^* a}(2a^2 - r^2) \tag{5.4}$$

which is valid for $r \leq a$ and where:

$$\frac{1}{E^*} = \frac{1 - \nu_I^2}{E_I} + \frac{1 - \nu_{II}^2}{E_{II}} \tag{5.5}$$

In equation (5.5), E_I and ν_I denote the dynamic modulus and Poisson's coefficient of the indented substrate; E_{II} and ν_{II} denote the dynamic modulus and Poisson's coefficient of the spherical indenter. Taking into account the latter as infinitely rigid compared to the plane substrate, the (5.5) can be simplified as follows:

$$\frac{1}{E^*} = \frac{1 - \nu_I^2}{E_I} \tag{5.6}$$

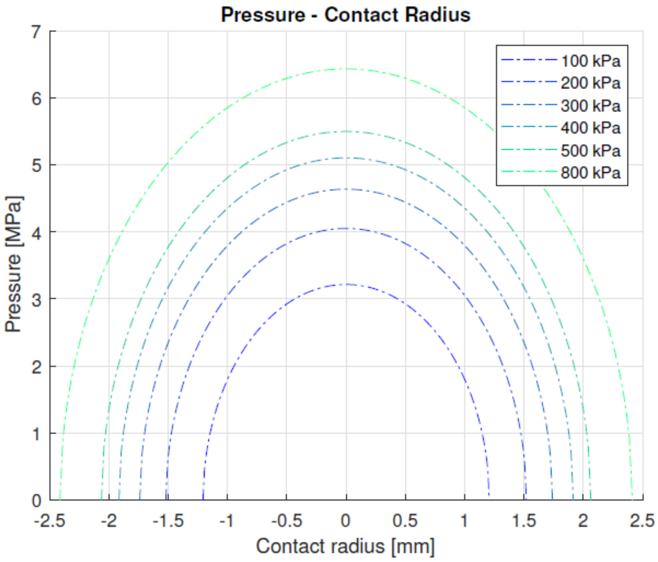

Fig. 5.4 Hertzian quadratic pressure distribution

By imposing equality between (5.2) and (5.4) the contact radius is estimated as:

$$a = \frac{\pi p_0 R}{2E^*} \tag{5.7}$$

and the indentation depth, d, is obtained as:

$$d = \frac{\pi a p_0}{2E^*} \tag{5.8}$$

Thanks to equations (5.7) and (5.8), the maximum contact pressure is defined as follows:

$$p_0 = \frac{2}{\pi} E^* \sqrt{\frac{d}{R}} \tag{5.9}$$

and the contact radius – indentation depth relationship is derived:

$$a^2 = dR \tag{5.10}$$

Substituting the equation (5.10) in the (5.9), the normal force during the contact is evaluated:

$$F = \frac{4}{3} E^* R^{0.5} d^{1.5} \tag{5.11}$$

The maximum pressure and the contact radius can be also written as function of the normal force:

$$p_0 = \sqrt[3]{\frac{6F{E^*}^2}{\pi^3 R^2}} \tag{5.12}$$

$$a = \sqrt[3]{\frac{3FR}{4E^*}} \tag{5.13}$$

It is also possible to determine the expression for the potential energy of the elastic deformation U. Since $-F = \frac{\partial U}{\partial d}$, the following expression is obtained:

$$U = \frac{8}{15} E^* R^{0.5} d^{2.5} \tag{5.14}$$

Finally, it can be interesting to focus on the friction coefficient. It is assumed that the frictional force F_T is proportional to the area of contact $A_r = \pi a^2$ and the shear strength, χ. The frictional force is, then, expressed by [130]:

$$F_T = \chi A_r = \chi \pi R d \tag{5.15}$$

The friction coefficient μ_H is calculated using the equation (5.11) and (5.15):

$$\mu_H = \frac{F_T}{F} = \pi \chi \left(\frac{3R}{4E^*}\right)^{\frac{2}{3}} W^{-\frac{1}{3}} \tag{5.16}$$

5.3.1 Interior stress field

For the case of purely normal indentation, where there is axis-symmetry, the calculation may profitably be carried out in cylindrical coordinates; in the case of a sliding sphere (or a sliding rubber compound and fixed substrate), this problem is better treated in Cartesian coordinates as there is no longer axis-symmetry [129]. Hamilton and Goodman [53, 131] used this technique, but they presented equations which required taking the imaginary part of functions. Explicit equations were given later by Hamilton [132] and Sackfield-Hills [128] and they are reproduced here [129]. The apex "N" states for a stress field due to only normal indentation force of a sphere on a rubber substrate; contrariwise, the apex "T" is used to denote that stress field is arisen from a tangential force of a sphere sliding on a rubber substrate with a constant maximum contact pressure p_0, which is estimated by means of Hertz's theory.

$$\begin{aligned}\frac{\sigma_{xx}^N}{p_0} = {} & \frac{(1-2\nu)}{3r^4}(x^2 - y^2)\left(1 - \frac{z^3}{u^3}\right) \\ & + \frac{z}{u}\left[(1+\nu)u \arctan(u^{-1}) - 2\nu - \frac{(1-\nu)u^2}{1+u^2} - \frac{(1-2\nu)x^2}{r^2(1+u^2)} \right. \\ & \left. - \frac{x^2 u^4}{(1+u^2)^2(u^4+z^2)}\right]\end{aligned} \tag{5.17}$$

$$\begin{aligned}\frac{\sigma_{yy}^{N}}{p_0} = \frac{(1-2\nu)}{3r^4}(x^2-y^2)\left(\frac{z^3}{u^3}-1\right) \\ &+\frac{z}{u}\left[(1+\nu)u\arctan(u^{-1})-2\nu-\frac{(1-\nu)u^2}{1+u^2}-\frac{(1-2\nu)y^2}{r^2(1+u^2)}\right. \\ &\left.-\frac{y^2u^4}{(1+u^2)^2(u^4+z^2)}\right]\end{aligned} \tag{5.18}$$

$$\frac{\tau_{xy}^{N}}{p_0} = -\frac{xyzu^3}{(1+u^2)^2(u^4+z^2)}+(1-2\nu)J \tag{5.19}$$

$$\frac{\sigma_{zz}^{N}}{p_0} = -\frac{z^3}{u(u^4+z^2)}+(1-2\nu)J \tag{5.20}$$

$$\frac{\tau_{xz}^{N}}{p_0} = -\frac{xz^2u}{(1+u^2)\,(u^4+z^2)} \tag{5.21}$$

$$\frac{\tau_{yz}^{N}}{p_0} = -\frac{yz^2u}{(1+u^2)\,(u^4+z^2)} \tag{5.22}$$

$$\frac{\sigma_{xx}^{T}}{\mu p_0} = -\left[\frac{\sigma_{yy}^{T}}{fp_0}+\frac{\sigma_{zz}^{T}}{fp_0}\right]-x(1+\nu)\left[\arctan(u^{-1})-\frac{u}{1+u^2}\right] \tag{5.23}$$

$$\begin{aligned}\frac{\sigma_{yy}^{T}}{\mu p_0} = 2\nu x\left[\frac{3}{8}\arctan(u^{-1})+\frac{u}{4(1+u^2)^2}+\frac{3u}{8(1+u^2)}-\frac{y^2u^5}{(1+u^2)^3(u^4+z^2)}\right] \\ &+(1-2\nu)z\left(\frac{\partial J}{\partial y}\right)\end{aligned} \tag{5.24}$$

$$\frac{\sigma_{zz}^{T}}{\mu p_0} = -\frac{xz^2u}{(1+u^2)(u^4+z^2)} \tag{5.25}$$

$$\frac{\tau_{yz}^{T}}{\mu p_0} = -\frac{xyzu^3}{(1+u^2)(u^4+z^2)} \tag{5.26}$$

$$\frac{\tau_{yz}^{T}}{\mu p_0} = -\frac{xyzu^3}{(1+u^2)(u^4+z^2)} \tag{5.27}$$

$$\frac{\tau_{xz}^{T}}{\mu p_0} = z\left[\frac{3}{2}\arctan(u^{-1})-\frac{1}{u}-\frac{u}{2(1+u^2)}-\frac{x^2u^3}{(1+u^2)^2(u^4+z^2)}\right] \tag{5.28}$$

$$\begin{aligned}\frac{\tau_{xy}^{T}}{\mu p_0} = 2\nu y\left[\frac{1}{8}\arctan(u^{-1})-\frac{u}{8(1+u^2)}+\frac{u}{4(1+u^2)^2}-\frac{x^2u^5}{(1+u^2)^3(u^4+z^2)}\right] \\ &-\frac{y}{2}\left[\arctan(u^{-1})-\frac{u}{1+u^2}\right]+(1-2\nu)z\left(\frac{\partial J}{\partial y}\right)\end{aligned} \tag{5.29}$$

Where the following parameters appear:

$$r^2 = x^2 + y^2 \tag{5.30}$$

$$J = \frac{xy}{3r^4}\left[\left(\frac{z}{u}\right)^3 - 3\left(\frac{z}{u}\right) + 2\right] \tag{5.31}$$

$$\frac{\partial J}{\partial x} = J\frac{y^2 - 3x^2}{xr^2} + \frac{ux^2yz}{r^2(u^4 + z^2)(1 + u^2)} \tag{5.32}$$

$$\frac{\partial J}{\partial y} = J\frac{x^2 - 3x^2}{yr^2} + \frac{uy^2xz}{r^2(u^4 + z^2)(1 + u^2)} \tag{5.33}$$

$$u^2 = \frac{1}{2}\left\{r^2 + z^2 - 1 + \sqrt{[(r^2 + z^2 - 1)^2 + 4z^2]}\right\} \tag{5.34}$$

On the axis of symmetry, for $x = y = 0$ the stress components due to normal loading are:

$$\frac{\sigma_{xx}^N}{p_0} = \frac{\sigma_{yy}^N}{p_0} = (1 + \nu)[1 - z\arctan(z^{-1})] - \frac{1}{2(1 + z^2)} \tag{5.35}$$

However, on the surface within the contact disk the stresses are:

$$\frac{\sigma_{xx}^N}{p_0} = \frac{1}{r^2}\left\{\frac{y^2 - x^2}{r^2}\ \frac{1 - 2\nu}{3}\left[(1 - r^2)^{3/2} - 1\right] - (x^2 + 2\nu y^2)\sqrt{1 - r^2}\right\} \tag{5.36}$$

$$\frac{\sigma_{yy}^N}{p_0} = \frac{1}{r^2}\left\{\frac{x^2 - x^2}{r^2}\ \frac{1 - 2\nu}{3}\left[(1 - r^2)^{3/2} - 1\right] - (y^2 + 2\nu x^2)\sqrt{1 - r^2}\right\} \tag{5.37}$$

$$\frac{\tau_{xy}^N}{p_0} = -\frac{(1 - 2\nu)xy}{r^2}\left\{\sqrt{1 - r^2} + \frac{2}{3r^2}\left[(1 - r^2)^{\frac{3}{2}} - 1\right]\right\} \tag{5.38}$$

$$\tau_{zy}^N = \tau_{xz}^N = 0 \tag{5.39}$$

And, outside the contact patch:

$$\frac{\sigma_{xx}^N}{p_0} = \frac{(1 - 2\nu)(x^2 - y^2)}{3r^4} \tag{5.40}$$

$$\frac{\sigma_{yy}^N}{p_0} = \frac{(1 - 2\nu)(x^2y^2)}{3r^4} \tag{5.41}$$

$$\frac{\tau_{yx}^N}{p_0} = \frac{2xy(1 - 2\nu)}{3r^4} \tag{5.42}$$

$$\tau_{zy}^N = \tau_{xz}^N = 0 \tag{5.43}$$

Turning on tangential loading due to sliding contact, this produces only one non-zero component on the z-axis, i.e.:

$$\frac{\tau_{zx}^{T}}{\mu p_0} = \frac{3}{2} z \arctan\left(\frac{1}{z}\right) - 1 - \frac{z^2}{2(1+z^2)} \tag{5.44}$$

Inside the contact patch, on the surface, the following stress components due to tangential loading are non-zero:

$$\frac{\sigma_{xx}^{T}}{\mu p_0} = -\frac{\pi}{2} x \left(1 + \frac{\nu}{4}\right) \tag{5.45}$$

$$\frac{\sigma_{yy}^{T}}{\mu p_0} = -\frac{3\pi \nu x}{8} \tag{5.46}$$

$$\frac{\tau_{yx}^{T}}{\mu p_0} = \frac{\pi y}{4}\left(\frac{\nu}{2} - 1\right) \tag{5.47}$$

$$\frac{\tau_{zx}^{T}}{\mu p_0} = -\sqrt{1 - r^2} \tag{5.48}$$

Lastly, on the surface outside the contact the following non-zero stress components due to tangential loading arise:

$$\frac{\sigma_{xx}^{T}}{\mu p_0} = \frac{x}{r^4}\left\{2(r^2 + \nu y^2)F_0 + \nu\left[3 - 4\left(\frac{x}{r}\right)^2\right]H_0\right\} \tag{5.49}$$

$$\frac{\sigma_{yy}^{T}}{\mu p_0} = -\frac{\nu x}{r^4}\left\{2x^2 F_0 + \left[1 - 4\left(\frac{y}{r}\right)^2\right]H_0\right\} \tag{5.50}$$

$$\frac{\tau_{yx}^{T}}{\mu p_0} = \frac{y}{r^4}\left\{2(r^2 - \nu x^2)F_0 + \nu\left[1 - 4\left(\frac{x}{r}\right)^2\right]H_0\right\} \tag{5.51}$$

where:

$$F_0 = -\frac{1}{2}\sqrt{r^2 - 1} + \frac{1}{2} r^2 \arctan\left(\frac{1}{\sqrt{r^2 - 1}}\right) \tag{5.52}$$

$$H_0 = -\frac{1}{2}\sqrt{(r^2 - 1)^3} + \frac{1}{2} r^4 \arctan\left(\frac{1}{\sqrt{r^2 - 1}}\right) - \frac{1}{4} r^2 \sqrt{r^2 - 1} \tag{5.53}$$

These relationships have been employed into the GrETA model for the friction coefficient estimation during the sliding of rubber block on a concrete substrate. Before applying this relationship, they have been validated with a numerical model [53] taking into account a suitable compound control volume according to the Sackfield and Hills hypothesis [128], as described in the following paragraphs.

5.4 Klüppel's multiscale contact model

The method used by Klüppel and Heinrich [1, 14] refers to the fractal scaling behaviour of many rough substrates and the linear viscoelastic response of the rubber [55]. Particularly, it considers hysteresis and adhesion contributions during sliding on rough substrates, whereby micro and macro roughness are taken.

5.4.1 Klüppel's theory: Hysteresis friction calculation

The hysteresis friction appears when local asperities deform the rubber sample and cause internal energy losses. According to the theory of Klüppel and Heinrich, this friction coefficient is obtained by integrating over a range of excitation frequencies corresponding to multiscale indentation mechanics during the sliding process:

$$\mu_{hys}(v_s) = \frac{F_{hys}}{F_N} = \frac{\langle \delta \rangle}{2\sigma_0 v_s} \int_{\omega_{min}}^{\omega_{max}} \omega E''(\omega) S(\omega) d\omega \qquad (5.54)$$

where:

- v_s is the sliding velocity;
- σ_0 is the normal stress during the indentation of the rubber on the substrate;
- $S(\omega)$ is the power spectral density of the road;
- $\langle \delta \rangle$ is the mean layer thickness of the excited volume V, which is assumed to increase linearly with the mean penetration depth $\langle z_p \rangle$ of the asperities in the rubber sample, scaled with a free parameter b.

As demonstrated in [14], a direct proportionality between the penetration depth and the normal stress subsists:

$$\langle z_p \rangle = \frac{\pi \xi_{\parallel}}{E'(\omega_{min})} \sigma_0 \qquad (5.55)$$

This results from a combined effect of the local non-linear increase of penetration depth with the normal stress according to the Hertz theory and the formation of new contact spots with increasing $\langle z_p \rangle$ [133][118, 133]. Therefore, the mean layer thickness is determined as:

$$\langle \delta \rangle = \frac{V}{A_0} = b \langle z_p \rangle \qquad (5.56)$$

where the parameter b depends on the strain percentage during the indentation [116], as shown in Fig. 5.5, in which the value of $\langle z_p \rangle$ is calculated at different stages during the indentation process.

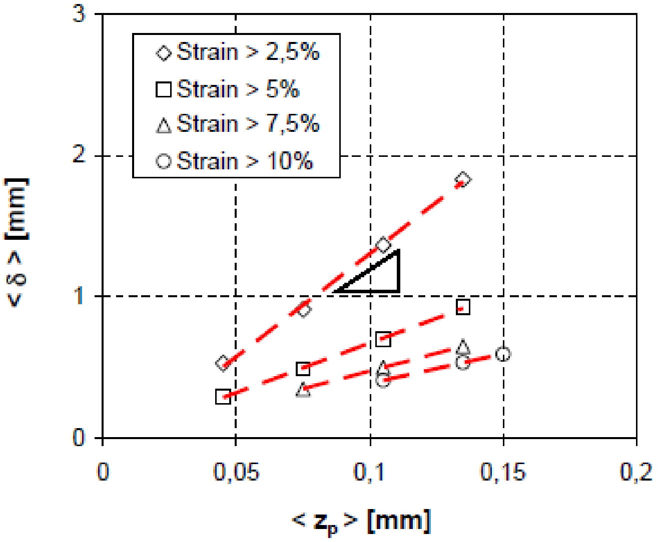

Fig. 5.5 Mean deformed layer as function of the mean depth. The slope displays the free parameter b [55]

In the case of two roughness scaling ranges, the equation (5.55) turns into the following:

$$\mu_{hys}(v_s) = \frac{F_{hys}}{F_N} = \frac{\langle \delta \rangle}{2\sigma_0 v_s} \left[\int_{\omega_{min}}^{\omega_x} \omega E''(\omega) S(\omega) d\omega + \int_{\omega_x}^{\omega_{max}} \omega E''(\omega) S(\omega) d\omega \right] \qquad (5.57)$$

Referring to the equation above, the macro-scale regime value only depends on the sliding velocity, while the micro-scale regime value is load and temperature-dependent because $\omega_{min} = 2\pi v_s \backslash \lambda_{min}$, where $\lambda_{\backslash min}$ is calculated according to the equation (4.37).

5.4.2 Klüppel's theory: Adhesion friction calculation

According to Klüppel's theory [1, 115], the adhesion friction contribute to the total friction is determined by the following expression:

$$\mu_{adh} = \frac{F_{adh}}{F_N} = \frac{\tau_s(v_s)}{\sigma_0} \frac{A_c(v_s, T, \sigma_0)}{A_0} \qquad (5.58)$$

In the above relationship, τ_s is the shear stress acting in the real contact area and depends on sliding velocity and viscoelastic properties of the compound. This stress is determined as follows:

$$\tau_s(v_s) = \tau_{s_0} \left(1 + \frac{\frac{E_\infty}{E_0}}{\left(1 + \frac{v_c}{v_s}\right)^n} \right) \qquad (5.59)$$

In equation (5.59) the following magnitudes are displayed:

- v_c is the critical velocity above which τ_s converges to a plateau value;
- E_∞/E_0 is the ratio of the dynamic modulus between glassy and rubbery state;
- τ_{s_0} is the shear stress at slow velocity. This magnitude is determined by the peeling length l_s and the interfacial energy γ_{rs} between the rubber and the substrate [114];
- n is the exponent gained from the power law behaviour of the relaxation time spectra $H(\tau)$ in the glass transition range, $H{\sim}\tau^m$, with exponent $0 < m < 1$:

$$n = \frac{1-m}{2-m} \tag{5.60}$$

In [114], Klüppel pointed out that the critical velocity v_c strongly depends on the glass transition temperature T_g of the rubber and the amount of filler. A crude estimate of v_c cam be obtained with an approach proposed by Persson [134], which is based on the relaxation time spectra for the glass transition according to the Rouse model and it yields:

$$v_c \approx v_0 \left(\frac{E_\infty}{E_0}\right)^3 \tag{5.61}$$

Here, $v_0 = a_0/(2\pi\tau_0)$ depends on an atomic cut-off length $a_0 \approx 10^{-10}\text{m}$ and the largest relaxation time τ_0 of the Rouse spectra, the so-called entanglement time, which is strongly affected by the glass transition temperature. The relaxation time spectrum $H(\tau)$ can be obtained from the viscoelastic master curves of the storage modulus by applying the iteration procedure of Williams and Ferry [135]:

$$H(\tau) = A(p)E'\left(\frac{d(\log_{10}(E'))}{d(\log_{10}(\omega))}\right)_{\omega=\tau^{-1}} \tag{5.62}$$

that is valid for $p < 1$ and $A(p)$ evaluated as follow:

$$A(p) = \frac{2-p}{s\Gamma\left(2-\frac{p}{s}\right)\Gamma\left(1+\frac{p}{2}\right)} \tag{5.63}$$

where p is the local slope of $H(\tau)$ for $\tau = 1/\omega$ and Γ is the Gamma function.

In equation (5.58), other magnitudes must be explained for the adhesive friction calculation:

- $A_c(v_s, T, \sigma_0)$ is the real contact area;
- A_0 is the nominal contact area;

The relationship between the real and nominal contact area strongly depends on the magnification at which the contact between the rubber and the substrate is considered. According to Klüppel's theory [116], the contact area of self-affine surfaces increases with decreasing length scale according to a specific power law. Particularly, considering the macro and micro-roughness scaling regimes, an extension of the formulation for the contact area at the cut-off length scale is proposed:

$$A_c(\lambda_{min}) = A_{c,0}\left(\frac{\lambda_x}{\xi_\parallel}\right)^{2-D_M}\left(\frac{\lambda_{min}}{\lambda_x}\right)^{2-D_m} \tag{5.64}$$

where $A_{c,0}$ is the external contact area, defined as the product of the considered summit contacts and the number of summits $n_S A_0$ [14]:

$$A_{c\_0} = \frac{\pi}{2}\lambda_c^2 n_s A_0 F_0(t) \tag{5.65}$$

Replacing the equation (5.65) and (4.37) in (5.64), the corresponding area of contact viewed in the wavelength scale $[\lambda_{min}, \xi_\parallel]$ is given by [1, 116]:

$$\frac{A_c(\lambda_{min})}{A_0} = \left[\frac{\xi_\parallel F_0^2(t)F_{3/2}(t_S)|E^*(\omega_{min})|\tilde{n}_s^2}{808\pi s^{3/2}\xi_\perp|E^*(\omega_{max})|}\right]^{\frac{1}{3}} \tag{5.66}$$

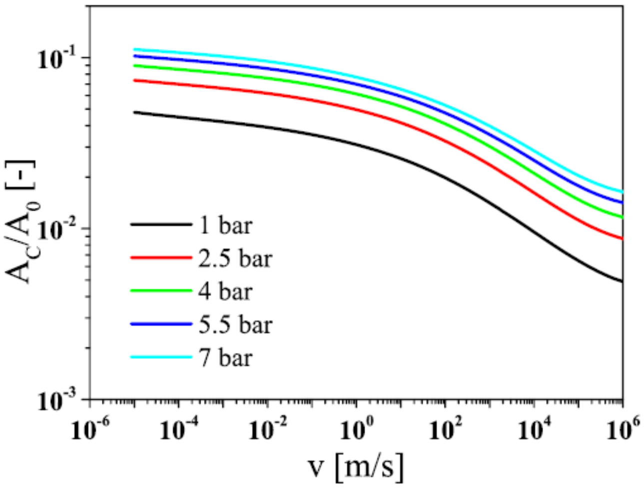

Fig. 5.6 Real-Nominal contact area ratio towards sliding velocity at different contact pressure [1]

In Fig. 5.6, the A_c/A_0 values towards sliding velocity at different contact pressure are shown. Particularly, it is noticeable that these trends exhibit the same physical phenomenon of the minimum contact length ones. As frequency (or sliding velocity) increases, the compound behaves glassier and a decrement of the real area values occur. On the other side, increasing the contact pressure, the mean indentation depth is higher with a consequently increment of the real contact area. Generally, the real contact area represents only a small fraction of the nominal surface area A_0 of less than 10%, especially at high velocities and small loads.

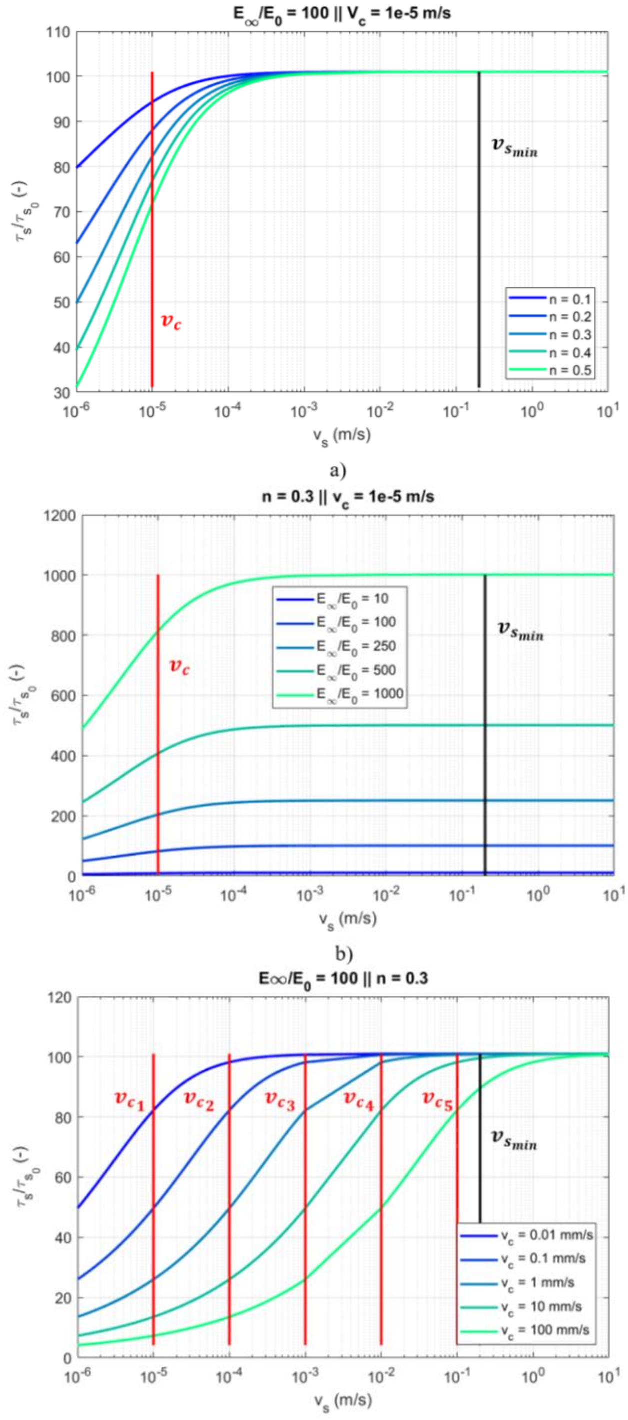

a)

b)

c)

Fig. 5.7 Normalised shear stress sensitivity analysis: a) varying n parameter; b) varying E_∞/E_0 ratio; c) varying v_c

As noticeable from the previous relationships, the adhesion friction coefficient is not simple to determine being the adhesive phenomena associated to the micro asperities' interaction with the compound molecules. Therefore, a sensitivity analysis of the parameters affecting the shear stress normalised respect to the τ_{s_0} for adhesion calculation has been carried out, as shown in Fig. 5.7, with the aim to comprehend how these magnitudes can affect the estimation in a working range reasonable with the tyre-road effective conditions in terms of sliding velocity according to the main Vehicle Dynamics references [6, 12, 136]. A shown in Fig. 5.7 a), the n parameters variations influence the slope of the shear stress curves in the lowest sliding velocity range, which is very far from the chosen minimum velocity value, $v_{s_{min}}$, almost equal to 0.2 m/s. On the other hand, in Fig. 5.7 b), different values of the ratio E_∞/E_0 meaningfully affect the plateau of the normalised local shear stress. However, this parameter value can be easily determined through the viscoelastic master curve of the complex dynamic modulus. In Fig. 5.7 c), instead, the variations of the critical velocity value v_c give rise to different sliding velocity at which the normalised shear stress starts to approach the plateau. Nevertheless, comparing the critical sliding velocity values to the chosen minimum velocity value $v_{s_{min}}$, the adhesive friction variations due to dependence on v_c could be neglected in the sliding range of interest for Vehicle Dynamics applications [49, 52]. Therefore, τ_{s_0} is the only parameter that must be determined through suitable experimental test session in order to properly estimate the shear stress and the adhesion friction coefficient according to (5.58).

5.4.3 Klüppel's theory: Friction coefficient results

In Fig. 5.8 and Fig. 5.9, the fits of the friction master curves, determined by means of Klüppel's model, on a rough and fine granite surfaces by the sum of adhesion and hysteresis contributions are shown, respectively [1]. Actually, the dry hysteresis friction is caused by energy losses on a broad frequency scale due to cyclic deformations of the rubber by asperities; the dry adhesion friction results from peeling effects governed by viscoelastic crack opening mechanisms between rubber and substrate.

It becomes obvious, that the two contributions describe the friction behaviour over a wider velocity range fairly well. Only for small velocities up to 1 mm/s, a systematic deviation between the theory and the experiments is displayed. Analysing the fitting parameter for the evaluation of the friction coefficient, the values of b are found to be almost constant but differ for the two substrates. The other fitting parameters show weak load dependence confirming that the theoretical formulation of contact conditions based on the Greenwood-Williamson integrals allows for a reasonable prediction of the observed load variation of the friction coefficient for dry friction measurements [1]. In addition, it is found that the dry friction coefficient decreases with increasing load for both substrates independent of velocity and temperature.

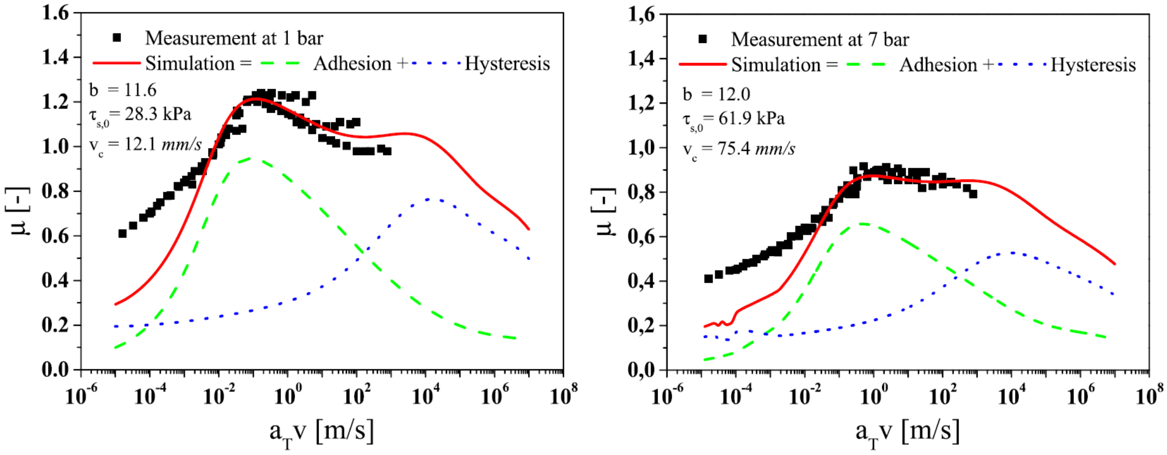
(a)

(b)

Fig. 5.8 Fitting of friction master curves on fine granite for 1 bar (a) and 7 bar (b) with fitting parameters shown in the inset [1]

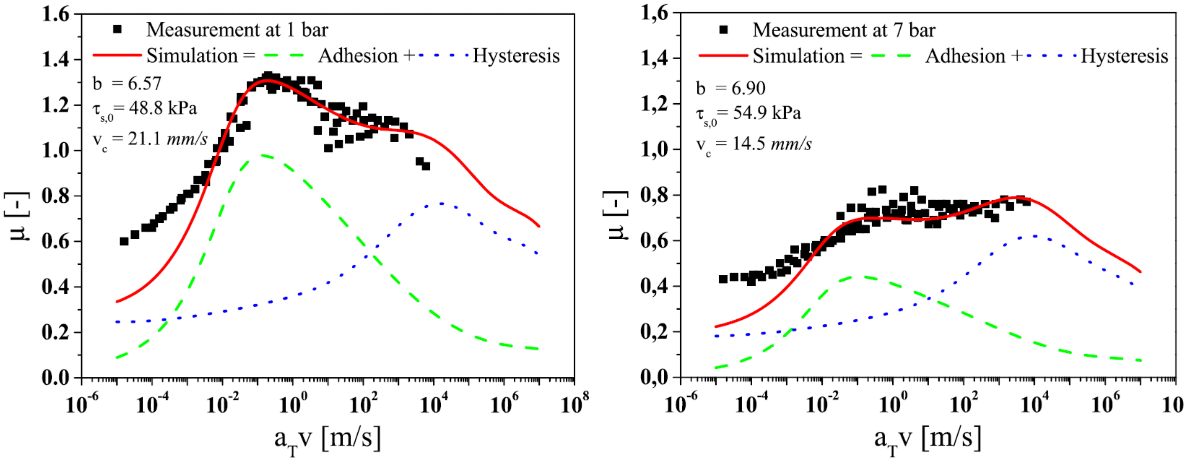
(a)

(b)

Fig. 5.9 Fitting of friction master curves on coarse granite for 1 bar (a) and 7 bar (b) with fitting parameters shown in the inset [1]

5.5 Persson's multiscale contact model

Persson has developed a theory that allows a certain number of lengths to be taken into account to define the friction coefficient. One of the main topics that Persson has analysed is the nature of the area of real contact and it is important to understand his contact theory.

A flat rubber squeezed against a hard surface with a periodic corrugation with wavelength λ and amplitude h is considered [16], as shown in Fig. 5.10. If the nominal contact area is A_0 and F_N is the load, the average normal stress $\sigma_0 = F_N/A_0$ is defined.

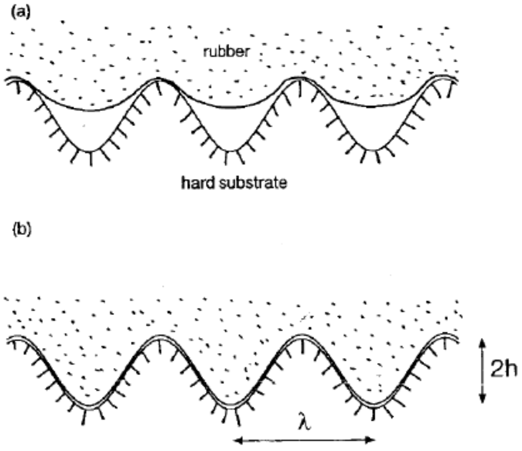

Fig. 5.10 Rubber substrate contact: a) small applied pressure; b) high applied pressure [15]

If a uniform stress σ acts within a circular area with radius R on the surface of a semi-infinite elastic body with modulus E, the displacement of a point P on the surface can be calculated as:

$$u \approx \frac{\sigma}{E} R \tag{5.67}$$

with reference to the Fig. 5.10, if $h/\lambda \approx \sigma_0$ the pressure σ_0 will be just large to deform the rubber to make contact with the substrate everywhere, but usually the ratio $h/\lambda \approx 1$ while $\sigma \neq E$. The pressure σ_0 is generally not able to deform the rubber to fill out the large surface cavities on a road. In case of sliding friction case, the displacement field, u_i, and similar for stress field, σ_i, is defined in this way:

$$u_i(\boldsymbol{q}, \omega) = \frac{1}{(2\pi)^3} \int d^2\boldsymbol{x} dt u_i(x, t) e^{-i(\boldsymbol{qx} - \omega t)} \tag{5.68}$$

where $\boldsymbol{x} = (x, y)$ and $\boldsymbol{q} = (q_x, q_y)$. According to Persson's theory [15], the hysteresis friction coefficient can be defined starting from the equation (5.68) and taking into account the frictional shear stress σ_f as follows [3]:

$$\mu_{hys} = \frac{1}{2} \int_{q_{min}}^{q_{max}} dq q^3 U(q) \times \int_0^{2\pi} d\phi \cos(\phi) \, Im\left(\frac{E^*(q v_s \cos(\phi))}{(1 - v_s^2)\sigma_0}\right) \tag{5.69}$$

where σ_0 is the nominal contact pressure, $U(q)$ the surface displacement power spectrum defined as function of a wavevector q, q_{min} is the smallest wavevector value associated with the macro roughness wavelength λ_{macro}, q_{max} is the truncating wavevector value (see paragraph 4.4.3 Persson's approach for the minimum contact length identification), E^* is the complex viscoelastic modulus of the rubber on the substrate.

However, the Persson's theory is obtained introducing various wise approximations in the real condition of partial contact, being the full contact a very remote condition in practical application, as shown in Fig. 5.10. The results of these conditions is a final calculation involving four nested integrals [3, 121]:

$$\mu_{hys} \cong \frac{1}{2}\int_{q_{min}}^{q_{max}} dq q^3 C(q) S(q) P(q) \times \int_0^{2\pi} d\phi \cos(\phi)\, Im\left(\frac{E^*(q v_s \cos(\phi))}{(1-v_s^2)\sigma_0}\right) \tag{5.70}$$

where:

$$P(q) = \frac{1}{\sqrt{\pi}}\int_0^{\sqrt{G}} dx\, e^{-\frac{x^2}{4}} = \mathrm{erf}\left(\frac{1}{2\sqrt{G}}\right) \tag{5.71}$$

$$G(q) = \frac{1}{8}\int_{q_{min}}^{q_{max}} dq q^3 C(q) \int_0^{2\pi} d\phi \left|\frac{E^*(q v_s \cos(\phi))}{(1-v_s^2)\sigma_0}\right|^2 \tag{5.72}$$

and:

$$S(q) = \gamma + (1-\gamma)P^2(q) \tag{5.73}$$

where γ = 0.5 is an empirical fitting constant obtained to match numerical results [3]. Notice that $P(q) = A(q)/A_0$ is the real contact area, normalized respect to the nominal one, observed at the magnification level $\xi = q/q_{min}$. The magnitude ϕ defines the angle between the sliding direction and the roughness profile orientation, as described in Fig. 5.11.

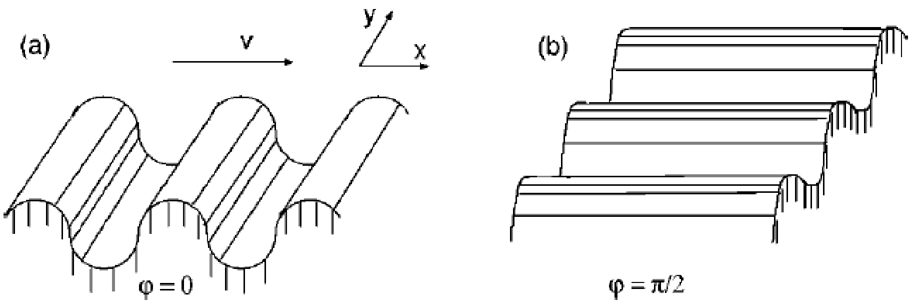

Fig. 5.11 Relative angle ϕ between sliding and wavelength directions [117]

As described in paragraph 4.4.3 Persson's approach for the minimum contact length identification, Ciavarella [3, 13] proposes a simplified formulation of Persson's multiscale theory for the friction due to viscoelastic losses suggesting only the finest “single scale” at the so called large wavevector cut-off contributes to the integration process.

5.5.1 Persson’s theory: adhesive friction calculation

The early theories of Persson have stated that the adhesion rubber-substrate interaction is not important due to the low distance cut-off in the sum over length scales, which is larger than 0.1 μm [15]. However, many studies have been carried out in order to analyse in-depth the adhesive contribution, which unfortunately remains even more radically empirical [1, 137]. The most recent empirical model proposed by Persson is quite similar to the Klüppel’s and is proportional to the frictional shear stress, which is a Gaussian-like curve as a function of the logarithm sliding velocity [3, 121]:

$$\mu_{adh} = \frac{\tau_f}{p_0}\frac{A_c}{A_0} \tag{5.74}$$

where:

$$\tau_f = \tau_{f_0}\exp\left[-c\left(log_{10}\left(\frac{v_s}{v_s^*}\right)\right)^2\right] \tag{5.75}$$

In equation (5.75), τ_{f_0} is the local shear stress in quasi-static conditions, which usually varies in the range of 8 $\pm$ 3 Mpa based on different studies on compounds and roughness data, v_s^* the critical sliding velocity and $c \approx 0.1$ a fitting parameter resulted in good agreement with the measurements [117]. These parameters, according to Persson’s experiments, are slightly dependent on the system studied and simulation conditions. However, Persson defines the critical sliding velocity as:

$$v_s^* = v_0\exp\left[-\frac{\epsilon}{k_B}\left(\frac{1}{T}-\frac{1}{T_g}\right)\right] \tag{5.76}$$

Where $v_0 = v_0^*\exp\,[(\epsilon/k_B)\,(T_0^{-1} - T_{g0}^{-1})] \approx 5e^{-7}$ m/s with $T_0 = (273 + T_{ref})\,K$, defining T_{ref} as the reference temperature of the frequency sweep of the compound master curve, $T_{g0} = (273 - T_g)\,K$ and $\epsilon \approx 1eV$, denoted as the activation energy.

5.5.2 Persson’s theory: friction coefficient results

Taking into account the relationships previously described for adhesion and hysteresis friction coefficient, a comparison of the Persson’s model output with the acquired experimental data according to the bench proposed in [117] is shown. In Fig. 5.12, the friction fit curves for an unfilled HNBR compound as function of sliding velocity for several different temperature are displayed. The blue markers are the experimental friction data at each condition.

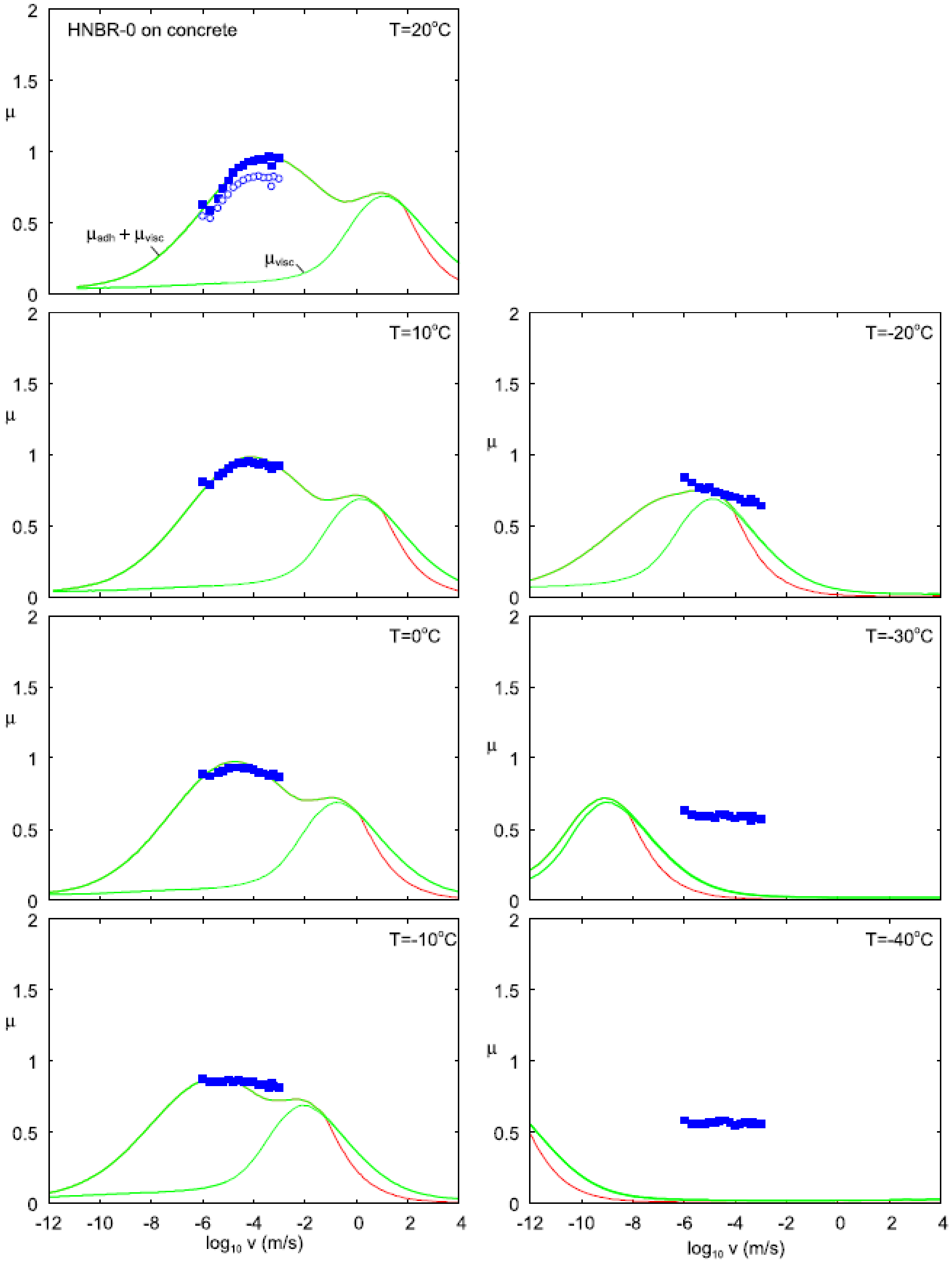

Fig. 5.12 Comparison of friction fit curves with experimental data according to Persson’s model [117]

The friction fit curves of both adhesion and hysteresis friction coefficient are also plotted. As noticeable, the hysteresis friction coefficient is very predominant in the global value starting from almost 0.2 m/s and, increasing the temperature, the μ_{hys} peak gradually shifts at high sliding velocities in accordance with the TTS principle for a viscoelastic compound. Furthermore, comparing the experiment data from 0°C with the model results, a very good fitting is displayed as a proof of the goodness of the Persson's theory in this sliding working range. The lack of experimental data at high sliding velocity from 0.2 m/s to 2 m/s does not provide a complete validation of the goodness of the predicted friction values, unless they are shifted in the frequency domain for the definition of a full friction master curve at the reference temperature thanks to the WLF relationship [117, 122], as shown in Fig. 5.13.

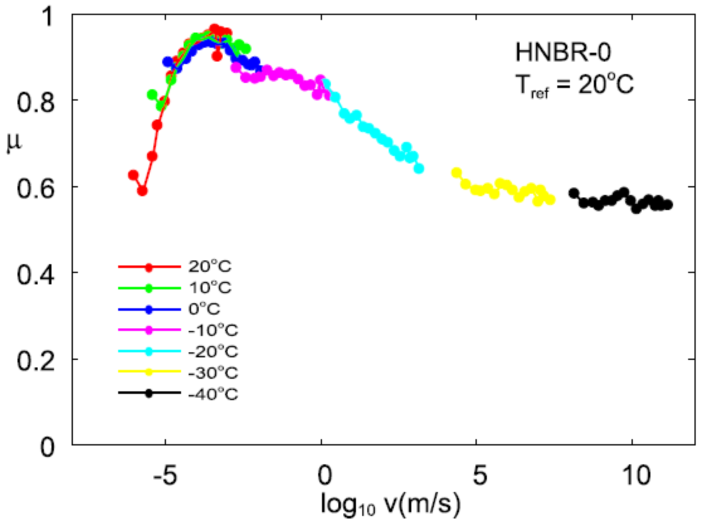

Fig. 5.13 Friction master curve at T = 20°C for an unfilled compound [117]

5.6 GrETA (Grip Estimation for Tyre Analyses) tyre-road contact model

As described in the previous paragraphs, the rubber friction is a phenomenon influenced by different variables, which are often hard and difficult to be measured; it depends on the macro and micro roughness, on the contact pressure arising in the footprint, on the rubber viscoelastic properties, like the storage modulus, loss modulus and loss factor, and their frequency and temperature influences, on the sliding velocity between the rubber and the road, on the temperature at the road-tyre interface.

In this section, a tyre/road friction model, called GrETA (acronym of Grip Estimation for Tyre Analyses), developed and optimized during the research activities at the Industrial Engineering Department of the University of Naples Federico II is presented. The model, taking into account the different aforementioned variables affecting the grip, allows the evaluation of the total grip intended as the sum of an adhesive component and a hysteretic one, as outlined in Fig. 5.14.

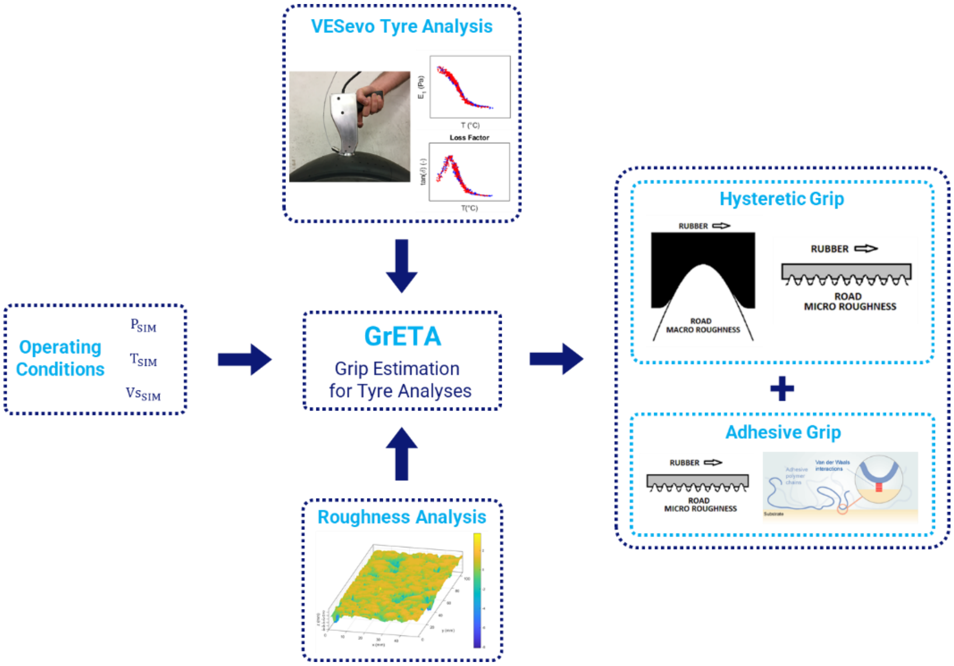

Fig. 5.14 Input variables for grip estimation through GrETA model

5.6.1 GrETA model overview

The GrETA model requires three main clusters of input variables to feed up the algorithms for the grip estimation:

- Roughness parameters: spatial frequency of macro asperities (λ_{macro}), average roughness (R_a), Hurst coefficient (H) and magnification level (ξ) are determined by means of HDC or PSD analyses;
- Compound viscoelastic properties of tyre tread: storage modulus (E_1), loss factor ($\tan(\delta)$) and WLF parameters (C_1, C_2, T_0) thanks to VESevo non-destructive analysis;
- Simulation operating conditions: nominal contact pressure (σ_0); compound temperature (T_{sim}) and sliding velocity ($v_{s\,sim}$).

The model allows the total friction evaluation as function of pressure, temperature or sliding velocity; for this purpose, the model allows the selection of the desired simulation interval for the mentioned operating conditions. The adhesive grip contribution, linked to the local bonds between the tread block and the road micro asperities, is evaluated using the generalized formulation of the Klüppel’s theory [1]:

$$\mu_{adh} = \frac{\tau_s(v_{s_{sim}})}{\sigma_0}\frac{A_c\left(T_{s_{sim}}, v_{s\,sim}, \sigma_0\right)}{A_0} \tag{5.77}$$

The hysteretic contribution, due to the cyclic deformation of a viscoelastic material, is evaluated with a power balance defined by Etienne-David [138], defined in equation (5.78), whose terms are calculated starting from a multiscale simplified approach based on the Hertzian contact mechanics theory, leading to results improved compared to ones described in [54].

$$\mu_{hys}\sigma_0 A_0 v_{s_{sim}} = \int_V w(x,y,z,t)dV \tag{5.78}$$

5.6.2 GrETA model input variables: roughness profile parameters

The first class of input variables are related to the roughness profile parameters. In this work, the analysis of the grip coefficient, carried out through the GrETA model and experimental benches at the Tyre Lab, was focused following asphalt specimens of 200x250 mm in Fig. 5.15.

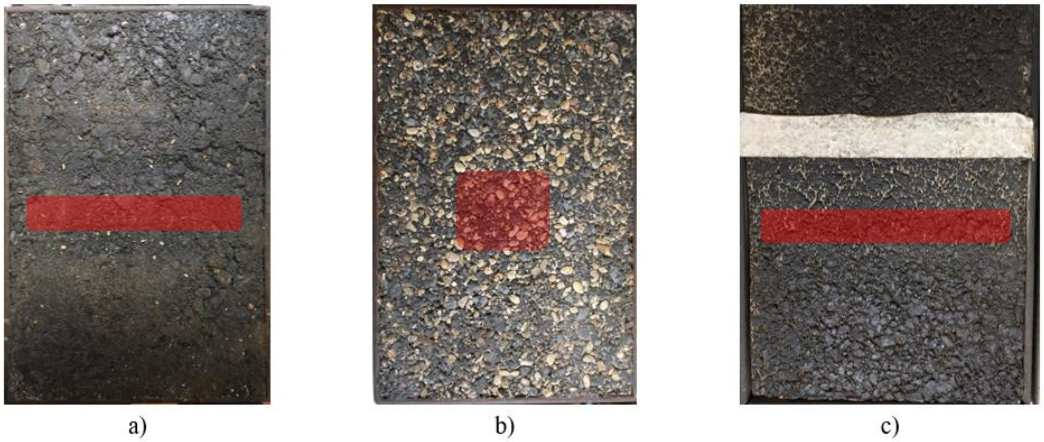

Fig. 5.15 a) Asphalt A; b) Asphalt B; c) Asphalt C. The red areas match with the scanned zones

For each surface, the roughness profile scans have been analysed by means of HDC and PSD 2D functions. The input parameters for the GrETA model are outlined in Table 5-1:

Table 5-1 Roughness parameters

Asphalt	Ra (mm)	λ_{macro} (mm)	λ_X (mm)	$\xi_\perp$ (mm)	H (-)	K (-)	S_k (-)
Asphalt A	0.275	3.60	0.9	0.5	0.625	5.10	-1.43
Asphalt B	0.799	4.20	1.4	1.3	0.955	2.17	-0.168
Asphalt C	0.513	3.58	1.0	1.1	0.705	6.28	-1.72

The asphalt B is characterized by a kurtosis value lower than 3: the profile has few high peaks and low valleys and this is quite confirmed comparing the Ra and λ_{macro} values, which are relatively high compared to the others. The skewness values also differentiate quite well the asphalts: the sample B looks very symmetric about the mean line being its S_k close to zero.

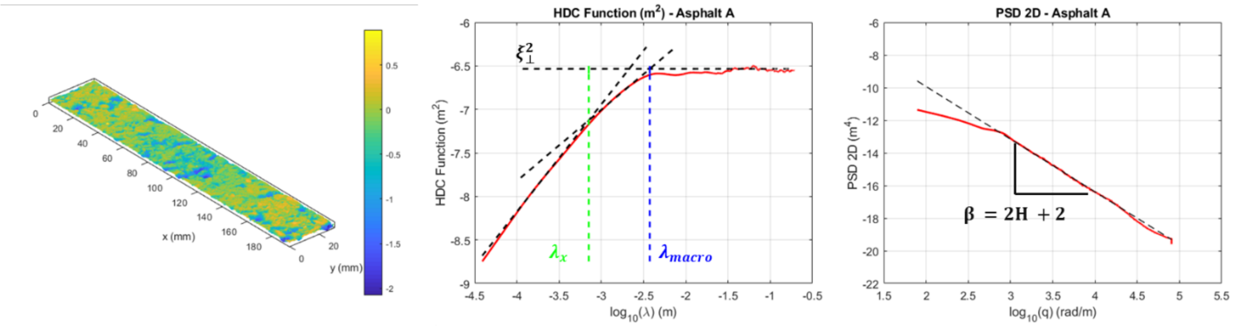

a) b) c)

Fig. 5.16 Asphalt A: a) 3D scan; b) HDC Function; c) PSD 2D Function

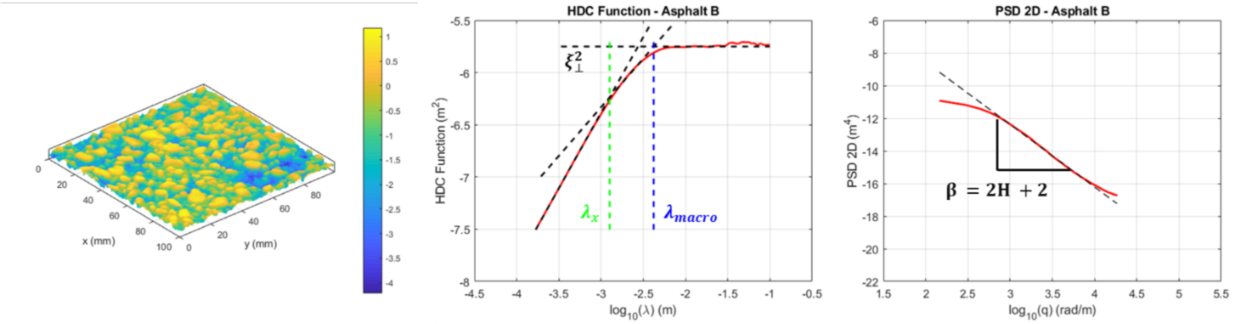

a) b) c)

Fig. 5.17 Asphalt B: a) 3D scan; b) HDC Function; c) PSD 2D Function

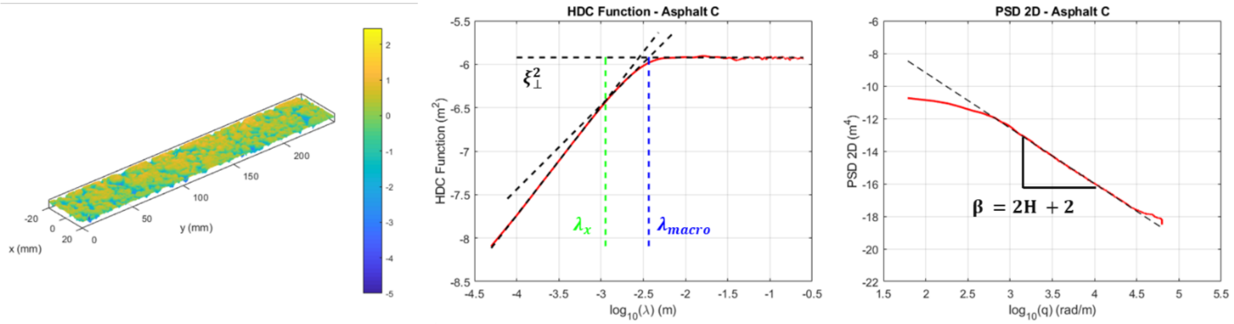

a) b) c)

Fig. 5.18 Asphalt C: a) 3D scan; b) HDC Function; c) PSD 2D Function

The 3D scan of a portion of the asphalt specimens together with the corresponding HDC and PSD functions are shown from Fig. 5.16 to Fig. 5.18. As noticeable, the main roughness parameters of Table 5-1 can be extrapolated from the above diagrams in order to feed up the tyre block – road contact mechanics implemented into the GrETA model for hysteretic and adhesive contributions to friction coefficient.

5.6.3 GrETA model input variables: tyre tread compound properties

As already mentioned, the viscoelastic characteristics of the tread compound are one of the main inputs for the GrETA model. They can be estimated by means of VESevo non-destructive testing, as described in paragraph 3.6 VESevo: innovative device for non-destructive viscoelasticity analysis, or performing a DMA on specific compound specimen, which is usually produced with a manufacturing process not totally similar to tyre one.

The viscoelastic storage modulus and loss factor can be provided in terms of temperature sweep master curves at a certain reference frequency, 1 Hz i.e.; otherwise, in the form of frequency sweep data. In both cases, these properties are transformed thanks to the WLF relationship [4, 54]: the evaluation of the viscoelasticity at different temperatures and frequencies is fundamental because it is necessary to consider the compound behaviour variation in response to the tyre-road contact: different wavelengths excite the material at different frequencies linked to the asperity wavelength by this expression:

$$f_i = \frac{v_s}{\lambda_i} \tag{5.79}$$

where, f_i is the solicitation frequency linked to the spatial frequency of the asperities, λ_i, through the sliding velocity of the tread block, v_s. In Fig. 5.19 the viscoelastic properties shift from the DMA reference curve at 1 Hz (black full line) to higher frequencies due to sliding on the roughness surface is shown. The values on y-axis are hidden due to the industrial confidentiality agreement with the compound manufacturer. As noticeable, the application of the WLF relationship not only moves the viscoelastic master curves but slightly changes their shape affecting the grip estimation in the fixed temperature range of interest, for example [20°C, 80°C].

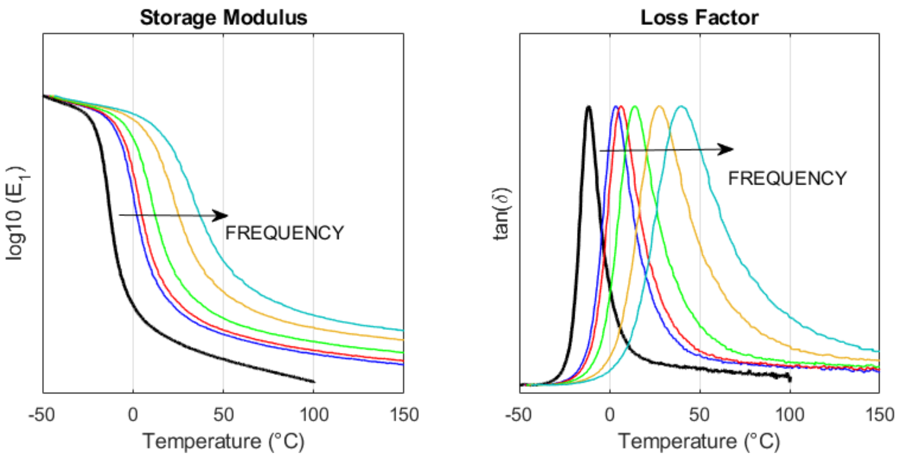

Fig. 5.19 Application of the WLF frequency shift from the black reference curve (DMA 1 Hz)

The maximum solicitation frequency that should affect the grip is almost 10^6 Hz. This magnitude could be reached in case of a very soft tread compound, which slides on a roughness surface with low microroughness wavelengths ($\sim 1\ \mu m$) according to the Klüppel's theory of λ_{Min} identification described in paragraph 4.4 Minimum contact length identification for self-affine surfaces. Generally, the commonest values of solicitation frequency during sliding are in the range of [10^4, 10^5 Hz] for microroughness wavelengths close to 0.1 mm.

5.6.4 GrETA model: Adhesive friction contribution

The molecular adhesion mechanism requires direct contact between the tyre rubber block and the road roughness. In the GrETA model therefore the adhesive contribution to friction is linked to the micro roughness and it is estimated by the following:

$$\mu_{adh} = \frac{F_{adh}}{F_N} = \frac{\tau_s(v_{s_{sim}})}{\sigma_0} \frac{A_c\left(T_{s_{sim}}, v_{s_{sim}}, \sigma_0\right)}{A_0} \tag{5.80}$$

where τ_s is the local shear stress acting in the real contact area and depends on the sliding velocity and the compound properties; σ_0 is the simulation nominal contact pressure, one of the GrETA model input; A_c is the effective contact area and A_0 is the nominal one. Each term is deeply described in the next sections:

Local shear stress

The shear stress is the local force needed to break the adhesive bounds at the road tyre interface. This is estimated through the semi-empirical expression proposed by Klüppel's theory [1, 116]:

$$\tau_s(v_S) = \tau_{s_0}\left(1 + \frac{E_\infty/E_0}{\left(1 + \frac{v_c}{v_S}\right)^n}\right) \tag{5.81}$$

Here, τ_{s_0} is the static shear stress in the limit of infinite slow velocities and v_c is a critical velocity above which τ_s converges to a plateau. E_∞/E_0 is the ration of the dynamic modulus between rubbery and glassy plateau states; whereas n is determined by means of equation (5.60). As demonstrated in Fig. 5.7, the v_c and n parameters do not affect the τ_s/τ_{s_0} trend in the sliding velocity range of interest in Automotive and Motorsport applications; therefore, they have been left as constants in the simulations: $v_c = 10\ mm/s$ and $n = 0.25$. The dynamic modulus ratio is determined thanks the VESevo measurements or DMA data provided by the tyre compound manufacturer. The τ_{s_0} values are estimated through an empirical formulation based on the experimental measurements carried out on the friction bench [139, 140], described in the next chapter, available at the Tyre Lab of the Department of Industrial Engineering. The relationship links the compound modulus E_0 and the roughness parameter m_2 to local τ_{s0} as follows:

$$\tau_{s0}(E_0, m2) = \left(aE_0^b\right)m_2^c \tag{5.82}$$

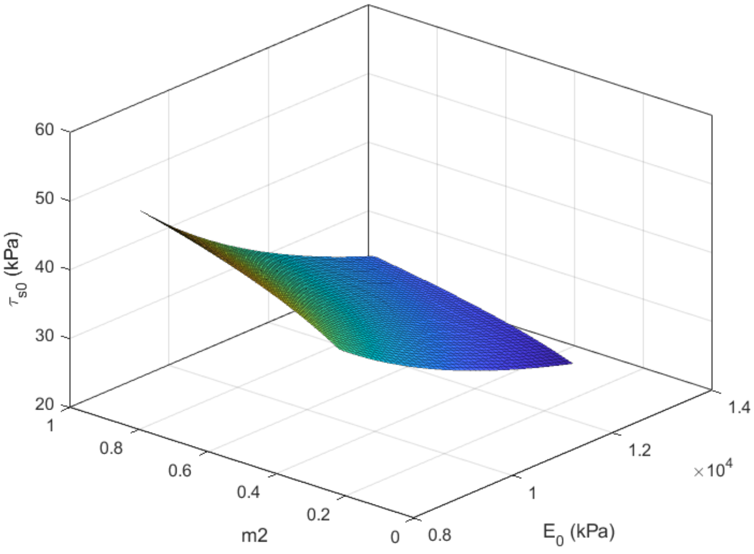

Fig. 5.20 τ_{s0} values towards the compound E0 and profile m2 parameters

In equation (5.82), a, b and c are fitting parameters based on experimental friction measurements, m_2 is the second momenta of roughness profile spectrum and it represents the mean square slope of the peaks spatial distribution as follows:

$$m_2 = \left\langle \left(\frac{dz}{dx}\right)^2 \right\rangle \tag{5.83}$$

Hence, lower the modulus value E_0, higher the τ_{s0} is. On the other side, the higher the m_2, higher the τ_{s0}. This means that a very soft compound sliding in quasi-static conditions on a surface with a relevant peak distribution is subjected to high local shear forces before starting the motion.

Effective contact Area

The effective contact area is a variable difficult to determine and many empirical formulations are advanced in the scientific literature [1, 2, 16] based on specific approaches. The main reason may lie in the lack of a reliable experimental method for its estimation.

For the adhesive friction contribution, the following empirical relationship has been considered based on the simplified Persson's theory [2], where the Gauss error function, denoted as *erf*, is considered as follows:

$$\frac{A_c(T, v_s)}{A_0} = \operatorname{erf}\left(\sigma_0 \frac{1 - \nu^2}{\sqrt{m2}\, E^*(T, v_s)}\right) \tag{5.84}$$

In equation (5.84), ν is the Poisson's coefficient, which is approximated as a constant value (~0.48), and E^* is the dynamic complex modulus of the tread compound sliding on the asphalt at the velocity v_s and the temperature T.

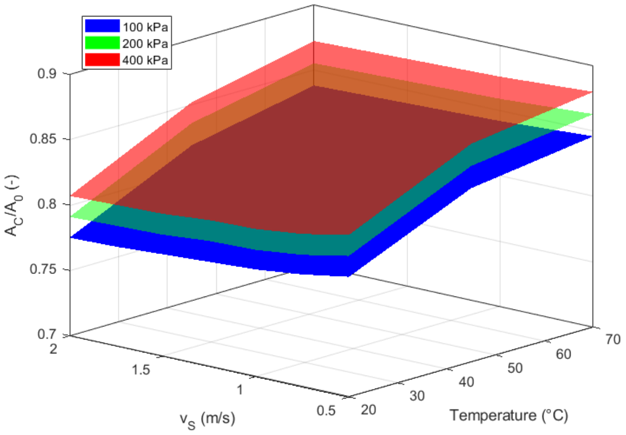

Fig. 5.21 A_C/A_0 values for a specific passenger tyre compound towards T, v_s and σ_0

As shown in Fig. 5.21, the A_C/A_0 ratio increases with the applied nominal pressure until it reaches a sort of saturation depending on the stiffness of the compound. The temperature particularly affects the value of the real contact area, being a crucial simulation parameter into adhesive contribution to friction. Contrarywise, lower the sliding velocity, slightly higher A_C/A_0: increasing the sliding velocity on a specific asphalt, the solicitation frequency is higher and consequently the compound behaves almost as a glassy material leading to lower values of the effective contact area compared to low speed ones.

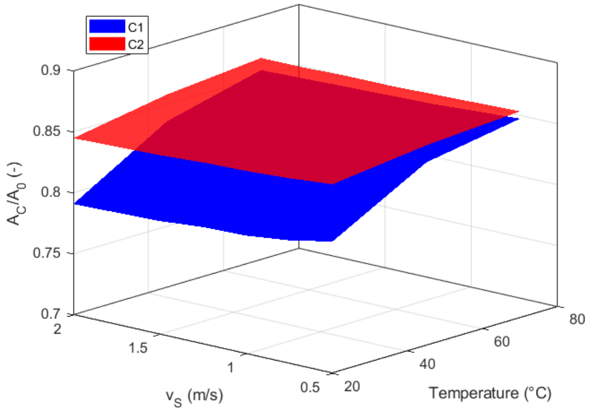

Fig. 5.22 A_C/A_0 values for two different passenger tyre compounds at σ_0 = 200 kPa

In Fig. 5.22, the comparison of A_C/A_0 values between two different tyre tread compounds are displayed. As noticeable, the C2 exhibits a flatter variation of the effective contact area compared to the C1, which is the same compound of Fig. 5.21, being the softer material. This means the contact area saturation should occur at lower values temperature and nominal contact pressure respect to other material specifications.

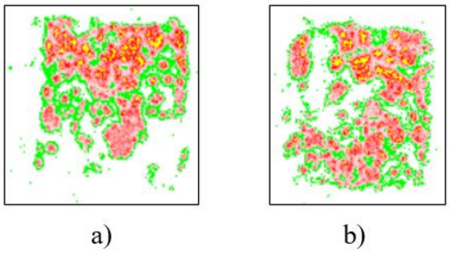
a) b)

Fig. 5.23 Experimental measurements of A_C/A_0 through pressure-sensitive paper on Asphalt A: a) C1; b) C2

To check the goodness of A_C/A_0 values for these compounds some preliminary measurements on asphalt A have been carried out using the Fujifilm pressure-sensitive paper. This product consists of two polyester bases. One is coated with a layer of micro-encapsulated colour forming material and the other with a layer of the colour-developing material.

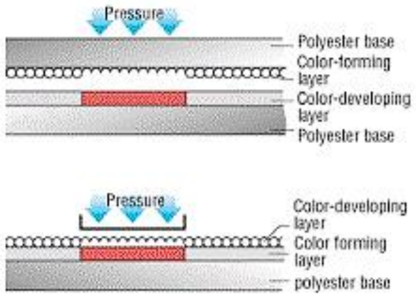

Fig. 5.24 Pressure-sensitive paper

When the normal load is applied in static conditions on the specimen positioned on the paper, the microcapsules are broken and the colour forming material reacts with the colour-developing film, printing the image of the pressed area, as shown in the scanned images in Fig. 5.23. The same scanner software, called FPD10e, provides the values of the pressed area and the average contact pressure reported in Table 5-2. Comparing the software values obtained with the pressure-sensitive paper to the equation (5.84) in Fig. 5.22, these data are not very different from the low speed and ambient temperature (∼20°C) ones.

Table 5-2 Contact Area parameters

Compound	Size (mm)	Fz (N)	σ_0 (Mpa)	σ_{avg} (Mpa)	A_C (mm^2)	A_C/A_0 (-)
C1	22x22	100 N	0.206	0.315	368	0.76
C2	22x22	100 N	0.206	0.290	407	0.841

This means that the proposed relationship is reliable for adhesive friction estimation, as shown in next subsection. However, further experiments with this type of pressure-sensitive paper will be carried out as post-doctoral research activities in order to provide a more robust validation and a new empirical formulation for real contact area estimation.

Adhesive friction maps

Typical adhesive friction maps estimated by equation (5.80) and varying the nominal contact pressure, temperature and sliding velocity simulation parameters are proposed in this subsection for the compounds C1 and C2, which are previously introduced. The viscoelastic properties of these specimens determined by means of VESevo testing procedure and normalized due to industrial confidentiality agreement are shown in Fig. 5.25.

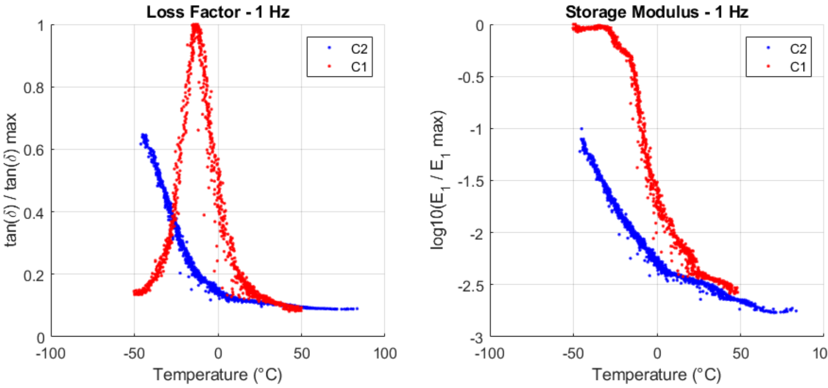

Fig. 5.25 Tyre tread compounds C1 and C2 viscoelastic properties obtained through VESevo testing

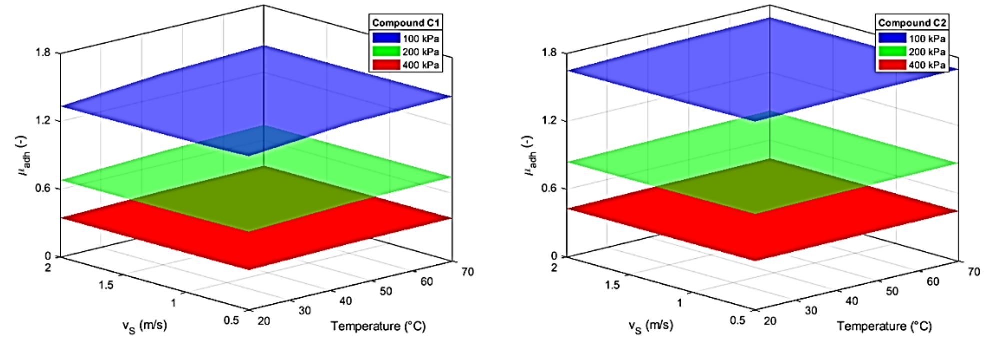

a)

b)

Fig. 5.26 Adhesive grip coefficient maps for compounds C1 and C2 on Asphalt A (Table 5-1)

In Fig. 5.26, the adhesion grip coefficient values for both compounds are plotted towards the sliding velocity, temperature, and nominal contact pressure. As noticeable, the v_s and T slightly affect the adhesion contribution to grip; contrariwise the compound properties and nominal pressure.

5.6.5 GrETA model: Hysteretic friction contribution

The hysteretic contribution to total friction is linked to the bulk deformation hysteresis in the rubber compound thickness. As already mentioned, this rate is evaluated by means of a power balance defined by the Etienne-David equation:

$$\mu_{hys}\sigma_0 A_0 v_{s_{sim}} = \int_V w(x,y,z,t)dV \tag{5.85}$$

where μ_{hys} is the unknown grip term depending on the stress field and train rate. To determine the energy dissipation due to hysteresis as results of the tyre-road interaction, the Hertzian contact mechanics theory and the Sackfield-Hills's equations (5.35) – (5.51) are taken into account.

The main improvement in this term calculation respect to the previous version [54] is the analysis at different wavelengths from macro roughness to micro one. Thus, the hysteretic contribution no longer depends on the macro asperities, but on a discrete spectrum of spatial frequencies. For this purpose, an empirical formulation for the estimation of the maximum magnification, ξ_{Max}, is provided depending on the compound and the simulation conditions, as well as compound, roughness and temperature.

Stress field evaluation

To evaluate the stress field distribution within the tread block during tyre-road interaction, the GrETA model is based on the following assumptions:

- The road asperity is modelled as a periodic axisymmetric rigid indenter with amplitude equal to R_a and frequency λ_{macro} in sliding contact with the tyre block:

$$z(x,y) = \left(R_a + R_a \cos\left(\frac{2\pi}{\lambda_{macro}} x\right)\right) \cdot \left(R_a + R_a \cos\left(\frac{2\pi}{\lambda_{macro}} y\right)\right) \tag{5.86}$$

- A generic sinusoidal indenter, corresponding to a wavelength between the macro and micro range, is defined by equation (5.87), where H is the Hurst coefficient and ξ_i the i-th magnification level, on which depend the generic λ_i and scaled R_a according to the self-affine profiles' theory.

$$z(x,y) = \left(R_a + R_a \cos\left(\frac{2\pi}{\lambda_{macro}} x\right) + \frac{R_a}{\xi_i^H} \cos\left(\frac{2\pi}{\lambda_i} x\right)\right) \cdot \left(R_a + R_a \cos\left(\frac{2\pi}{\lambda_{macro}} y\right) + \frac{R_a}{\xi_i^H} \cos\left(\frac{2\pi}{\lambda_i} y\right)\right) \tag{5.87}$$

- The tyre tread block in contact with the sinusoidal road asperity is modelled as a homogeneous and isotropic parallelepiped, whose dimensions depend on the considered wavelength and the tread thickness t as follows:

$$V = \lambda_i \times \lambda_i \times t \tag{5.88}$$

- The sinusoidal indenter-tyre block contact is studied by means of Hertz theory. Particularly, the indenter is approximated to a sphere, whose radius R depends on the roughness parameters as expressed in equation (5.89), being the assumption of small deformation valid for compounds of passenger or track tyres.

$$R_i = \frac{\lambda_i^2}{4\pi^2 R_{a_i}} \tag{5.89}$$

The applied normal load, F_i, is equal to:

$$F_i = \sigma_0 \lambda_{macro}^2 N_{C_i} \tag{5.90}$$

Where σ_0 is the simulation nominal pressure and N_{C_i} is the number of contacts between the tread block and the roughness asperities corresponding to a spatial frequency λ_i.

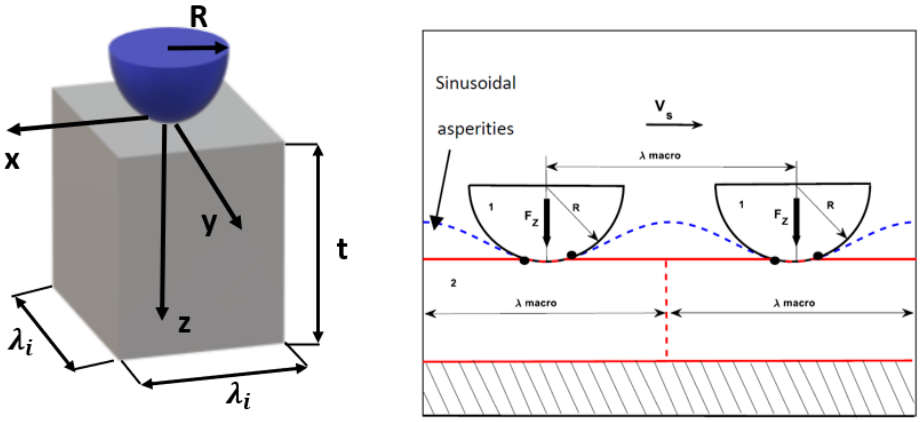

a) b)

Fig. 5.27 a) indenter-rubber volume representation; b) Sinusoidal road indentation

Once determined the contact radius corresponding to $\lambda_i = \lambda_{macro}$ through equations (5.13) and (5.90), the number of contacts at i-th wavelength within the compound area λ_i^2 can be iteratively evaluated as follows:

$$N_{C_i} = \frac{\pi a_{i-1}^2}{\lambda_i^2} N_{C_{i-1}} \tag{5.91}$$

Obviously, the number of contacts assigned on the macro wavelength is approximated to 1:

$$N_{C_{i=1}} = N_{C_{macro}} = \frac{\pi a_{macro}^2}{\lambda_{macro}^2} \sim 1 \tag{5.92}$$

Further assumptions must be considered before evaluating the stress field distribution:

- The stress values are determined with respect to the assigned reference system in Fig. 5.27a. The coordinates x, y and z are dimensioned with respect to the contact radius relative to the wavelength considered;
- To account for the simultaneous effect of several adjacent road asperities, five indenters are supposed to work;
- To decrease the error related to the balance between applied load and induced stress field, the thickness t is scaled on the number of contacts N_{C_i} occurring in the tread volume area λ_i^2 in the plane XY. However, it is necessary to highlight that the Sackfield-Hills relationship for stress calculation is valid in case of contact between the sphere and infinite plane of the substrate: infinite dimensions cannot be assigned in the algorithm, a good compromise is achieved by using the above-mentioned dimensions.

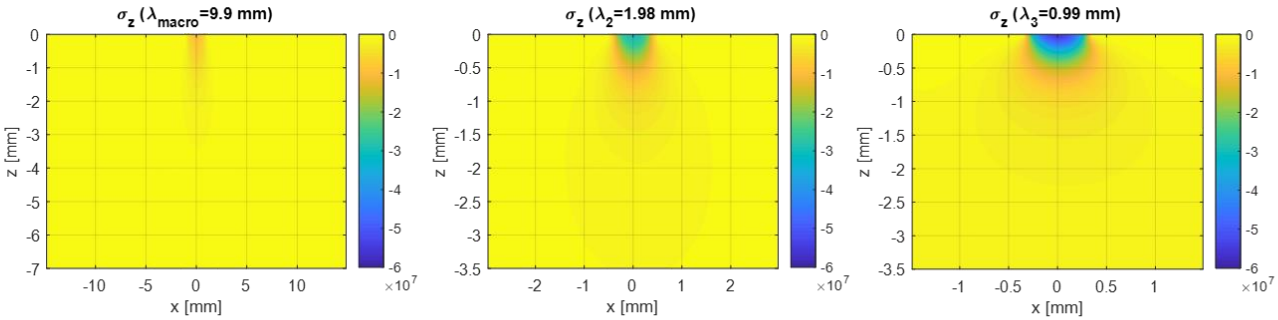

Fig. 5.28 σ_z values in XZ plane of the tread block volume at different wavelengths

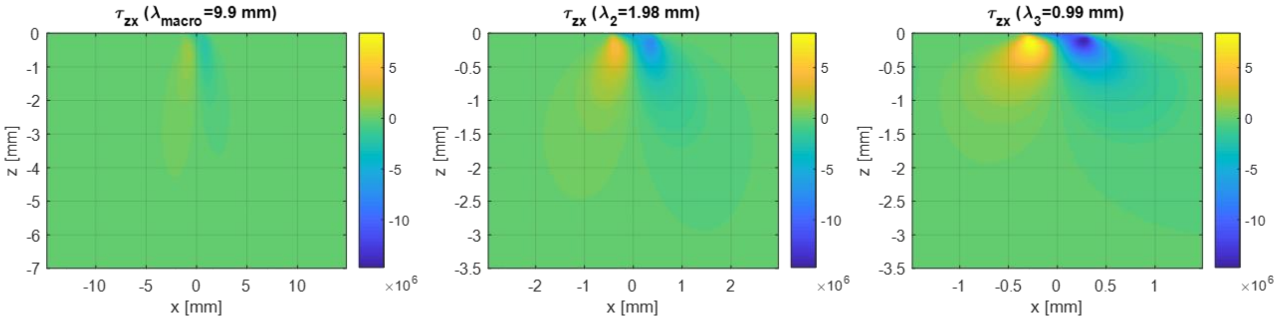

Fig. 5.29 τ_{zx} values in XZ plane of the tread block volume at different wavelengths

In Fig. 5.28 and 5.29, different stress field components matching with three asperity wavelengths are shown. As noticeable, the stress values tend to increase passing from the larger wavelength to the smaller ones. This is also due to high values reached by the maximum pressure, p_0, inside the contact patch considering the smaller frequencies in the Hertzian contact, as a result of equation (5.12). This singularity is outlined in Fig. 5.20 at different nominal pressure of simulation.

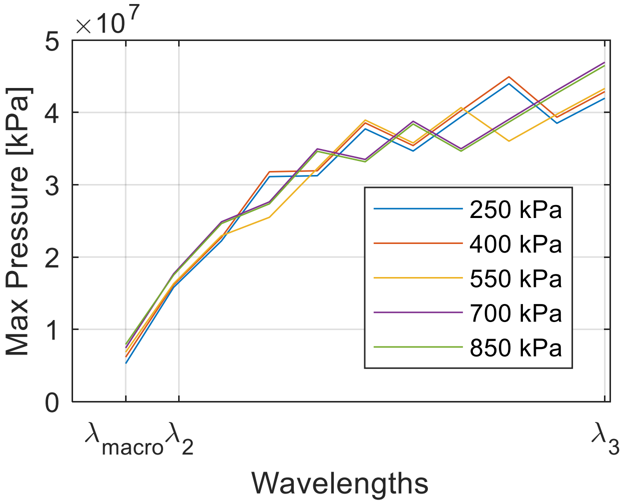

Fig. 5.30 Maximum contact pressure value at different wavelengths and assigned σ_0

Power dissipation evaluation

In equations (5.78) and (5.85), the quantity $w(x, y, z, t)$ represents the power loss at each point of the deformed elementary volume at the time t, when a rigid roughness surface slides at speed v_s under a normal load F_i; σ and $\dot{\varepsilon}$ are the stress and strain rate tensors.

Hypothesizing a constant sliding velocity, each stress-strain cycle can be considered as performed in a period equal to:

$$T = \frac{\lambda}{v_s} \tag{5.93}$$

hence, the average power loss in the period is:

$$w(x, y, z) = \frac{1}{T}\int_0^T w(x, y, z, t)dt \tag{5.94}$$

This power loss occurring in (5.78), (5.85) and (5.94) can be expressed for the entire compound volume considered and equalled to the dissipation linked to friction forces:

$$W_{diss}(t) = \int_V w(x, y, z)dV = \int_V \sigma(x, y, z, t)\frac{d\varepsilon}{dt}(x, y, z, t)dV \tag{5.95}$$

Assuming the external solicitation linked to sinusoidal road asperities as periodic, the strain can be expressed as follows:

$$\varepsilon(t) = \mathrm{E}_0 \sin(\omega t) \tag{5.96}$$

The associated stress field in case of viscoelastic material is:

$$\sigma(t) = \Sigma_0 \sin(\omega t + \delta) \tag{5.97}$$

Therefore, the equation (5.85) can be rewritten as:

$$W_{diss} = \int_V \left[\frac{1}{T}\int_0^T \Sigma_0 \sin(\omega t + \delta)\, \omega \mathrm{E}_0 \cos(\omega t)\, dt\right] dV \tag{5.98}$$

following the calculation in the Appendix A:

$$W_{diss} = \frac{1}{2}\omega \Sigma_0 \mathrm{E}_0 \sin(\delta) \tag{5.99}$$

Being $\omega = 2\pi v_s/\lambda_i$, the equation (5.99) linked to the generic wavelength turns into:

$$W_{diss_i} = \frac{\pi v_s}{\lambda_i}\Sigma_0 \mathrm{E}_0 \sin(\delta) \tag{5.100}$$

The strain field in the above relation is evaluated using the linear constitutive equations while the viscoelastic nature of the rubber is taken into account by means of the $\sin(\delta)$:

$$\varepsilon_x = \frac{1}{E'}\left[\sigma_x - \nu\left(\sigma_y + \sigma_z\right)\right] \tag{5.101}$$

$$\varepsilon_y = \frac{1}{E'}\left[\sigma_y - \nu(\sigma_x + \sigma_z)\right] \tag{5.102}$$

$$\varepsilon_z = \frac{1}{E'}\left[\sigma_z - \nu\left(\sigma_y + \sigma_x\right)\right] \tag{5.103}$$

$$\gamma_{xy} = \frac{2(1+\nu)}{E'}\tau_{xy} \tag{5.104}$$

$$\gamma_{xz} = \frac{2(1+\nu)}{E'}\tau_{xz} \tag{5.105}$$

$$\gamma_{yz} = \frac{2(1+\nu)}{E'}\tau_{yz} \tag{5.106}$$

The dissipated power is evaluated for each wavelength considered in hysteretic grip calculation in case of multi-contact grip model. To evaluate the total dissipated power, it is not possible to add the individual contributions for each λ_i otherwise the total power would diverge. To overcome this problem, it was decided to assign a weight, $w_{p,i}$ linked to the wavelength corresponding to each contribution, obviously taking into account the number of contacts:

$$w_{p,i} = \frac{N_{C_i}\lambda_i}{\sum_{i=1}^{M}\lambda_i} \tag{5.107}$$

Hence, the total dissipated power in the control volume is determined as follows:

$$W_{tot} = \sum_{i=1}^{M} w_{p,i} \cdot W_{diss,i} \tag{5.108}$$

The total hysteretic contribution is consequentially defined as:

$$\mu_{hys}\sigma_0 A_0 v_s = W_{tot} = \sum_{i=1}^{M} w_{p,i} \cdot W_{diss,i} \tag{5.109}$$

In Fig. 5.31, the typical values of the weight assigned to each power loss at different λ_i is shown: increasing the magnification level, the weight reduces and converges to a plateau value depending on the number of contacts at each spatial frequency. On the other hand, the single power loss contribution drastically increases close to the micro wavelength: this phenomenon depends on the hysteretic behaviour of the compound, which exhibits higher $\tan(\delta)$ values increasing the solicitation frequency linked to v_s and λ_i.

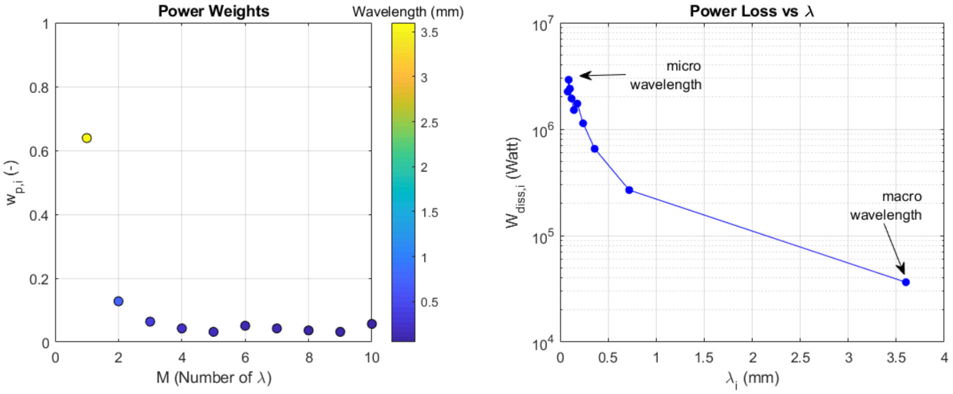

Fig. 5.31 Weight on power loss vs λ_i (left plot); power loss vs λ_i (right plot)

The value of the lowest wavelength affecting the hysteretic grip during the sliding on a specific roughness profile depends on the simulation conditions and asphalt type. Klüppel's theory, as described in paragraph 4.4 Minimum contact length identification for self-affine surfaces provides an identification procedure of the minimum contact length starting from a modified Greenwood-Williamson approach. However, this formulation could be very complex to be implemented in a tyre-road contact model based on a different approach for hysteresis calculation. Therefore, an empirical formulation based on experimental friction measurements (see Chapter 6) is proposed in this section in order to overcome the limit associated with the truncation of the roughness power spectrum during compound-road local interaction.

$$\xi_{Max} = \frac{\lambda_{macro}}{\lambda_{micro}} = (p_1 m_2 + p_2)\sqrt{E_1(T)^{p_3}} \tag{5.110}$$

where p_1, p_2 and p_3 are fitting coefficients of the above relationship, which was identified on different storage modulus values at different temperatures and fixed simulation contact pressure.

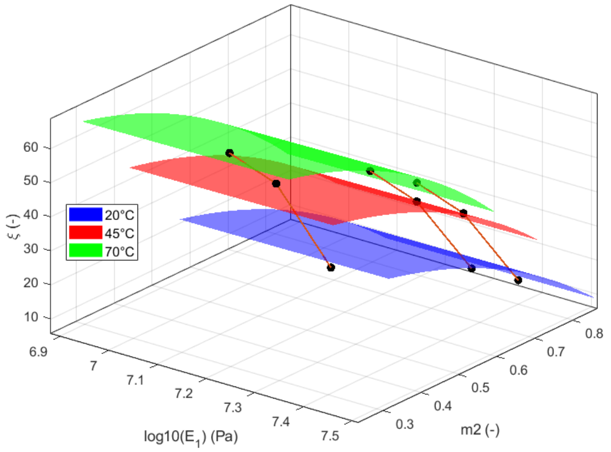

Fig. 5.32 3D maps of maximum magnification level towards E1 and m2 at different temperatures

In Fig. 5.32, the values of maximum magnification level towards the compound storage modulus and roughness parameter m_2 are displayed. As noticeable, increasing the temperature, different surfaces of ξ_{Max} are determined since the compound exhibits lower storage modulus, contrariwise increasing the m_2 lower values of magnification are identifiable due to the high mean square slope of the peaks. The red lines with black markers represent the ξ_{Max} values of the compound C1 in Fig. 5.25.

5.6.6 GrETA model: friction maps results

Once explained the adhesion and friction contribution determined by means of the GrETA model, the total grip can be expressed as follows:

$$\mu = \mu_{adh} + \mu_{hys} \tag{5.111}$$

In this section, some examples of friction maps for the asphalt A, B and C in Fig. 5.15 are reported. For this application, the compound C1 and C2 viscoelastic properties in Fig. 5.5 are taken into account.

The simulation conditions are the following:

- Sliding velocity range v_s → [0.25, 2] m/s;
- Compound temperature T → [20, 70] °C;
- Nominal contact pressure $\sigma_0 = 200$ kPa.

The friction map results are shown in Fig. 5.33. The friction coefficient values exhibit different variations among the considered asphalts depending on the viscoelastic behaviour of the compound. The C2 specification, i.e., exploits less grip on asphalt B compared to C1, due to lower values of $\tan(\delta)$ according to VESevo characterization in Fig. 5.25. Hence, the hysteretic contribution is different. For both materials, the overall grip increases towards the sliding velocity: this is in accordance with dissipation due to viscoelasticity for high solicitation frequencies. Furthermore, the temperature effect on C1 compound is predominant compared to C2.

Further simulation results are shown in Fig. 5.34 and they refer to three different truck tyres, whose viscoelastic properties have been characterized by means of DMA frequency sweep curves at 25°C. The DMA values are normalized respect to the maximum values of loss factor.

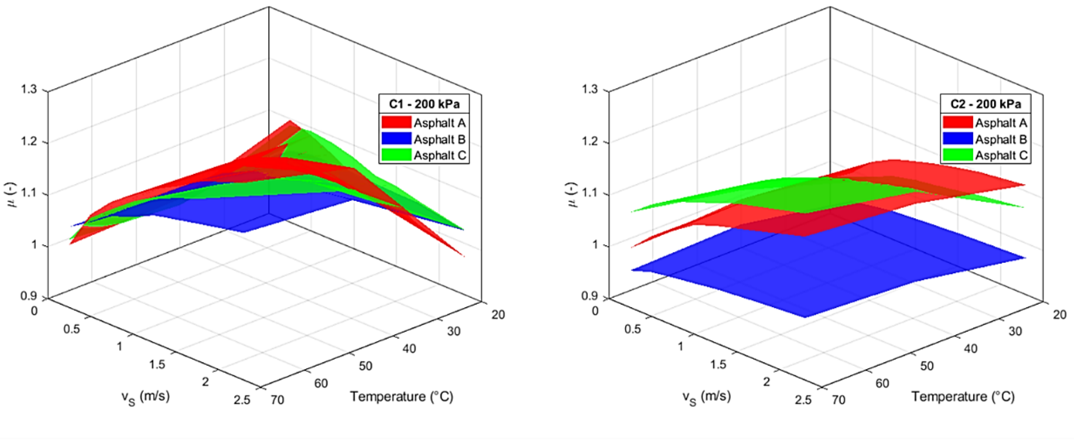

a) b)

Fig. 5.33 Friction maps for compounds C1 and C2 on three different asphalts for σ_0 = 200 kPa

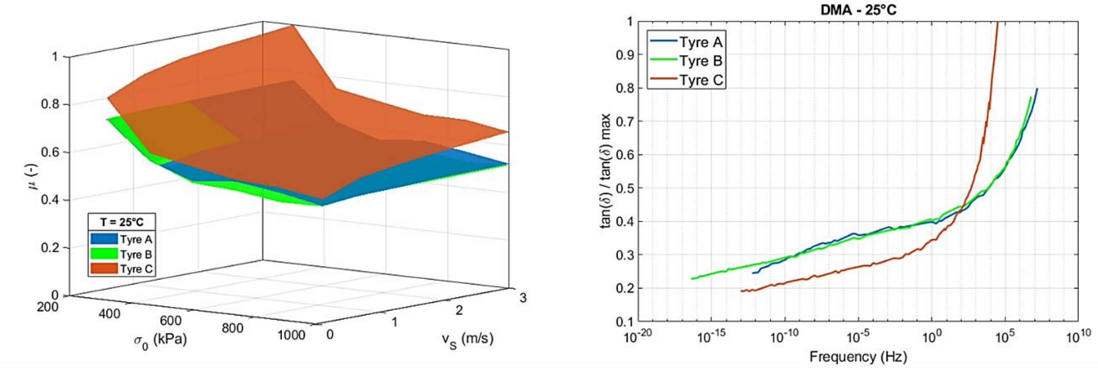

a) b)

Fig. 5.34 Friction maps for three different truck tyres on asphalt C at 25°C

As depicted in the above friction diagrams, the tyre C exhibits higher grip values at 25°C in the pressure and sliding velocity simulation ranges compared to the others. These results are in accordance with the DMA: Tyre C is characterized by greater $\tan(\delta)$ in the sliding frequency range [10^2, 10^6] Hz.

Hence, the friction results outlined in this paragraph are obtained by using a multi-contact model, called GrETA, based on the Hertzian theory and assumptions for tyre-road indentation analysis. The grip values are determined as overall contribution of adhesive grip and hysteretic grip. The latter requires the knowledge of viscoelastic properties and time-temperature relationship, which can be provide by means of VESevo measurements or DMA. A preliminary feedback on the trustworthiness of the proposed approach will be analysed in the next chapter, where a comparison of GrETA model outputs and the experimental data acquired with the British Pendulum evo bench is described in-depth.

Chapter 6

Experimental methodologies for friction coefficient analysis

6.1 Overview on the state of the art in experimental friction estimation

The experimental friction estimation is a very complex topic in the contact analysis, as well as the compound characterization. In the tribology studies, different types of friction tester have been developed.

The Da Vinci's experiments were the first in this scientific topic capable of providing some measurements of the friction between two different bodies. Nowadays, many linear friction tester [141] are based on this "ancient" bench layout, because it is as simple as smart: it consists of a table on which a substrate is fixed and on which the sample can slide, as shown in Fig. 6.1. The compound is loaded by means of a calibrated weight and moved by adding an additional weight connected to its free end.

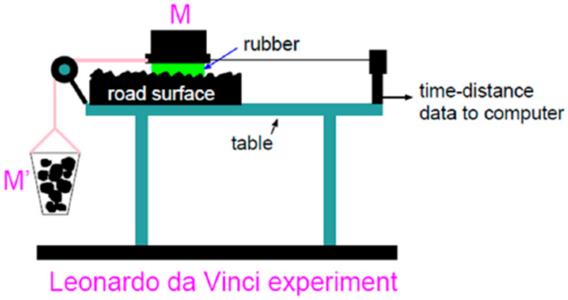

Fig. 6.1 Linear friction bench based on Da Vinci's experiment

In the modern era, Grosch's tribometer is considered one of the main examples of this category on linear testers [122]. The device, shown in Fig, 6.2, consists of a test sample pad, attached to a sample holder and pressed against the surface by a calibration load. To measure the frictional force, a U-spring dynamometer is connected to the holder by means of two steel wires. The test surface is driven by a motor coupled to a multi-ratio gearbox, that provides sliding speeds in a wide range. The sample and the track surface are enclosed in a temperature and humidity-controlled chamber. However, over the years, researchers have adopted various layouts to improve the friction coefficient measurements, evolving from the principles proposed in Grosch's work. Particularly, have been developed linear friction testers (LFT), whose moving part can be the rough surface or the sample holder [141].

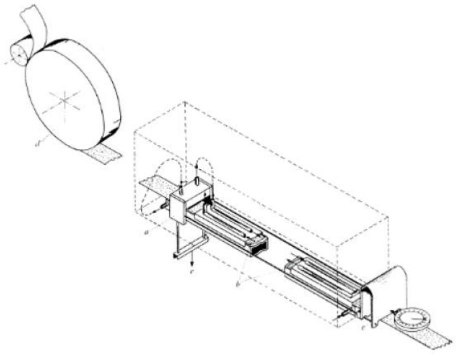

Fig. 6.2 Schematic representation of Grosch's tribometer

In Fig. 6.3, two examples of LFT with different moving parts are shown. The bench in the left representation is used by Klüppel [1] for his experimental investigation of temperature and load effects on the dry friction of tyre tread compound based on the movement of the granite substrate against the specimen, on which is applied a normal load; the other is a schematic representation of the LFT used at Vienna University [142], which provides a measure of frictional forces by moving the viscoelastic sample on a fixed rough substrate.

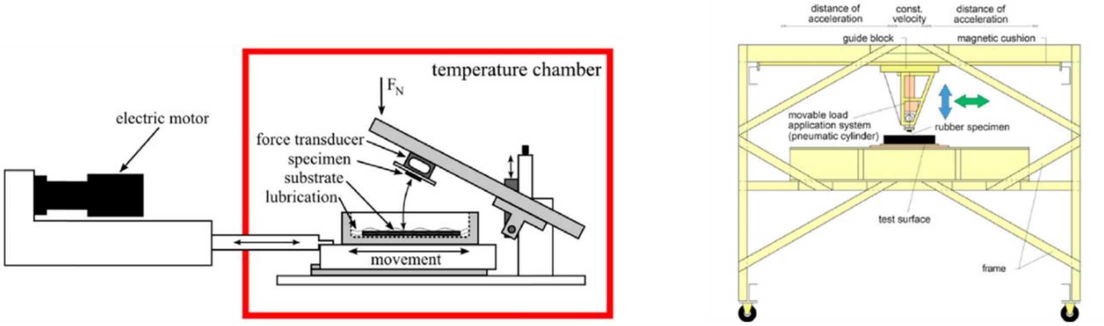

a) b)

Fig. 6.3 a) LFT with moving asphalt; b) LFT with moving sample holder

Other types of friction tester developed in the last years are the rolling friction testers. This category of devices makes use of the principle of double-disk tribometer, which consists of two discs rotating against each other. In tyre testing, this test equipment reproduces, on a small scale, the design of the tyre on drum [141], as shown in Fig. 6.4. Particularly, Liu et al. [143] have developed a high-speed test rig aiming to simulate the impact and release mechanics of tread block. The device consists of a small wheel with a rubber belt coating, which drives a bi-wheel with a steel surface. The small wheel is mounted directly on a solid base and is driven by an electric motor, while the big wheel is mounted on a solid base by a moving rock arm; lastly, another couple of stiff arms are used to lock the wheel shaft position, to obtain the desired value of interference between two wheels and to apply a compression the tread block sample.

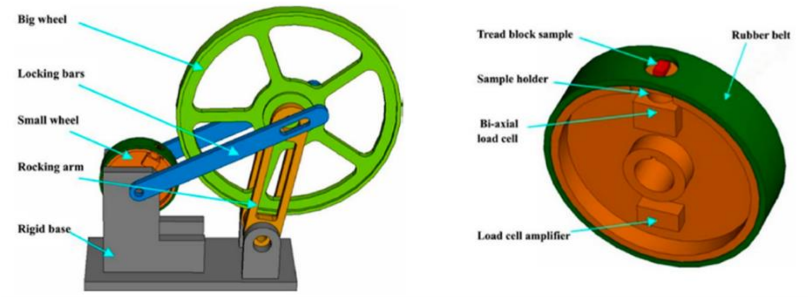

a) b)

Fig. 6.4 a) Rolling test rig; b) main component of driving wheel [143]

Further classes of tribometers belong to the pin on disk (PoD) and British Pendulum (BP), shown in Fig. 6.5. The first type is one of the most popular to study the friction and the wear and they are designed and constructed to study the complex friction phenomena in many engineering applications, from railway to tyre and biomedical fields. Conventional PoD machines provide a normal contact load between a stationary pin and a revolving disk and measure the resulting frictional force to evaluate the coefficient of friction [144, 145]. PoD tests can use different contact geometries (point contact, flat contact, line contact). Besides, the British Pendulum (BP) is widely accepted as a device for both on field and laboratory friction testing. The BP test is described in ASTM E303 [146] as a laboratory testing method to find the skid resistance of pavement surface. It is a low speed (<10 km/h) which is usually related to the micro-texture of road surface. In many researches, BP is used to perform the asphalt characterization [147].

In this chapter, the experimental friction investigation carried out with an evolved version of the BP during the research period at the Department of Industrial engineering is described. The data acquired by this bench on different tyre specimens have been further compared to the GrETA models results to provide a robust validation and outline the future scenarios of the research activities linked to experimental friction estimation.

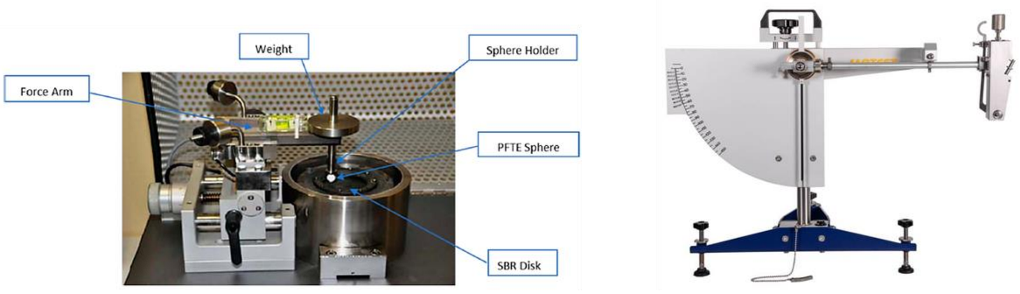

a) b)

Fig. 6.5 a) PoD tribometer proposed by Carbone et al. [148]; b) British pendulum

6.2 Friction experimental analysis through BP-evolved

6.2.1 Test bench description

The proposed tribological bench available at the Tyre Lab of the Department of Industrial Engineering (DII) at Federico II University is based on an evolved version of the classic British Pendulum tester for skid resistance measurements. Contrariwise the old configuration of the BP-evo [139, 140], which was developed during previous collaborations of the DII with Bridgestone Italia, this updated version has a new configuration of the load cell capable of reading the three forces channels (the tangential and the normal ones) according to the sensor reference system. The BP-evo and its conceptual scheme are shown in Fig. 6.6.

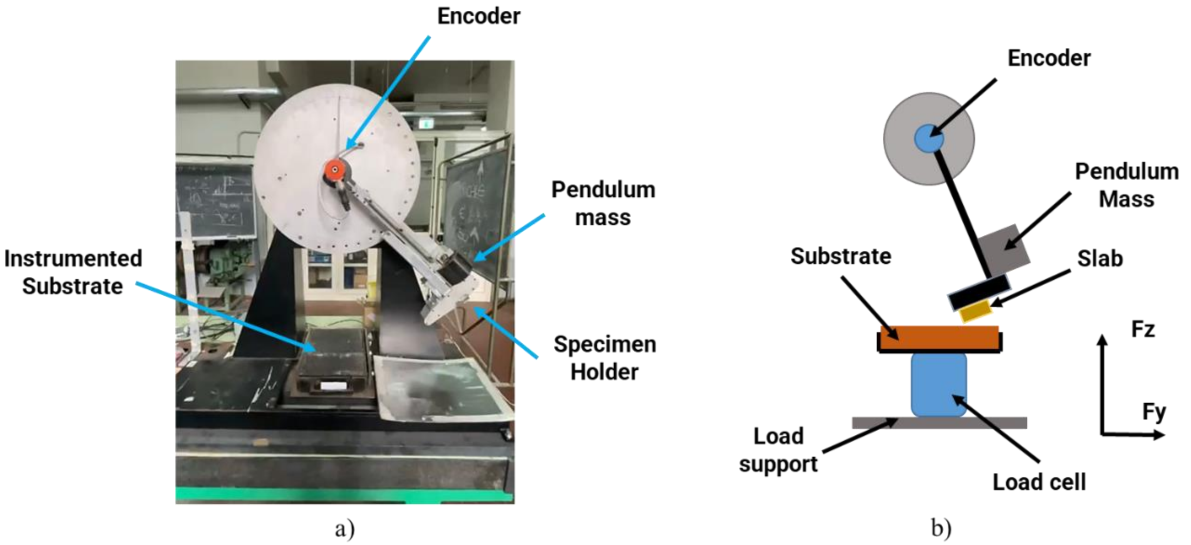

a)

b)

Fig. 6.6 a) British Pendulum evolved; b) test bench scheme

As represented in these figures, the tri-axial load cell is fixed on a rigid support and the rough substrate is fixed above the sensor. The cell is positioned in order to acquire positive normal load F_z and negative tangential force F_y along the sliding direction; moreover, the positioning is centred with respect to the plane of the pendulum motion allowing to acquire of neglectable values of F_x. The previous layout of the BP-evo included the load cell mounted on the pendulum arm, making the acquired signals processing more complicated due to inertial forces calculation and detraction from the global values. An encoder is installed in the revolute join to measure the angular speed of the pendulum arm, on which is fixed a mass so that the sliding body exhibits enough potential energy to win the frictional resistance forces. On the opposite side of the arm, a 100 N pre-loaded spring is mounted and a levers system exploits the spring reaction on the tread specimen holder.

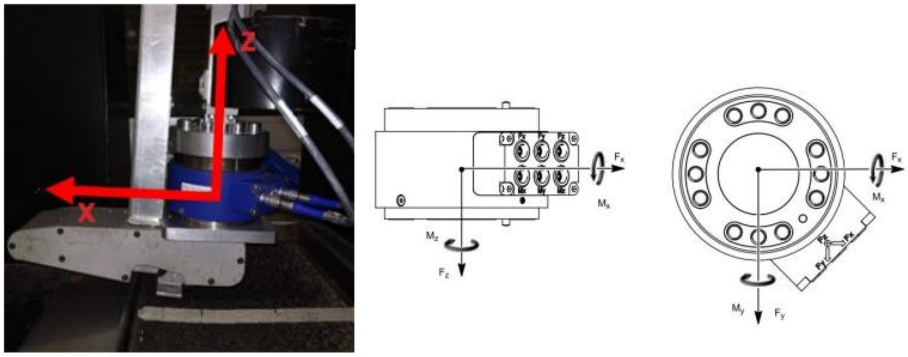

Fig. 6.7 Previous load cell configuration and reference system

The pre-load spring is changeable and particular attention is dedicated to the levers system with spring, whose stiffness is responsible for the contact pressure reached at the specimen/road interface, as shown in Fig. 6.8. The 20x20 mm specimens are usually obtained from tyre tread or compound slabs and then fixed on the holder, which can be regulated so that the material correctly slides. The distance between the revolute join and the substrate is adjustable thanks to a regulation mechanism beyond the pendulum. This regulation is fundamental in order to set the proper sliding distance. The forces and encoder signals are acquired by an A/D board and processed in Matlab environment to convert the respectively from Volt to N/m and rad/s.

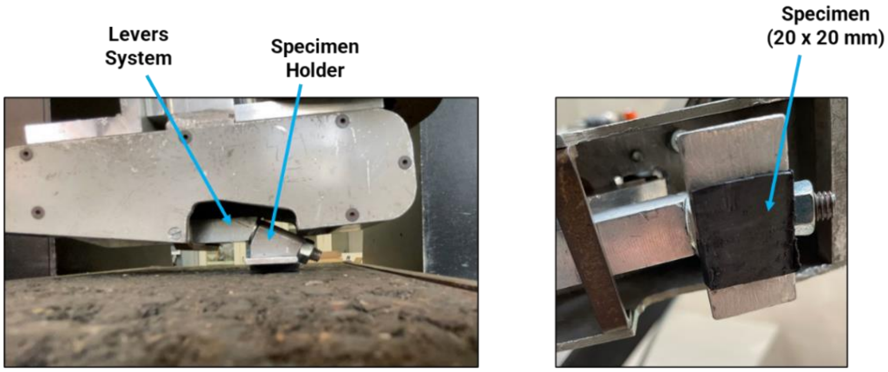

a) b)

Fig. 6.8 a) Levers-spring system acting on specimen; b) specimen fixed on suitable holder

A regulable release mechanism of the pendulum arm is available in order to change the starting position and perform a set of measurements with high repeatability, as shown in Fig. 6.9. It is important to change the drop position because different sliding velocity ranges can be reached during the motion and therefore, the friction coefficient values with respect to v_s can be analysed in the post-processing phase.

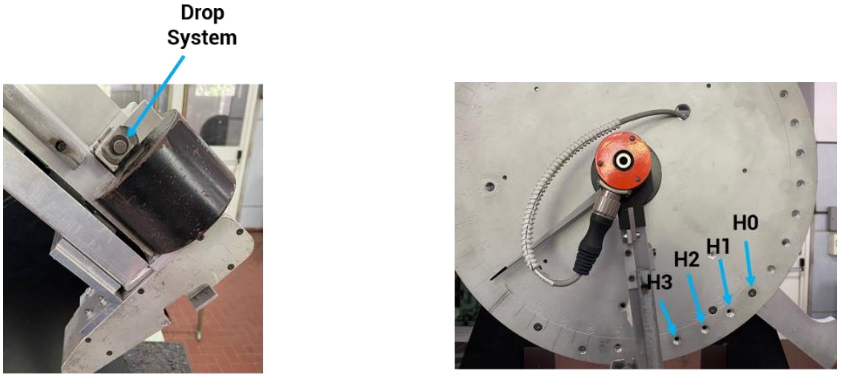

a) b)

Fig. 6.9 a) Pendulum drop button; b) Different starting position of the mass

6.2.2 Raw data acquisition and testing procedure

To acquire the data during the sliding of the pendulum arm on the instrumented substrate, a self-made GUI has been developed in collaboration with Bridgestone Italia in Matlab environment. The force signals and the sliding velocity can be acquired thanks to the interface shown in Fig. 6.10 and the A/D data logger plugged into the laptop for storing. The A/D board communicates with the encoder and the load cell.

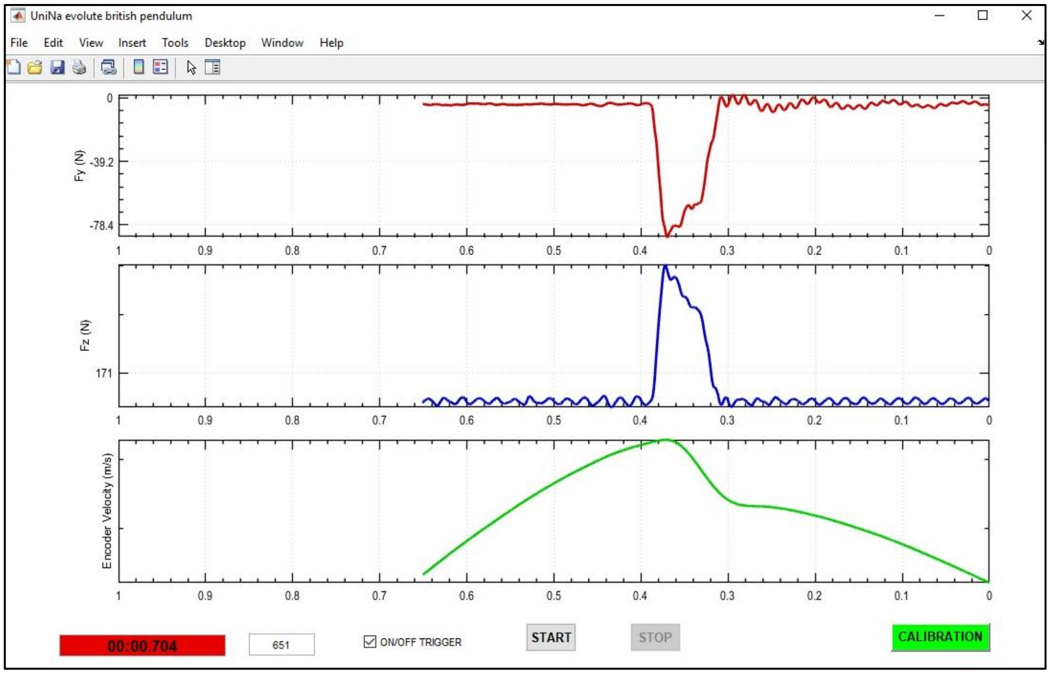

Fig. 6.10 Data acquisition GUI for BP-evo testing

Once pushed the start button on the GUI, the signals are acquired only if the motion of the pendulum art starts, because a trigger on the $\Delta\omega$ has been set.

For each testing condition in terms of temperature and sliding velocity combination, 10 measurements are carried out with the aim to achieve a tread off between specimen wear and enough data for an average evaluation of the friction coefficient value. The typical signals acquired by means of the GUI over 10 measurements are shown in Fig. 6.11, in which each colour matches with a different test.

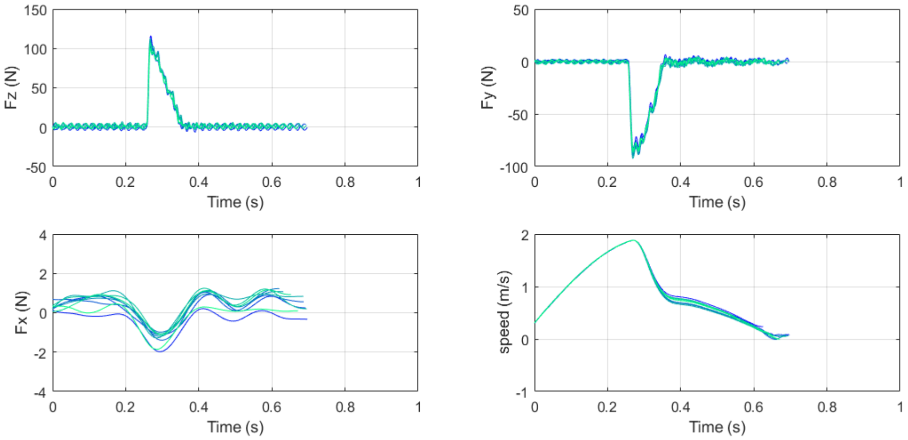

Fig. 6.11 Typical signals acquired over 10 tests with the BP-evo

As noticeable in the above subplots, the F_x values are very low compared to the others and then, it can be neglected in the evaluation of the total tangential force. Moreover, the velocity values are very similar among the 10 measurements as proof of the testing repeatability procedure and drop mechanism of the mass (it is expressed in m/s because for each test condition is measured the length of the pendulum). The reference system of the load cell on the rigid basement is oriented so that the F_y are considered negative. Both F_z and F_y before and after the contact are zero but, during the specimen/substrate interaction, they reach an absolute maximum and then decreases until the contact with the substrate ends and the maximum deceleration is observed.

The testing procedure consists of performing 10 measurements for the DOE outlined in Table 6-1. For each substrate-temperature-starting position combination, 100 N pre-load spring is taken into account, because higher pre-load values do not affect the friction coefficient due to the levers system acting on the specimen holder and lowers give rise to nominal contact pressure far from the working range of the tested compounds, which belongs to truck/passenger automotive fields. The four different starting positions are chosen in order to analyse the friction coefficient in the sliding velocity range [0.5, 2] m/s.

Table 6-1 DOE for BP-evo testing

Temperature	20°C	45°C	70°C	
Starting Position	H0	H1	H2	H3
Pre-Load Spring	100 N	100 N	100 N	100 N
Substrate	Asphalt A	Asphalt B	Asphalt C	

Lower values of sliding velocity cannot be reached through the BP-evo testing because it would require very small contact lengths to avoid the pendulum stop during the specimen/road interaction: actually, if the motion starts from an almost vertical position of the mass with respect to the asphalt, the pendulum does not have enough potential energy to overcome the frictional resistance and the test is not useful. The friction coefficient of each specimen can be easily analysed with respect to the compound temperature: before starting the single test, a thermal gun is used to warm the specimen up to the temperature of interest, which is measured and checked by means of an IR pyrometer. Once the temperature and starting position combinations are completed on a specific asphalt, the latter is usually changed choosing from the available described in Fig. 5.15 and the compound specimen is also replaced to avoid the wear could affect the friction estimation. It is important to highlight that a sort of “scrubbing” of the new specimen is always carried out on the selected asphalt because the requires a sort of “stabilization” before exploiting the effective friction coefficient. The scrubbing procedure consists of N test at ambient temperature, in which the pendulum slides starting from the same initial position, H0 for example. The amount of repetition N depends on the compound behaviour unless the corresponding friction coefficient reaches a stable average value as shown in Fig. 6.12.

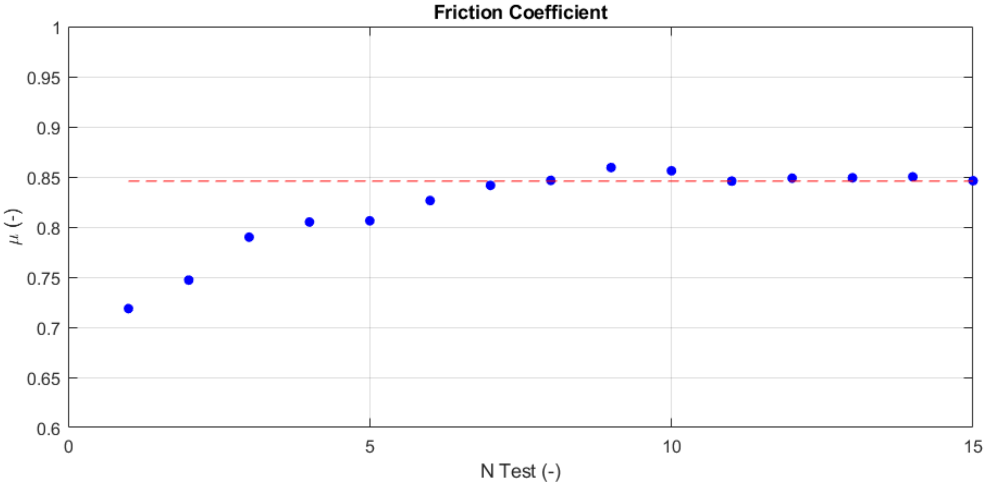

Fig. 6.12 Scrubbing procedure on a new tread compound specimen

6.2.3 Friction coefficient estimation from BP-evo data

The friction coefficient can be estimated by processing the raw data acquired through BP-evo testing. For this purpose, the forces and sliding velocity have to be analysed in the time range corresponding to the contact phase between the compound specimen and the instrumented substrate. In the approach proposed in this paragraph, it is assumed that the contact starts when the maximum pendulum velocity is reached and it finishes when the F_z is close to 10 N. This threshold has been chosen because a significant part of the specimen area would no longer be in contact with the asphalt in correspondence with this normal load value. The signals extrapolated are displayed in red in Fig. 6.13.

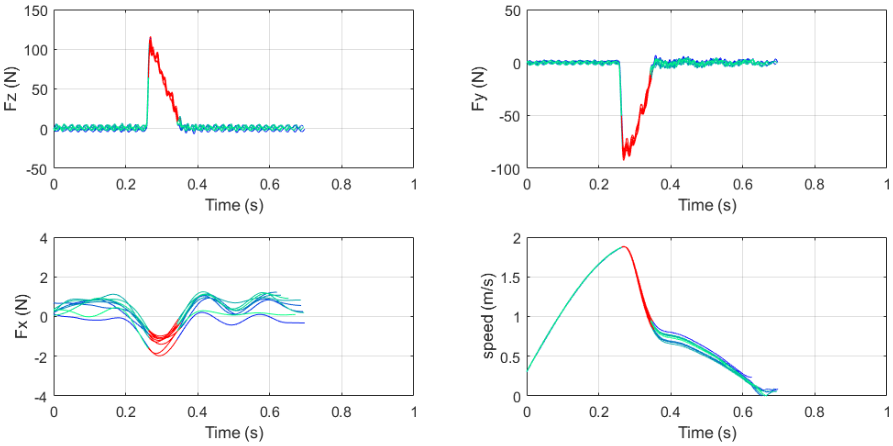

Fig. 6.13 Signals extrapolated in the contact phase (red lines)

Once extrapolated the signals in the contact phase, the ratio of the absolute value of F_y respect to the normal force, F_z, is analysed towards the measured velocity. In Fig. 6.14a, the ratio values towards the velocity for each test at ambient temperature and starting position H10 are shown. In this diagram, the friction coefficient exhibits a stable trend in the middle-velocity range (or time range), where a full contact with the rubber area and the substrate usually occurs; in the lower and higher velocity ranges, this ratio exhibits a little noise since the contact at the leading edges is not complete and therefore, these areas are excluded in the analysis. In Fig. 6.14b, the average value of the F_y/F_z in the highlighted area are displayed for every single test. The standard deviation of the μ_{avg} over 10 measurements is very low (~0.03) as proof of the trustworthiness of the test procedure repeatability, except for the first test, whose mean value is a bit out of the range.

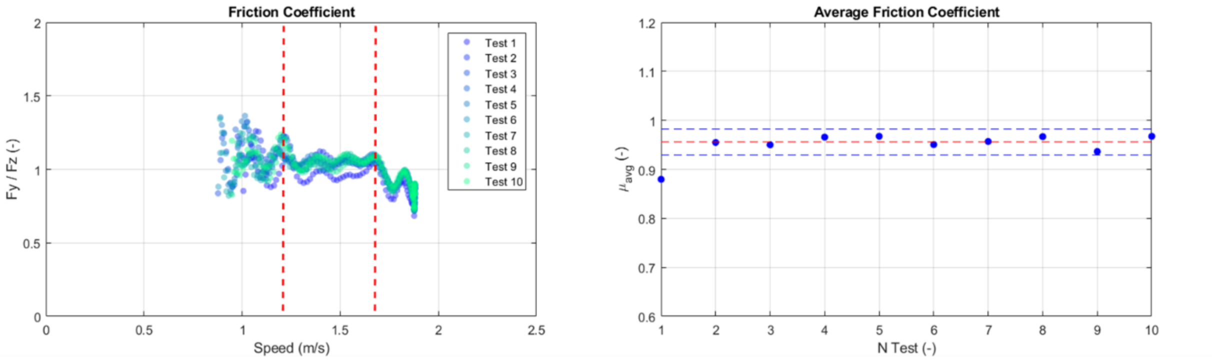

a) b)

Fig. 6.14 a) Forces ratio towards the measured speed; b) average friction coefficient over 10 tests

This processing approach can be carried out on experimental data acquired also for other starting positions test (H0, H1, H2, H3). In Fig. 6.15a, the raw values of the ratio acquired at different starting position at 20°C and using the 100N pre-load spring are displayed through specific colour makers: the acquisitions would seem to be linked together in the entire velocity range even if the pendulum release position changes. This means that a specific trend of friction coefficient towards the velocity can be identified. According to the previous the described procedure, the average friction values with their standard deviation evaluated in the velocity range of interest for each cluster of data is portrayed in Fig. 6.15b. Each error maker is considered with respect to the mean value of the sliding velocity for the corresponding range. It is interesting to point out that some data are superposed in certain velocity ranges, but the area corresponding to different average v_s, leading to specific trends of the μ_{avg}. The values displayed in Fig. 6.15b and the corresponding contact length chosen for each start position are outlined in Table 6-2.

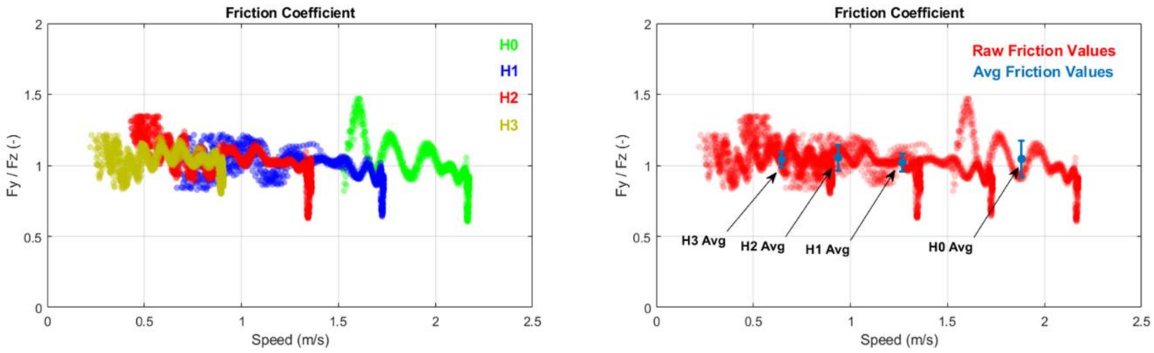

a) b)

Fig. 6.15 a) Forces ratio at different pendulum starting positions; b) average friction coefficient towards the velocity

Table 6-2 Testing parameters and output friction values

Position	Pre-Load	T (°C)	v_s (m/s)	L_{cont} (cm)	μ_{avg} (-)	μ_{std} (-)
H0	100 N	20°C	1.88	10	1.045	0.128
H1	100 N	20°C	1.26	9.6	1.022	0.062
H2	100 N	20°C	0.93	8.0	1.055	0.090
H3	100 N	20°C	0.64	5.0	1.042	0.039

As noticeable in the table data, the contact length changes with the starting position: it is necessary to reduce this parameter depending on the x0 of the pendulum because the mass characterised by lower potential energy before starting the contact because the mass is endowed with an ever lower potential energy to be able to overcome the frictional resistance forces.

Hence, taking into account the friction values representation in Fig. 6.15, the experimental results obtained by means of BP-evo testing on different truck/passenger tyre compound specimens is described in the next paragraph to perform a sensitivity analysis on frictional behaviour following the DOE in Table 6-1.

6.2.4 Friction coefficient results on different compound specifications

The experimental analysis of friction coefficient data acquired through VESevo testing is performed on different slabs specimens belonging to different tyre tread compound application. Each compound has been characterised employing the VESevo, as described in 3.6 VESevo: innovative device for non-destructive viscoelasticity analysis. In Fig. 6.16 the master curves normalised to the maximum value is reported for 5 compounds used for experimental analysis through BP-evo.

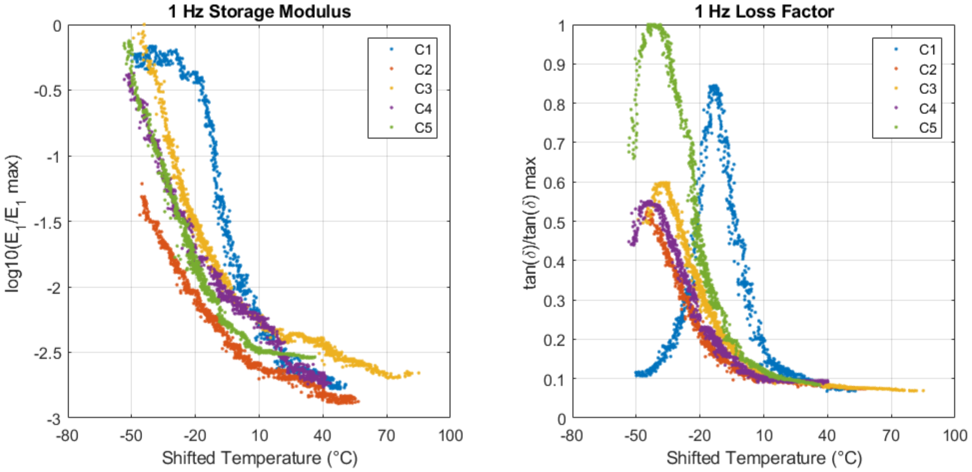

Fig. 6.16 VESevo 1Hz normalised master curves for compounds of interest

The compound C1 and C2 are the same described in Fig. 5.25. It is again clear how the VESevo measurements can recognize the different compound properties in terms of loss factor peak values and glass transition temperatures thanks to the algorithm proposed in paragraph 3.6 VESevo: innovative device for non-destructive viscoelasticity analysis.

The experimental friction measurements are performed following the DOE outlined in Table 6-2. The results are displayed in terms of subplot for each tyre tread specimen with the aim to identify the friction coefficient variations due to roughness – sliding conditions effects. The author highlights that the experimental results at low speed could be affected by inaccuracies due to the low sliding distance for the completion of the pendulum motion.

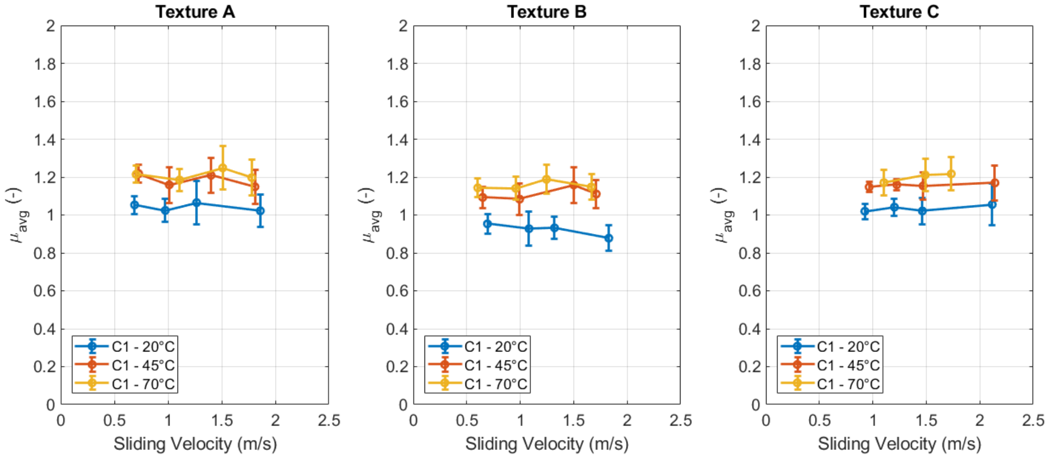

Fig. 6.17 Compound C1 friction results on three different textures with 100 N pre-load spring

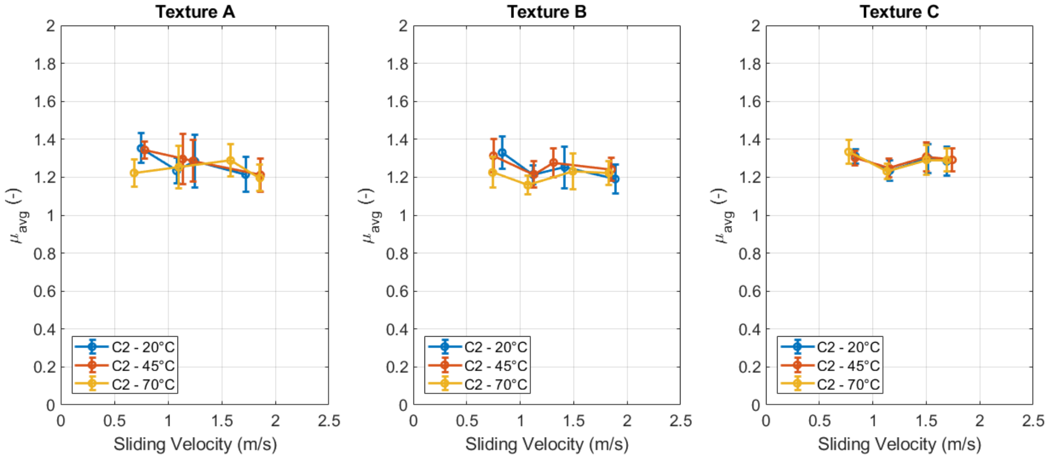

Fig. 6.18 Compound C2 friction results on three different textures with 100 N pre-load spring

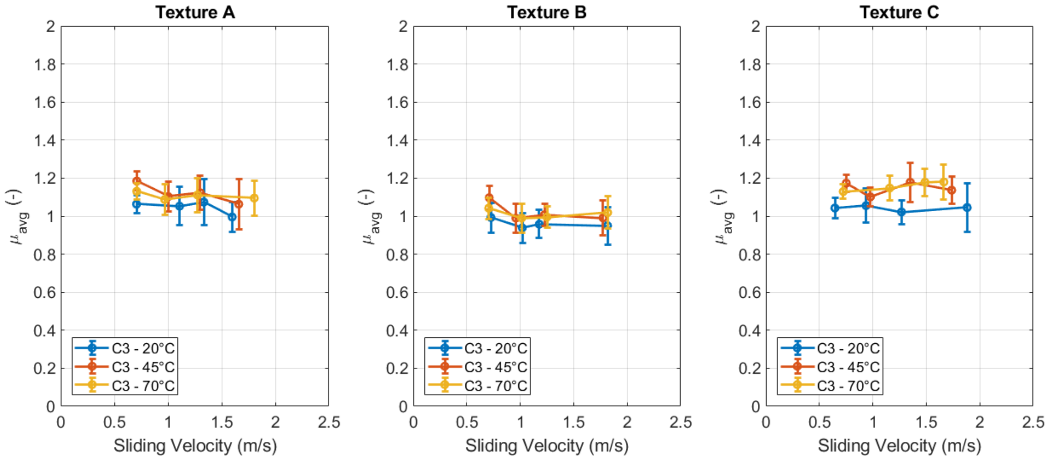

Fig. 6.19 Compound C3 friction results on three different textures with 100 N pre-load spring

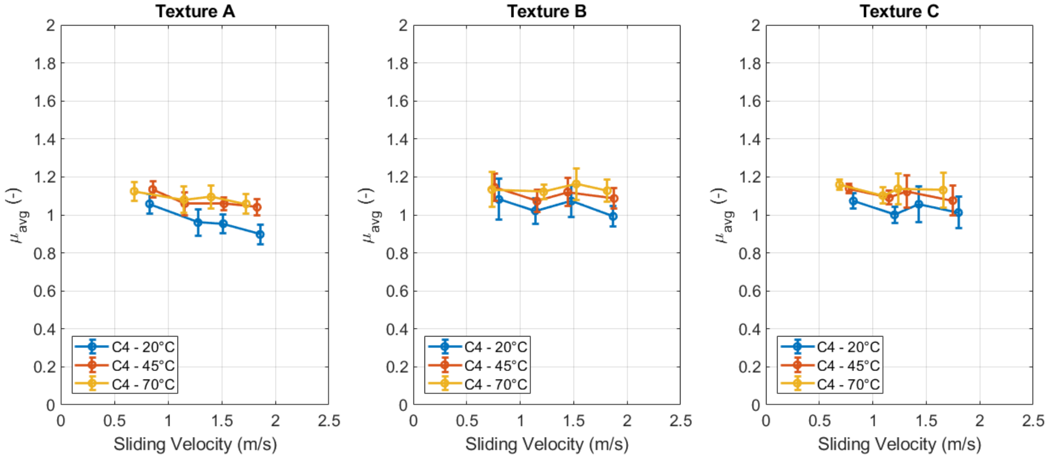

Fig. 6.20 Compound C4 friction results on three different textures with 100 N pre-load spring

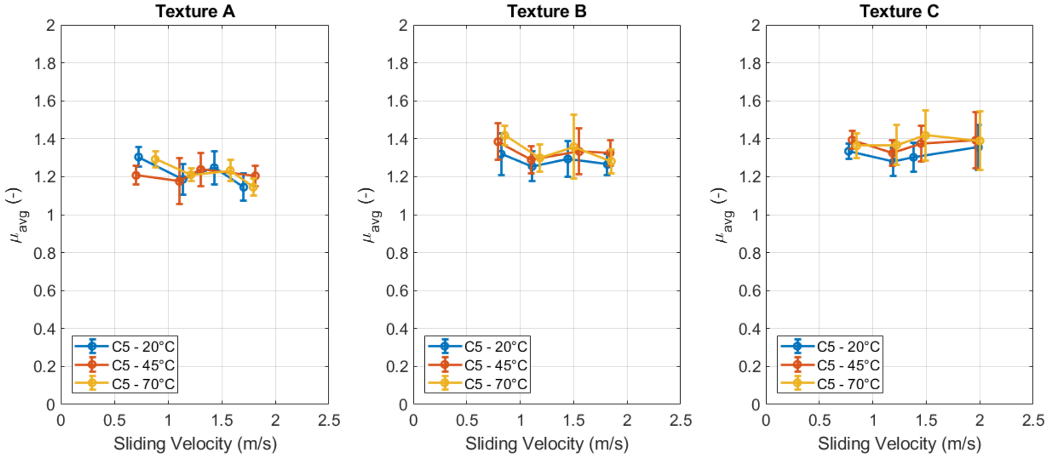

Fig. 6.21 Compound C5 friction results on three different textures with 100 N pre-load spring

In Fig. 6.17-21, different trends of friction coefficient towards temperature and sliding velocity for each texture and compound specimen. Particularly, compound C2 exhibits very slight variations due to temperature on texture C, while differences can be detected in the case of the other textures. The specimen C1 displays a lower average grip on texture B, especially at 20°C:

this is confirmed from the roughness parameters synthesized in Table 5-1; moreover, C1's friction values are affected by temperature compared to the others thanks to higher loss factor in the temperature range [-20, 10]°C, which must be considered in the equivalent scale linked to the solicitation frequency $f = v_s/\lambda$. However, the overall results are affected by the low-relevant variation of viscoelastic properties towards the temperature, especially the loss factor: these materials are for truck tyre applications, which do not usually exhibit relevant performance increasing the temperature working condition, excepted compound C1 and C5.

In Fig. 6.22, the comparison of friction results among the tested compounds is displayed for each texture at 20°C towards the sliding velocity range of the experiment. Compounds C2 and C5 exhibit higher grip values on all considered textures compared to other specimens. Besides, compound C4 presents the lowest friction coefficient on texture A and similar values to C1 and C3 on texture C: this is a clear indication of how each compound interacts differently with the macro and micro asperities of the considered asphalts leading to different friction coefficients.

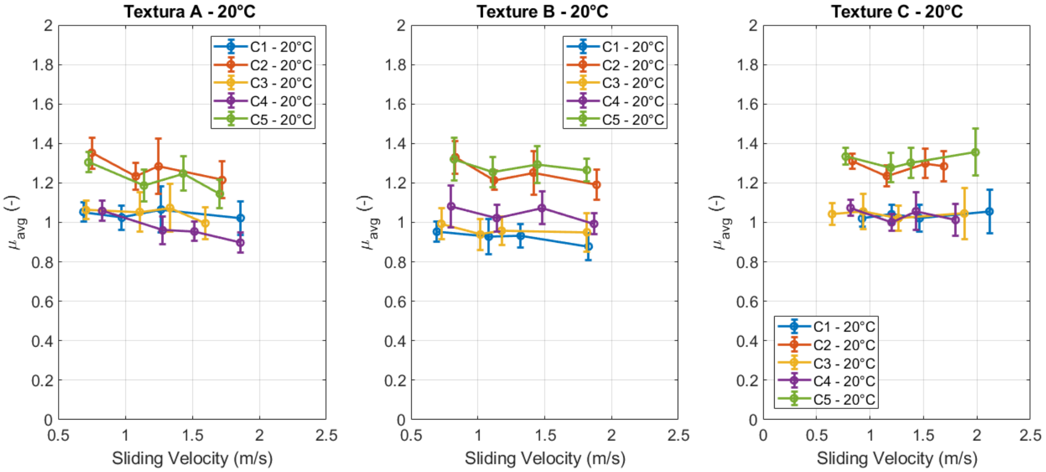

Fig. 6.22 Friction results differences between compounds highlighted at 20°C

6.2.5 Quasi-static friction measurements through BP-evo

The quasi-static friction measurements can be carried out through the BP-evo according to the bench layout displayed in Fig. 6.23, which is similar to Da Vinci's experiment described in Fig. 6.1. The main target of these measurements is the evaluation of the τ_{s0} for each compound on different textures to feed up the relationship for forces estimation in adhesive grip contribution, as defined in equation (5.81) in paragraph 5.6.4 GrETA model: Adhesive friction contribution

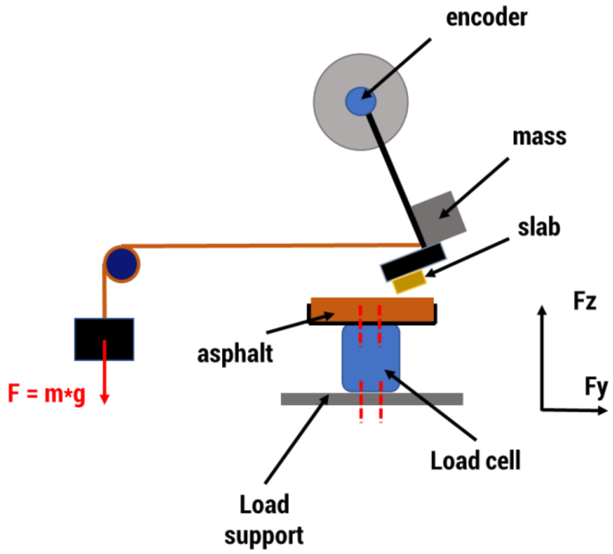

Fig. 6.23 Friction results differences between compounds highlighted at 20°C

As shown in Fig. 6.23, an inextensible rope is fixed to the pendulum arm in such a way as to guarantee the sliding of the specimen on the surface with a tangential force linked to the weight through a pulley system. The value of the weight is chosen to make the sliding as much as possible quasi-static and measure the corresponding normal force utilizing the load cell, which is close to the pre-load spring value of 100 N. The τ_{s0} values extrapolated from these experiments on the compounds in Fig. 6.16 towards the roughness of the available textures (Table 5-1) are shown in Fig. 6.24. In this diagram, different values of quasi-static shear stress are estimated for each compound at the same normal loading conditions and texture. This means that each specimen exhibits a specific behaviour in quasi-static conditions according to the E_0 values, which are identified through fractional derivative model introduced in paragraph 2.3.4 Generalized Maxwell models.

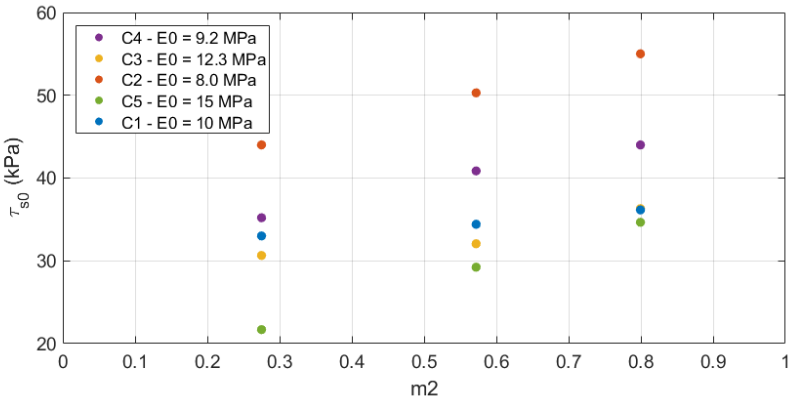

Fig. 6.24 Quasi-static shear stress on 5 compounds.

6.3 GrETA Model and experimental friction results comparison

The experimental friction results described in paragraph 6.2.4 Friction coefficient results on different compound specifications have been compared to GrETA model values to verify the trustworthiness of the simulations. The proposed contact mechanics model has been fed up with the road parameters in Table 5-1, the viscoelastic properties obtained with VESevo measurements and displayed in Fig. 6.16, the WLF parameters provided by the manufacturer. The simulation conditions are chosen similar to experimental measurements ones.

In Fig. 6.25-29, the comparisons between GrETA and BP-evo measurements for the compounds analysed on three different textures are shown. The model can reproduce quite faithfully the trends of the experimental measurements both in different asphalt and temperature conditions, especially in the velocity range [1, 2] m/s. In some cases, a mismatch between data and model occurs at low velocity and this may be due to the lower reliability of BP-evo because of small contact lengths ≤ 5 cm.

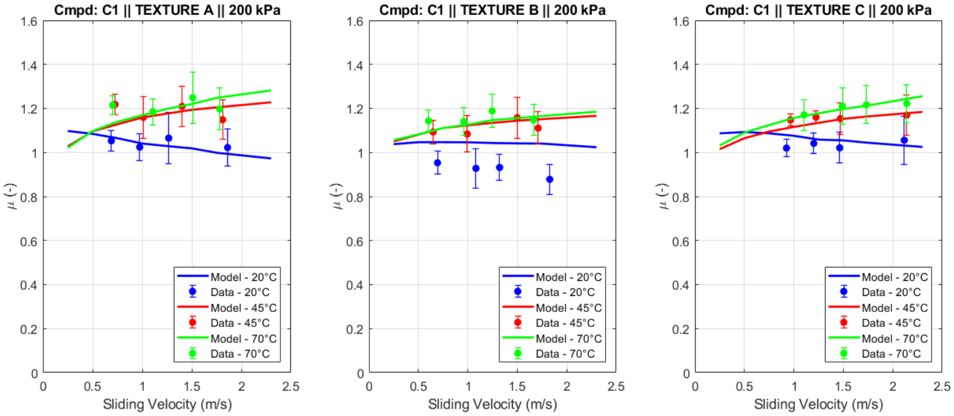

Fig. 6.25 Experimental friction results compared to GrETA simulation - Compound C1

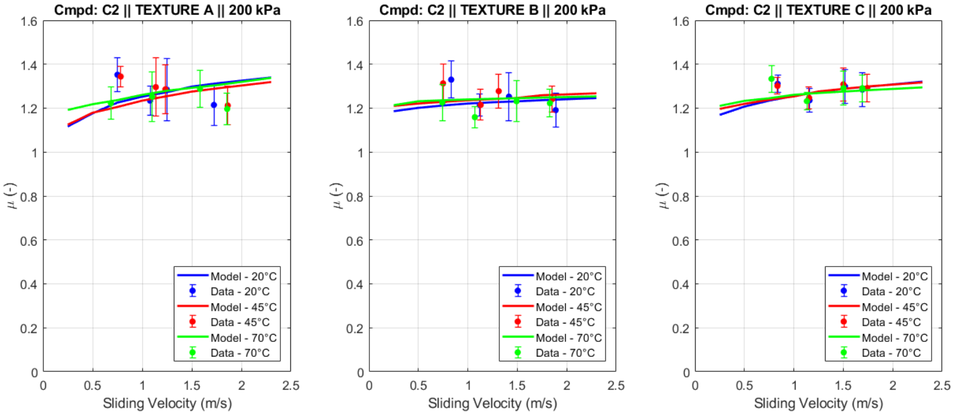

Fig. 6.26 Experimental friction results compared to GrETA simulation - Compound C2

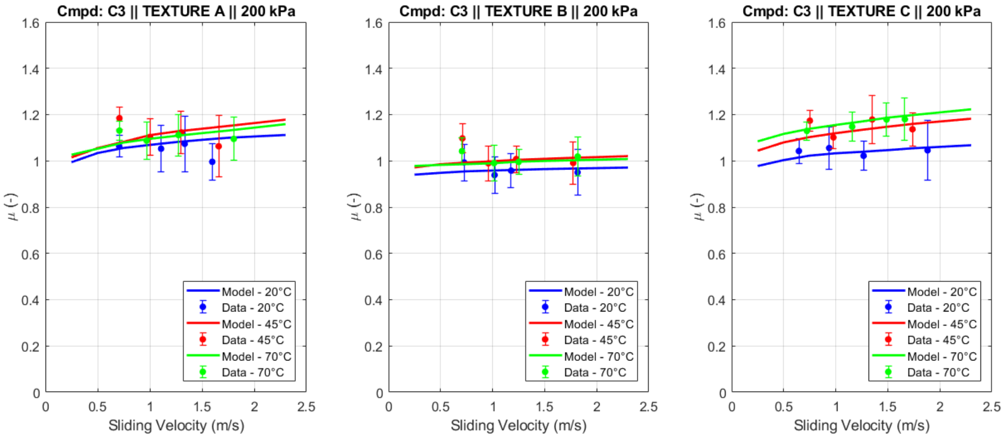

Fig. 6.27 Experimental friction results compared to GrETA simulation - Compound C3

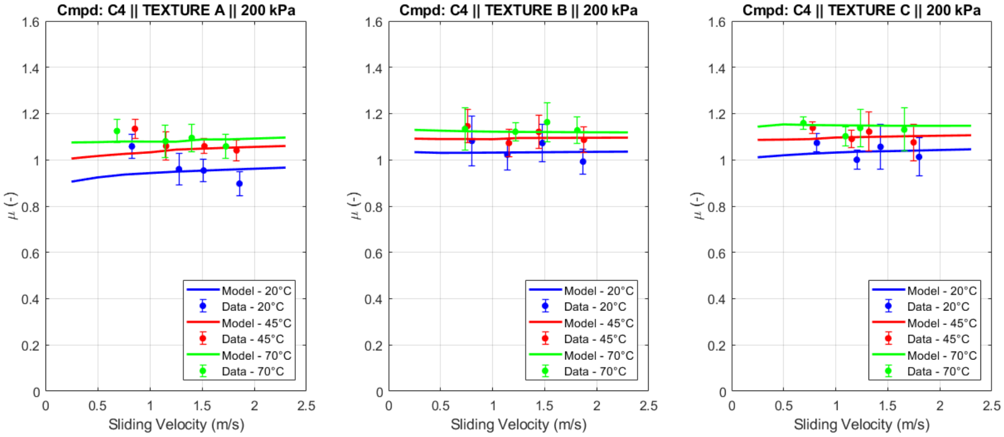

Fig. 6.28 Experimental friction results compared to GrETA simulation - Compound C4

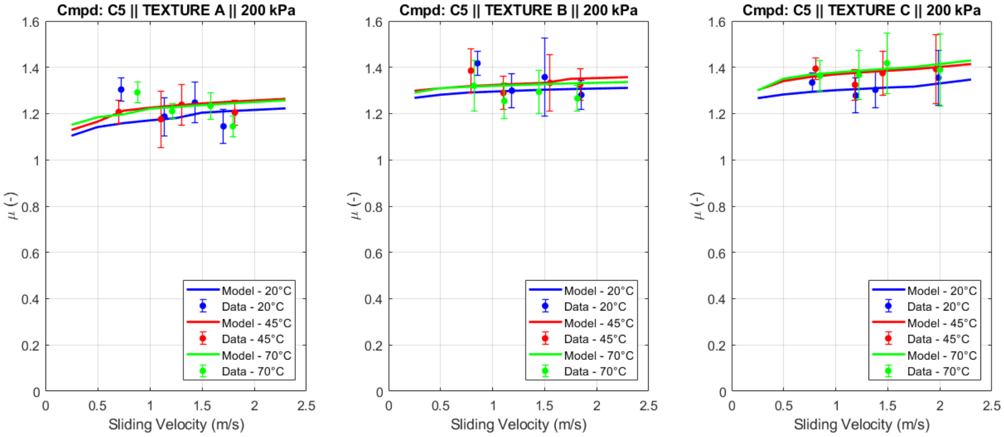

Fig. 6.29 Experimental friction results compared to GrETA simulation - Compound C5

Furthermore, the model seems to reproduce quite well the particular frictional behaviour of compounds: in the case of specimen C2, both model and experimental data exhibit very neglectable variations with the increasing temperature, especially on texture B and C; on texture A the test results are characterized by a higher dispersion and therefore a clear trend cannot be compared to the model. The GrETA model has been also capable of recognizing the frictional behaviour changes of compound C1: the experimental data, such as the model results, exhibit a slightly increasing trend towards the sliding velocity, which may be since a relevant hysteretic contribution occurs at high frequencies, at both 45°C and 70°C; contrariwise, a slightly decrement is noticeable at 20°C of model and BP-evo data.

However, the experimental results and their comparison with the GrETA predictions are a preliminary case study outlined in the thesis work and they can be considered as a forerunner for the next development in friction testing and contact modelling for automotive applications. Further experimental data in different contact pressure, temperature and sliding conditions should be considered in order to provide a more robust validation of the proposed model. Taking into account the GrETA model implementation and BP-evo bench layout, there are some limits to the proposed results that can be further explained. The BP-evo is advantageous because it guarantees an almost stable temperature during the sliding, even if a climatic cell is not available; on the other side, it is disadvantageous because:

- It cannot provide a reliable friction value at low speed due to intrinsic limits in the pendulum system;
- It cannot provide friction measurements at different contact pressure because of the levers system through which the pre-load spring acts on the specimen holder. This mechanism should be modified or experiments with a smaller specimen in terms of dimension should be taken into account.

Concerning the GrETA model:

- The estimation of the minimum contact wavelength at which the hysteretic contribution must be truncated is a crucial limit in the proposed model, as well as in the others available in the scientific literature. To improve the empirical relationship proposed in (5.111), further experiments on a wider number of textures considering different compound specification is an essential activity to focus on;
- The estimation of the power loss due to compound hysteresis should be improved parallel to the optimization of the minimum contact length identification;
- The adhesion contribution requires an improvement of the quasi-static shear stress estimation. This activity needs an advanced bench characterized by an electrical engine (or a stepper type) together with a gearbox to be sure of the sliding limit conditions;

- The effective contact area is another main variable to be optimized in the adhesion friction calculation thanks to a wider experimental session with the pressure-sensitive film.

6.4 Pin on Disk tribometer experiments at the UniNa Tyre Lab

The Pin on Disk (PoD) tribometer is another bench available at the UniNa Tyre Lab at the Department of Industrial Engineering [149, 150]. The PoD is mainly focused on the experimental analysis of the adhesive behaviour of compounds being the texture usually marble (R_a = 0.16 µm) or glass (R_a = 0.03 µm). in some cases, two kinds of abrasive paper are used (R_a = 0.14 µm or R_a = 0.120 µm). The elements of the machine are:

- An electric motor, driven by an inverter;
- A metal disk, moved by the motor through a belt, that can be covered with another disk of different material;
- An arm on which a rubber specimen is housed;
- An incremental encoder, installed on the disk axis in order to measure is angular position and velocity;
- An optical pyrometer pointed on the disk surface in the proximity of the contact exit edge, that provides an estimation of the temperature at the interface;
- A thermocouple located in the neighbourhood of the specimen used to measure ambient temperature.

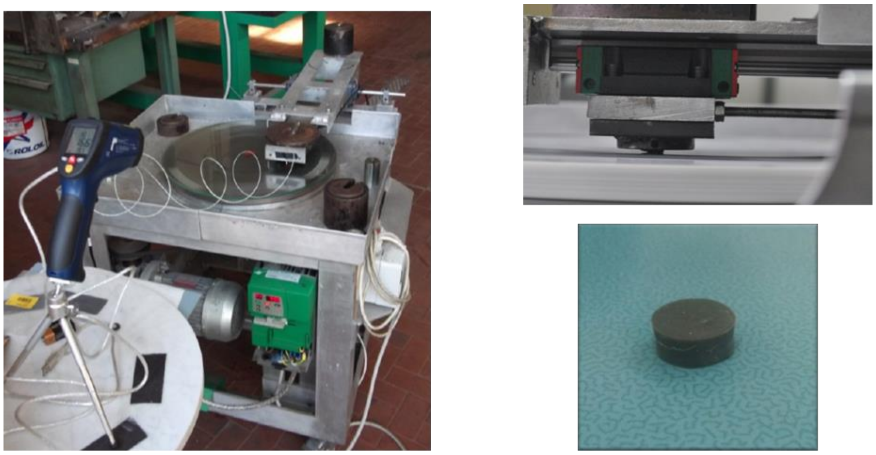

a) b)

Fig. 6.30 a) Pin on Disk tribometer at the UniNA Tyre Lab; b) dimension and holder of the specimen

The arm is vertically approached to the rotating disk surface and through the application of calibrated weights on the arm, the normal force between the specimen and disk can be varied. The specimen, which is usually 12-mm diameter sample, is usually heated through a thermal gun and the test duration is 3 seconds, which is enough to guarantee a stable value for tangential force measurement by the load cell.

As previously introduced, the adhesion contribution is strictly connected with the micro-texture of the substrate profile; adopting surfaces characterized by low macro-roughness makes the hysteretic friction contribution neglectable, pointing the attention to the adhesive mechanics.

The proposed experimental analysis has been carried out on four different specimens, which are the same introduced in paragraphs 3.3.1 Experimental sessions and modulus evaluation and 3.6.5 Comparison of VESevo results to DMA reference curves. The normalized viscoelastic properties obtained by dual cantilever DMA are resumed in Fig. 6.31.

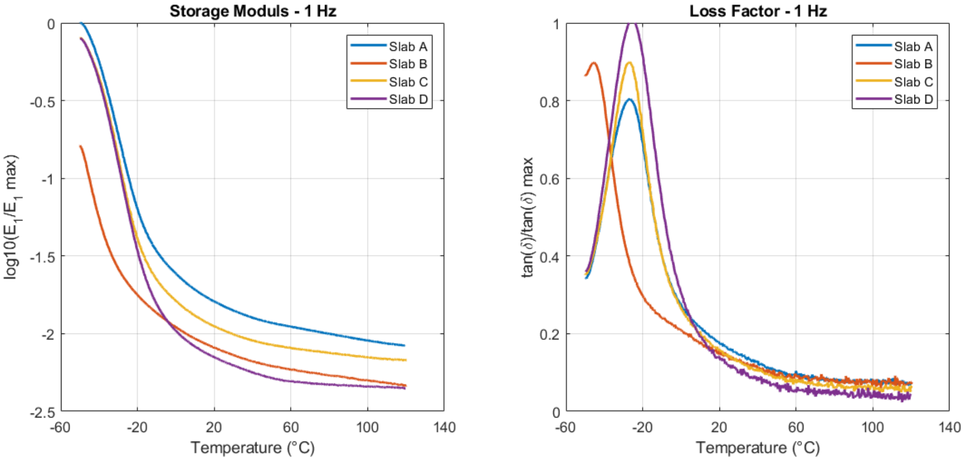

Fig. 6.31 Normalized storage modulus and loss factor obtained through DMA @1Hz

The measurements of the adhesion friction coefficient have been performed taking into account the testing parameters outlined in Table 6-3. The test cannot be carried at higher temperatures because a climatic cell is not available and it is not to keep the temperature stable over the 50°C. Moreover, the low-speed acquisitions could be affected by stick-slip phenomenon and 0.05 m/s is the low limit value at which perform the experiments.

The experimental friction values at different sliding velocity, temperature and normal load are displayed in Fig. 6.32-33. The effect of the increasing contact pressure (or normal load) is clear at both 25°C and 40°C: the average friction values for all the compounds decreases with respect to the applied load. This result is fairly in accordance with Fig. 5.26 GrETA’s adhesion friction maps.

Table 6-3 DOE for Pin on Disk tribometer

Temperature	25°C		40°C	
Sliding Velocity	0.05 m/s	0.3 m/s	0.7 m/s	1 m/s
Normal Load	5 N	15 N	25 N	
Substrate	Marble disk			

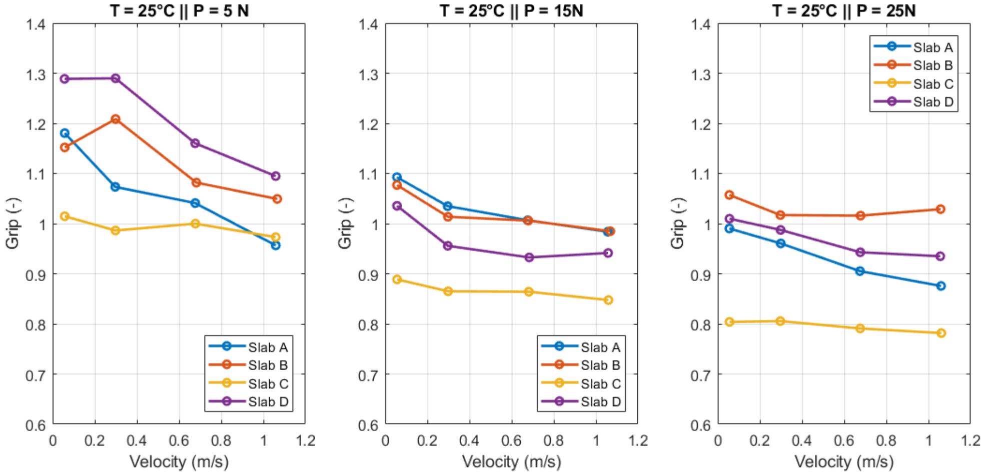

Fig. 6.32 Friction coefficient results at 25°C for the available slabs

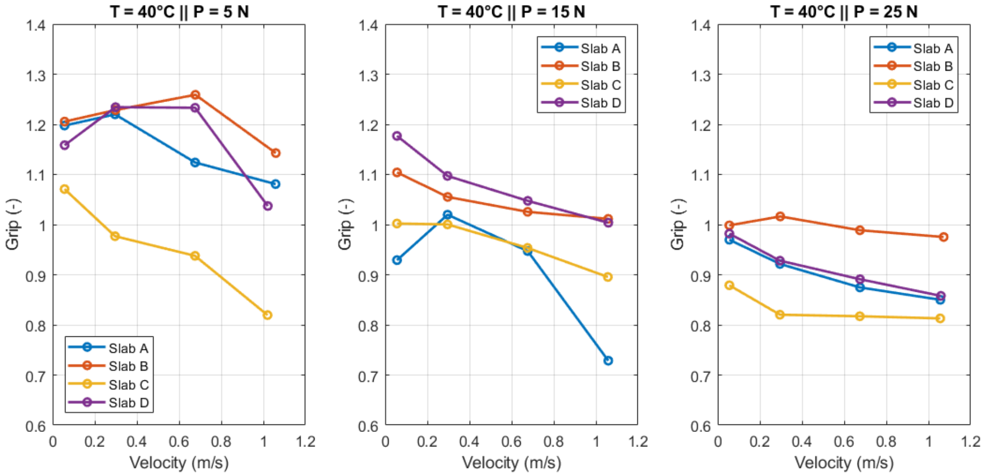

Fig. 6.33 Friction coefficient results at 40°C for the available slabs

The temperature marginally affects the adhesion frictional behaviour on the marble of these compounds. This may be due to the relatively neglectable variations of viscoelastic properties of these materials in the experimented temperature range. Furthermore, the frictional behaviour of slab A is very singular compared to the other materials: it exhibits a relatively high storage modulus low plateau and its friction values are similar to slab D ones, which exhibits the lowest E_1 values at the test temperatures. This should be an effect of the "micro-hysteresis" contribution to the overall frictional behaviour of the material due to micro-roughness of the marble.

Hence, the results shown in this paragraph define the limits of the UniNa PoD tribometer, which can be overcome by improving the experimental testing procedures at high temperatures, as well as the chance of sliding on different textures with the aim to propose a further frictional behaviour sensitivity together with the BP-evo bench.

6.5 Design of an innovative friction tester at UniNa Tyre Lab

To overcome the limits of the tribometers described in the previous paragraphs, a new test rig system for friction analysis has been conceived. It was designed to provide several tribological and mechanical testing solutions. The device is an automatic tester, developed mainly for the measurement of friction, wear and lubrication. The tester, using linear reciprocating movement, can be also used for many other purposes, as well as fatigue or scratch tests. Actually, its wide range of testing parameters, contact geometries and add-on options allow users to conduct testing by simulating all in-service conditions, like different movement modes (linear, reciprocating), contact modes (point, area), speed, lubrication, materials, high temperatures, etc.

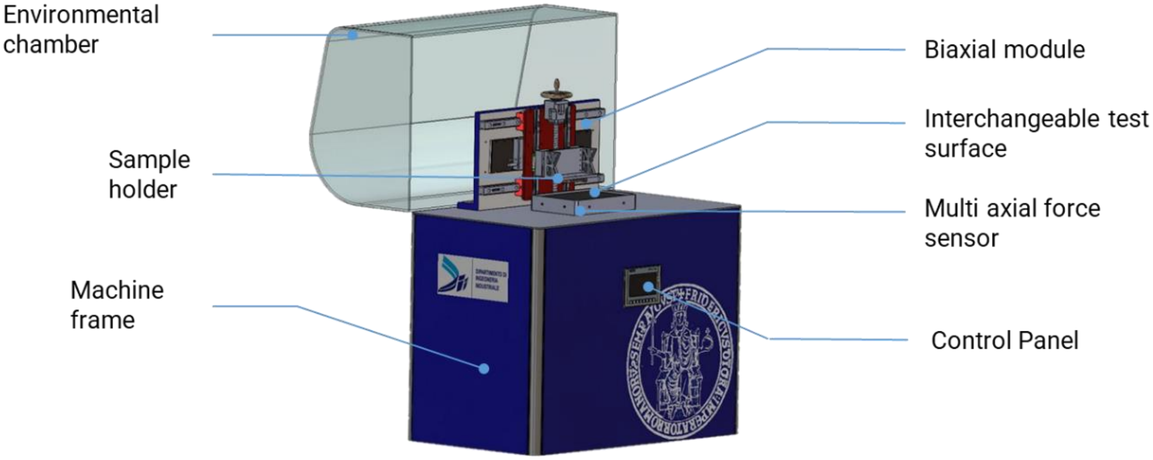

Fig. 6.34 Key instrument features of the innovative friction tester

The bench is shown in Fig. 6.34. It is designed for vertical loads up to 900N and axial loads up to 1300N. The tester provides testing solutions adhering to different textures, which is a key feature for tyre applications. The test is fully automated with a speed control from 0.01 to 1 m/s. The environmental chamber is developed in order to keep the temperature stable during the acquisitions, contrariwise to the available tribometers at the UniNa Tyre Lab. The bench is surely easy to use and safe for users. The biaxial module is characterized by the following features:

- Movable and manual Z-axis configuration to apply normal load. The load in the radial direction is supported by the guide rail, with a maximum capacity of 900 N and a travel distance of 200 mm;
- The module is interchangeable making the testing rig modular and allowing to perform different tests;
- A high-performance iron core motor offers the possibility to combine high acceleration and speed with high continuous force. The maximum tangential force expectable is almost 1300N with an acceleration peak value of 7.5 ms^{-2};
- The presence of a bespoke sample holder allows changing quickly different test sample applied to a mounting plate. Thanks to the F_z load, local contact pressures in the range between 0.3 and 8 bar can be simulated, according to the size of the contact patch of the sample.

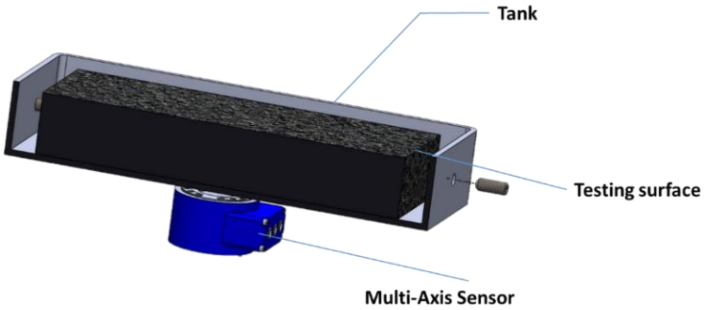

Fig. 6.35 Interchangeable testing surface

The interchangeable testing surface is a key requirement of the innovative bench. In the configuration displayed in Fig. 6.35, an aluminium tank mounted on a high precision force sensor hosts the texture of interest for the frictional experiments. The maximum testing rig surface is about 200x300 mm. The multi-axis sensor is capable of measuring the forces and torques on the three axes with a range of up to 10 kN (axially) and 2kN (tangentially).

Hence, the features and the instrumentation of this innovative bench should be in future applications very useful for:

- Investigation of different friction conditions;
- Investigation of the influence of temperature/road roughness/contact pressure on rubber friction;
- Preliminary investigation on wear phenomena and the corresponding dependencies.

The above-mentioned analyses will be part of crucial research and empirical activities aimed at robust rubber-substrate contact modelling starting from a wider amount of experimental and more reliable data.

Conclusions and Further Developments

In the presented thesis the author's PhD path has been described starting from the analysis of viscoelasticity phenomena involved in tyre-road interaction and culminating with a preliminary experimental analysis of frictional behaviour between the rubber compound and the substrate.

The main target of the research activity has dealt with the innovative characterization methodology through the VESevo, which has been developed thanks to the precious support of the Applied Mechanics research team of the Industrial Engineering Department of University Federico II. The idea of this device was born during the research activities in collaboration with the main tyre manufacturers and Motorsport racing teams in order to overcome the limits in their applications and respond to the need of the tyre viscoelastic analysis in different conditions in terms of temperature, wear and ageing.

The viscoelastic characterization of tyre compounds has been also aimed at the comprehension of the contact phenomena between the tread and the substrate for automotive applications. For this purpose, the road profile analysis in terms of macro and micro asperity scales has been a further theoretical study to be examined in detail during the research period. The most common theories concerning the contact problem on self-affine surfaces, such as Klüppel's and Persson's, are a baseline to understand the hypothesis and different approaches for the friction coefficient prediction, which remains one of the most complex scientific topics to be comprehended in Vehicle Dynamics. To analyse the phenomena concerning the multi-contact problem between viscoelastic materials and rough surfaces, GrETA model has been further developed starting from its first version, which did not consider the hysteretic friction as a contribution of the entire power spectrum of the texture. The main advantage of the introduction of the GrETA model relies on the possibility to predict the friction variations induced by different tread compounds characterized by means of VESevo.

To identify the parameters of the GrETA model, the final part of the PhD program has involved a preliminary experimental friction analysis thanks to the tribometers available at the UniNa Tyre Lab of the Industrial Engineering Department. The evolved and instrumented version of the British Pendulum, which was developed during previous collaborations with Bridgestone Italia, has led to an estimation of experimental friction maps in order to further investigate the temperature, compound and texture effects of the grip; contrariwise, pin on disk tribometer has been useful for analysis of almost pure adhesive contribution on compound-substrate interaction with respect to temperature, contact pressure and sliding velocity. However, the author would highlight that the friction data acquired during the PhD period should be considered as a baseline for the GrETA model validation because they did not cover all the possible working range of a tyre compound. Actually, the experimental solutions adopted are characterized by the following constraints:

- The British Pendulum (BP-evo) cannot provide a reliable friction value at low speed due to intrinsic limits in the pendulum system;
- The British Pendulum (BP-evo) cannot provide friction measurements at different contact pressure because of the levers system through which the pre-load spring acts on the specimen holder. This mechanism should be modified or experiments with a smaller specimen in terms of dimension should be taken into account;
- The Pin on Disk tribometer cannot provide a reliable friction estimation at high temperatures due to the lack of a climatic chamber and testing procedure;
- The Pin on Disk tribometer layout cannot provide experimental friction analysis on rough surfaces but only on marble/glass for pure adhesion contribution or sandpaper for micro-hysteresis phenomena comprehension.

The limitations above-mentioned have brought out the need to develop a new friction tester, which is described in the last chapter of the PhD’s thesis. The key features of this bench will guarantee to overcome the limits of the Bp-evo and PoD and it will open to further research and experimental activities that should improve the analysis of frictional behaviour of tyre compounds, the identification of GrETA model parameters and then starting a preliminary experimental study of wear phenomena of tyres.

Appendix A

As described in paragraph 5.6.5 GrETA model: Hysteretic friction contribution, the hysteretic friction contribution can be determined by the power balance between the frictional power and the power loss due to viscoelasticity in the compound volume control according to Etienne-David's theory [138]:

$$\mu_{hys}\sigma_0 A_0 v_S = \int_V \left[\frac{1}{T_0}\int_0^{T_0} \sigma(x,y,z,t)\,\frac{d\varepsilon(x,y,z,t)}{dt}\,dt\right] dV \tag{A.1}$$

where μ_{hys} is the hysteretic friction, σ_0 is the nominal contact pressure, A_0 is the nominal contact area, v_S the sliding velocity, σ the stress field and ε the strain field. If the stress and strain fields are expressed by harmonic functions (this is legitim thanks to GrETA hypothesis):

$$\frac{1}{T_0}\int_0^{T_0} \sigma(x,y,z,t)\,\frac{d\varepsilon(x,y,z,t)}{dt}\,dt \;= \frac{1}{T_0}\int_0^{T_0} \omega\Sigma_0 \sin(\omega t+\delta)\,\mathrm{E}_0 \cos(\omega t)\,dt \tag{A.2}$$

If the following trigonometric function is used:

$$\sin(\omega t+\delta) = \sin(\omega t)\cos(\delta) + \cos(\omega t)\sin(\delta) \tag{A.3}$$

The equation (A.2) turns in the following:

$$\frac{\Sigma_0\omega \mathrm{E}_0}{T_0}\left[\int_0^{T_0} \cos^2(\omega t)\sin(\delta)\,dt + \int_0^{T_0} \cos(\omega t)\sin(\omega t)\cos(\delta)\right] \tag{A.4}$$

Where:

$$\cos^2(\omega t) = \frac{1+\cos(2\omega t)}{2} \tag{A.5}$$

$$cos(\omega t) sin(\omega t) = \frac{sin(2\omega t)}{2} \tag{A.6}$$

Finally, the equation is the following:

$$\frac{\Sigma_0\omega \mathrm{E}_0}{T_0}\left[\int_0^{T_0} \frac{1+\cos(2\omega t)}{2} + \int_0^{T_0} \frac{sin(2\omega t)}{2}\cos(\delta)\right] \tag{A.7}$$

where:

$$\int_0^{T_0} \frac{1}{2}\sin(\delta)\,dt = \frac{1}{2}\sin(\delta)\,T_0 \tag{A.8}$$

$$\int_0^{T_0} \frac{\cos(2\omega t)}{2}\sin(\delta)\,dt = \frac{1}{4\omega}\sin(\delta)\sin\,(2\omega T_0) \tag{A.9}$$

$$\int_0^{T_0} \frac{\sin(2\omega t)}{2} \cos(\delta)\, dt = -\frac{1}{4\omega} \cos(\delta) \left[\cos(2\omega T_0) - \cos(2\omega 0)\right] \qquad \text{(A.10)}$$

According to the following:

$$\omega T_0 = 2\pi$$

$$sin(2\omega T_0) = sin(4\omega\pi) = 0$$

$$\cos(4\omega\pi) - \cos(2\omega 0) = 1 - 1 = 0$$

The final relationship is obtained:

$$\frac{\Sigma_0 \omega \mathrm{E}_0}{T_0} \left(\frac{1}{2} \sin(\delta)\, T_0\right) = \frac{1}{2} \omega \Sigma_0 \mathrm{E}_0 \qquad \text{(A.11)}$$

Which allows the evaluation of hysteretic friction as explained in paragraph 5.6.5 GrETA model: Hysteretic friction contribution.

References

[1] Lang A, Klüppel M. Influences of temperature and load on the dry friction behaviour of tire tread compounds in contact with rough granite. *Wear* 2017; 380–381: 15–25.

[2] Carbone G, Lorenz B, Persson BNJ, et al. Contact mechanics and rubber friction for randomly rough surfaces with anisotropic statistical properties. *Eur Phys J E* 2009; 29: 275–284.

[3] Genovese A, Carputo F, Ciavarella M, et al. Analysis of multiscale theories for viscoelastic rubber friction. *Lect Notes Mech Eng* 2020; 1125–1135.

[4] Ferry JD. *Viscoelastic properties of polymers*. Epub ahead of print 1980. DOI: 10.1149/1.2428174.

[5] Williams ML, Landel RF, Ferry JD. The Temperature Dependence of Relaxation Mechanisms in Amorphous Polymers and Other Glass-forming Liquids. *J Am Chem Soc* 1955; 77: 3701–3707.

[6] Gent EAN, Walter JD. The Pneumatic Tire. *Sci Am* 1898; 45: 18408–18409.

[7] Mark JE, Erman B, Roland M. *The science and technology of rubber*. 2013. Epub ahead of print 2013. DOI: 10.1016/C2011-0-05820-9.

[8] Guiggiani M. Mechanics of the Wheel with Tire. In: *The Science of Vehicle Dynamics: Handling, Braking, and Ride of Road and Race Cars*. 2014. Epub ahead of print 2014. DOI: 10.1007/978-94-017-8533-4.

[9] Guiggiani M. *The Science of Vehicle Dynamics: Handling, Braking, and Ride of Road and Race Cars*. 2018. Epub ahead of print 2018. DOI: 10.1007/978-3-319-73220-6.

[10] Jazar RN, Jazar RN. Tire Dynamics. In: *Advanced Vehicle Dynamics*. Springer International Publishing, 2019, pp. 1–113.

[11] Calabrese F, Farroni F, Timpone F. A flexible ring tyre model for normal interaction. *Int Rev Model Simulations* 2013; 6: 1301–1306.

[12] Pacejka HB. *Tire and Vehicle Dynamics*. 2006. Epub ahead of print 2006. DOI: 10.1016/B978-0-7506-6918-4.X5000-X.

[13] Genovese A, Farroni F, Papangelo A, et al. A Discussion on Present Theories of Rubber Friction, with Particular Reference to Different Possible Choices of Arbitrary Roughness Cutoff Parameters. *Lubricants* 2019; 7: 85.

[14] Klüppel M, Heinrich G. Rubber Friction on Self-Affine Road Tracks. *Rubber Chem Technol*

2000; 73: 578–606.

[15] Persson BNJ. Theory of rubber friction and contact mechanics. *J Chem Phys* 2001; 115: 3840–3861.

[16] Lorenz B, Persson BNJ, Fortunato G, et al. Rubber friction for tire tread compound on road surfaces. *J Phys Condens Matter* 2013; 25: 095007.

[17] Farroni F, Sakhnevych A, Timpone F. A three-dimensional multibody tire model for research comfort and handling analysis as a structural framework for a multi-physical integrated system. *Proc Inst Mech Eng Part D J Automob Eng* 2019; 233: 136–146.

[18] Guiggiani M. *The science of vehicle dynamics : handling, braking, and ride of road and race cars*.

[19] Farroni F, Flavio. T.R.I.C.K.-Tire/Road Interaction Characterization & Knowledge - A tool for the evaluation of tire and vehicle performances in outdoor test sessions. *Mech Syst Signal Process* 2016; 72–73: 808–831.

[20] Popov VL. Thermal Effects in Contacts. In: *Contact Mechanics and Friction*. Berlin, Heidelberg: Springer Berlin Heidelberg, pp. 199–205.

[21] Lakes RS. *Viscoelastic materials*. Cambridge University Press, 2009.

[22] Lakes R. *Viscoelastic materials*. Cambridge: Cambridge University Press, 2009. Epub ahead of print 2009. DOI: 10.1017/CBO9780511626722.

[23] Wang MJ. Effect of polymer-filler and filler-filler interactions on dynamic properties of filled vulcanizates. *Rubber Chem Technol* 1998; 71: 520–589.

[24] Knauss WG, Emri I, Lu H. Mechanics of Polymers: Viscoelasticity. 2008; 49–96.

[25] Chevalier Y, Vinh JT. *Mechanics of Viscoelastic Materials and Wave Dispersion*. 2013. Epub ahead of print 2013. DOI: 10.1002/9781118623114.

[26] Renaud F, Dion J-LL, Chevallier G, et al. A new identification method of viscoelastic behavior: Application to the generalized Maxwell model. *Mech Syst Signal Process* 2011; 25: 991–1010.

[27] Greaves GN, Greer AL, Lakes RS, et al. Poisson's ratio and modern materials. *Nat Mater* 2011; 10: 823–837.

[28] Sahputra IH, Echtermeyer AT. Effects of temperature and strain rate on the deformation of amorphous polyethylene: A comparison between molecular dynamics simulations and experimental results. *Model Simul Mater Sci Eng*; 21. Epub ahead of print 2013. DOI:

10.1088/0965-0393/21/6/065016.

[29] Geethamma VG, Kalaprasad G, Groeninckx G, et al. Dynamic mechanical behavior of short coir fiber reinforced natural rubber composites. *Compos Part A Appl Sci Manuf* 2005; 36: 1499–1506.

[30] Lakes RS. Viscoelastic measurement techniques. *Review of Scientific Instruments* 2004; 75: 797–810.

[31] Landel RF. A Two-Part Tale: The WLF Equation and Beyond Linear Viscoelasticity. *Rubber Chem Technol* 2006; 79: 381–401.

[32] Holm S, Holm S. Models of Linear Viscoelasticity. In: *Waves with Power-Law Attenuation*. Springer International Publishing, 2019, pp. 67–93.

[33] Markovitz H. Boltzmann and the Beginnings of Linear Viscoelasticity. *Trans Soc Rheol* 1977; 21: 381–398.

[34] Gurtin ME, Sternberg E. On the linear theory of viscoelasticity. *Arch Ration Mech Anal* 1962; 11: 291–356.

[35] Wang X, Zhao K, Zhao H. Finite element simulation of biofilm viscoelastic behavior under various loadings. *J Mech Med Biol*; 18. Epub ahead of print 1 August 2018. DOI: 10.1142/S0219519418500562.

[36] Caputo M, Mainardi F. Linear models of dissipation in anelastic solids. *La Riv del Nuovo Cim* 1971; 1: 161–198.

[37] Pritz T. Measurement methods of complex Poisson’s ratio of viscoelastic materials. *Appl Acoust* 2000; 60: 279–292.

[38] Pritz T. Analysis of four-parameter fractional derivative model of real solid materials. *J Sound Vib* 1996; 195: 103–115.

[39] Pritz T. Five-parameter fractional derivative model for polymeric damping materials. *J Sound Vib* 2003; 265: 935–952.

[40] Di Paola M, Pirrotta A, Valenza A. Visco-elastic behavior through fractional calculus: An easier method for best fitting experimental results. *Mech Mater* 2011; 43: 799–806.

[41] Mark JE, Erman BR. *Science and Technology of Rubber*. 2005. Epub ahead of print 2005. DOI: 10.1016/B978-0-12-464786-2.X5000-7.

[42] Lion A, Johlitz M. *Constitutive models for Rubber X : proceedings of the 10th European Conference on Constitutive Models for Rubber (ECCMR X), Munich, Germany, 28-31*

August 2017).

[43] Koeller RC. Applications of fractional calculus to the theory of viscoelasticity. *J Appl Mech Trans ASME* 1984; 51: 299–307.

[44] Genovese A, Carputo F, Maiorano A, et al. Study on the Generalized Formulations with the Aim to Reproduce the Viscoelastic Dynamic Behavior of Polymers. *Appl Sci* 2020; 10: 2321.

[45] Meral FCC, Royston TJJ, Magin R. Fractional calculus in viscoelasticity: An experimental study. *Commun Nonlinear Sci Numer Simul* 2010; 15: 939–945.

[46] Sasso M, Palmieri G, Amodio D. Application of fractional derivative models in linear viscoelastic problems. *Mech Time-Dependent Mater* 2011; 15: 367–387.

[47] Palmeri A, Ricciardelli F, De Luca A, et al. State Space Formulation for Linear Viscoelastic Dynamic Systems with Memory. *J Eng Mech* 2003; 129: 715–724.

[48] Pintelon R (Rik), Schoukens J (Johan). *System identification : a frequency domain approach*. Wiley, 2012.

[49] Farroni F, Russo R, Timpone F. Experimental Investigations on Rubber Friction Coefficient Dependence on Visco-Elastic Characteristics, Track Roughness, Contact Force, and Slide Velocity. *Tire Sci Technol* 2017; 45: 3–24.

[50] Schoff CK. Dynamic mechanical analysis. *CoatingsTech* 2008; 5: 44.

[51] Krevelen DW van. *Properties of polymers : their correlation with chemical structure ; their numerical estimation and prediction from additive group contributions*. Elsevier, 1997.

[52] Farroni F, Saknevych A, Timpone F. Development of a Grip and Thermodynamics Sensitive Procedure for the Determination of Tyre / Road Interaction Curves Based on Outdoor Test Sessions. 2015.

[53] Carputo F, Farroni F, Genovese A, et al. An analysis on stress field distribution of a deformable rubber specimen due to indentation. In: *AIMETA 2017 - Proceedings of the 23rd Conference of the Italian Association of Theoretical and Applied Mechanics*. 2017.

[54] Arricale VM, Brancati R, Carputo F, et al. A physical-analytical model for friction hysteretic contribution estimation between tyre tread and road asperities. In: *Lecture Notes in Mechanical Engineering*. 2020, pp. 1061–1074.

[55] Le Gal A, Klüppel M. Investigation and modelling of rubber stationary friction on rough surfaces. *J Phys Condens Matter*; 20. Epub ahead of print 2008. DOI: 10.1088/0953-

8984/20/01/015007.

[56] Duncan J. Principles and Applications of Mechanical Thermal Analysis. In: *Principles and Applications of Thermal Analysis*. Blackwell Publishing Ltd, 2008, pp. 119–163.

[57] Gabbott P. *Principles and Applications of Thermal Analysis*. Oxford, UK: Blackwell Publishing Ltd. Epub ahead of print 16 April 2008. DOI: 10.1002/9780470697702.

[58] Mondragón I, Solar L, Nohales A, et al. Properties and structure of cyanate ester/polysulfone/organoclay nanocomposites. *Polymer (Guildf)* 2006; 47: 3401–3409.

[59] Boquillon N, Fringant C. Polymer networks derived from curing of epoxidised linseed oil: Influence of different catalysts and anhydride hardeners. *Polymer (Guildf)* 2000; 41: 8603–8613.

[60] Nien Y-H, Chen J. Studies of the mechanical and thermal properties of cross-linked poly(methylmethacrylate-acrylic acid-allylmethacrylate)-modified bone cement. *J Appl Polym Sci* 2006; 100: 3727–3732.

[61] ASTM D5279 - 13 Standard Test Method for Plastics: Dynamic Mechanical Properties: In Torsion.

[62] O'Connell PA, McKenna GB. Large deformation response of polycarbonate: Time-temperature, time-aging time, and time-strain superposition. *Polym Eng Sci* 1997; 37: 1485–1495.

[63] Hsich HSY. Composite rheology - I. Elastomer-filler interaction and its effect on viscosity. *J Mater Sci* 1982; 17: 438–446.

[64] Szabo TL, Wu J. A model for longitudinal and shear wave propagation in viscoelastic media. *J Acoust Soc Am* 2000; 107: 2437–2446.

[65] Unseld K, Albohr O, Herrmann V, et al. *New Indentation Methods for the Characterisation of Elastomer Composites*, http://www.all-electronics.de/ai/resources/58f7eb2af86.pdf (accessed 29 May 2020).

[66] Sneddon IN. The elastic stresses produced in a thick plate by the application of pressure to its free surfaces. *Math Proc Cambridge Philos Soc* 1946; 42: 260–271.

[67] Sneddon IN. The relation between load and penetration in the axisymmetric boussinesq problem for a punch of arbitrary profile. *Int J Eng Sci* 1965; 3: 47–57.

[68] Pharr GM. An improved technique for determining hardness and elastic modulus using load and displacement sensing indentation experiments. *J Mater Res* 1992; 7: 1564–1583.

[69] White CC, Vanlandingham MR, Drzal PL, et al. Viscoelastic characterization of polymers using instrumented indentation. II. Dynamic testing. *J Polym Sci Part B Polym Phys* 2005; 43: 1812–1824.

[70] Harding JW, Sneddon IN. The elastic stresses produced by the indentation of the plane surface of a semi-infinite elastic solid by a rigid punch. *Math Proc Cambridge Philos Soc* 1945; 41: 16–26.

[71] Sneddon IN. The relation between load and penetration in the axisymmetric boussinesq problem for a punch of arbitrary profile. *Int J Eng Sci* 1965; 3: 47–57.

[72] Oliver WC, Brotzen FR. On the generality of the relationship among contact stiffness, contact area, and elastic modulus during indentation. *J Mater Res* 1992; 7: 613–617.

[73] Wang L, Liu X. Characterization of viscoelastic materials by quasi-static and dynamic indentation. *Meas Sci Technol*; 25. Epub ahead of print 2014. DOI: 10.1088/0957-0233/25/6/064017.

[74] Vriend NM, Kren AP. Determination of the viscoelastic properties of elastomeric materials by the dynamic indentation method. *Polym Test* 2004; 23: 369–375.

[75] Shimizu S, Yanagimoto T, Research MS-J of materials, et al. Pyramidal indentation load–depth curve of viscoelastic materials. *cambridge.org*.

[76] Dao M, Chollacoop N, Van Vliet KJ, et al. *Computational modeling of the forward and reverse problems in instrumented sharp indentation*. 2001.

[77] Herbert EG, Oliver WC, Pharr GM. Nanoindentation and the dynamic characterization of viscoelastic solids. *J Phys D Appl Phys* 2008; 41: 9.

[78] Vanlandingham MR, Chang NK, Drzal PL, et al. Viscoelastic characterization of polymers using instrumented indentation. I. Quasi-static testing. *J Polym Sci Part B Polym Phys* 2005; 43: 1794–1811.

[79] Meththananda IM, Parker S, Patel MP, et al. The relationship between Shore hardness of elastomeric dental materials and Young's modulus. *Dent Mater* 2009; 25: 956–959.

[80] Kunz J, Studer M. Determining the Modulus of Elasticity in Compression via the Shore A Hardness Theoretical Background. *Kunststoffe Int* 2006; 1–3.

[81] Boussinesq J. *Application des potentiels à l'étude de l'équilibre et du mouvement des solides élastiques: principalement au calcul des déformations et des pressions que*. 1885.

[82] Timoshenko SP, Gere JM, Prager W. Theory of Elastic Stability, Second Edition. *J Appl*

Mech 1962; 29: 220–221.

[83] Xu ZH, Li X. Effects of indenter geometry and material properties on the correction factor of Sneddon's relationship for nanoindentation of elastic and elastic-plastic materials. *Acta Mater* 2008; 56: 1399–1405.

[84] Ewoldt RH, Hosoi AE, McKinley GH. New measures for characterizing nonlinear viscoelasticity in large amplitude oscillatory shear. *J Rheol (N Y N Y)* 2008; 52: 1427–1458.

[85] Landais C. Ultrasonic Methods for the Characterization of Complex Materials and Material Systems : Polymers , Structured Polymers , Soft Tissue and Bone. 2011; 92.

[86] Schmerr LW. *Fundamentals of Ultrasonic Nondestructive Evaluation: A Modeling Approach (Springer Series in Measurement Science and Technology)*. 2016.

[87] Laugier P, Haïat G. Bone quantitative ultrasound. *Bone Quant Ultrasound* 2011; 1–468.

[88] Lionetto F, Montagna F, Maffezzoli A. Ultrasonic dynamic mechanical analysis of polymers. *Appl Rheol* 2005; 15: 326–335.

[89] Lionetto F, Maffezzoli A. Polymer characterization by ultrasonic wave propagation. *Advances in Polymer Technology* 2008; 27: 63–73.

[90] Mc Hugh J. Ultrasound Technique for the Dynamic Mechanical Analysis (DMA) of Polymers. 2008; 63–64.

[91] Krautkrämer J, Krautkrämer H. *Ultrasonic Testing of Materials*. Springer Berlin Heidelberg, 1990. Epub ahead of print 1990. DOI: 10.1007/978-3-662-10680-8.

[92] Carlson JE, Van Deventer J, Scolan A, et al. Frequency and temperature dependence of acoustic properties of polymers used in pulse-echo systems. *Proc IEEE Ultrason Symp* 2003; 1: 885–888.

[93] Nolle AW, Sieck PW. Longitudinal and transverse ultrasonic waves in a synthetic rubber. *J Appl Phys* 1952; 23: 888–894.

[94] Maiorano A, Napolitano Dell'Annunziata G, Rocca E. Experimental measurements through ultrasounds for viscoelasticity analysis. In: *IOP Conference Series: Materials Science and Engineering*. IOP Publishing Ltd, p. 012005.

[95] Sakhnevych A, Genovese A, Maiorano A, et al. An ultrasound method for characterization of viscoelastic properties in frequency domain at small deformations. *Proc Inst Mech Eng Part C J Mech Eng Sci* 2021; 095440622110057.

[96] *ECHOGRAPH 1095 Digital Ultrasonic Flaw Detector*.

[97] Waltz RA, Morales JL, Nocedal J, et al. An interior algorithm for nonlinear optimization that combines line search and trust region steps. *Math Program*. Epub ahead of print 2006. DOI: 10.1007/s10107-004-0560-5.

[98] Betts JT. Solving the nonlinear least square problem: Application of a general method. *J Optim Theory Appl* 1976; 18: 469–483.

[99] Gill PE, Murray W. Algorithms for the Solution of the Nonlinear Least-Squares Problem. *SIAM J Numer Anal* 1978; 15: 977–992.

[100] Schultz JW. Dielectric Spectroscopy in Analysis of Polymers. In: *Encyclopedia of Analytical Chemistry*. John Wiley & Sons, Ltd, 2000. Epub ahead of print 30 October 2000. DOI: 10.1002/9780470027318.a2004.

[101] Alegria A, Colmenero J. Dielectric relaxation of polymers: Segmental dynamics under structural constraints. *Soft Matter* 2016; 12: 7709–7725.

[102] Asami K. Characterization of heterogeneous systems by dielectric spectroscopy. *Progress in Polymer Science (Oxford)* 2002; 27: 1617–1659.

[103] Schultz JW. Dielectric Spectroscopy in Analysis of Polymers. In: *Encyclopedia of Analytical Chemistry*. Chichester, UK: John Wiley & Sons, Ltd. Epub ahead of print 30 October 2000. DOI: 10.1002/9780470027318.a2004.

[104] Farroni F, Genovese A, Maiorano A, et al. Development of an Innovative Instrument for Non-destructive Viscoelasticity Characterization: VESevo. In: *Mechanisms and Machine Science*. Springer, 2021, pp. 804–812.

[105] Carputo F, Genovese A, Maiorano A, et al. Experimental Activity for the Analysis of Tires Tread Responses at Different Conditions with a Dynamic Dial Indicator. 2020, pp. 1045–1060.

[106] Cho JR, Lee HW, Jeong WB, et al. Numerical estimation of rolling resistance and temperature distribution of 3-D periodic patterned tire. *Int J Solids Struct* 2013; 50: 86–96.

[107] ISO. ISO 28580: Passenger car, truck and bus tyres — Methods of measuring rolling resistance — Single point test and correlation of measurement results. 2009; 2009: 34.

[108] Torbruegge S, Wies B. Characterization of pavement texture by means of height difference correlation and relation to wet skid resistance. *J Traffic Transp Eng (English Ed* 2015; 2: 59–67.

[109] Popov VL. *Contact mechanics and friction: Physical principles and applications*. Springer

Berlin Heidelberg, 2010. Epub ahead of print 2010. DOI: 10.1007/978-3-642-10803-7.

[110] Bhushan B. *Modern Tribology Handbook, Two Volume Set*. 2000. Epub ahead of print 2000. DOI: 10.1201/9780849377877.

[111] Gadelmawla ES, Koura MM, Maksoud TMA, et al. Roughness parameters. *J Mater Process Technol* 2002; 123: 133–145.

[112] Genovese A, Carputo F, Ciavarella M, et al. Analysis of multiscale theories for viscoelastic rubber friction. In: *Lecture Notes in Mechanical Engineering*. Springer, 2020, pp. 1125–1135.

[113] Cannon JW, Mandelbrot BB. The Fractal Geometry of Nature. *Am Math Mon* 1984; 91: 594.

[114] Le Gal A, Yang X, Klüppel M. Evaluation of sliding friction and contact mechanics of elastomers based on dynamic-mechanical analysis. *J Chem Phys*; 123. Epub ahead of print 2005. DOI: 10.1063/1.1943410.

[115] Heinrich G, Klüppel M, Vilgis TA. Evaluation of self-affine surfaces and their implication for frictional dynamics as illustrated with a Rouse material. *Comput Theor Polym Sci* 2000; 10: 53–61.

[116] Le Gal A, Guy L, Orange G, et al. Modelling of sliding friction for carbon black and silica filled elastomers on road tracks. *Wear* 2008; 264: 606–615.

[117] Wang J, Tiwari A, Sivebaek IM, et al. Quantitative characterization of surface topography using spectral analysis. *Phys Rev E - Stat Nonlinear, Soft Matter Phys* 2020; 19: 1–8.

[118] Contact of nominally flat surfaces. *Proc R Soc London Ser A Math Phys Sci* 1966; 295: 300–319.

[119] Greenwood JA, Putignano C, Ciavarella M. A Greenwood & Williamson theory for line contact. *Wear* 2011; 270: 332–334.

[120] Tomanik E, Chacon H, Teixeira G. A simple numerical procedure to calculate the input data of Greenwood-Williamson model of asperity contact for actual engineering surfaces. *Tribol Ser* 2003; 41: 205–215.

[121] Tolpekina T, Pyckhout-Hintzen W, Persson BNJ. Linear and Nonlinear Viscoelastic Modulus of Rubber. *Lubricants* 2019; 7: 22.

[122] Grosch KA. Visco-elastic properties and the friction of solids: Relation between the friction and visco-elastic properties of rubber. *Nature* 1963; 197: 858–859.

[123] Grosch KA. The Rolling Resistance, Wear and Traction Properties of Tread Compounds.

Rubber Chem Technol 1996; 69: 495–568.

[124] Smith RH. *Analyzing Friction in the Design of Rubber Products and Their Paired Surfaces*. CRC Press. Epub ahead of print 24 March 2008. DOI: 10.1201/9780849381379.

[125] Kummer H. *Unified theory of rubber and tire friction*. University Park: Pennsylvania State University College of Engineering, 1966.

[126] Savkoor AR. On the friction of rubber. *Wear* 1965; 8: 222–237.

[127] Bowden FP, Tabor D. Friction, lubrication and wear: A survey of work during the last decade. *British Journal of Applied Physics* 1966; 17: 1521–1544.

[128] Sackfield A, Hills D. A note on the hertz contact problem: A correlation of standard formulae. *J Strain Anal Eng Des* 1983; 18: 195–197.

[129] *Mechanics of Elastic Contacts*. Elsevier, 1993. Epub ahead of print 1993. DOI: 10.1016/c2009-0-24029-3.

[130] Nakajima Y. *Advanced tire mechanics*. Springer Singapore, 2019. Epub ahead of print 3 April 2019. DOI: 10.1007/978-981-13-5799-2.

[131] Hamilton GM, Goodman LE. The stress field created by a circular sliding contact. *J Appl Mech Trans ASME* 1964; 33: 371–376.

[132] M HG. Explicit equations for the stresses beneath a sliding spherical contact. *Proc Inst Mech Eng Part C Mech Eng Sci* 1983; 197: 53–59.

[133] Hertz H. Miscellaneous Papers. *Arch Androl* 1983; 11: 197–222.

[134] Persson BNJ, Brener EA. Crack propagation in viscoelastic solids. *Phys Rev E - Stat Nonlinear, Soft Matter Phys* 2005; 71: 036123.

[135] Williams ML, Ferry JD. Second approximation calculations of mechanical and electrical relaxation and retardation distributions. *J Polym Sci* 1953; 11: 169–175.

[136] Pacejka HB, Sharp RS. Shear Force Development by Pneumatic Tyres in Steady State Conditions: A Review of Modelling Aspects. *Veh Syst Dyn* 1991; 20: 121–175.

[137] Schallamach A. How does rubber slide? *Wear* 1971; 17: 301–312.

[138] Étienne S, David L. *Introduction à la physique des polymères*. 2012.

[139] Ciaravola V, Farroni F, Fortunato G, et al. An evolved version of the British pendulum tester for the experimental investigation of contact between tire tread and rough surfaces. *Eng Lett* 2017; 25: 1–8.

[140] Arricale VM, Carputo F, Farroni F, et al. Experimental investigations on tire/road friction

dependence from thermal conditions carried out with real tread compounds in sliding contact with asphalt specimens. In: *Key Engineering Materials*. Trans Tech Publications Ltd, 2019, pp. 261–266.

[141] Genovese A, D'Angelo GA, Sakhnevych A, et al. Review on friction and wear test rigs: An overview on the state of the art in tyre tread friction evaluation. *Lubricants* 2020; 8: 91.

[142] Eberhardsteiner J, Fidi W, Liederer W. Experimental determination of adhesive friction properties of rubber on plain surfaces. *Kautschuk und Gummi, Kunststoffe* 1998; 51: 773–781.

[143] Liu F, Sutcliffe MPF, Graham WR. Prediction of tread block forces for a free-rolling tyre in contact with a smooth road. *Wear* 2010; 269: 672–683.

[144] Abdo J, Zaier R. A novel pin-on-disk machine for stick-slip measurements. *Mater Manuf Process* 2012; 27: 751–755.

[145] Farroni F, Rocca E, Russo R, et al. Experimental investigations about adhesion component of friction coefficient dependence on road roughness, contact pressure, slide velocity and dry/wet conditions. In: *Proceedings of the Mini Conference on Vehicle System Dynamics, Identification and Anomalies*. 2012.

[146] ASTM. *ASTM E 303-93 Standard Test Method for Measuring Surface Frictional Properties Using the British*. 2018.

[147] Qasrawi H, Asi I. Effect of bitumen grade on hot asphalt mixes properties prepared using recycled coarse concrete aggregate. *Constr Build Mater* 2016; 121: 18–24.

[148] Carbone G, Putignano C. A novel methodology to predict sliding and rolling friction of viscoelastic materials: Theory and experiments. *J Mech Phys Solids* 2013; 61: 1822–1834.

[149] Farroni F, Russo R, Timpone F. Experimental investigations on rubber friction coefficient dependence on visco-elastic characteristics, track roughness, contact force, and slide velocity. *Tire Sci Technol* 2017; 45: 3–24.

[150] Farroni F, Rocca E, Russo R, et al. Experimental investigations about adhesion component of friction coefficient dependence on road roughness, contact pressure, slide velocity and dry/wet conditions. In: *Proceedings of the Mini Conference on Vehicle System Dynamics, Identification and Anomalies*. 2012, pp. 303–317.